Mechanisms, Active Sites, and Promoters for the Direct Synthesis of Hydrogen Peroxide on Pd-Based Catalysts

By

Anthony D. Plauck

A dissertation submitted in partial fulfillment of

the requirements for the degree of

Doctor of Philosophy

(Chemical Engineering)

at the

UNIVERSITY OF WISCONSIN-MADISON

2016

Date of final oral examination: 11/21/2016

The dissertation is approved by the following members of the Final Oral Committee:

Manos Mavrikakis, Professor, Chemical & Biological Engineering
James A. Dumesic, Professor, Chemical & Biological Engineering
George W. Huber, Professor, Chemical & Biological Engineering
Victor M. Zavala, Assistant Professor, Chemical & Biological Engineering
Ive Hermans, Associate Professor, Chemistry
Eric E. Stangland, Principal Research Scientist, The Dow Chemical Company

Abstract

The widespread use of hydrogen peroxide (H_2O_2) for catalytic oxidations is limited by the wasteful process by which it is currently produced: the anthraquinone process. The direct synthesis of H_2O_2 (DSHP) is a promising alternative process. One primary technical obstacle to its commercialization is the identification of sufficiently active and selective heterogeneous catalysts. Although Pd is a promising active component that is used in most catalyst formulations, two factors have restricted the search directions for improved DSHP catalysts to experimental trial and error: (i) the reaction mechanisms are not resolved, and (ii) the active site requirements are poorly understood. Addressing these factors is complicated by the existence of multiple side reactions and the inherent complexities of heterogeneous catalysts and the DSHP reaction environment.

In this dissertation, we employ density functional theory calculations to develop an atomic-scale understanding of the DSHP on Pd-based catalysts. We propose reaction mechanisms and analyze Pd's intrinsic reactivity toward forming H_2O_2 versus H_2O from H_2 and O_2. We also develop an experimentally-consistent microkinetic model that describes H_2O_2 decomposition on Pd; one of the major drawbacks of Pd catalysts is high activity toward this undesirable reaction. Through these studies we highlight specific mechanistic challenges, including the identification of likely rate-limiting steps. We then consider how catalyst structure and composition can be modified to mitigate these challenges. We analyze the impact of the coordinative saturation of the Pd surface, the role of halides and Au as catalytic promoters, and the effect of phase transformations induced by the reaction environment.

Our work demonstrates the utility of computational chemistry in deconvoluting complex catalytic systems – especially when coupled with experimental and microkinetic analyses. The results can potentially be used to build a framework that guides the search for new DSHP catalysts.

Acknowledgements

I would first like to thank my advisor, Professor Manos Mavrikakis. He struck a healthy balance between challenging me and understanding my capacity as a graduate student. Professor Mavrikakis has been a constant source of deep insights, and his methodical yet creative approach to research has positively influenced my thinking process. I hope to carry his passion for research and his strong work ethic with me in my future endeavors.

Although not my official co-advisor, Professor James A. Dumesic has also been an invaluable mentor during my studies. I greatly appreciate all the time he has invested in my project, especially his guidance and patience with the experimental aspects. I also thank him for serving on my preliminary exam and defense committees. On that note, I extend my thanks to the rest of the CBE faculty for their support and feedback during my studies. In particular, I thank Professor Christos T. Maravelias and Professor Michael D. Graham for serving on my preliminary and fourth year exam committees. I also thank Professor George W. Huber, Professor Ive Hermans, and Professor Victor M. Zavala for serving on my defense committee.

The work presented in this thesis has been in collaboration with (and funded by) The Dow Chemical Company. I am grateful to all of our Dow collaborators for their contributions to this work, particularly the opportunity to learn from their expertise. I thank Jack Kruper, Edward Lee, and Thomas Gilbert for initiating this project and for their continued support during its course. I especially thank Eric E. Stangland, this project's Principal Investigator from Dow; his encouragement, flexibility, and eagerness to assist all aspects of this project have undoubtedly eased my studies. I also thank Eric for serving on my defense committee. Finally, I thank all other Dow collaborators who have provided valuable feedback throughout our many teleconferences,

including David Barton, Wayne Blaylock, Ken Marshall, Sam Mistretta, Doran Bennett, and Junqiang Liu.

I would also like to express my gratitude to the many members of the UW-Madison CBE department staff for their support. In particular, I am grateful for computer support from Todd Ninman, Russ Poyner, and Mary Heimbecker, and I am grateful for purchasing assistance from Christi Levenson and Michelle Kirch. I also thank Joel Lord and Eric Codner for technical assistance.

I would like to recognize the guidance from Professor Fuat E. Celik during my first year at UW-Madison, as well as collaboration with Professor Ana C. Alba-Rubio on a significant portion of this thesis. (I am especially grateful for the tireless nights and weekends she spent on the electron microscope.) I wish them both the best of luck in their academic careers.

I also thank all the members of the Computational Surface Science and Catalysis group. In particular, I am grateful for many lengthy and always fruitful discussions with [soon to be] Professor Srinivas Rangarajan – his future students will be privileged to have him as their Professor. I thank Dr. Luke T. Roling for his friendship and for countless research discussions, which I hope were mutually beneficial. I am also grateful to Dr. Jeffrey Herron, Dr. Guowen Peng, Dr. Sha Li, Dr. Yunhai Bai, Dr. Suyash Singh, and Lang Xu for always providing thoughtful responses to my technical questions. I extend this thanks to all other colleagues in the CBE department who I have interacted with over the past years. I thank Professor Thomas J. Schwartz and Dr. Ronald Carrasquillo for allowing me to bombard them with experimental questions and for equipment training. I am especially grateful for my lunch buddies, Dr. Mark Politz and Dr.

Max Mellmer (also my housemate of three years); hopefully we move on to healthier eating habits post-graduation…

Lastly, I would like to thank my family for love and support: Darryl, Diane, Nick, and Greg. I also thank Mr. and Mrs. Lee for a continuous supply of kimchi and other Korean delectables. Importantly, I thank my girlfriend Angel, who has endured me during the entirety of this experience.

Table of Contents

List of Figures

List of Tables

Chapter 1: Introduction

1.1 Green Chemistry and Heterogeneous Catalysis

The guiding principle of "green chemistry" is to eliminate or minimize the intrinsic hazards of chemical products and processes.[1] It is a proactive rather than remedial approach to reducing risks posed by the chemical industry – both to the environment and to human beings – while meeting modern society's demand for chemical products.[2] Numerous texts have been devoted to the continued development and dissemination of the concepts of green chemistry, and the importance of this issue is also recognized with national awards including the U.S. Presidential Green Chemistry Challenge.[3]

Many challenges to implementing new (or modifying existing) chemical processes that meet the criteria of green chemistry[1] can involve identifying improved catalytic materials – in particular, heterogeneous catalysts, which afford more facile recovery and recycling compared to their homogeneous counterparts.[4] Catalysts enable chemical syntheses to proceed at low temperatures and pressures to increase energy efficiency, are reusable as opposed to stoichiometric

reagents, and can help minimize the waste produced per amount of desired product.[5] However, heterogeneous catalysts can be complex materials. They are primarily composed of an active component dispersed on a high surface area support material. A combination of diverse experimental and theoretical techniques is often necessary to establish the relationships between the structure/composition of the active component and catalytic performance that will aid catalyst design. This thesis focuses on the development of improved Pd-based catalysts for an alternative, greener production process for hydrogen peroxide (H_2O_2): the direct synthesis of H_2O_2.

1.2 Hydrogen Peroxide – A Green Oxidant, Produced by a Not-So-Green Process

Hydrogen peroxide is a versatile and environmentally benign chemical oxidant that has the potential to decrease the environmental impact of numerous manufacturing processes.[6, 7] Water is the only byproduct of its use. The largest demand for H_2O_2 is in the pulp and paper industry, where H_2O_2 can be used to displace or completely replace chlorinated compounds.[8-10] H_2O_2 is also an important chemical oxidant for the treatment of industrial wastewater.[11, 12] Furthermore, the utilization of H_2O_2 for selective oxidation reactions represents a growing field and has garnered a number of Presidential Green Chemistry Challenge awards;[3] H_2O_2 can be used to oxidize alcohols, olefins, and sulfides under mild conditions, replacing deleterious heavy metal and organic stoichiometric oxidants, among others.[13-15] In 2006, the annual global market for H_2O_2 was estimated to be 2.2 million metric tons,[10] and a recent market report by Global Industry Analysts, Inc. projects that the annual worldwide demand for H_2O_2 will exceed 5.7 million metric tons by 2022.[16]

Despite the efficacy of H_2O_2 as a green oxidant, the introduction and expansion of chemical processes that utilize H_2O_2 can be limited by the high cost of its production. Nearly all H_2O_2 used in industry today is produced by the anthraquinone (AO) process.[17] The basic description of the

AO process is simple: an alkyl anthraquinone is cyclically hydrogenated by H_2 to the hydroquinone, and then auto-oxidized in air to liberate H_2O_2 and regenerate the alkyl anthraquinone (Figure 1.1). The major drawbacks of the AO process are tied to the many unit operations surrounding these two reaction steps. First, the hydrogenation catalyst (typically palladium or Raney nickel) must be filtered from the working solution (a solvent mixture containing the dissolved anthraquinone/hydroquinone) prior to the oxidation reactor to prevent catalytic H_2O_2 decomposition. Second, the H_2O_2 is extracted from the oxidized working solution using water, and residual water is removed from the working solution by drying. Third, the working solution must be purified and regenerated because the solvent mixture and anthraquinone form degradation products during their continuous circulation; some degradation products, particularly those formed in the hydrogenation reactor, cannot be regenerated and lead to waste generation. Moreover, some of the working solution is stripped by the air used in the oxidation reactor. There are also additional unit operations required to process the crude H_2O_2 that is extracted from the working solution: organic and metallic contaminants are removed from the crude H_2O_2 by treatments such as solvent extraction and ion-exchange, and distillation is usually applied to further purify and concentrate the H_2O_2 to 50-70 wt % H_2O_2 for commercial distribution.[17]

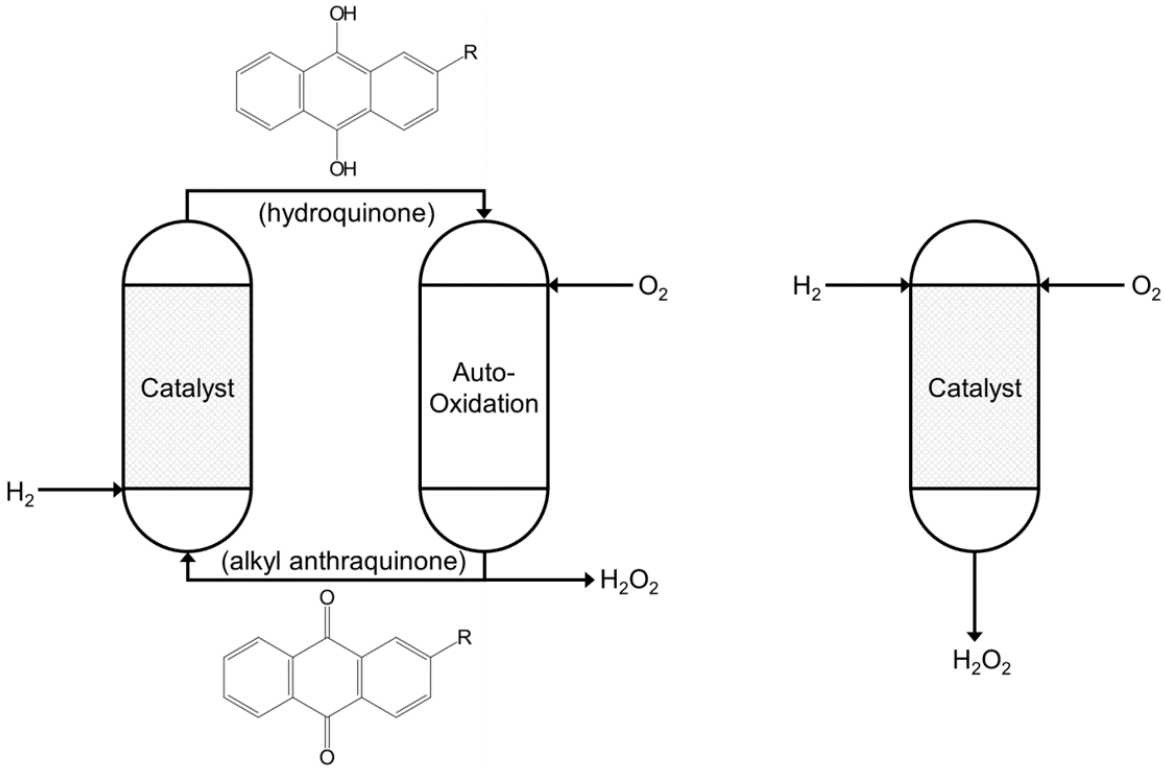

The Anthraquinone Process (AO Process) **The Direct Synthesis of H_2O_2 (DSHP)**

Figure 1.1 Simplified diagram of the overall reactions that produce H_2O_2 in the AO process and the DSHP. Other unit operations involved in the AO process, including extraction, purification, and distillation, are not included here but are described in the text. The DSHP is generally performed in a liquid solvent such as water.

Clearly, the AO process can be considered a less than green process due to significant waste generation, utilization of large amounts of organic solvents and quinone (which themselves can be synthesized by processes that generate toxic wastes), high energy consumption by the many unit operations, and the requirement for a large-scale plant due to economies of scale. A consequence of the latter is that H_2O_2 is often produced far from its point-of-use and must be stabilized and transported. The single-step direct synthesis of H_2O_2 (DSHP) from H_2 and O_2 using a heterogeneous transition metal catalyst is a promising alternative to the AO process (Figure 1.1).[18] Not only would a DSHP process enable on-site production of H_2O_2 for small- to medium-scale processes, increasing the attraction and feasibility of H_2O_2 as a green oxidant, but the DSHP process itself would be green: this reaction can be performed in a single reactor using an aqueous

solvent, and the only side product is water. García-Serna et al[19] discuss the economic viability of a DSHP process in comparison with the existing AO process. There is also the potential to couple selective oxidation processes with the *in situ* direct synthesis of H_2O_2, such as in the epoxidation of propylene.[15, 20, 21] However, a DSHP process has not yet been commercialized even though its origins date back as far as 1914.[22] A primary technical obstacle toward the implementation of a DSHP process is finding sufficiently active and selective heterogeneous catalysts – highlighted by the abundance of review articles published on this subject within the last ten years.[15, 18, 19, 23-28]

1.3 Catalytic Challenges for the Direct Synthesis of H_2O_2

Both the AO process and the DSHP produce H_2O_2 from H_2 and O_2 (Figure 1.1). The former separates the hydrogenation (catalytic) and oxidation (non-catalytic) steps and therefore avoids side reactions that can occur between H_2 and [O_2 or H_2O_2] over the catalyst – as well as direct catalytic H_2O_2 decomposition. It is these side reactions that constitute a selectivity challenge for DSHP catalysts, because H_2, O_2, H_2O_2, and catalyst are all present in the same reactor. The complete reduction of O_2 to H_2O is more thermodynamically favorable than the partial reduction of O_2 to H_2O_2:

[**Reaction 1**] $H_2(g) + O_2(g) \rightarrow H_2O_2(l)$ $\Delta G°_{298K} = -120.4$ kJ mol^{-1},

[**Reaction 2**] $H_2(g) + O_2(g) \rightarrow H_2O(l) + ½O_2(g)$ $\Delta G°_{298K} = -237.1$ kJ mol^{-1},

Consequently, H_2O_2 decomposition (disproportionation),

[**Reaction 3**] $H_2O_2(l) \rightarrow H_2O(l) + ½O_2(g)$ $\Delta G°_{298K} = -116.7$ kJ mol^{-1},

and H_2O_2 hydrogenation by H_2,

[**Reaction 4**] $H_2O_2(l) + H_2(g) \rightarrow 2H_2O(l)$ $\Delta G°_{298K} = -353.8$ kJ mol^{-1},

are also thermodynamically favorable reactions. The optimal DSHP catalyst must therefore selectively produce H_2O_2 at high rates and preserve H_2O_2 from decomposition.

Pd is the most studied transition metal catalyst for the DSHP, but pure Pd is generally poorly selective toward H_2O_2 and is highly active toward the H_2O_2 decomposition reactions.[26, 29-31] There is a large body of experimental literature concerning catalyst preparation methodology, pretreatment conditions, and reaction conditions, from which some widely-accepted strategies have emerged to enhance Pd's activity and selectivity. These include alloying Pd with Au[32-36] or Pt,[37-40] adding acids or using CO_2 as the gas-phase diluent (which itself acidifies aqueous reaction media by forming carbonic acid), and adding halides in the form of hydrogen halides or halide salts.[18, 26] Nonetheless, systematic improvements to Pd-based catalysts are limited by two factors: the *reaction mechanisms* for H_2O_2 synthesis, H_2O synthesis, and H_2O_2 decomposition have not been resolved, and the *active sites* remain poorly understood.

Insights into the DSHP reaction mechanisms have mainly been derived from fitting semi-empirical rate expressions (e.g., power law rate expressions) to experimental kinetics data and lack a detailed description of the elementary surface processes.[41-51] There are also some examples where theoretical calculations have been used to explore elementary steps.[52-56] The H_2O_2 synthesis mechanism is normally assumed to proceed through the sequential hydrogenation of molecular oxygen on the catalyst surface, i.e. $O_2 \rightarrow OOH \rightarrow H_2O_2$, with OOH as the key intermediate. The nature of the hydrogenation steps may be more complex than a direct reaction between surface-bound hydrogen atoms and oxygen, specifically when the DSHP is performed in a liquid solvent; some researchers propose solvent-assisted hydrogenations[56, 57] and even a direct role of solvated protons.[58-60] Furthermore, Dissanayake and Lunsford demonstrated that no $H_2{}^{16}O{}^{18}O$ is formed from a reactant mixture of [$^{18}O_2$ + $^{16}O_2$] with H_2 over a Pd/SiO_2 catalyst,[61] which suggests that

breaking the O-O bond is irreversible on Pd and leads to H_2O formation. A catalyst selective toward H_2O_2, then, must not break the O-O bond, but still needs to dissociate H_2. While the O-O bond in gas-phase O_2 is stronger than the H-H bond in H_2, adding H atoms to O_2 progressively weakens the O-O bond (Table 1.1). More mechanistic analyses should be performed to discern the O-O bond breaking channel(s) that are likely to produce H_2O, understand the nature of the hydrogenation steps, and identify which elementary step(s) are rate and selectivity determining on Pd catalysts for the DSHP – also considering the secondary H_2O_2 decomposition reactions.

Table 1.1 Experimental gas-phase bond enthalpies.[62]

Species	**$\Delta H°_{298K}$ / kJ mol^{-1}**
$H_2 \rightarrow H + H$	436.0
$O_2 \rightarrow O + O$	498.4
$OOH \rightarrow O + OH$	286.1
$H_2O_2 \rightarrow OH + OH$	214.1

The microscopic properties (binding energies, activation barriers) that differentiate competing reaction mechanisms and ultimately regulate the macroscopic kinetics can be sensitive to the structure and composition of the active site. Unfortunately, conventional synthesis techniques for supported metal catalysts (e.g., impregnation[63]) do not provide tight control over the metal nanoparticles, and this problem can amplify when other components are introduced. A variety of surface structures exists, which all may contribute to the observed kinetics to difference degrees. There have been no definitive conclusions regarding the site requirements for active and selective H_2O_2 synthesis, nor what sites are responsible for H_2O_2 decomposition on Pd-based catalysts. Another complication is that the reaction environment can modify these sites, even though there have been substantial efforts to correlate the structural/compositional features of freshly synthesized and characterized Pd-based catalysts with experimental reactivity. H_2 and O_2 can both form surface/bulk phases with Pd (hydride,[64] oxide[65]). Seemingly contradictory studies

claim reduced Pd,[30, 66, 67] oxidized Pd,[46, 68-70] or a coexistence of the two[71] to be the active phase for H_2O_2 formation. The possibility of bulk Pd hydride as an active phase has been given considerably less attention,[46, 53] despite the fact that a Pd hydride phase is thermodynamically favorable under the typical temperatures and H_2 pressures employed for the DSHP. Various hypotheses also exist concerning the role of catalytic promoters, specifically the halides – which are known to increase selectivity toward H_2O_2 and suppress H_2O_2 decomposition.[26, 29, 47, 57, 66, 68, 72-74] Evidently, characterizing the active sites and their interaction with promoters in the DSHP is difficult through experiments alone due to the complexities of the heterogeneous catalyst and reaction environment.

1.4 Elucidating Mechanisms and Active Sites by Density Functional Theory

Advances in high-performance computing and modern electronic structure theoretical methods such as density functional theory (DFT)[75] have allowed researchers to model chemical phenomena that would otherwise be demanding – and sometimes inaccessible – to study with current experimental techniques. In terms of heterogeneous catalysis, DFT calculations provide atomic-scale resolution on the structures of intermediates and transition states, and so reaction mechanisms can be evaluated comprehensively at the level of individual elementary steps. The fundamental insights from DFT calculations have proven critical to the understanding of mechanisms for many industrially important reactions that include Fischer-Tropsch synthesis,[76-79] the water-gas shift reaction,[80-82] methanol synthesis,[83] and ammonia synthesis.[84]

Although the accuracy of DFT methods in some cases can be sufficient, for example, to differentiate competing reaction pathways and determine the likely rate-limiting step(s) on the sole basis of DFT calculations, many of the studies highlighted above demonstrate the importance of coupling DFT calculations with experimental measurements of reaction kinetics – e.g., in a

microkinetic model.[85, 86] Feedback between experiments and theory is important to the development of models that best capture the surface chemistry and the nature of the active sites under realistic operational conditions.

Ultimately, the chemical challenges identified through these mechanistic analyses can be overcome by proper material design.[87-89] Computational models have facilitated the deconvolution of structural, compositional, and environmental factors that can contribute to the reactivity of real catalysts – in particular, by explaining how these factors affect electronic structure.[90-96] One can then systematically propose design criteria for improved catalysts. There are an increasing number of examples in the literature where these theoretical foundations have supported the identification of improved catalysts for specific reactions (e.g., hydrogen evolution,[97, 98] steam reforming,[99] and electrochemical oxygen reduction[100-102]).

1.5 Thesis Scope

Search directions for new or improved DSHP catalysts are currently limited to experimental trial and error. In this thesis, we demonstrate the utility of density functional theory calculations – in some cases, coupling with experiments and microkinetic modeling – toward developing more detailed knowledge of the DSHP reaction mechanism on Pd-based catalysts and the effects of catalyst structure/composition on the underlying energetics. Our results can inform the search for better catalysts through (i) defining key activity- and selectivity-determining parameters and (ii) elucidating how we can tune these parameters to enhance catalyst performance in the DSHP. More generally, the mechanistic insights can be extended to *in situ* H_2O_2 synthesis for selective oxidation reactions, which can facilitate the realization of these greener oxidation processes in the chemical industry.

The main areas of advancement are in: elucidating elementary reaction mechanisms for the direct synthesis – and subsequent decomposition – of H_2O_2 on Pd, including kinetically-limiting steps and the impact of catalyst surface structure (Chapters 3 and 4); clarifying the essential roles of catalytic promoters in these mechanisms (halides, Chapters 5 and 6; and Au, Chapter 7); and understanding how changes to the surface/bulk state of Pd, induced by the reaction environment, can affect reactivity (Chapter 8). We conclude this thesis by summarizing our key results and providing recommendations for future work.

More specifically, in Chapter 3 we calculate thermodynamic and kinetic parameters for direct H_2O_2 versus H_2O formation mechanisms from H_2 and O_2 on the late transition metals (Pd, Pt, Cu, Ag, and Au). We compare energetics on the close-packed (111) and more open (100) facets, which indicate that none of the monometallic surfaces are expected to be both selective and active for direct H_2O_2 synthesis. In particular, selectivity toward H_2O_2 on Pd is limited by facile O-O bond dissociation in the OOH and O_2 surface intermediates on the (111) and (100) facets, respectively. We then analyze the mechanisms for H_2O_2 decomposition on these same facets of Pd in Chapter 4. We construct an experimentally-consistent mean-field microkinetic model based on our DFT-derived kinetic and thermodynamic parameters, which enables prediction of the flux-carrying and rate controlling steps in addition to the nature of the active Pd surfaces under reaction conditions.

Chapters 3 and 4 help to explain why *unmodified* Pd is generally found to be ineffective for the DSHP. We then consider the effect of adsorbed halides on the DSHP reaction mechanisms in Chapters 5 and 6. In Chapter 5, our DFT calculations on Pd(111) suggest that the primary role of adsorbed halides is to decrease the exothermicity – and raise kinetic barriers – of O-O bond dissociation in O_2 and OOH, and to restrict the re-adsorption of H_2O_2. We predict similar functions

for the halides on Pd(100) in Chapter 6, but our DFT calculations in this chapter also demonstrate that halides are less effective at these functions on more coordinatively undersaturated features of Pd compared to Pd(111). However, halides also preferentially populate the more coordinatively undersaturated Pd facets to a greater degree. In Chapter 7, we exploit an established synthesis technique, electroless deposition, to deposit sub-monolayer amounts of Au onto pre-existing Pd nanoparticles supported on silica. Although these Au-Pd bimetallic catalysts neither increase selectivity toward H_2O_2 nor suppress its decomposition compared with their monometallic Pd counterparts, *ex situ* spectroscopic measurements of adsorbed CO indicate that contiguous Pd ensembles remain at the surface of the bimetallic Au-Pd catalysts; this finding reinforces DFT calculations from the literature, which predict complete isolation of Pd atoms by Au to be desirable for limiting O-O bond dissociation. Finally, in Chapter 8 we use DFT calculations to examine the reactivity of Pd as the surface, subsurface, and bulk saturate with hydrogen. Subsurface penetration of hydrogen is facile at the typical temperatures and partial pressures of H_2 employed for the DSHP, but its potential role in the DSHP has not been characterized.

We begin with a brief background on density functional theory and the experimental methods employed in this thesis (Chapter 2).

Chapter 2: Overview of Methods

2.1 Background: The Shrödinger Equation and Density Functional Theory

Here we provide a brief synopsis regarding the development of density functional theory. We refer the reader to other works[75, 103-105] for more detailed accounts.

The time-independent Shrödinger equation is the fundamental equation for the quantum mechanical description of a physical system:

$$H\psi = E\psi$$

where ψ is the wavefunction, E is the total energy of the system, and H is the Hamiltonian operator. The form of the Hamiltonian depends on the system of interest, and the solutions provide energetic information as well as the probability distributions for all constituent particles.

Systems relevant to catalysis are complex (i.e., containing many electrons interacting with many nuclei). Fortunately, the electronic and nuclear wavefunctions can be decoupled by the Born-Oppenheimer Approximation; that is, the electronic wavefunctions can be solved for a given

arrangement of atomic nuclei because of the much faster motion of electrons due to their small mass, relative to the nuclei. The Hamiltonian describing the electronic wavefunction, $\psi_{electronic}$, can then be expressed as:

$$H = \underbrace{\sum_{i=1}^{N} \frac{-\hbar^2}{2m} \nabla_i^2}_{\textbf{kinetic energy}} + \underbrace{\sum_{i=1}^{N} V_{electron-nuclei}(r_i) + \sum_{i=1}^{N} \sum_{j<i} V_{electron-electron}(r_i, r_j)}_{\textbf{potential energy}}$$

where the sums are over all N electrons, $\hbar$ is the reduced Planck constant, m is the mass of an electron, and the r_i are the spatial coordinates for each electron. There are three terms in this Hamiltonian: the first is the sum of each electron's kinetic energy, the second is the sum of the interaction energy between each electron and all atomic nuclei ($V_{electron\text{-}nuclei}$), and the third is the sum of the interaction energy between different electrons ($V_{electron\text{-}electron}$). (Note that the electronic wavefunction also has a spin component for each electron, in addition to the spatial coordinates.) The last term of the Hamiltonian presents the largest challenge to solving the Shrödinger equation because the electron-electron interaction potential depends on simultaneously knowing the spatial distribution of all electrons. Solving this many-body problem require further approximations to the Hamiltonian.

Density functional theory (DFT) is one approach that was developed in the 1960's by Hohenberg, Kohn, and Sham.[106, 107] Hohenberg and Kohn proved two mathematical theorems that provided the foundation for DFT, and then Kohn and Sham derived a set of equations (the Kohn-Sham equations) that established how to implement DFT in practice.

A central concept of DFT is that the electron density ($n(r)$) at any given set of spatial coordinates r can be expressed as a summation of the one-electron wave functions (ψ_i):

$$n(r) = \sum_{i=1} |\psi_i(r_i)|^2$$

(Note again that these one-electron wave functions also have a spin component.) According to the first theorem from Hohenberg and Kohn, the ground state energy of the Shrödinger equation, *E*, is a *unique functional* of this electron density:

$$E = E[n(r)]$$

Furthermore, the second theorem from Hohenberg and Kohn states that the electron density corresponding to the full solution of the Shrödinger equation is the same electron density that *minimizes the energy of the functional.* (Therefore, the ground-state electron density can be found by varying the electron density until the energy of the functional is minimized.) Kohn and Sham then demonstrated that a set of *self-consistent one-electron equations* can be solved to minimize *E[n(r)]* (the Kohn-Sham equations), effectively *replacing the many-body electron problem*:

$$\left[\underbrace{\frac{-\hbar^2}{2m}\nabla_i^2}_{\textbf{kinetic energy}} + \underbrace{V_{electron-nuclei}(r) + V_{Hartree} + V_{XC}(r)}_{\textbf{potential energy}}\right]\psi_i(r_i) = \varepsilon_i\psi_i(r_i)$$

As with the Hamiltonian corresponding to the full Shrödinger equation, there are kinetic and potential energy contributions; however, the solutions to the Kohn-Sham equations are functions of only three spatial coordinates instead of *3N* spatial coordinates. The first potential energy term again corresponds to the interaction between an electron and the all atomic nuclei. The second potential energy term, the Hartree potential, corresponds to the interaction between a given electron and the total electron density *n(r)*. These two potential energy terms are readily defined. The third potential energy term, V_{XC}, is the exchange-correlation potential. This term

contains corrections for the self-interaction introduced in $V_{Hartree}$ (because each electron is part of the total electron density) as well as other quantum mechanical effects, but the exact form of V_{XC} is unknown. The functional derivative of V_{XC} with respect to the electron density is the exchange-correlation functional, $E_{XC}(r)$, and there are various functionals that have been developed to approximate $E_{XC}(r)$.[104] We employ the exchange-correlation functional developed by Perdew and Wang (PW91) in this thesis.[108, 109]

The Kohn-Sham equations are solved by an iterative procedure, which involves defining a trial electron density, solving the Kohn-Sham equations with that density (yielding the ψ_i), using the ψ_i to re-calculate the electron density, and updating the trial electron density if it does not match re-calculated electron density (i.e., the solutions ψ_i must be self-consistent). Once this procedure has converged to a self-consistent set of ψ_i, which defines the ground state electron density, the ground state energy can be calculated.

2.2 Applications of Density Functional Theory to Catalysis

We utilize density functional theory primarily to calculate the ground state energies of different atomic configurations. This enables structural optimization and extraction of catalytically important parameters. In particular, we are interested in deriving thermochemical (adsorption and surface reaction energies) and kinetic (activation energy barriers) parameters on surface models that represent potential active sites.

2.2.1 Slab models to describe metal nanoparticles

On typical supported metal catalysts, the dispersed metal particles contain hundreds of atoms for metal particle sizes as small as a few nanometers. Modeling such a system using DFT calculations is intractable in terms of the required computational resources. Instead, we can define

simpler models to represent various surface features exposed by such metal nanoparticles (Figure 2.1). Many of the late transition metals, including Pd, adopt the face-centered-cubic (fcc) structure, and the most thermodynamically stable surface terminations (i.e., the facets exhibiting the lowest surface energies) are the close-packed (111) facet, followed by the more open (100) facet. Barring any strong particle-support interactions and assuming that crystallinity is retained, supported fcc metal nanoparticles on the order of a few nanometers or larger should expose a substantial proportion of these two facets to minimize their total surface energy – in addition to defect sites such as corners and edges. Therefore, in the absence of direct experimental evidence regarding the active site(s) for the DSHP on Pd, the (111) and (100) facets are reasonable starting points.

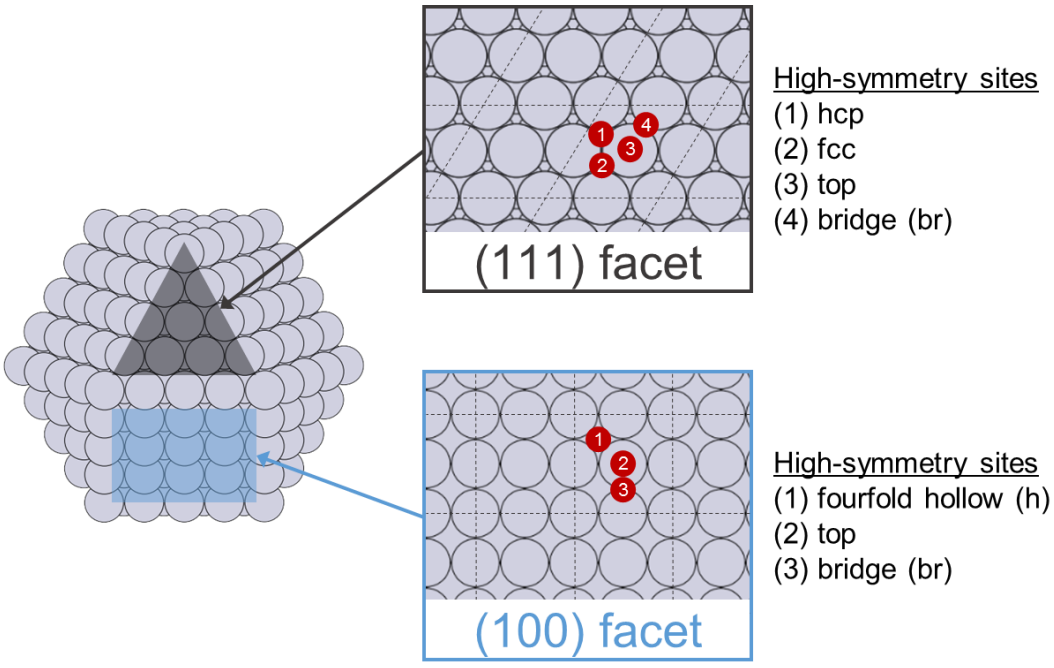

Figure 2.1 (left) Pictorial representation of an fcc metal nanoparticle (ca. 2 nm) with the close-packed (111) and more open (100) planar facets dominating the exposed surface. (right) Top-down views of the (111) and (100) facets used in slab models. Each model is periodic along the surface plane, and the repeating unit cells are demarcated by dotted black lines (in these examples, (2 × 2) unit cells are defined). The numbered red circles within each image show the high-symmetry binding sites. The majority of computational work presented in this thesis evaluates reactivity on these planar surface models.

We model different surface facets separately using a slab geometry with a periodic structure along the surface (Figure 2.1), and using a periodic basis set of plane waves. The choice

of surface unit cell size is a compromise between avoiding interactions between adsorbates in neighboring unit cells and minimizing computational cost; an additional consideration is accurate representation of experimentally-relevant adsorbate phases/coverages, if this information is available. A sufficiently large vacuum region is included between the periodically repeating slabs in the z-direction to prevent interactions between neighboring slabs. The bottom metal layers in the slab model are generally fixed at their truncated bulk equilibrium lattice positions, and the top layers can be relaxed – for modeling adsorption on one side of the slab. The number of total (and relaxed) slab layers chosen for the slab model depends on the convergence of the quantities of interest, e.g. binding energies. At the beginning of each chapter, we describe the specific density functional theory parameters and slab model geometry employed in that chapter.

2.2.2 Binding and surface reaction energies

The binding energy (BE) of a species to a metal surface is readily calculated once the surface model is defined. First, an initial guess for the adsorption geometry is made, and then a geometry optimization is performed based on the calculated energy gradient until the Hellmann-Feynman forces on atoms are below a specified value. Multiple initial guesses are necessary to probe the unique binding sites (Figure 2.1), because the geometry optimization finds only the local minima near the initial guess. (We note that for adsorbates containing multiple atoms, different conformational arrangements must also be considered in the search for the most stable minimum energy adsorption structure – in addition to the different binding sites.) Once the minimum energy adsorption structure is identified, its calculated total energy ($E_{slab+adsorbate}$), less the energy of the clean slab (E_{slab}) and the energy of the adsorbate in the gas-phase ($E_{gas\text{-}phase\ adsorbate}$), yields the binding energy. The energy of the adsorbate in the gas-phase is calculated by placing the isolated adsorbate in a sufficiently large unit cell to prevent interactions with neighboring unit cells. Figure

2.2 provides a pictorial representation of the binding energy calculation. In all subsequent chapters, the conventional "*" is appended to a species to denote its adsorption onto the metal slab (e.g., O* represents an oxygen atom adsorbed to a metal slab).

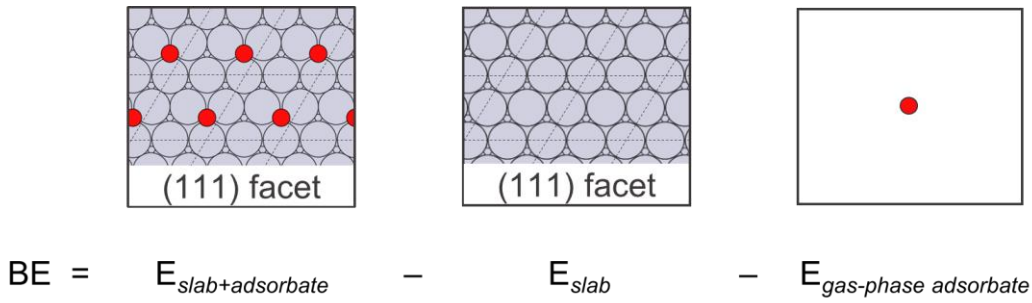

Figure 2.2 Binding energy calculation for an adsorbate on the (111) facet of an fcc metal. The adsorbate (red circle) is at the fcc site on the (111) facet. In the top-down slab images, the repeating unit cells ((2 × 2) unit cell, for this example) are demarcated by dotted black lines.

Surface reaction energies (ΔE) for elementary steps can also be calculated from the DFT-derived total energies:

$$\Delta E = \Sigma E_{products} - \Sigma E_{reactants}$$

For example, the bimolecular reaction between A* and B* on the surface to form AB*, is calculated as:

$$\Delta E = (E_{AB*} + E_{slab}) - (E_{A*} + E_{B*}), \text{ for the surface reaction } A* + B* \rightarrow AB* + *$$

where the clean slab energy (E_{slab}) is included in the products because of the empty surface site (represented by the "*" that stands alone).

2.2.3 Vibrational frequencies

The vibrational frequencies of gas-phase or adsorbed species can be used to calculate their zero-point energy and entropy. We assume all atoms to be quantum harmonic oscillators and diagonalize the mass-weighted Hessian matrix to obtain the vibrational frequencies. The Hessian matrix is calculated using a second order finite difference approximation of the force derivatives,

displacing atoms with step size of 0.015 Å from their equilibrium positions.[110] We then calculate the zero-point energy (ZPE) of a system from these vibrational frequencies (υ_i):

$$\text{ZPE} = \Sigma\ (½ \times h \times \upsilon_i)$$

where h is Planck's constant, and the sum is over all vibrational frequencies. In the computational methods section of each chapter, we explicitly note when the DFT-derived energies have been corrected for the ZPE. The entropy is calculated from the vibrational frequencies by summing the vibrational partition functions.[85]

2.2.4 Activation energy barriers

In order to calculate the activation energy barrier for an elementary process, we need the energy corresponding to the transition state and the initial state. There are a number of different algorithms that implement DFT calculations to identify transition state energies.[111-114] We use the climbing image-nudged elastic band (CI-NEB) method[112, 115] in this thesis. The general NEB method locates the minimum energy pathway between two adjacent local minima (the initial and final states). First, intermediate "images" are generated between the initial and final states by linear interpolation; these images are linked by an elastic band, which keeps the images evenly spaced along the reaction coordinate. Then, the intermediate images are optimized to minimize the forces perpendicular to the elastic band (the "real" forces), constrained by the artificial spring forces parallel to the band. The converged NEB calculation yields the minimum energy pathway. The CI modification to the NEB method also yields the transition state structure at the saddle point of the minimum energy pathway. We can verify that the transition state structure represents a true saddle point by identifying a single imaginary frequency among its normal vibrational modes.

The activation energy barrier (E_a, the difference in total energy between the transition and initial states), coupled with the entropy of the initial and transition states, can be used to calculate the rate constant for an elementary step. Transition state theory defines the rate constant (k) based on an assumed equilibrium between the transition state complex and the initial reactant state:

$$k = k_B \times T \times h^{-1} \times \exp(-\Delta G^{\ddagger} \times k_B^{-1} \times T^{-1}) \quad ; \quad \Delta G^{\ddagger} = \Delta H^{\ddagger} - T \times \Delta S^{\ddagger}$$

where k_B is the Boltzmann constant, T is the temperature, h is Planck's constant, and $\Delta G^{\ddagger}$, $\Delta H^{\ddagger}$, and $\Delta S^{\ddagger}$ are the changes in free energy, enthalpy, and entropy between the initial state and transition state. The DFT-derived activation energy barrier can be used to approximate $\Delta H^{\ddagger}$, and $\Delta S^{\ddagger}$ can be calculated from the vibrational frequencies.[85, 86]

We note that only gas-phase DFT calculations, as described in Section 2.2, are employed throughout this thesis. This means that we neglect energetic contributions induced by a liquid-solid interface, even though the DSHP is most often performed using a heterogeneous catalyst that is submersed in a liquid solvent. We address the inclusion of potential solvent effects in our recommendations for future work (Chapter 9).

2.3 Experimental System

All reactivity experiments for H_2O_2 decomposition over Pd (Chapter 4) and H_2O_2 synthesis/decomposition over Au-Pd (Chapter 7) are performed in a 50 mL Parr Instrument Company Hastelloy C-276 autoclave operated in batch mode. The autoclave is equipped with an overhead magnetic stirrer, a heating mantle, a pressure gauge, and a fixed thermocouple that has its tip submerged in the liquid phase during reaction. The liquid solvent consists of either ultra-pure water (18 MΩ × cm) or a mixture of ultra-pure water with methanol (Sigma-Aldrich 322415, anhydrous 99.8 %). The H_2O_2 used for decomposition experiments is diluted from a non-stabilized

30 wt % H_2O_2 solution (< 10 ppb Cl^-, Gigabit, KMG). Gas mixtures are supplied by Airgas, and a high-performance liquid chromatography pump (HPLC pump, Chrom Tech Series 1) is used to charge the reactor with liquid feed for H_2O_2 decomposition experiments. For reactions performed at sub-ambient temperature, the autoclave is submerged in a liquid reservoir and cooled to the desired temperature using a refrigerated bath circulator (ARCTIC A25, Thermo Scientific).

The H_2O_2 produced or consumed is quantified by titration of the reaction solution with $Ce(SO_4)_2$ (FLUKA-Sigma-Aldrich 34253, 0.05 M), using ferroin as indicator. Analysis of the gas-phase is performed by gas-chromatography (GC-2014 with thermal conductivity detector, Restek HayeSep DB 80/100 mesh column, 2 m, 2.0 mm ID, Ar carrier gas, Shimadzu Scientific Instruments, Inc). Catalysts are synthesized in-house from the appropriate metal precursors and support material. Details of catalyst synthesis and the specific reaction procedures/conditions are described in the relevant chapters.

Chapter 3: Mechanisms and Structure Sensitivity of the Gas-Phase Oxygen-Hydrogen Reaction on the Late Transition Metals[i]

3.1 Introduction

We begin our study by examining the reaction of hydrogen and oxygen gases over transition metal catalysts, which has been a long-standing interest in the catalysis community.[116] Not only does this reaction played an important role in fundamental surface science studies,[117-119] but catalytic control of the hydrogen-oxygen reaction also has practical applications that include energy generation by proton exchange membrane fuel cells (PEMFCs),[120, 121] the *in situ* activation of O_2 by H_2 for selective oxidation reactions,[122, 123] and the direct synthesis of hydrogen peroxide (DSHP) – the latter being the primary subject of this thesis.

Transition metals are commonly employed as heterogeneous catalysts for these applications. For example, Pt is one of the most widely studied materials for the electrocatalytic

[i] Calculations on Au and Ag were performed in collaboration with Jan Scheffczyk during his time at UW-Madison.

reduction of oxygen at the cathode of PEMFCs,[124] and Pd is actively investigated for the direct synthesis of H_2O_2.[24, 35, 125, 126] In practice, these transition metals are dispersed as nanoparticles onto a support material, and both the composition and structure of the nanoparticles may influence catalytic performance.

Simplified theoretical models based on the binding properties of small reaction intermediates (namely, O* or OH*) to various transition metal surfaces are able to successfully capture experimentally measured activity trends in the electrocatalytic reduction of oxygen at the cathode of PEMFCs.[127, 128] A common assumption in these models is that the activation barriers for electrochemical proton-electron transfer can be approximated as a function of the reaction thermochemistry, which varies with applied potential.[127, 129] These models have been further utilized to explain the increased activity (with respect to polycrystalline Pt) of mono- and bi-metallic catalysts with engineered structures,[101, 130, 131] and in some cases to predict improved catalysts for the electrochemical reduction of O_2.[132]

Fewer developments have been made toward explanatory and/or predictive models for the direct, non-electrochemical reaction of oxygen with hydrogen to produce H_2O_2 or to utilize for *in situ* selective oxidation reactions; some recent theoretical work can be found in references # [47, 53-56, 133, 134]. Unlike in the electrochemical system where oxygen reduction is decoupled from hydrogen activation – and complete reduction of O_2 to H_2O is generally desirable to maximize fuel cell efficiency – the direct, non-electrochemical reaction of hydrogen and oxygen necessitates a catalyst that can both activate H_2 and partially reduce O_2, where selectivity toward H_2O represents a wasteful consumption of the more expensive H_2 reagent. Not only can hydrogen activation require overcoming a significant kinetic barrier depending on the substrate,[135] but hydrogenation reactions can involve surface-bound atomic hydrogen, and the associated kinetic barriers[55] may

differ substantially from those barriers for the corresponding electrochemical proton-electron transfer.[129] Given these fundamental differences, it is pertinent to understand the compositional and structural properties that control catalytic activity and selectivity during the direct, non-electrochemical reaction of hydrogen and oxygen gases.

In a previous publication from our group, we used DFT calculations to systematically study the direct reaction of hydrogen with oxygen on the (111) facet of eight transition metals (Rh, Ir, Ni, Pd, Pt, Cu, Ag, and Au).[55] In this chapter, we extend that analysis to the more coordinatively undersaturated (100) facet of Pd, Pt, Cu, Ag, and Au to elucidate the structure sensitivity of this reaction. Rh, Ir, and Ni are not included here because O_2 dissociation was calculated to be very facile on the (111) facet of these metals,[55] suggesting that O_2 readily dissociates prior to reacting with hydrogen. The (100) facet is the next most stable facet of these fcc metals. We consider product formation pathways to H_2O versus H_2O_2, and include the calculation of kinetic barriers for both H_2 dissociation and direct hydrogenations of oxygenated intermediates by surface-bound hydrogen atoms. We utilize our results to provide insight into the most likely reaction pathways and the potentially rate-limiting steps – comparing the intrinsic reactivity of the (111) and (100) facets.

3.2 Computational Methods

The DACAPO total energy code was used for all DFT calculations in this chapter.[90, 136] The exchange-correlation energy and potential were described using the self-consistent PW91 generalized gradient approximation functional (GGA-PW91[108, 109]), and the electron density was determined by iterative diagonalization of the Kohn-Sham Hamiltonian, Fermi population of the Kohn-Sham states (k_BT = 0.1 eV), and Pulay mixing of the resulting electron density.[137] The Kohn-Sham one-electron valence states were expanded in a basis of plane waves with a kinetic energy

cutoff of 25 Rydberg, and all total energies were extrapolated to $k_BT = 0$ eV. The ionic cores were described by ultrasoft Vanderbilt pseudopotentials.[138]

The slab model for the (111) facets was identical to that used in reference # [55], consisting of a periodically repeated (2 × 2) unit cell with four atomic layers fixed at their bulk equilibrium positions. The slab model for the (100) facets also consisted of a (2 × 2) unit cell with four atomic layers, but the top two layers were allowed to relax, and the bottom two layers were fixed. Both the (111) and (100) surface unit cells correspond to 0.25 monolayer (ML) coverage for a single adsorbate. At least 12 Å of vacuum was used to separate slabs from their successive images in the z-direction. Adsorbates were only permitted on one exposed surface, and the dipole moment was corrected accordingly.[139, 140] The bulk metal equilibrium PW91 lattice constants for Pd, Pt, Cu, Ag, and Au were calculated previously[55] (corresponding experimental values[141] in brackets) to be 3.99 Å [3.89 Å], 4.00 Å [3.92 Å], 3.66 Å [3.62 Å], 4.18 Å [4.08 Å], and 4.14 Å [4.09 Å], respectively. All calculations involving molecular oxygen were performed spin-polarized. The surface Brillouin zone was sampled using 18 special Chadi-Cohen k-points[142] for the (111) facets and a (6 × 6 × 1) Monkhorst-Pack k-point mesh[143] for the (100) facets.

The convergence criterion for binding energy (BE) calculations was that the Hellmann-Feynman forces acting on atoms be less than 0.05 eV $Å^{-1}$ in the final structure. All binding and transition state energies in this chapter were corrected for the zero-point energy (ZPE). Activation energy barriers were calculated using the climbing image-nudged elastic band method (CI-NEB)[112, 115] with at least seven intermediate images along the reaction pathway, and the convergence criterion was that the magnitude of the forces on all images be less than 0.1 eV $Å^{-1}$ (or 0.05 eV $Å^{-1}$ for the hydrogen dissociation step). The transition states were verified by identifying a single imaginary vibrational mode along the reaction coordinate. All reaction

energies and activation barriers are reported with respect to the infinitely separated reactants and products, unless stated otherwise. The majority of the data for the (111) facets were taken directly from a previous publication.[55]

The discussions in Sections 3.3.1-3.3.5 are based on the ZPE-corrected total energy calculations described above, which represent the energetics at 0 K and in vacuum. In Sections 3.3.6-3.3.7 we also consider the effect of reaction conditions. We analyzed the relative thermodynamic stability of each adsorbed intermediate (at 0.25 ML coverage) by calculating the free energy of adsorption with respect to a gas-phase reservoir of the H_2 and O_2 reactants at a specified temperature and pressure (Section 3.3.6), analogous to the construction of *ab initio* phase diagrams.[144] We defined the grand potential (Ω) for each combination of a single intermediate adsorbed to a metal surface as:

$$\Omega = E_{slab+adsorbate} - E_{slab} - N_{H2} \times \mu_{H2} - N_{O2} \times \mu_{O2} - T \times S$$

where N_{H2} and N_{O2} are the stoichiometric coefficients of H_2 and O_2 required to form the adsorbate molecule, μ_{H2} and μ_{O2} are the ideal gas chemical potentials of H_2 and O_2 at the specified temperature and pressure, T is the absolute temperature, and S is the entropy of the adsorbate on the slab. The entropy of the adsorbate on the slab was approximated as its local entropy (i.e., the total gas-phase entropy of the free adsorbate less its 3D translational entropy). The chemical potentials of H_2 (and O_2) were calculated as:

$$\mu_{H2}(P,T) = E_{H2} + \mu_{0,H2}(P_0,T) + k_B \times T \times \ln(P\ P_0^{-1})$$

where E_{H2} is the DFT-derived total energy of gas-phase H_2, $\mu_{0,H2}$ is the difference in chemical potential of H_2 between 0 K and the specified temperature at a pressure P_0 of 1 atm (taken from

the *NIST-JANAF Thermochemical Tables*[62]), P is the pressure in atm, and k_B is the Boltzmann constant.

The maximum rate analysis employed in section 3.3.7 was developed by Farberow et al[145] and was used to calculate the maximum theoretical rate and most likely rate-limiting step along each proposed reaction pathway based on the DFT-calculated energetics. We refer the reader to the original publication for the detailed maximum rate analysis procedure.[145] The assumptions included in the maximum rate analysis follow: there is a single rate-limiting step along each pathway, all other steps are quasi-equilibrated, and the coverage of vacant sites is unity. The maximum rate was then calculated from the free energies of the stable gas-phase reactants/products and the transition state using transition state theory. We again approximated the entropy of adsorbates on the slab to be the local entropy, and the entropy of a transition state was set equal to that of the initial state entropy (final state entropy) for bond-breaking steps (bond-forming steps). The enthalpy of an adsorbed species was calculated by adding the DFT-derived binding energy to the enthalpy of the gas-phase adsorbate, and the enthalpy of a transition state was calculated by adding the DFT-derived activation barrier to the enthalpy at the initial state.[145]

3.3 Results and Discussion

Scheme 3.1 is the proposed reaction network for the direct reaction of H_2 and O_2 over a transition metal surface. Steps (1) and (2) are molecular oxygen adsorption and dissociative hydrogen adsorption, respectively. Molecular hydrogen shows no significant stabilizing interaction with any of the metal surfaces considered here except for the (111) and (100) facets of Pd and Pt; this H_2* precursor state is discussed in a subsequent section. O_2* can undergo sequential hydrogenations by H* to form OOH* (step 3a) and then H_2O_2* (step 4a) followed by desorption (step 5a), which represents the partial reduction of O_2. Alternatively, O_2 can be completely reduced

to H_2O through any of the three O-O bond dissociation pathways: the dissociative path (step 3b), the peroxyl path (step 4b), and the peroxide path (step 5b). Following O-O bond dissociation, H* can directly hydrogenate the O* and OH* fragments (steps 6-7). H_2O can be formed either from direct hydrogenation of OH* by H* (step 7) or from OH* disproportionation (step 8).

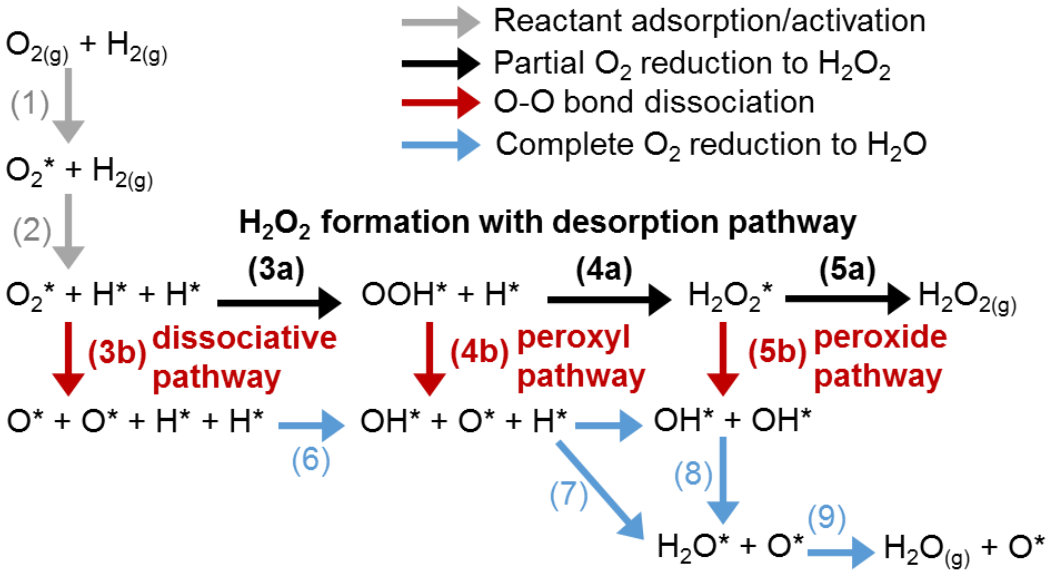

Scheme 3.1 The proposed reaction network for the direct reaction of H_2 and O_2 over transition metal surfaces. There is one primary pathway for H_2O_2 formation ("H_2O_2 formation with desorption"), and there are three pathways for H_2O formation that each involve breaking the O-O bond ("dissociative", "peroxyl", and "peroxide"). Each numbered step represents a unique elementary step. Numbered steps corresponding to hydrogenation of dioxygen species include an "a", while the competing O-O dissociation steps include a "b". A second hydrogen molecule is required to close the catalytic cycle for water formation (e.g., to reduce the O* species to H_2O following step (9), or to reduce both OH* species to H_2O following step (5b)). The "*" denotes an adsorbed species, and the "(g)" denotes a gas-phase species.

Within this mechanistic framework, we first present binding properties of adsorbates, reaction energies, and kinetic barriers calculated on the (100) facet of Pd, Pt, Cu, Ag, and Au, comparing to results previously calculated on the (111) facet. We then develop potential energy surfaces (PES) to evaluate the most favorable pathways toward H_2O and H_2O_2 and discuss which intermediates are most likely to be abundant on the surface. We finally employ a maximum rate analysis[145] to identify the potentially rate-limiting steps, and to quantitatively compare the intrinsic activity of the (111) and (100) facets of these metals.

3.3.1 Thermochemistry of adsorbed species

Table 3.1 provides binding properties for H*, O*, OH*, H_2O*, and H_2*, and the corresponding binding geometries are depicted in Figure 3.1. We calculate stronger binding on the (100) facet, as is anticipated due to the more coordinatively undersaturated nature of the (100) facet (each metal surface atom is coordinated to 8 nearest neighbors on the (100) facet, compared to 9 on the (111) facet); the only exception is for H* binding on Ag, although H*'s energetic preference for Ag(111) is only 0.05 eV. The energy difference between H* binding on the (111) facet versus the (100) facet is also weak (< 0.1 eV) for Pd, Cu, and Au, while for Pt the (100) facet is energetically favored by almost 0.2 eV. The (100) facet generally shows a much stronger preference for the open-shell oxygenated intermediates. For example, O* binds more strongly to Cu(100) by 0.52 eV compared to Cu(111), and the difference in OH* binding energy on Pt(100) and Pt(111) is 0.70 eV.

Table 3.1 ZPE-corrected binding energies (in eV) and site preferences for H*, H_2* O*, OH*, and H_2O* on the (100) facet of Pd, Pt, Cu, Ag, and Au. The numbers in parenthesis show the difference in binding energy between the (100) and (111)[a] facets for each species, where a negative value indicates stronger binding on the (100) facet. The "-" indicates that the species does not bind to the surface (or for the case of H_2* on Pt(100), dissociates spontaneously).

Metal	H*		H_2*		O*		OH*		H_2O*	
	BE	Site	BE	Site	BE	Site	BE	Site	BE	Site
Pd	-2.74 (-0.04)	h	-0.28 (-0.15)	top	-3.90 (-0.26)	h	-2.43 (-0.39)	br	-0.30 (-0.09)	top
Pt	-2.73 (-0.19)	br	- (0.10)	-	-3.74 (-0.15)	br	-2.52 (-0.70)	br	-0.27 (-0.09)	top
Cu	-2.26 (-0.04)	h	- (-)	-	-4.65 (-0.52)	h	-2.91 (-0.23)	h	-0.22 (-0.06)	top
Ag	-1.87 (0.05)	br	- (-)	-	-3.63 (-0.50)	h	-2.57 (-0.29)	h	-0.15 (-0.02)	top
Au	-2.10 (-0.10)	br	- (-)	-	-2.69 (-0.26)	h[b]	-1.99 (-0.52)	br	-0.13 (-0.04)	top

[a]Data for the (111) facet are taken directly from reference # [55].
[b]Four-fold hollow site spontaneously reconstructs to a three-fold hollow site.

H_2O* binds weakly to all surfaces with a maximum BE of -0.30 eV on Pd(100), and H_2O* always binds most stably to a top site with the O-H bonds pointing nearly parallel to the surface

plane. The hydrogen molecule does not show any significant stabilizing interaction on Cu, Ag, or Au, but our calculations do suggest the existence of a molecular precursor state that binds with the H-H bond stretched over a top site on Pd(111), Pd(100), and Pt(111). The H-H bond lengths in this precursor state are 0.842 Å, 0.854 Å, and 0.955 Å (compared to 0.754 Å calculated for gas-phase H_2), and the BEs are -0.13 eV, -0.28 eV, and -0.10 eV on Pd(111), Pd(100), and Pt(111), respectively. Evidence for a molecular precursor on Pd(111) and Pd(100) has also been presented in other theoretical works with the calculated H-H bond lengths comparable to those reported here.[146-148]

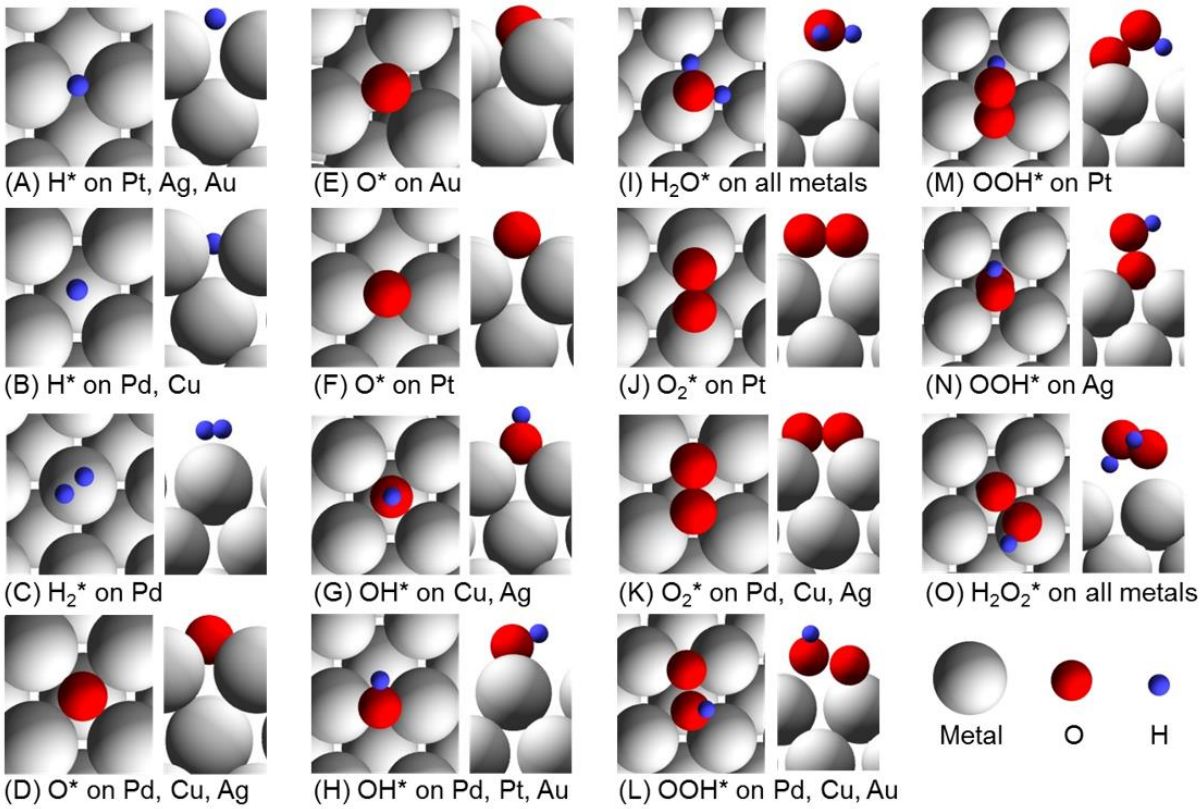

Figure 3.1 (A-O) Top-down and side views of the preferred binding geometries for adsorbates on the (100) facet of Pd, Pt, Cu, Ag, and Au. The gray spheres are metal slab atoms, the red spheres are oxygen atoms, and the blue spheres are hydrogen atoms. (E) For atomic oxygen adsorption on Au(100), the fourfold hollow site spontaneously reconstructs to a threefold hollow site. Pd(100) is the only (100) surface on which we found a stable H_2* precursor.

The binding properties and geometries of the dioxygen intermediates are presented in Table 3.2 and Figure 3.1, and we again calculate stronger binding on the (100) facet compared with

binding on the (111) facet for each metal. In general, the O-O bond lengths for adsorbed species increase moving from the (111) facet to the (100) facet, suggesting that the (100) facet further weakens the intramolecular O-O bonds. O_2* binds to two bridge sites, over a hollow site, on Pd(100), Cu(100), and Ag(100), and retains no significant magnetic moment. The binding geometry of O_2* on Pt(100) is a top-top configuration, and O_2* retains a significant fraction of its gas-phase magnetic moment; this top-top binding configuration for O_2* on the (100) surfaces of Pd, Cu, and Ag (although less stable than the bridge-bridge configuration) also retains some of its gas-phase magnetic moment. O_2* only physisorbs to Au(100) over two top sites, with nearly thermoneutral binding; this is similar to its interaction with Au(111), where no significant stabilization is found.[55] The difference in binding energy of O_2* on Cu(100) versus Cu(111) represents the largest disparity in binding strength of all surface species, wherein Cu(100) binds O_2* stronger than Cu(111) by 1 eV.

Table 3.2 ZPE-corrected binding energies (in eV) and site preferences for dioxygen species (O_2*, OOH*, and H_2O_2*) on the (100) facet of Pd, Pt, Cu, Ag, and Au.The numbers in parenthesis show the difference in binding energy between the (100) and (111)a facets for each species, where a negative value indicates stronger binding on the (100) facet. The O-O bond distances (in Å), d_{O-O}, are also provided, as well as the magnetic moment (mag. mom., in μB) for adsorbed O_2 (values in parenthesis for d_{O-O} and mag. mom. correspond to the (111) facet).

Metal	O_2*				OOH*			H_2O_2*		
	BE	Site	d_{O-O}[c]	mag. mom.	BE	Site	d_{O-O}[c]	BE	Site	d_{O-O}[c]
Pd	-1.27	hollow	1.41	0.00	-1.28	bent br	1.51	-0.36	top	1.49
	(-0.77)		(1.35)	(0.09)	(-0.33)		(1.46)	(-0.06)		(1.48)
Pt	-0.97	top-top	1.35	0.66	-1.36	bent br	1.45	-0.33	top	1.48
	(-0.51)		(1.34)	(0.54)	(-0.40)		(1.45)	(-0.04)		(1.47)
Cu	-1.50	hollow	1.51	0.00	-1.70	bent br	1.55	-0.35	top	1.49
	(-1.00)		(1.48)	(0.00)	(-0.26)		(1.54)	(-0.08)		(1.48)
Ag	-0.50	hollow	1.44	0.00	-1.26	upright h	1.50	-0.21	top	1.48
	(-0.38)		(1.30)	(1.02)	(-0.26)		(1.50)	(-0.03)		(1.47)
Au	-0.01	top-top	1.28	1.46	-0.72	bent br	1.47	-0.19	top	1.48
	(-)[b]		(-)[b]	(-)[b]	(-0.38)		(1.47)	(-0.03)		(1.47)

[a]Data for the (111) facet are taken directly from reference # [55].
[b]O_2 does not adsorb to Au(111).
[c]the calculated d_{O-O} for gas-phase O_2, OOH, and H_2O_2 are 1.24 Å, 1.35 Å, and 1.48 Å, respectively.

OOH* adopts both bent and upright configurations on the (100) surfaces with the non-hydrogenated oxygen atom bound to either a bridge site or a hollow site. Finally, similar to H_2O*, H_2O_2* preferentially binds to top sites through one oxygen atom on all (111) and (100) facets with the O-H bond on the other oxygen atom pointing toward the surface; for each metal, H_2O_2* has a preference (albeit a weak one, < 0.1 eV for all metals) to bind to the (100) facet compared to the (111) facet.

3.3.2 Kinetics of O-O bond dissociation

Figure 3.2A-C compares the kinetic barriers calculated for O-O bond dissociation in O_2*, OOH*, and H_2O_2* on the (100) and (111) facets. The corresponding reaction energies for all elementary steps on the (100) facet can be found in Table S3.1. Ford et al[55] observed that the binding energy of O* is a good descriptor for the ability of these (111) facets to break the O-O bond, i.e., weaker binding energies of O* indicate larger O-O bond dissociation barriers, and this trend is reasonably consistent with the results calculated on the (100) facet. Furthermore, the observation of lower activation barriers for O-O bond dissociation on the (100) facet compared to the (111) facet is consistent with the more coordinatively undersaturated nature of the (100) facet with respect to the (111) facet, that is, easier bond-breaking is expected on the (100) facet.

O_2* is the most difficult to dissociate of the dioxygen species, particularly on Ag(100), Ag(111), Au(100), and Au(111) where the barriers exceed 0.9 eV. Although Pd(111) and Pt(111) show significant barriers for O_2* dissociation (> 0.7 eV), these barriers are greatly reduced on Pd(100) and Pt(100) to 0.30 and 0.15 eV, respectively. We note that the barrier calculated for O_2* dissociation on Pt(100) corresponds to a diffusion barrier from its most stable top-top binding site toward the hollow site, followed by spontaneous O-O bond dissociation; the transition state geometry and calculated barrier closely resemble those reported in a previous publication for O_2*

dissociation on Pt(100) that were calculated using similar computational parameters.[149] Both Cu(111) and Cu(100) can readily dissociate molecular oxygen. The only surfaces on which the O_2* dissociation barrier is energetically favorable to the O_2* desorption barrier are Cu(111), Pd(100), Pt(100), and Cu(100).

Hydrogenation of O_2* to OOH* or H_2O_2* significantly weakens the O-O bond. OOH* is particularly unstable with respect to decomposition on both the (100) and (111) facets of Cu, Pd, and Pt, where all activation barriers are below 0.2 eV; we expect OOH* to be a short-lived intermediate on these clean surfaces, complicating identification of OOH* on these metals by *in situ* experiments. The (100) and (111) facets of Ag and Au have a greater resistance to O-O bond dissociation in OOH*; in fact, inelastic neutron spectroscopy (INS) experiments performed during the reaction of hydrogen with oxygen over a Au catalyst supported on TiO_2 provide evidence for surface OOH* species.[150]

Au is the only candidate among these late transition metals that may be able to effectively release H_2O_2* once it forms, exhibiting O-O dissociation barriers above 0.4 eV for H_2O_2* on both its (111) and (100) facets (which exceed the desorption barriers to H_2O_2(g)). While there is some variation in the ability of the (111) facet of Cu, Pd, Pt, and Ag to dissociate H_2O_2* (barriers range from 0.11 eV to 0.25 eV), the (100) facet of these metals dissociates H_2O_2 nearly spontaneously (barriers range from 0.05 eV to 0.08 eV). These calculations suggest that the tendency for clean metal surfaces to decompose rather than to release H_2O_2* increases with increasing coordinative undersaturation of the surface metal atoms due to two contributing factors: slightly increased binding strength of H_2O_2* (increased desorption barrier, Table 3.2), and decreased O-O bond dissociation barrier.

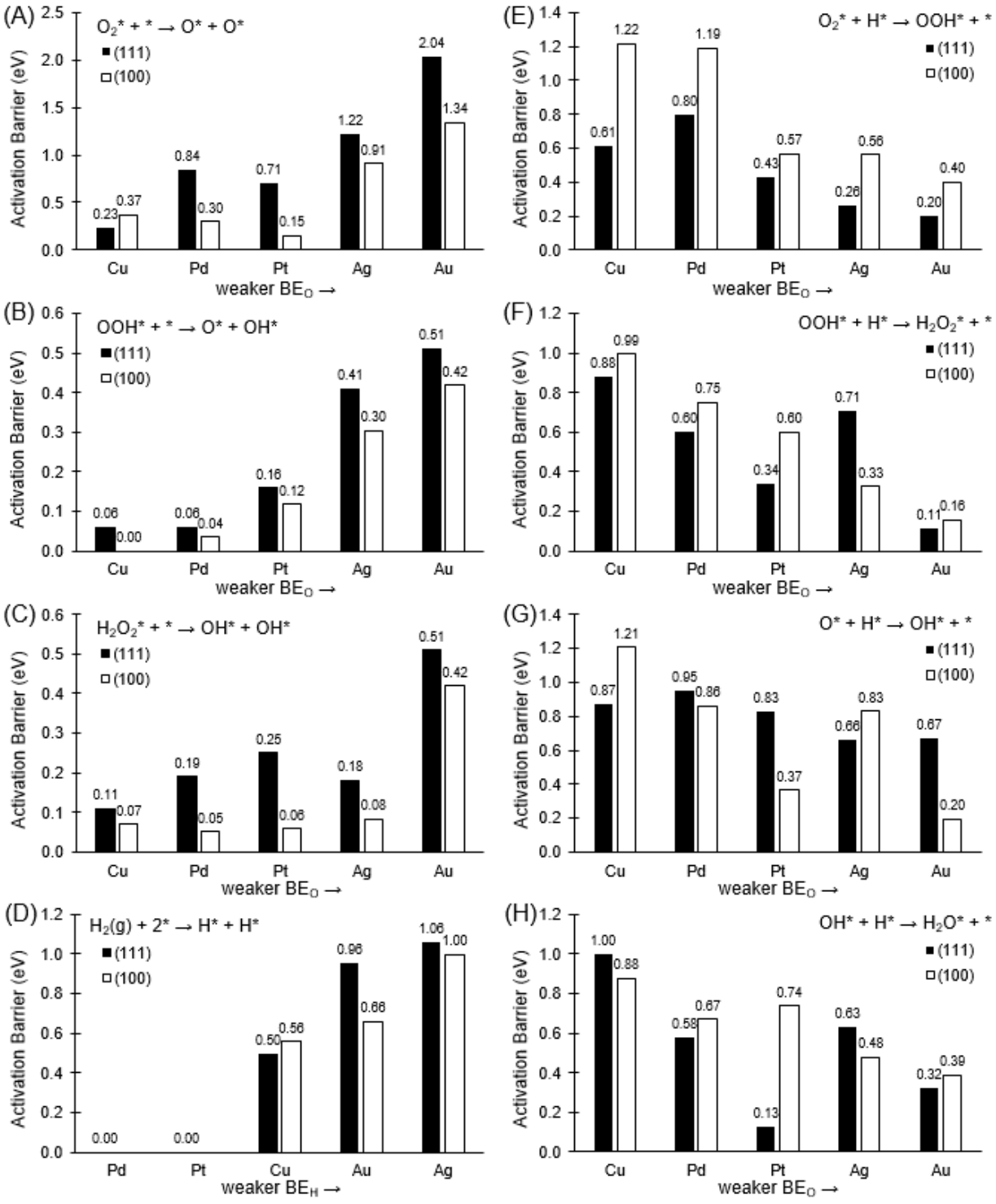

Figure 3.2 Activation energy barriers for (A-C) O-O bond dissociation, (D) H-H bond dissociation, and (E-H) O-H bond formation on the (111) and (100) facets. In (A-C) and (E-H), the metals are arranged (left to right) in order of decreasing binding energy of O* (BE_O), which takes the same order on each facet. In (D), the metals are arranged (left to right) in order of decreasing binding energy of H* (BE_H), which takes the same order on each facet. Black filled bars are for the (111) facet, and white filled bars are for the (100) facet. The numerical values for the activation barriers are also included above each bar. Data for the (111) facet are taken from reference # [55].

3.3.3 Kinetics of H-H bond dissociation

Protons and electrons generated at the anode provide the reducing power for the electrochemical reduction of O_2 at the cathode of PEMFCs. However, in the direct reaction of H_2 and O_2 the same catalyst that is utilized to reduce O_2 must also activate H_2. H_2 dissociates nearly spontaneously on both the (111) and (100) facets of Pd and Pt, consistent with previously reported results,[135, 146, 151, 152] but H_2 dissociation on those facets of Cu, Ag, and Au requires overcoming a significant activation barrier. All of these activation barriers are provided in Figure 3.2D, wherein barriers on the (111) facet are calculated using the same computational model as in reference # [55]. These calculated barriers are in good agreement with results available in the computational literature for Cu,[153, 154] Ag,[155-157] and Au.[158, 159] The lowest barrier for H_2 dissociation is 0.50 eV on Cu(111), and the highest barrier is 1.06 eV on Ag(111). The difference in H_2 activation barrier between the (111) and (100) facets is small on Cu and Ag (less than 0.1 eV, relatively structure-insensitive), but Au exhibits a considerably lowered barrier (by 0.3 eV) moving from its (111) to its (100) facet. In addition to requiring a large activation energy, the (111) and (100) facets of both Au and Ag also exhibit an endothermic reaction energy for H_2 dissociative adsorption, suggesting that a low population of H* is available on these surfaces for hydrogenation reactions.

The trend in the H-H bond dissociation barrier on each facet is similar to the trend observed for the O-O bond dissociation barrier; in this case, the binding energy of H* (rather than O*) is a strong indicator of the ability of these metal surfaces to dissociate H_2, with stronger binding of H* indicating smaller activation barriers. Moreover, the binding energies of O* and H* are poorly correlated on both the (111) facet and the (100) facet. We then emphasize that in addition to the binding energy of O* (or OH*), which have been successfully employed as activity descriptors for the electrochemical reduction of O_2,[127] the binding energy of H* should be considered as an

additional descriptor for the direct reaction of H_2 with O_2 to capture the catalyst's ability to dissociate H_2 – parallel to the work of Rankin and Greeley.[56]

3.3.4 Kinetics of O-H bond formation

Hydrogenation of oxygen-containing intermediates by H* can require overcoming large kinetic barriers. Figure 3.2E-H presents the activation barriers for hydrogenations of O_2*, OOH*, O*, and OH* by H* on the (100) facet, with the metals again arranged in order of decreasing binding energy of O*. Data for the (111) facet are also provided for comparison.[55] We can extract a few trends from this data set. First, hydrogenation of the dioxygen species (O_2* and OOH*) is generally more difficult on the (100) facet compared to the (111) facet for each metal; an exception is for the activation barrier for OOH* hydrogenation to H_2O_2* on Ag(100), where the barrier is calculated to be lower than that on Ag(111) by ca. 0.4 eV. Second, for a given facet, the hydrogenation barrier generally decreases with decreasing binding energy of O*. These trends are opposite to those observed for O-O bond dissociation barriers discussed in a previous section, and indicate that the "cross trends" behavior discussed in reference # [55] for the (111) facet is also displayed on the (100) facet. That is, the binding energy of O* may be used to delineate regimes in which H_2O, H_2O_2, or metal oxide formation dominate: a surface that binds O* too strongly can easily generate O* but has difficulty forming O-H bonds, suggesting a tendency for the surface to irreversibly oxidize; more moderate binding of O* can still facilitate O-O bond dissociation, but also indicates that the surface can more readily hydrogenate O*/OH* to H_2O; and even weaker binding of O* further facilitates O-H bond formation but resists O-O bond dissociation – although too weak binding of O* may limit O_2* uptake.

The hydrogenations of O* and OH*, to some degree, also follow the trend of decreasing activation barrier with decreasing binding energy of O* for a given facet, but there is no uniform

trend in the magnitude of the activation barrier moving from the (111) to the (100) facet. Nonetheless, we note that when hydrogenation of O* to OH* is easier on the (100) facet compared to the (111) facet, for a given metal, then the subsequent hydrogenation of OH* to H_2O* is more difficult on the (100) facet compared to the (111) facet (and vice versa). Pt exhibits particularly large differences between O* and OH* hydrogenation barriers on both its (111) and (100) facets, and our calculated energetics are in good agreement with previous calculations in the literature.[149] O* hydrogenation has a large activation barrier of 0.83 eV on Pt(111), while the barrier is greatly reduced to ca. 0.37 eV on Pt(100). Conversely, OH* hydrogenation has a very small barrier of 0.13 eV on Pt(111), while this step has a barrier of 0.74 eV on Pt(100). These calculations show that the reactions between O*/OH* and H* to form H_2O exhibit a strong structure sensitivity on the (111) and (100) facet of these fcc metals.

O-H bond formation does not exclusively require H*, even in the direct reaction of H_2 and O_2. O-H containing intermediates may exchange hydrogen atoms through bimolecular elementary steps.[133, 160] The disproportionation of two OH* species to form H_2O* and O* is one route to H_2O formation from OH* that does not involve direct hydrogenation by H* (Scheme 3.1). This bond-transfer step is endothermic on the (100) facet of Pd, Pt, Cu, Ag, and Au by 0.17, 0.53, 0.44, 0.86, and 0.65 eV, respectively. The activation barriers for these steps, with respect to an initial state of infinitely separated OH*, are nearly spontaneous in all cases; there is no significant overbarrier, and therefore the activation barriers can be well-approximated by the reaction energies.

3.3.5 Analysis of reaction pathways using potential energy surfaces

We plot PESs for molecular adsorption of O_2, dissociative adsorption of H_2, and then sequential reaction of H* with O_2* in Figure 3.3 for the (100) and (111) facets. These PESs allow us to predict the point at which the O-O bond is likely to break – that is, which of the dissociative,

peroxyl, and peroxide pathways (Scheme 3.1) leading to complete O_2 reduction to H_2O are likely to be active on each metal surface – or if H_2O_2 can form and desorb without O-O bond breaking.

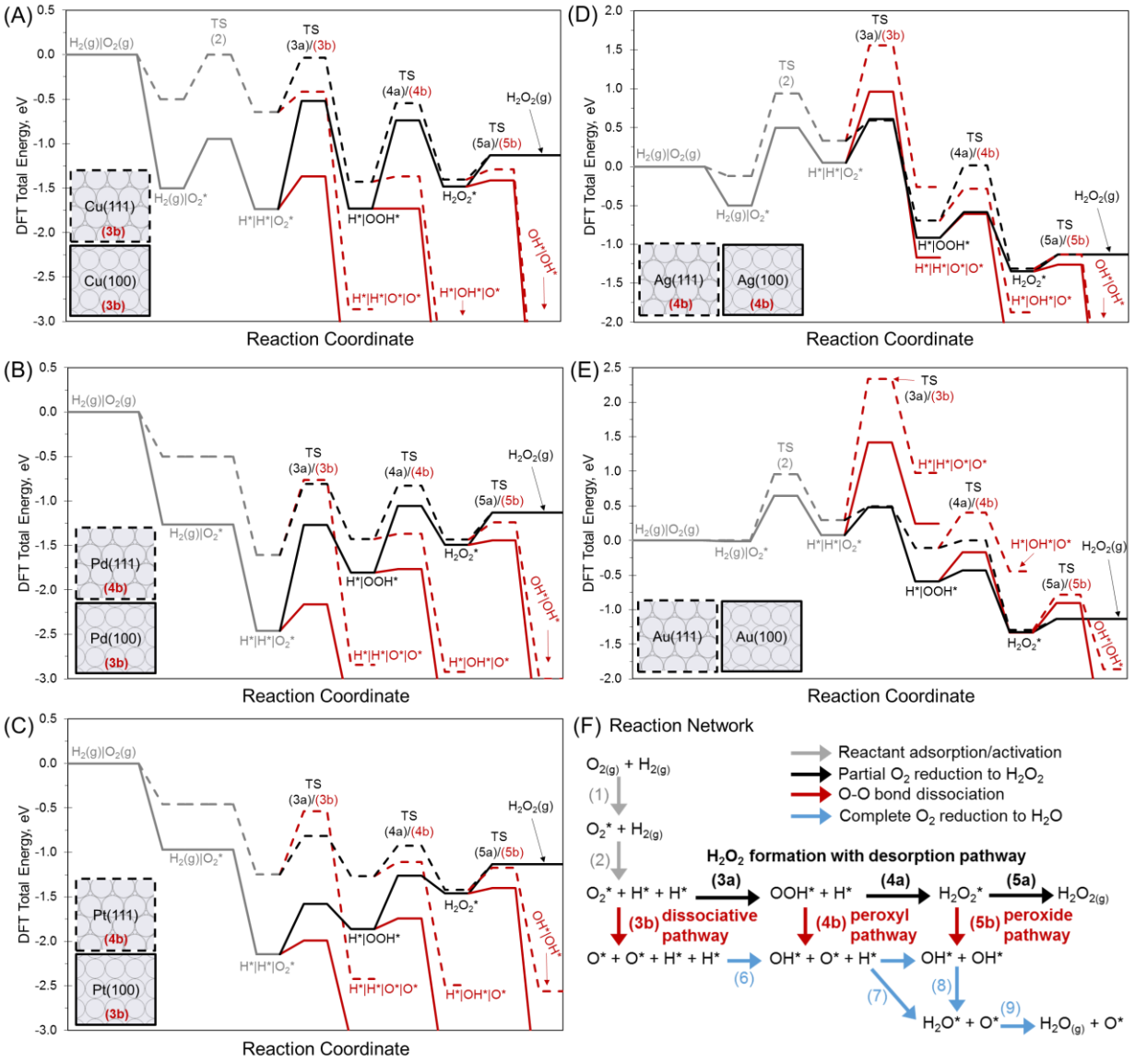

Figure 3.3 PESs for the direct reaction of O_2 and H_2 on the (111) and (100) facets of (A) Cu, (B) Pd, (C) Pt, (D) Ag, and (E) Au, comparing the sequential addition of H* to O_2* with the competing O-O bond dissociation steps. The "*" denotes an adsorbed species, the "(g)" denotes a gas-phase species, and the "TS" denotes a transition state. For each subfigure (A-E): the dotted lines correspond to the (111) facet, and the solid lines correspond to (100) facet; the gray lines correspond to reactant adsorption/activation, the black lines correspond to the "H_2O_2 formation with desorption pathway", and the red lines correspond to the three O-O bond dissociation pathways leading to H_2O formation ("dissociative", "peroxyl", and "peroxide"); the step numbers under "TS" can be referenced to Scheme 3.1, which is provided in subfigure (F) for convenience; the insets depict top-down views of the (111) and (100) facets, and the numbers within each inset designate the first O-O bond dissociation step that has a lower activation barrier than the competing O-H bond formation step. Data for the (111) facet are taken from reference # [55].

We follow the most energetically favorable pathway, starting from gas-phase H_2 and O_2. The PESs for the (100) facets are generally downshifted (lower in energy) with respect to the PESs for the (111) facets due to the stronger interaction of the (100) facets with both adsorbed species and transition states. On Pd(100), the dissociative pathway in which O_2* decomposes directly to O* is kinetically favored by 0.89 eV, compared to O_2* hydrogenation to OOH*. This differs from the energetics on Pd(111), where the hydrogenation of O_2* is slightly kinetically favored by 0.04 eV. Therefore we would expect significant OOH* formation on Pd(111) but not on Pd(100). Even if OOH* does form on Pd(100), its subsequent decomposition is calculated to be nearly spontaneous – as on Pd(111). The conclusions for Pt(100) are qualitatively similar to those for Pd(100), where the calculations also suggest the primary reaction pathway to be the dissociative pathway leading to H_2O formation.

The results on the coinage metals vary significantly moving down the periodic table (from Cu to Ag to Au). Metallic Cu readily dissociates O_2* on both its (100) and (111) facets, preventing formation of the OOH* intermediate, and the dissociative pathway for H_2O formation dominates. On Ag(100), hydrogenation of O_2* to OOH* is kinetically favored by 0.35 eV compared to O_2* dissociation. The subsequent hydrogenation of OOH* to H_2O_2* is competitive with OOH* decomposition, with a difference in activation barrier of only 0.03 eV (favoring OOH* decomposition); this deviates from the energetics on Ag(111), wherein the corresponding difference is 0.30 eV favoring OOH* decomposition. These energetics suggest that some H_2O_2* can form on Ag(100), but the H_2O_2* decomposition barrier of 0.08 eV is smaller than the H_2O_2* desorption barrier by 0.13 eV. We thus anticipate that both the peroxyl and peroxide pathways can be active on Ag(100), whereas the peroxyl pathway dominates on Ag(111). Similar to Au(111), Au(100) is the only (100) facet of the metals considered in this work on which the calculated

energy barriers favor H_2O_2* formation and desorption over its decomposition. The O-O bond dissociation barriers exceed the hydrogenation barriers by 0.94 eV on Au(100) (1.84 eV on Au(111)) for O_2* and by 0.26 eV on Au(100) (0.40 eV on Au(111)) for OOH*.

One final observation from these potential energy surfaces is that recombination of the O* and/or OH* fragments resulting from O-O bond dissociation is very thermodynamically unfavorable and is characterized by large kinetic barriers on the (100) facets of Pd, Pt, Cu, and Ag; the easiest O-O bond reformation step is O* + O* → O_2 * + * on Pt(100) with an activation barrier of 1.13 eV, and the most difficult O-O bond reformation step is OH* + OH* → H_2O_2* + * on Cu(100) with an activation barrier of 3.32 eV. Even for the case of Au, where O-O bond reformation steps can be exothermic (e.g., O* + O* → O_2* + * has a reaction energy of -0.17 eV on Au(100)), large kinetic barriers also hinder O-O bond reformation on Au(100) with the easiest of these steps being O* + OH* → OOH* + * with a kinetic barrier of 1.16 eV. Thus, any H_2O_2 that forms on clean metallic surfaces will likely originate from an intact O_2 molecule. This can be corroborated experimentally by feeding a mixture of $^{16}O_2$ and $^{18}O_2$ during the direct reaction of H_2 and O_2, and using Raman spectroscopy to distinguish $H_2{}^{16}O_2$, $H_2{}^{18}O_2$, and $H_2{}^{16}O^{18}O$ products[61] – the latter species representing the case where an O-O bond reformation step carries significant reaction flux. A similar conclusion is reached for the (111) facet of these metals.

3.3.6 Prediction of the most likely abundant surface intermediates

The energetic span, i.e. the lowest (and highest) energy states, of the full PESs for the direct reaction of H_2 and O_2 can yield predictions about which species are most (and least) likely to populate the different metal surfaces. A complete list of isomeric states on each metal facet is provided in Tables S3.2 and S3.3, including the stability of each state with respect to the reference state of the gas-phase reactants. Adsorbed molecular and atomic fragments (OH* and H*)

represent the deepest potential wells on the (100) facet of the more oxophillic metals (Cu, Pd, Pt), while the closed shell product H_2O^* is the most stable state on the (111) facet for all metals. In addition, atomic fragments (H* and/or O*) represent the least stable state on the (111) and (100) facets of Ag and Au, again highlighting the weak ability of these metals to activate bonds in the reactant molecules. Examining the lowest and highest energy states on the PES is constrained by the stoichiometry assigned to the reference state (e.g., $2H_2(g) + O_2(g)$ versus $H_2(g) + O_2(g)$) and does not include information about reaction conditions (e.g., temperature and entropic effects) unless we are to recast the PES in terms of the free energy.

We address those limitations of our PESs by constructing *ab initio* phase diagrams to evaluate the relative thermodynamic stability of each intermediate as a function of reaction feed conditions (temperature and partial pressures of H_2 and O_2). The results are plotted in Figure 3.4 for the (100) and (111) facets. The conditions in Figure 3.4 are chosen to investigate the effect of varying the H_2:O_2 ratio at a fixed partial pressure of O_2 and at 298 K, which is a relevant temperature to experimental conditions reported in both patents and academic literature for the direct synthesis of H_2O_2, oxygen reduction in fuel cells, and propylene oxidation using H_2O_2 generated *in situ*. In particular, the latter is also performed at significantly elevated temperatures[161, 162] and so we include the effect of increasing temperature to 398 K in Figure S3.1.

We predict that H_2O^* is the most stable surface species in both H_2-lean and H_2-rich conditions on the (100) and (111) facets of Pd, Pt, Ag, and Au. The next most stable species on these facets is generally OH*, whose stability is more competitive with H_2O^* on the (100) facet compared to the (111) facet for each metal. On Cu(111), OH* is favored to H_2O^* only under H_2-lean conditions at 298 K when partial pressures of H_2 are nearly three orders of magnitude less than those of O_2. On Cu(100), OH* is favored to H_2O^* even when the partial pressure of H_2

exceeds that of O_2 by an order of magnitude at 298 K. These results are reasonably consistent with the conclusions drawn from examination of the maximum and minimum energy states on the PESs, which are derived from our DFT-derived total energy calculations (i.e. they represent the energetics at 0 K in vacuum and do not account for reaction conditions). Overall these thermodynamic calculations suggest a significant population of H_2O* on all metals, with OH* as the second most abundant intermediate (except on Cu(100), where OH* is predicted to be most abundant over the conditions considered). Increasing the temperature (Figure S3.1), decreasing the partial pressure of H_2 relative to that of O_2, or moving from the (111) to the (100) facet stabilizes OH* relative to H_2O*. Notably, O_2* is one of the least stable surface intermediates on all (111) facets.

We note that the thermodynamic analysis in Figure 3.4 treats each species independently (no co-adsorption states containing different intermediates are considered), does not consider coverage-dependent interactions between surface species[91, 145, 163] (only the single-species binding energies calculated at 0.25 ML coverage in the unit cell have been used), and assumes that the surface remains metallic with adsorbates only on the top metal layer (e.g., phase transformations to surface/bulk oxides do not occur). The analysis also ignores the possible kinetic limitations to the formation of the various surface intermediates. Therefore, the conclusions should be interpreted with caution and only serve as a first approximation to the most likely abundant surface intermediates. Experimentally consistent microkinetic models, and confirmation by *in situ* spectroscopic experiments,[164] are ultimately necessary to identify the most abundant surface intermediates and their coverage under reaction conditions.

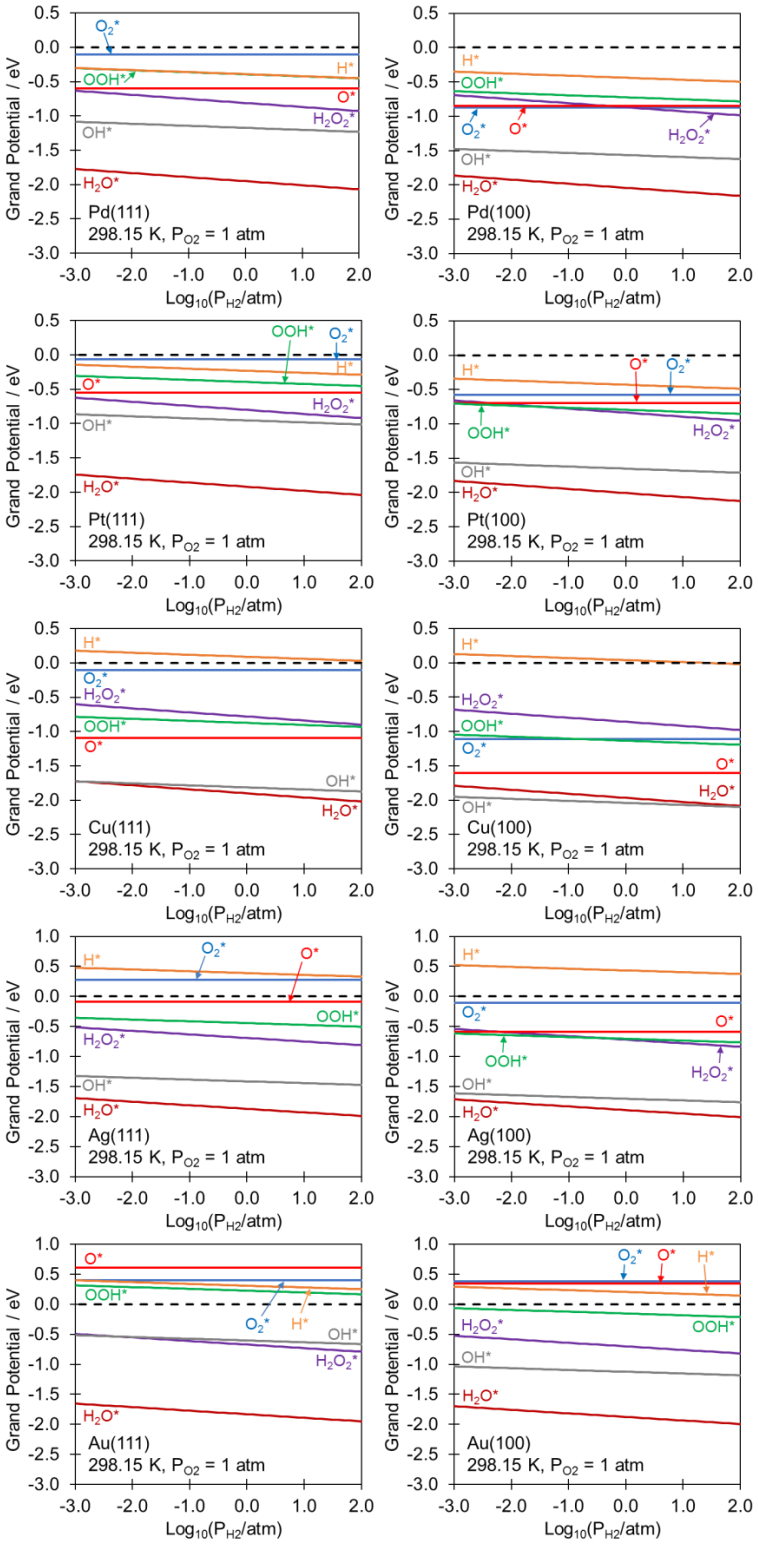

Figure 3.4 Stability of each surface intermediate (at 0.25 ML coverage in a (2 × 2) surface unit cell) relative to gas-phase reservoirs of the H_2 and O_2 reactants at 298.15 K. These diagrams are analogous to *ab initio* phase diagrams, wherein a more negative grand potential indicates a more stable species. The dotted black line at a grand potential of 0.0 eV indicates the stability of the clean surface (no adsorbates).

3.3.7 Maximum rate analysis of pathways and potential rate-limiting steps

To further analyze the intrinsic activity of the *clean* metal surfaces toward the direct reaction of H_2 with O_2, we perform a maximum rate analysis following the formalism of Farberow et al.[145] This procedure improves upon our PES-based pathway analysis by also including effects of entropy, temperature, and partial pressure under realistic reaction conditions. We apply the maximum rate analysis to each of the four pathways defined in Scheme 3.1 (H_2O_2 formation with desorption, and the dissociative, peroxyl, and peroxide pathways leading to H_2O formation), calculating the maximum rate and identifying the most likely rate-limiting step at 298 K. The results of the maximum rate analysis are summarized in Table 3.3 for the (111) facet and the (100) facet, with the complete data provided in Tables S3.4 and S3.5.

First, we observe that the rate-limiting step predicted by the maximum rate analysis can depend on both the identity and structure of the metal substrate. For example, H_2 dissociation is the slowest step on the (111) facets of the coinage metals (Cu, Ag, and Au) and remains limiting on the (100) facets of Cu and Ag, but H_2 dissociation is not the slowest step for any pathway on Au(100). Sluggish H_2 dissociation significantly lowers the maximum rates predicted for the coinage metals compared with those for Pd and Pt. In addition, the step $O_2* + * \rightarrow 2O*$ is slowest in the dissociative pathway on the (111) facets of all metals (except that of Cu), but does not limit that pathway on the (100) facets (except that of Au) due to the significantly reduced O-O bond dissociation barriers on the (100) facets.

Second, the hydrogenations of O* and OH* to form H_2O* never limit the maximum rate of any pathways considered here (Tables S3.4 and S3.5). This means that, on all surfaces, H_2O readily forms once the O-O and H-H bonds break. The only hydrogenation step that we predict to be kinetically limiting is the first addition of H* to O_2* to form OOH* on Pd(111) and Au(100).

Table 3.3 Summary of the maximum rate (r_{max}) and rate-limiting step for each pathway, as predicted by the maximum rate analysis. The complete data for the maximum rate analysis are tabulated in Tables S3.4 and S3.5. The more active facet for each pathway is indicated in bold face under the r_{max} column heading. Pathways and step numbers are in reference to Scheme 3.1. Rates are calculated at a temperature of 298.15 K and H_2, O_2, and H_2O partial pressures of 1.0 atm, 1.0 atm, and 0.010 atm, respectively. The H_2O partial pressure corresponds to 1 % conversion of H_2 with 100 % selectivity toward H_2O.

	Pathway	r_{max} / s^{-1}		Rate-limiting Step	
		(111)	(100)	(111)	(100)
Cu	H_2O_2 desorption	**2.2**	2.8×10^{-1}	(2) $H_{2(g)} + 2* \rightarrow 2H*$	(2) $H_{2(g)} + 2* \rightarrow 2H*$
	Dissociative	**2.2**	2.8×10^{-1}	(2) $H_{2(g)} + 2* \rightarrow 2H*$	(2) $H_{2(g)} + 2* \rightarrow 2H*$
	Peroxyl	**2.2**	2.8×10^{-1}	(2) $H_{2(g)} + 2* \rightarrow 2H*$	(2) $H_{2(g)} + 2* \rightarrow 2H*$
	Peroxide	**2.2**	2.8×10^{-1}	(2) $H_{2(g)} + 2* \rightarrow 2H*$	(2) $H_{2(g)} + 2* \rightarrow 2H*$
Pd	H_2O_2 desorption	9.1×10^{6}	$\mathbf{2.2\times10^{8}}$	(3a) $O_2* + H* \rightarrow OOH* + *$	(1) $O_{2(g)} + * \rightarrow O_2*$
	Dissociative	1.3×10^{-1}	$\mathbf{2.2\times10^{8}}$	(3b) $O_2* + * \rightarrow 2O*$	(1) $O_{2(g)} + * \rightarrow O_2*$
	Peroxyl	9.1×10^{6}	$\mathbf{2.2\times10^{8}}$	(3a) $O_2* + H* \rightarrow OOH* + *$	(1) $O_{2(g)} + * \rightarrow O_2*$
	Peroxide	9.1×10^{6}	$\mathbf{2.2\times10^{8}}$	(3a) $O_2* + H* \rightarrow OOH* + *$	(1) $O_{2(g)} + * \rightarrow O_2*$
Pt	H_2O_2 desorption	1.9×10^{8}	$\mathbf{2.2\times10^{8}}$	(1) $O_{2(g)} + * \rightarrow O_2*$	(1) $O_{2(g)} + * \rightarrow O_2*$
	Dissociative	4.3	$\mathbf{2.2\times10^{8}}$	(3b) $O_2* + * \rightarrow 2O*$	(1) $O_{2(g)} + * \rightarrow O_2*$
	Peroxyl	1.9×10^{8}	$\mathbf{2.2\times10^{8}}$	(1) $O_{2(g)} + * \rightarrow O_2*$	(1) $O_{2(g)} + * \rightarrow O_2*$
	Peroxide	1.9×10^{8}	$\mathbf{2.2\times10^{8}}$	(1) $O_{2(g)} + * \rightarrow O_2*$	(1) $O_{2(g)} + * \rightarrow O_2*$
Ag	H_2O_2 desorption	9.7×10^{-10}	$\mathbf{1.2\times10^{-8}}$	(2) $H_{2(g)} + 2* \rightarrow 2H*$	(2) $H_{2(g)} + 2* \rightarrow 2H*$
	Dissociative	1.8×10^{-14}	$\mathbf{1.2\times10^{-8}}$	(3b) $O_2* + * \rightarrow 2O*$	(2) $H_{2(g)} + 2* \rightarrow 2H*$
	Peroxyl	9.7×10^{-10}	$\mathbf{1.2\times10^{-8}}$	(2) $H_{2(g)} + 2* \rightarrow 2H*$	(2) $H_{2(g)} + 2* \rightarrow 2H*$
	Peroxide	9.7×10^{-10}	$\mathbf{1.2\times10^{-8}}$	(2) $H_{2(g)} + 2* \rightarrow 2H*$	(2) $H_{2(g)} + 2* \rightarrow 2H*$
Au	H_2O_2 desorption	5.5×10^{-8}	$\mathbf{2.3\times10^{-5}}$	(2) $H_{2(g)} + 2* \rightarrow 2H*$	(3a) $O_2* + H* \rightarrow OOH* + *$
	Dissociative	2.4×10^{-30}	$\mathbf{2.6\times10^{-18}}$	(3b) $O_2* + * \rightarrow 2O*$	(3b) $O_2* + * \rightarrow 2O*$
	Peroxyl	5.5×10^{-8}	$\mathbf{2.3\times10^{-5}}$	(2) $H_{2(g)} + 2* \rightarrow 2H*$	(3a) $O_2* + H* \rightarrow OOH* + *$
	Peroxide	5.5×10^{-8}	$\mathbf{2.3\times10^{-5}}$	(2) $H_{2(g)} + 2* \rightarrow 2H*$	(3a) $O_2* + H* \rightarrow OOH* + *$

Third, the peroxyl pathway to H_2O, the peroxide pathway to H_2O, and the H_2O_2 formation with desorption pathway always share the same rate-limiting step on a specific surface; and that rate-limiting step always precedes addition of the second hydrogen atom to molecular oxygen. Moreover, the maximum rate for the dissociative pathway to form H_2O is always less than or equivalent to the maximum rates for all other pathways (on a specific surface). Together these observations imply that we cannot distinguish pathways on the basis of comparing maximum rates – except for disregarding the dissociative pathway to H_2O on Pd(111), Pt(111), Ag(111), Au(111), and Au(100) due to maximum rates many orders of magnitude lower than the competing pathways. The result of a single shared rate-limiting step among competing pathways on a given surface also leads us to expect the product distribution to be dictated by the overall thermodynamics, assuming all steps after the rate-limiting step are quasi-equilibrated, and therefore H_2O would always the

primary product. We then anticipate that none of these *clean* monometallic surfaces can be selective toward H_2O_2. In order to achieve selectivity toward H_2O_2 rather than H_2O, elementary steps involving O-O bond dissociation, or O-H bond formation in O* or OH*, must also become kinetically limiting in each of the dissociative, peroxyl, and peroxide pathways to H_2O.

The qualitative conclusions from the maximum rate analysis are quite insensitive to changing the temperature or to changing the partial pressures of gas-phase species within an order of magnitude, because the calculated rates generally differ by many orders of magnitude. This same assessment is presented in Farberow et al.[145] However, those authors also demonstrate the importance of using surface models that reflect the state of the catalyst surface under realistic reaction conditions, i.e. including appropriate spectator species in the DFT calculations. It is well-known that spectator species can significantly modify the binding properties of both intermediates and transition states through adsorbate-adsorbate interactions[165-168] – or even enable alternative reaction pathways that are not feasible at low surface coverage.

Our analysis utilizes DFT energetics derived from spectator-free surface models, and so knowledge of the abundant surface intermediates under reaction conditions should be used to revise the surface models and repeat the maximum rate analysis. As discussed in the previous section, it is difficult to define the state of catalytic surfaces under reaction conditions based solely on DFT-calculated thermodynamics and in the absence of experimentally-validated microkinetic models or direct experimental evidence. We note that spectator coverage effects are generally observed to facilitate bond-forming steps and hinder bond-breaking steps. Those trends suggest that a highly covered surface might more adversely affect the dissociative, peroxyl, and peroxide pathways to H_2O than the H_2O_2 formation and desorption pathway, because O-O bond-breaking might become more difficult, while O-H bond formation might become easier. Nonetheless, the

reaction rates on the (111) and (100) facets of Cu, Ag, and Au might become even further limited by difficult H_2 dissociation if the surface is highly covered with adsorbates. The maximum rate analysis based on the clean surface energetics also suggests that the (100) facet is generally more active than the (111) facet (Table 3.3); but there is also a stronger thermodynamic driving force to populate the (100) facet with intermediates (Figure 3.4) – and so the relative activity of these facets may depend strongly on the surface coverage under reaction conditions.

3.4 Conclusions

In this chapter, we calculated thermodynamic and kinetic parameters for the direct, non-electrochemical reaction of H_2 and O_2 gases on the (100) facet of Pd, Pt, Cu, Ag, and Au using periodic DFT-GGA, and we have compared these results with previous calculations on the close-packed (111) facet of these late transition metals. Our goal was to determine the trends in oxygen reduction activity and selectivity when the coordinative saturation of the substrate decreases, including identification of the potentially rate-limiting steps and the most likely abundant surface intermediates. We find that, compared to the (111) facet of each metal, the (100) facet generally binds intermediates and transition states more strongly, lowers kinetic barriers for O-O bond dissociation, and raises kinetic barriers for O-H bond formation in dioxygen species. The latter two effects are particularly disadvantageous if the partial reduction product (H_2O_2) is desired – such as in the DSHP or for *in situ* activation of O_2 during selective oxidation reactions. A direct comparison of activation barriers for O-O bond dissociation and O-H bond formation in the dioxygen intermediates reveals that: O_2* is likely to dissociate before forming OOH* on Pd(100), Pt(100), Cu(111), and Cu(100); OOH* decomposition is favored to H_2O_2* formation on Pd(111), Pt(111), Ag(111), and Ag(100); and significant H_2O_2* formation may only be possible on Au(111) and Au(100).

We then performed a maximum rate analysis using realistic reaction conditions and demonstrate that the most likely rate-limiting step can depend on both the identity and structure of the metal surface. However, we predict none of the surfaces to be limited by their ability to (i) dissociate the O-O bond in OOH*/H_2O_2*, or (ii) hydrogenate O*/OH*, both of which are distinctly tied to H_2O formation rather than H_2O_2 formation; instead, all rate-limiting steps in the H_2O formation pathways are shared with the pathway toward H_2O_2 formation. This suggests that the intrinsic reactivity of the clean transition metal surfaces is to completely reduce O_2 to H_2O – independent of the surface structure – and therefore a primary challenge when tailoring catalysts for the partial reduction of O_2 is to identify substrates on which steps distinct to H_2O formation (e.g., O-O bond dissociation) become kinetically limiting. Our maximum rate analysis also shows that H_2 dissociation is generally the slowest step on the coinage metals (Cu, Ag, and Au), highlighting the importance of considering H_2 activation when developing predictive models for this reaction.

A caveat of our analysis is that our thermodynamic and kinetic parameters pertain to *clean* metal surfaces and do not consider the effect of surface coverage, which may significantly modify the calculated surface energetics. We therefore also provided a thermodynamic analysis based on the construction of free energy diagrams to provide insight into the most likely candidates for surface-abundant intermediates, but experimental insight (spectroscopic evidence, experimentally-consistent microkinetic models) is ultimately required to improve the accuracy of the surface models used in our DFT calculations.

Supplementary Figures, Tables, and Methods for Chapter 3

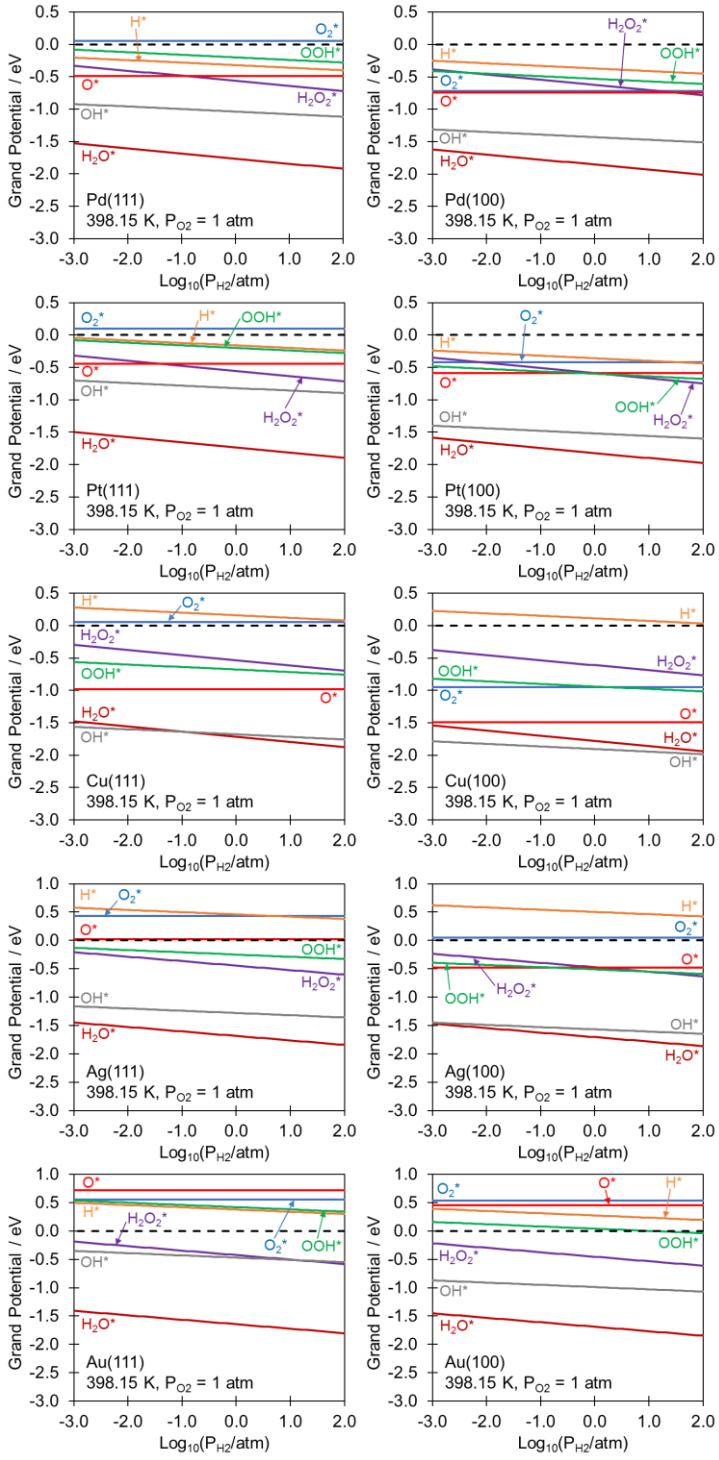

Figure S3.1 Stability of each surface intermediate (at 0.25 ML coverage in a (2 × 2) surface unit cell) relative to gas-phase reservoirs of the H_2 and O_2 reactants at 398.15 K. These diagrams are generated in an analogous manner to *ab initio* phase diagram, wherein a more negative grand potential indicates a more stable species. The dotted black line at a grand potential of 0.0 eV indicates the stability of the clean surface (no adsorbates).

Table S3.1 Reaction energies, ΔE, (and activation energy barriers, E_a, in parenthesis) for all elementary steps on the (100) facet of Pd, Pt, Cu, Ag, and Au. Step numbers are in reference to Scheme 3.1. All values are reported with respect to the infinitely separated reactants and products. No activation barriers are calculated for adsorption and desorption steps (assumed equal to the reaction energy, if endothermic, or zero barrier if the reaction is exothermic) with the exception of dissociative H_2 adsorption. The initial state of the activation barrier calculation for elementary step 8, corresponding to two OH* co-adsorbed in the unit cell, is generally stabilized through hydrogen bonding with respect to infinitely separated OH* species. The subsequent activation barrier for hydrogen atom transfer is nearly spontaneous in the exothermic direction, and the corresponding transition state energy can be lower in energy than the final state energy of the infinitely separated O* and H_2O* products. Therefore, we simply report the activation barriers as equal to the reaction energies at infinite separation for step 8.

Elementary Step		ΔE (E_a), in eV				
		Pd(100)	Pt(100)	Cu(100)	Ag(100)	Au(100)
(1)	$O_{2(g)} + * \rightarrow O_2*$	-1.27 (-)	-0.97 (-)	-1.50 (-)	-0.50 (-)	-0.01 (-)
(2)	$H_{2(g)} + * \rightarrow 2H*$	-1.19 (0.00)	-1.17 (0.00)	-0.24 (0.56)	0.55 (1.00)	0.09 (0.66)
(3a)	$O_2* + H* \rightarrow OOH* + *$	0.67 (1.19)	0.28 (0.57)	0.00 (1.22)	-0.96 (0.56)	-0.67 (0.40)
(3b)	$O_2* + * \rightarrow 2O*$	-0.98 (0.30)	-0.97 (0.15)	-2.25 (0.37)	-1.22 (0.91)	0.17 (1.34)
(4a)	$OOH* + H* \rightarrow H_2O_2* + *$	0.29 (0.73)	0.40 (0.60)	0.25 (0.99)	-0.43 (0.33)	-0.74 (0.16)
(4b)	$OOH* + * \rightarrow O* + OH*$	-1.83 (0.02)	-1.68 (0.12)	-2.63 (0.00)	-1.70 (0.30)	-0.74 (0.42)
(5b)	$H_2O_2* + * \rightarrow OH* + OH*$	-2.29 (0.05)	-2.50 (0.06)	-3.25 (0.07)	-2.72 (0.08)	-1.58 (0.42)
(6)	$O* + H* \rightarrow OH* + *$	-0.17 (0.86)	-0.42 (0.37)	-0.37 (1.21)	-1.45 (0.83)	-1.58 (0.20)
(7)	$OH* + H* \rightarrow H_2O* + *$	0.00 (0.67)	0.11 (0.74)	0.07 (0.88)	-0.59 (0.48)	-0.92 (0.39)
(8)	$OH* + OH* \rightarrow H_2O* + O*$	0.17 (0.17)	0.53 (0.53)	0.44 (0.44)	0.86 (0.86)	0.65 (0.65)
(9)	$H_2O* \rightarrow H_2O_{(g)} + *$	0.30 (-)	0.27 (-)	0.22 (-)	0.15 (-)	0.13 (-)
(5a)	$H_2O_2* \rightarrow H_2O_{2(g)} + *$	0.36 (-)	0.33 (-)	0.35 (-)	0.21 (-)	0.19 (-)

Table S3.2 Stability of all isomeric states in reference to the reactant state of [$2H_{2(g)}$+$O_{2(g)}$] for the (111) facet. All energies are in eV, and are calculated from the DFT-derived total energies[55] (i.e., these represent the relative energies at 0 K and under vacuum) with respect to species at infinite separation from each other (denoted by the "|"). Isomers are arranged in order of decreasing stability (more positive energy relative to the reactant state) for each surface. The most stable state for each surface is in bold face.

Isomers	Pd(111)	Isomers	Pt(111)	Isomers	Cu(111)	Isomers	Ag(111)	Isomers	Au(111)
$2H_2O$*	**-4.80**	**$2H_2O$***	**-4.74**	**$2H_2O$***	**-4.70**	**$2H_2O$***	**-4.64**	**$2H_2O$***	**-4.56**
$H_2O_{(g)}$|H_2O*	-4.60	$H_2O_{(g)}$|H_2O*	-4.56	H_2O*|OH*|H*	-4.57	$H_2O_{(g)}$|H_2O*	-4.51	$H_2O_{(g)}$|H_2O*	-4.48
H_2O*|OH*|H*	-4.46	$2H_2O_{(g)}$	-4.38	$H_2O_{(g)}$|H_2O*	-4.54	$2H_2O_{(g)}$	-4.38	$2H_2O_{(g)}$	-4.38
$2H_2O_{(g)}$	-4.38	H_2O*|OH*|H*	-4.05	2OH*|2H*	-4.43	H_2O*|OH*|H*	-3.84	H_2O*|OH*|H*	-3.07
H_2O*|O*|2H*	-4.38	H_2O*|O*|2H*	-3.98	$H_2O_{(g)}$|OH*|H*	-4.41	$H_2O_{(g)}$|OH*|H*	-3.71	$H_2O_{(g)}$|OH*|H*	-2.98
$H_2O_{(g)}$|OH*|H*	-4.25	$H_2O_{(g)}$|OH*|H*	-3.87	$2H_2O_{(g)}$	-4.38	$H_{2(g)}$|2OH*	-3.48	$H_{2(g)}$|H_2O*|O*	-1.94
$H_2O_{(g)}$|O*|2H*	-4.17	$H_2O_{(g)}$|O*|2H*	-3.80	$H_{2(g)}$|2OH*	-4.28	2OH*|2H*	-3.03	$H_{2(g)}$|2OH*	-1.86
2OH*|2H*	-4.11	2OH*|2H*	-3.35	2H*|$H_{2(g)}$|2O*	-3.99	$H_{2(g)}$|H_2O*|O*	-2.68	H_2O*|O*|2H*	-1.65
OH*|3H*|O*	-4.03	OH*|3H*|O*	-3.28	H_2O*|O*|2H*	-3.86	H_2O*|O*|2H*	-2.23	2OH*|2H*	-1.57
4H*|2O*	-3.95	4H*|2O*	-3.21	OH*|3H*|O*	-3.72	$H_2O_{(g)}$|O*|2H*	-2.10	$H_2O_{(g)}$|O*|2H*	-1.56
2H*|$H_{2(g)}$|2O*	-3.44	$H_{2(g)}$|H_2O*|O*	-3.19	$H_{2(g)}$|H_2O*|O*	-3.71	$H_{2(g)}$|OH*|H*|O*	-1.87	H_2O_2*|$H_{2(g)}$	-1.29
$H_{2(g)}$|H_2O*|O*	-3.27	2H*|$H_{2(g)}$|2O*	-3.12	$H_2O_{(g)}$|O*|2H*	-3.70	OH*|3H*|O*	-1.42	$H_2O_{2(g)}$|$H_{2(g)}$	-1.13
$H_{2(g)}$|2OH*	-3.00	$H_{2(g)}$|2OH*	-2.56	$H_{2(g)}$|OH*|H*|O*	-3.57	H_2O_2*|$H_{2(g)}$	-1.31	H_2O_2*|2H*	-1.00
$H_{2(g)}$|OH*|H*|O*	-2.92	$H_{2(g)}$|OH*|H*|O*	-2.49	4H*|2O*	-3.01	2H*|$H_{2(g)}$|2O*	-1.17	$H_2O_{2(g)}$|2H*	-0.84
4H*|O_2*	-2.71	H_2O_2*|2H*	-2.21	$2H_{2(g)}$|2O*	-2.72	$H_2O_{2(g)}$|$H_{2(g)}$	-1.13	$H_{2(g)}$|OH*|H*|O*	-0.44
H_2O_2*|2H*	-2.54	OOH*|3H*	-2.05	OOH*|3H*	-1.57	H_2O_2*|2H*	-0.86	OH*|3H*|O*	-0.15
OOH*|3H*	-2.53	4H*|O_2*	-2.03	H_2O_2*|2H*	-1.55	$2H_{2(g)}$|2O*	-0.72	OOH*|H*|$H_{2(g)}$	-0.11
$H_2O_{2(g)}$|2H*	-2.24	$H_2O_{2(g)}$|2H*	-1.92	OOH*|H*|$H_{2(g)}$	-1.43	OOH*|H*|$H_{2(g)}$	-0.70	$2H_{2(g)}$|O_2*	0.00
4H*|$O_{2(g)}$	-2.21	$2H_{2(g)}$|2O*	-1.64	H_2O_2*|$H_{2(g)}$	-1.40	$H_2O_{2(g)}$|2H*	-0.68	$2H_{2(g)}$|$O_{2(g)}$	0.00
$2H_{2(g)}$|2O*	-1.74	4H*|$O_{2(g)}$	-1.57	$H_2O_{2(g)}$|2H*	-1.28	OOH*|3H*	-0.24	OOH*|3H*	0.19
2H*|$H_{2(g)}$|O_2*	-1.61	H_2O_2*|$H_{2(g)}$	-1.42	$H_2O_{2(g)}$|$H_{2(g)}$	-1.13	$2H_{2(g)}$|O_2*	-0.12	2H*|$H_{2(g)}$|2O*	0.25
H_2O_2*|$H_{2(g)}$	-1.43	OOH*|H*|$H_{2(g)}$	-1.27	4H*|O_2*	-0.79	$2H_{2(g)}$|$O_{2(g)}$	0.00	2H*|$H_{2(g)}$|O_2*	0.29
OOH*|H*|$H_{2(g)}$	-1.43	2H*|$H_{2(g)}$|O_2*	-1.25	2H*|$H_{2(g)}$|O_2*	-0.65	4H*|2O*	0.19	2H*|$H_{2(g)}$|$O_{2(g)}$	0.29
$H_2O_{2(g)}$|$H_{2(g)}$	-1.13	$H_2O_{2(g)}$|$H_{2(g)}$	-1.13	$2H_{2(g)}$|O_2*	-0.50	2H*|$H_{2(g)}$|O_2*	0.33	4H*|O_2*	0.59
2H*|$H_{2(g)}$|$O_{2(g)}$	-1.11	2H*|$H_{2(g)}$|$O_{2(g)}$	-0.79	4H*|$O_{2(g)}$	-0.29	2H*|$H_{2(g)}$|$O_{2(g)}$	0.45	4H*|$O_{2(g)}$	0.59
$2H_{2(g)}$|O_2*	-0.50	$2H_{2(g)}$|O_2*	-0.46	2H*|$H_{2(g)}$|$O_{2(g)}$	-0.15	4H*|O_2*	0.79	$2H_{2(g)}$|2O*	0.68
$2H_{2(g)}$|$O_{2(g)}$	0.00	$2H_{2(g)}$|$O_{2(g)}$	0.00	$2H_{2(g)}$|$O_{2(g)}$	0.00	4H*|$O_{2(g)}$	0.91	4H*|2O*	1.27

Table S3.3 Stability of all isomeric states in reference to the reactant state of [$2H_{2(g)}$+$O_{2(g)}$] for the (100) facet. All energies are in eV, and are calculated from the DFT-derived total energies (i.e., these represent the relative energies at 0 K and under vacuum) with respect to species at infinite separation from each other (denoted by the "|"). Isomers are arranged in order of decreasing stability (more positive energy relative to the reactant state) for each surface. The most stable state for each surface is in bold face.

Isomers	Pd(100)	Isomers	Pt(100)	Isomers	Cu(100)	Isomers	Ag(100)	Isomers	Au(100)
$2H_2O$*	**-4.99**	**2OH*|2H***	**-5.14**	**2OH*|2H***	**-4.97**	**$2H_2O$***	**-4.68**	**$2H_2O$***	**-4.65**
H_2O*|OH*|H*	-4.98	H_2O*|OH*|H*	-5.03	H_2O*|OH*|H*	-4.90	$H_2O_{(g)}$|H_2O*	-4.53	$H_2O_{(g)}$|H_2O*	-4.52
2OH*|2H*	-4.98	$2H_2O$*	-4.92	$2H_2O$*	-4.83	$2H_2O_{(g)}$	-4.38	$2H_2O_{(g)}$	-4.38
H_2O*|O*|2H*	-4.81	$H_2O_{(g)}$|OH*|H*	-4.76	$H_{2(g)}$|2OH*	-4.74	H_2O*|OH*|H*	-4.10	H_2O*|OH*|H*	-3.73
OH*|3H*|O*	-4.81	OH*|3H*|O*	-4.72	$H_2O_{(g)}$|OH*|H*	-4.68	$H_{2(g)}$|2OH*	-4.06	$H_2O_{(g)}$|OH*|H*	-3.60
$H_2O_{(g)}$|H_2O*	-4.69	$H_2O_{(g)}$|H_2O*	-4.65	$H_2O_{(g)}$|H_2O*	-4.61	$H_2O_{(g)}$|OH*|H*	-3.95	$H_{2(g)}$|2OH*	-2.90
$H_2O_{(g)}$|OH*|H*	-4.68	H_2O*|O*|2H*	-4.60	OH*|3H*|O*	-4.60	2OH*|2H*	-3.51	2OH*|2H*	-2.81
4H*|2O*	-4.64	$2H_2O_{(g)}$	-4.38	H_2O*|O*|2H*	-4.53	$H_{2(g)}$|H_2O*|O*	-3.20	$H_{2(g)}$|H_2O*|O*	-2.25
$H_2O_{(g)}$|O*|2H*	-4.51	$H_2O_{(g)}$|O*|2H*	-4.34	$2H_2O_{(g)}$	-4.38	H_2O*|O*|2H*	-2.65	H_2O*|O*|2H*	-2.16
$2H_2O_{(g)}$	-4.38	4H*|2O*	-4.29	$H_{2(g)}$|OH*|H*|O*	-4.36	$H_{2(g)}$|OH*|H*|O*	-2.62	$H_2O_{(g)}$|O*|2H*	-2.02
$H_{2(g)}$|2OH*	-3.79	$H_{2(g)}$|2OH*	-3.96	$H_2O_{(g)}$|O*|2H*	-4.30	$H_2O_{(g)}$|O*|2H*	-2.50	$H_{2(g)}$|OH*|H*|O*	-1.33
4H*|O2*	-3.66	$H_{2(g)}$|OH*|H*|O*	-3.54	$H_{2(g)}$|H_2O*|O*	-4.29	OH*|3H*|O*	-2.07	H_2O_2*|$H_{2(g)}$	-1.32
$H_{2(g)}$|H_2O*|O*	-3.62	$H_{2(g)}$|H_2O*|O*	-3.43	4H*|2O*	-4.22	$2H_{2(g)}$|2O*	-1.72	OH*|3H*|O*	-1.24
$H_{2(g)}$|OH*|H*|O*	-3.62	4H*|O_2*	-3.32	2H*|$H_{2(g)}$|2O*	-3.99	H_2O_2*|$H_{2(g)}$	-1.34	H_2O_2*|2H*	-1.23
2H*|$H_{2(g)}$|2O*	-3.44	2H*|$H_{2(g)}$|2O*	-3.12	$2H_{2(g)}$|2O*	-3.75	2H*|$H_{2(g)}$|2O*	-1.17	$H_2O_{2(g)}$|$H_{2(g)}$	-1.13
OOH*|3H*	-3.00	OOH*|3H*	-3.04	4H*|O_2*	-1.97	$H_2O_{2(g)}$|$H_{2(g)}$	-1.13	$H_2O_{2(g)}$|2H*	-1.04
H_2O_2*|2H*	-2.69	H_2O_2*|2H*	-2.64	OOH*|3H*	-1.97	OOH*|H*|$H_{2(g)}$	-0.91	OOH*|H*|$H_{2(g)}$	-0.59
2H*|$H_{2(g)}$|O_2*	-2.46	4H*|$O_{2(g)}$	-2.35	2H*|$H_{2(g)}$|O_2*	-1.74	H_2O_2*|2H*	-0.79	OOH*|3H*	-0.50
4H*|$O_{2(g)}$	-2.39	$H_2O_{2(g)}$|2H*	-2.31	OOH*|H*|$H_{2(g)}$	-1.73	4H*|2O*	-0.62	$2H_{2(g)}$|O_2*	-0.01
$H_2O_{2(g)}$|2H*	-2.33	2H*|$H_{2(g)}$|O_2*	-2.14	H_2O_2*|2H*	-1.72	$H_2O_{2(g)}$|2H*	-0.58	$2H_{2(g)}$|$O_{2(g)}$	0.00
$2H_{2(g)}$|2O*	-2.25	$2H_{2(g)}$|2O*	-1.94	$2H_{2(g)}$|O_2*	-1.50	$2H_{2(g)}$|O_2*	-0.50	2H*|$H_{2(g)}$|O_2*	0.08
OOH*|H*|$H_{2(g)}$	-1.80	OOH*|H*|$H_{2(g)}$	-1.86	H_2O_2*|$H_{2(g)}$	-1.48	OOH*|3H*	-0.36	2H*|$H_{2(g)}$|$O_{2(g)}$	0.09
H_2O_2*|$H_{2(g)}$	-1.49	H_2O_2*|$H_{2(g)}$	-1.46	$H_2O_{2(g)}$|2H*	-1.37	$2H_{2(g)}$|$O_{2(g)}$	0.00	$2H_{2(g)}$|2O*	0.15
$2H_{2(g)}$|O_2*	-1.27	2H*|$H_{2(g)}$|$O_{2(g)}$	-1.17	$H_2O_{2(g)}$|$H_{2(g)}$	-1.13	2H*|$H_{2(g)}$|O_2*	0.05	4H*|O2*	0.17
2H*|$H_{2(g)}$|$O_{2(g)}$	-1.19	$H_2O_{2(g)}$|$H_{2(g)}$	-1.13	4H*|$O_{2(g)}$	-0.47	2H*|$H_{2(g)}$|$O_{2(g)}$	0.55	4H*|$O_{2(g)}$	0.18
$H_2O_{2(g)}$|$H_{2(g)}$	-1.13	$2H_{2(g)}$|O_2*	-0.97	2H*|$H_{2(g)}$|$O_{2(g)}$	-0.24	4H*|O_2*	0.60	2H*|$H_{2(g)}$|2O*	0.25
$2H_{2(g)}$|$O_{2(g)}$	0.00	$2H_{2(g)}$|$O_{2(g)}$	0.00	$2H_{2(g)}$|$O_{2(g)}$	0.00	4H*|$O_{2(g)}$	1.10	4H*|2O*	0.34

Table S3.4 Maximum rates of elementary steps in competing mechanisms (Scheme 3.1) on the clean (111) facets. Rates are calculated at a temperature of 298.15 K and H_2, O_2, and H_2O partial pressures of 1.0 atm, 1.0 atm, and 0.010 atm, respectively. The H_2O partial pressure corresponds to 1 % conversion of H_2 with 100 % selectivity toward H_2O. The limiting step in each pathway, on each surface, is shaded in red. K_i is the equilibrium constant for step i, and $K_i^{\ddagger}$ is equilibrium constant for the production of the activated complex [ ]‡ of step i from the initial state of step i.

Hydrogen Peroxide Formation with Desorption Pathway								
Step	**Overall reaction**	**Rate constant**	r_{max} [s^{-1}]				
			Cu(111)	**Pd(111)**	**Pt(111)**	**Ag(111)**	**Au(111)**
(1) $O_{2(g)} + * \rightarrow O_2*$	$O_{2(g)} + * \leftrightarrow [O_2*]^{\ddagger}$	$K_1^{\ddagger}$	1.6E+08	1.9E+08	**1.9E+08**	2.0E+08	2.1E+08
(2) $H_{2(g)} + 2* \rightarrow 2H*$	$H_{2(g)} + 2* \leftrightarrow [2H*]^{\ddagger}$	$K_2^{\ddagger}$	**2.2E+00**	7.5E+08	7.5E+08	**9.7E-10**	**5.5E-08**
(3a) $O_2* + H* \rightarrow OOH* + *$	$O_{2(g)} + 1/2H_{2(g)} + 2* \leftrightarrow [OOH* + *]^{\ddagger}$	$K_1K_2^{1/2}K_{3a}^{\ddagger}$	1.1E+02	**9.1E+06**	6.8E+09	3.0E-04	6.5E-04
(4a) $OOH* + H* \rightarrow H_2O_2* + *$	$O_{2(g)} + H_{2(g)} + 2* \leftrightarrow [H_2O_2* + *]^{\ddagger}$	$K_1K_2K_{3a}K_{4a}^{\ddagger}$	6.8E+08	3.7E+13	1.8E+15	2.3E-01	3.4E-01
(5a) $H_2O_2* \rightarrow H_2O_{2(g)} + *$	$O_{2(g)} + H_{2(g)} + * \leftrightarrow [H_2O_{2(g)} + *]^{\ddagger}$	$K_1K_2K_{3a}K_{4a}K_{5a}^{\ddagger}$	1.2E+22	1.5E+22	1.5E+22	1.6E+22	1.6E+22
Dissociative Pathway to H_2O							
Step	**Overall reaction**	**Rate constant**	r_{max} [s^{-1}]				
			Cu(111)	**Pd(111)**	**Pt(111)**	**Ag(111)**	**Au(111)**
(1) $O_{2(g)} + * \rightarrow O_2*$	$O_{2(g)} + * \leftrightarrow [O_2*]^{\ddagger}$	$K_1^{\ddagger}$	1.6E+08	1.9E+08	1.9E+08	2.0E+08	2.1E+08
(2) $H_{2(g)} + 2* \rightarrow 2H*$	$H_{2(g)} + 2* \leftrightarrow [2H*]^{\ddagger}$	$K_2^{\ddagger}$	**2.2E+00**	7.5E+08	7.5E+08	9.7E-10	5.5E-08
(3b) $O_2* + * \rightarrow 2O*$	$O_{2(g)} + 2* \leftrightarrow [O* + O*]^{\ddagger}$	$K_1K_{3b}^{\ddagger}$	2.6E+09	**1.3E-01**	**4.3E+00**	**1.8E-14**	**2.4E-30**
(6) $O* + H* \rightarrow OH* + *$	$1/2O_{2(g)} + 1/2H_{2(g)} + 2* \leftrightarrow [OH* + *]^{\ddagger}$	$K_1^{1/2}K_2^{1/2}K_{3b}^{1/2}K_6^{\ddagger}$	2.6E+15	7.7E+13	2.3E+12	9.6E-04	2.2E-14
(7) $OH* + H* \rightarrow H_2O* + *$	$1/2O_{2(g)} + H_{2(g)} + 2* \leftrightarrow [H_2O* + *]^{\ddagger}$	$K_1^{1/2}K_2K_{3b}^{1/2}K_6K_8^{\ddagger}$	4.7E+23	1.2E+28	1.8E+29	1.2E+18	9.9E+10
(9) $H_2O* \rightarrow H_2O_{(g)} + *$	$1/2O_{2(g)} + H_{2(g)} + * \leftrightarrow [H_2O_{(g)} + *]^{\ddagger}$	$K_1^{1/2}K_2K_{3b}^{1/2}K_6K_8K_{10}^{\ddagger}$	2.0E+43	2.4E+43	2.4E+43	2.5E+43	2.6E+43
Peroxyl Pathway to H_2O							
Step	**Overall reaction**	**Rate constant**	r_{max} [s^{-1}]				
			Cu(111)	**Pd(111)**	**Pt(111)**	**Ag(111)**	**Au(111)**
(1) $O_{2(g)} + * \rightarrow O_2*$	$O_{2(g)} + * \leftrightarrow [O_2*]^{\ddagger}$	$K_1^{\ddagger}$	1.6E+08	1.9E+08	**1.9E+08**	2.0E+08	2.1E+08
(2) $H_{2(g)} + 2* \rightarrow 2H*$	$H_{2(g)} + 2* \leftrightarrow [2H*]^{\ddagger}$	$K_2^{\ddagger}$	**2.2E+00**	7.5E+08	7.5E+08	**9.7E-10**	**5.5E-08**
(3a) $O_2* + H* \rightarrow OOH* + *$	$O_{2(g)} + 1/2H_{2(g)} + 2* \leftrightarrow [OOH* + *]^{\ddagger}$	$K_1K_2^{1/2}K_{3a}^{\ddagger}$	1.1E+02	**9.1E+06**	6.8E+09	3.0E-04	6.5E-04
(4b) $OOH* + * \rightarrow O* + OH*$	$O_{2(g)} + 1/2H_{2(g)} + 2* \leftrightarrow [O* + OH*]^{\ddagger}$	$K_1K_2^{1/2}K_{3a}K_{4b}^{\ddagger}$	3.6E+24	2.7E+16	5.6E+14	2.3E+11	2.2E-02
(6) $O* + H* \rightarrow OH* + *$	$O_{2(g)} + 3/2H_{2(g)} + 2* \leftrightarrow [OH* + *]^{\ddagger} + H_2O_{(g)}$	$K_1K_2^{3/2}K_{3a}K_{4b}K_6^{\ddagger}K_{10}K_8$	2.4E+52	7.3E+50	2.2E+49	9.1E+33	2.0E+23
(7) $OH* + H* \rightarrow H_2O* + *$	$1/2O_{2(g)} + H_{2(g)} + 2* \leftrightarrow [H_2O* + *]^{\ddagger}$	$K_1^{1/2}K_2K_{3a}^{1/2}K_{4b}^{1/2}K_6^{1/2}K_8^{\ddagger}$	4.7E+23	1.2E+28	1.8E+29	1.2E+18	9.9E+10
(9) $H_2O* \rightarrow H_2O_{(g)} + *$	$1/2O_{2(g)} + H_{2(g)} + * \leftrightarrow [H_2O_{(g)} + *]^{\ddagger}$	$K_1^{1/2}K_2K_{3a}^{1/2}K_{4b}^{1/2}K_6^{1/2}K_8K_{10}^{\ddagger}$	2.0E+43	2.4E+43	2.4E+43	2.5E+43	2.6E+43
Peroxide Pathway to H_2O							
Step	**Overall reaction**	**Rate constant**	r_{max} [s^{-1}]				
			Cu(111)	**Pd(111)**	**Pt(111)**	**Ag(111)**	**Au(111)**
(1) $O_{2(g)} + * \rightarrow O_2*$	$O_{2(g)} + * \leftrightarrow [O_2*]^{\ddagger}$	$K_1^{\ddagger}$	1.6E+08	1.9E+08	**1.9E+08**	2.0E+08	2.1E+08
(2) $H_{2(g)} + 2* \rightarrow 2H*$	$H_{2(g)} + 2* \leftrightarrow [2H*]^{\ddagger}$	$K_2^{\ddagger}$	**2.2E+00**	7.5E+08	7.5E+08	**9.7E-10**	**5.5E-08**
(3a) $O_2* + H* \rightarrow OOH* + *$	$O_{2(g)} + 1/2H_{2(g)} + 2* \leftrightarrow [OOH* + *]^{\ddagger}$	$K_1K_2^{1/2}K_{3a}^{\ddagger}$	1.1E+02	**9.1E+06**	6.8E+09	3.0E-04	6.5E-04
(4a) $OOH* + H* \rightarrow H_2O_2* + *$	$O_{2(g)} + H_{2(g)} + 2* \leftrightarrow [H_2O_2* + *]^{\ddagger}$	$K_1K_2K_{3a}K_{4a}^{\ddagger}$	6.8E+08	3.7E+13	1.8E+15	2.3E-01	3.4E-01
(5b) $H_2O_2* + * \rightarrow 2OH*$	$O_{2(g)} + H_{2(g)} + 2* \leftrightarrow [OH* + OH*]^{\ddagger}$	$K_1K_2K_{3a}K_{4a}K_{5b}^{\ddagger}$	2.6E+21	3.8E+20	2.5E+19	5.2E+18	6.3E+12
(7) $OH* + H* \rightarrow H_2O* + *$	$1/2O_{2(g)} + H_{2(g)} + 2* \leftrightarrow [H_2O* + *]^{\ddagger}$	$K_1^{1/2}K_2K_{3a}^{1/2}K_{4a}^{1/2}K_{5b}^{1/2}K_8^{\ddagger}$	4.7E+23	1.2E+28	1.8E+29	1.2E+18	9.9E+10
(9) $H_2O* \rightarrow H_2O_{(g)} + *$	$1/2O_{2(g)} + H_{2(g)} + * \leftrightarrow [H_2O_{(g)} + *]^{\ddagger}$	$K_1^{1/2}K_2K_{3a}^{1/2}K_{4a}^{1/2}K_{5b}^{1/2}K_8K_{10}^{\ddagger}$	2.0E+43	2.4E+43	2.4E+43	2.5E+43	2.6E+43

Table S3.5 Maximum rates of elementary steps in competing mechanisms (Scheme 3.1) on the clean (100) facets. Rates are calculated at a temperature of 298.15 K and H_2, O_2, and H_2O partial pressures of 1.0 atm, 1.0 atm, and 0.010 atm, respectively. The H_2O partial pressure corresponds to 1 % conversion of H_2 with 100 % selectivity toward H_2O. The limiting step in each mechanism, on each surface, is shaded in red. K_i is the equilibrium constant for step i, and $K_i^{\ddagger}$ is equilibrium constant for the production of the activated complex [ ]‡ of step i from the initial state of step i.

Hydrogen Peroxide Formation with Desorption Pathway

Step		Overall reaction	Rate constant	r_{max} [s^{-1}]				
				Cu(100)	Pd(100)	Pt(100)	Ag(100)	Au(100)
(1)	$O_{2(g)} + * \rightarrow O_2*$	$O_{2(g)} + * \leftrightarrow [O_2*]^{\ddagger}$	$K_1^{\ddagger}$	1.8E+08	2.2E+08	2.2E+08	2.3E+08	2.4E+08
(2)	$H_{2(g)} + 2* \rightarrow 2H*$	$H_{2(g)} + 2* \leftrightarrow [2H*]^{\ddagger}$	$K_2^{\ddagger}$	2.8E-01	8.7E+08	8.7E+08	1.2E-08	7.1E-03
(3a)	$O_2* + H* \rightarrow OOH* + *$	$O_{2(g)} + 1/2H_{2(g)} + 2* \leftrightarrow [OOH* + *]^{\ddagger}$	$K_1K_2^{1/2}K_{3a}^{\ddagger}$	3.1E+09	1.2E+14	2.6E+19	1.1E-03	2.3E-05
(4a)	$OOH* + H* \rightarrow H_2O_2* + *$	$O_{2(g)} + H_{2(g)} + 2* \leftrightarrow [H_2O_2* + *]^{\ddagger}$	$K_1K_2K_{3a}K_{4a}^{\ddagger}$	1.2E+12	2.5E+17	9.0E+20	3.1E+09	7.6E+06
(5a)	$H_2O_2* \rightarrow H_2O_{2(g)} + *$	$O_{2(g)} + H_{2(g)} + * \leftrightarrow [H_2O_{2(g)} + *]^{\ddagger}$	$K_1K_2K_{3a}K_{4a}K_{5a}^{\ddagger}$	1.4E+22	1.7E+22	1.7E+22	1.8E+22	1.8E+22

Dissociative Pathway to H_2O

Step		Overall reaction	Rate constant	r_{max} [s^{-1}]				
				Cu(100)	Pd(100)	Pt(100)	Ag(100)	Au(100)
(1)	$O_{2(g)} + * \rightarrow O_2*$	$O_{2(g)} + * \leftrightarrow [O_2*]^{\ddagger}$	$K_1^{\ddagger}$	1.8E+08	2.2E+08	2.2E+08	2.3E+08	2.4E+08
(2)	$H_{2(g)} + 2* \rightarrow 2H*$	$H_{2(g)} + 2* \leftrightarrow [2H*]^{\ddagger}$	$K_2^{\ddagger}$	2.8E-01	8.6E+08	8.7E+08	1.2E-08	7.1E-03
(3b)	$O_2* + * \rightarrow 2O*$	$O_{2(g)} + 2* \leftrightarrow [O* + O*]^{\ddagger}$	$K_1K_{3b}^{\ddagger}$	1.1E+24	1.6E+21	4.9E+18	8.3E-03	2.6E-18
(6)	$O* + H* \rightarrow OH* + *$	$1/2O_{2(g)} + 1/2H_{2(g)} + 2* \leftrightarrow [OH* + *]^{\ddagger}$	$K_1^{1/2}K_2^{1/2}K_{3b}^{1/2}K_6^{\ddagger}$	1.7E+19	2.7E+20	1.1E+26	6.1E+01	3.2E+00
(7)	$OH* + H* \rightarrow H_2O* + *$	$1/2O_{2(g)} + H_{2(g)} + 2* \leftrightarrow [H_2O* + *]^{\ddagger}$	$K_1^{1/2}K_2K_{3b}^{1/2}K_6K_8^{\ddagger}$	2.2E+30	8.0E+33	1.2E+34	5.6E+24	2.1E+20
(9)	$H_2O* \rightarrow H_2O_{(g)} + *$	$1/2O_{2(g)} + H_{2(g)} + * \leftrightarrow [H_2O_{(g)} + *]^{\ddagger}$	$K_1^{1/2}K_2K_{3b}^{1/2}K_6K_8K_{10}^{\ddagger}$	2.3E+43	2.7E+43	2.7E+43	2.9E+43	3.0E+43

Peroxyl Pathway to H_2O

Step		Overall reaction	Rate constant	r_{max} [s^{-1}]				
				Cu(100)	Pd(100)	Pt(100)	Ag(100)	Au(100)
(1)	$O_{2(g)} + * \rightarrow O_2*$	$O_{2(g)} + * \leftrightarrow [O_2*]^{\ddagger}$	$K_1^{\ddagger}$	1.8E+08	2.2E+08	2.2E+08	2.3E+08	2.4E+08
(2)	$H_{2(g)} + 2* \rightarrow 2H*$	$H_{2(g)} + 2* \leftrightarrow [2H*]^{\ddagger}$	$K_2^{\ddagger}$	2.8E-01	8.6E+08	8.7E+08	1.2E-08	7.1E-03
(3a)	$O_2* + H* \rightarrow OOH* + *$	$O_{2(g)} + 1/2H_{2(g)} + 2* \leftrightarrow [OOH* + *]^{\ddagger}$	$K_1K_2^{1/2}K_{3a}^{\ddagger}$	3.1E+09	1.2E+14	2.6E+19	1.1E-03	2.3E-05
(4b)	$OOH* + * \rightarrow O* + OH*$	$O_{2(g)} + 1/2H_{2(g)} + 2* \leftrightarrow [O* + OH*]^{\ddagger}$	$K_1K_2^{1/2}K_{3a}K_{4b}^{\ddagger}$	9.8E+29	2.9E+22	1.8E+22	4.1E+17	2.2E+06
(6)	$O* + H* \rightarrow OH* + *$	$O_{2(g)} + 3/2H_{2(g)} + 2* \leftrightarrow [OH* + *]^{\ddagger} + H_2O_{(g)}$	$K_1K_2^{3/2}K_{3a}K_{4b}K_6^{\ddagger}K_{10}K_8$	1.6E+56	2.6E+57	1.1E+63	5.7E+38	3.0E+37
(7)	$OH* + H* \rightarrow H_2O* + *$	$1/2O_{2(g)} + H_{2(g)} + 2* \leftrightarrow [H_2O* + *]^{\ddagger}$	$K_1^{1/2}K_2K_{3a}^{1/2}K_{4b}^{1/2}K_6^{1/2}K_8^{\ddagger}$	2.2E+30	8.0E+33	1.2E+34	5.6E+24	2.1E+20
(9)	$H_2O* \rightarrow H_2O_{(g)} + *$	$1/2O_{2(g)} + H_{2(g)} + * \leftrightarrow [H_2O_{(g)} + *]^{\ddagger}$	$K_1^{1/2}K_2K_{3a}^{1/2}K_{4b}^{1/2}K_6^{1/2}K_8K_{10}^{\ddagger}$	2.3E+43	2.7E+43	2.7E+43	2.9E+43	3.0E+43

Peroxide Pathway to H_2O

Step		Overall reaction	Rate constant	r_{max} [s^{-1}]				
				Cu(100)	Pd(100)	Pt(100)	Ag(100)	Au(100)
(1)	$O_{2(g)} + * \rightarrow O_2*$	$O_{2(g)} + * \leftrightarrow [O_2*]^{\ddagger}$	$K_1^{\ddagger}$	1.8E+08	2.2E+08	2.2E+08	2.3E+08	2.4E+08
(2)	$H_{2(g)} + 2* \rightarrow 2H*$	$H_{2(g)} + 2* \leftrightarrow [2H*]^{\ddagger}$	$K_2^{\ddagger}$	2.8E-01	8.6E+08	8.7E+08	1.2E-08	7.1E-03
(3a)	$O_2* + H* \rightarrow OOH* + *$	$O_{2(g)} + 1/2H_{2(g)} + 2* \leftrightarrow [OOH* + *]^{\ddagger}$	$K_1K_2^{1/2}K_{3a}^{\ddagger}$	3.1E+09	1.2E+14	2.6E+19	1.1E-03	2.3E-05
(4a)	$OOH* + H* \rightarrow H_2O_2* + *$	$O_{2(g)} + H_{2(g)} + 2* \leftrightarrow [H_2O_2* + *]^{\ddagger}$	$K_1K_2K_{3a}K_{4a}^{\ddagger}$	1.2E+12	2.5E+17	9.0E+20	3.1E+09	7.6E+06
(5b)	$H_2O_2* + * \rightarrow 2OH*$	$O_{2(g)} + H_{2(g)} + 2* \leftrightarrow [OH* + OH*]^{\ddagger}$	$K_1K_2K_{3a}K_{4a}K_{5b}^{\ddagger}$	2.9E+23	9.2E+23	1.9E+23	7.8E+20	7.5E+14
(7)	$OH* + H* \rightarrow H_2O* + *$	$1/2O_{2(g)} + H_{2(g)} + 2* \leftrightarrow [H_2O* + *]^{\ddagger}$	$K_1^{1/2}K_2K_{3a}^{1/2}K_{4a}^{1/2}K_{5b}^{1/2}K_8^{\ddagger}$	2.2E+30	8.0E+33	1.2E+34	5.6E+24	2.1E+20
(9)	$H_2O* \rightarrow H_2O_{(g)} + *$	$1/2O_{2(g)} + H_{2(g)} + * \leftrightarrow [H_2O_{(g)} + *]^{\ddagger}$	$K_1^{1/2}K_2K_{3a}^{1/2}K_{4a}^{1/2}K_{5b}^{1/2}K_8K_{10}^{\ddagger}$	2.3E+43	2.7E+43	2.7E+43	2.9E+43	3.0E+43

Chapter 4: Active Sites and Mechanisms for H_2O_2 Decomposition over Pd Catalysts[i]

4.1 Introduction

Chapter 3 explored mechanisms for direct H_2O_2 and H_2O synthesis from H_2 and O_2 on Pd, Pt, Cu, Ag, and Au, and discussed the factors that may limit activity and selectivity toward H_2O_2. The remaining chapters focus on Pd-based catalysts. Pd is widely recognized as the most effective transition metal for the DSHP in the experimental literature – but only when promoters are present.[26] This is consistent with the DFT-derived energetics from Chapter 3, because the clean Pd surfaces can readily dissociate the O_2* and/or OOH* surface intermediates to prevent H_2O_2 formation. Experiments also show that pure Pd is also highly active for H_2O_2 decomposition.[30, 31, 169, 170] Therefore, a common goal in many of the modifications made to Pd catalysts and the

[i] A. Plauck, E. E. Stangland, J. A. Dumesic and M. Mavrikakis, "Active sites and mechanisms for H_2O_2 decomposition over Pd catalysts", *PNAS* **2016**, *113*, E1973.

reaction medium (acids, halides, alloying)[18, 26] is to not only improve primary selectivity toward H_2O_2, but to also minimize H_2O_2 decomposition.

The H_2O_2 decomposition reactions (Reactions 3 and 4, reproduced below from Chapter 1) can significantly decrease overall yield as the reaction progresses, even on catalysts where the primary selectivity toward H_2O_2 is high:[24, 171]

[**Reaction 3**] $H_2O_2(l) \rightarrow H_2O(l) + ½O_2(g)$ $\Delta G°_{298K} = -116.7$ kJ mol^{-1},

[**Reaction 4**] $H_2O_2(l) + H_2(g) \rightarrow 2H_2O(l)$ $\Delta G°_{298K} = -353.8$ kJ mol^{-1}.

Some experiments suggest that the active sites for H_2O_2 synthesis and decomposition on Pd-based catalysts may be different.[24, 30] Hutchings and coworkers[35] demonstrated that the H_2O_2 decomposition reactions could be almost completely suppressed by pre-treating the carbon support material with HNO_3 prior to metal deposition; this pre-treatment affected the dispersion of Pd and Au on the carbon support, and resulted in a stable catalyst with > 95 % selectivity for H_2O_2 during the DSHP reaction. They also recently found that on oxide-supported Pd catalysts, an appropriate second metal oxide component coupled with a heat treatment cycle could also "shut off" the H_2O_2 decomposition reactions.[172] Clearly, a detailed understanding of the active site(s) and elementary reaction mechanisms for the undesirable decomposition reactions would benefit the identification of improved catalysts. Nonetheless, there is still much work to be performed to elucidate the optimal structure and composition of Pd-based catalysts for the DSHP; some recent important contributions on this front can be found in references # [47, 58, 71, 126, 171, 173].

This chapter will focus on the mechanism and the nature of the dominant active site(s) responsible for H_2O_2 decomposition (Reaction 3, with no H_2 present) under conditions relevant to a DSHP process. We highlight key factors which will aid in the identification of improved DSHP catalysts that exhibit minimal H_2O_2 decomposition activity. These findings are also relevant to

transition metal catalyzed oxidation reactions that utilize H_2O_2 – whether produced *in situ* or fed as reactant – but whose efficiency may be limited by catalytic H_2O_2 decomposition.[20, 122, 174, 175]

4.2 Methods

4.2.1 Density functional theory

Periodic Pd(111) and Pd(100) slabs were chosen as representative models for the planar surfaces of the supported Pd nanoparticles used in the experiments. Pd(111) and Pd(100) have the lowest surface free energies among the clean Pd facets, and a truncated octahedron minimizes the total surface free energy for Pd particles > 3-5 nm based on a Wulff construction.[176, 177] Therefore, in the absence of strong particle-support interactions, both of these Pd surfaces are expected to be in high abundance.

All DFT calculations in this chapter were performed using the DACAPO total energy code,[90, 136] employing the self-consistent PW91 generalized gradient approximation (GGA-PW91)[108, 109] to describe the exchange correlation energy and potential, and ultrasoft pseudopotentials[138] to describe the ionic cores. Electron density was determined by iterative diagonalization of the Kohn-Sham Hamiltonian, Fermi population of the Kohn-Sham states (k_BT = 0.1 eV), and Pulay mixing of the resulting electron density.[137] The total energy was then extrapolated to k_BT = 0 eV. The Kohn-Sham one-electron valence states were expanded using a plane wave basis with kinetic energy below 25 Ry.

The (111) and (100) metal surfaces were modeled using a slab geometry with a periodically repeated (2 × 2) unit cell and four atomic layers; this corresponds to 1/4 monolayer (ML) coverage of a single adsorbate placed in the unit cell. The surface Brillouin zone was sampled using 18 special Chadi-Cohen[142] k-points for the (111) slabs, and a (6 × 6 × 1) Monkhorst-Pack[143] k-point mesh for the (100) slabs. All slab layers were fixed for calculations on the (111) slabs (previous

calculations show minimal effect of surface relaxation on the calculated energetics for a similar system[55]), while the top two metal layers were allowed to relax in the (100) slabs. 14 Å of vacuum separated successive slabs in the z-direction, and adsorption was only permitted on one of the two available surfaces with the electrostatic potential adjusted accordingly.[139, 140] The equilibrium PW91 bulk Pd lattice constant has been calculated previously[55] to be 3.99 Å (experimental value is 3.89 Å[141]). Calculations involving O_2 were performed spin-polarized.

All reported DFT results in this chapter have been corrected for the zero-point energy (ZPE). The minimum energy paths for elementary steps were calculated using the climbing image nudged elastic band method (CI-NEB)[112, 115] with at least 7 intermediate images, and the transition state was verified by identification of a single imaginary frequency along the reaction coordinate.

4.2.2 Experiments

A 0.09 wt% Pd/spSiO_2 (spSiO_2 denotes the spherical silica support) catalyst was prepared for reaction kinetics experiments. The spSiO_2 was synthesized by a modified Stöber process[178] described in a previous publication,[179] resulting in spherical silica particles (ca. 100-200 nm in diameter) with no internal pore structure and a Brunauer-Emmett-Teller (BET) surface area of 21 m^2 g^{-1}.[179] The Pd was loaded onto the spSiO_2 by vacuum evaporative impregnation (in a rotary evaporator) using a solution of Pd (II) acetate dissolved in dichloromethane. The dried material was reduced in a quartz cell following a procedure described in reference # [180] to promote formation of large Pd particles (average particle size of 5.6 +/- 2.4 nm determined from scanning transmission electron microscopy (STEM) images of the Pd/spSiO_2 catalyst) that better compare to the Pd(111) and Pd(100) DFT models. This heat treatment procedure involved a temperature ramp to 673 K (10 K min^{-1}) and 3 h hold at 673 K in flowing H_2 (30 mL min^{-1}), followed by cooling to room temperature under flow of Ar (30 mL min^{-1}) and passivation with 1% O_2 in Ar.

The Pd surface site density was determined by irreversible CO uptake experiments at 300 K, using an apparatus and procedure described previously,[181] and applying a surface stoichiometry of 2:3 for CO:surface Pd atom.[180]

H_2O_2 decomposition experiments were performed in a 50 mL Parr Instrument Company Hastelloy C-276 autoclave containing an overhead magnetic stirrer, a fixed thermocouple, and a pressure gauge. A Teflon liner was used in all experiments to minimize contact of H_2O_2 with metallic components in the autoclave. Blank experiments were performed prior to each reaction to ensure negligible contributions to H_2O_2 decomposition from the stirrer/thermowell/liner; these wetted parts of the reactor were passivated using 25 vol % HNO_3 in cases where significant H_2O_2 decomposition was measured in the absence of catalyst. The bare spSiO_2 support (no Pd loaded) was shown to be inert toward H_2O_2 decomposition over all conditions studied.

In a typical reaction, the autoclave was loaded with catalyst, sealed, and purged with Ar. The autoclave was then pressurized to 450 psi with 4 % H_2 in Ar (Airgas), and held at 323 K for 1 h to reduce the passivated Pd nanoparticles. After cooling to room temperature, the autoclave was again purged with Ar, pressurized to 115 psi with Ar, and cooled to the desired reaction temperature using a refrigerated bath circulator (ARCTIC A25 Thermo Scientific). 12.5 grams of the H_2O_2 feed solution (0.08-0.60 M H_2O_2 in H_2O) was prepared by dilution of a non-stabilized 30 wt % H_2O_2 solution (< 10 ppb Cl^-, Gigabit, KMG) in ultra-pure water (18 MΩ × cm), cooled to reaction temperature, and then charged into the autoclave using a high performance liquid chromatography (HPLC) pump (Chrom Tech Series 1). The resulting pressure in the autoclave prior to reaction was 150 psi. Stirring (1200 rpm) was then started. Conversion of H_2O_2 was determined by titration of the final solution with 0.05 M $Ce(SO_4)_2$ using ferroin as indicator.

Initial reaction rates were calculated by fitting a line through a plot of the moles H_2O_2 consumed versus time for conversions under 15 % and normalizing to the total number of Pd surface atoms determined by the CO uptake experiments; all conversion versus time data points were replicated at least two times. The apparent activation energy barrier was determined over a temperature range of ca. 25 K, and the apparent reaction order with respect to H_2O_2 was determined by varying the feed concentration of H_2O_2 with all other reaction parameters constant. The apparent reaction order with respect to the O_2 product was determined by varying P_{O2} in the gas phase using a 25 % O_2 in Ar mixture, with all other conditions invariant. This mixture was introduced immediately after charging the autoclave with the H_2O_2 feed, prior to stirring.

4.2.3 Microkinetic model

A mean-field microkinetic model was developed to describe the experimentally measured reaction rates, reaction orders, and apparent activation barrier. The model parameters were defined using a procedure described in our previous work,[80, 83, 85] utilizing the ZPE-corrected BEs and activation energy barriers determined through DFT as initial guesses; pre-exponential factors and entropies were derived from the DFT-calculated vibrational frequencies. The maximum adsorbate coverage permitted was 1 ML, and adsorption/desorption steps were assumed to be quasi-equilibrated. In the case that the microkinetic model-predicted adsorbate coverage exceeded the minimum adsorbate coverage in the context of the unit cell used in the DFT calculations (1/4 ML), the DFT calculations were repeated with the appropriate spectator species co-adsorbed in the unit cell. Note that although the experimental measurements were performed in a three-phase system using conditions relevant to a DSHP process, no corrections were made to the DFT calculations to reflect potential interaction with the liquid phase. Further details are provided in the supplementary section at the end of this chapter.

4.3 Results

The decomposition of H_2O_2 has been studied both in the vapor-phase[182] and aqueous phase[183] (thermal, non-catalyzed), and over a variety of materials including metal oxides[184-186] and metal ions in solution.[187, 188] Based on these studies, we have compiled an encompassing network of 17 elementary reactions involving four closed-shell species (H_2O_2, H_2O, O_2, H_2) and four surface intermediates (O, H, OH, OOH), shown in Table 4.1. Elementary reactions are classified as follows: adsorption/desorption, O-O bond scission, dehydrogenation, and hydrogen-transfer. Note that the majority of DFT calculations presented in this chapter are based on Chapter 3 (for Pd(100)) and a previous publication from our group[55] (for Pd(111)). We provide the energetics again in this chapter for convenience, and discuss them in more detail as they pertain to H_2O_2 decomposition on Pd. We have also performed DFT calculations for additional reaction steps not considered in Chapter 3: the hydrogen-transfers. We determine below that the hydrogen-transfer steps are critical to describing the H_2O_2 decomposition mechanism; these steps have not been thoroughly explored on Pd in previous computational literature.

4.3.1 Thermochemistry and binding configurations of reaction intermediates on clean Pd

Table 4.1 summarizes the most stable adsorption sites and binding energies for all surface species on Pd(111) and Pd(100). Images of the individual adsorbates in their preferred binding geometry on Pd(100) can be viewed in Figure 4.1; refer to reference # [55] for the corresponding images on Pd(111). The Pd(100) facet is more open than the Pd(111) one and binds all intermediates more strongly.

The BE of atomic hydrogen (H*) on Pd(100) is -2.74 eV, only 0.04 eV stronger than its BE on Pd(111). H* preferentially binds to the fcc site on Pd(111) and the hollow site on Pd(100). Furthermore, H* is expected to be mobile on Pd(100), as the BE of H* on a bridge site of Pd(100)

is only 0.14 eV less stable than that on the hollow site. Similarly, on Pd(111) the BE of H* constrained to a bridge site is 0.14 eV less stable than that on the fcc site.

Table 4.1 Calculated binding energies (BE) of adsorbed species, their preferred adsorption sites, and O-O bond lengths (d_{O-O}) on Pd(111) and Pd(100). Reference energy corresponds to the adsorbate in the gas phase far away from the metal surface.

	Pd(111)[a]			Pd(100)		
Species	Adsorption Site	BE / eV	d_{O-O} / Å[b]	Adsorption Site	BE / eV	d_{O-O} / Å[b]
H*	fcc	-2.70	-	hollow	-2.74	-
O*	fcc	-3.64	-	hollow	-3.90	-
OH*	bridge-tilted	-2.03	-	bridge-tilted	-2.43	-
OOH*	bent-top	-0.94	1.46	bent-bridge	-1.28	1.51
H_2O*	top	-0.22	-	top	-0.30	-
H_2O_2*	top	-0.32	1.48	top	-0.36	1.49
O_2*	top-bridge	-0.50	1.35	hollow	-1.27	1.41

[a]Data based on reference # [55].
[b]Calculated gas-phase d_{O-O} for O_2, OOH, and H_2O_2 are 1.24, 1.35, and 1.48 Å, respectively.

Atomic oxygen (O*) has the same site preferences as H* on both Pd(111) and Pd(100). The binding strength of O* on Pd(100) is -3.90 eV, which is 0.26 eV stronger than that on Pd(111). Moreover, O* has a strong preference for the hollow site on Pd(100), with the next best adsorption site (bridge) being less stable by 0.48 eV. On Pd(111) the next best adsorption site for O* is the hcp site, which is 0.15 eV less stable than O* binding to the fcc site.

Hydroxyl (OH*) is often proposed to be the initial intermediate generated during H_2O_2 decomposition, resulting from homolytic O-O bond cleavage in H_2O_2.[189] OH* binds most stably to the bridge site on both Pd(111) and Pd(100) with the O-H bond tilted away from the surface plane. The BE of OH* on Pd(100) is -2.43 eV, which is 0.40 eV stronger than the BE on Pd(111). OH* binding at the hollow site of Pd(100) is only 0.05 eV weaker than on the bridge site, which is similar to the difference in energy between OH* binding at the fcc site and bridge site on Pd(111) (0.08 eV).

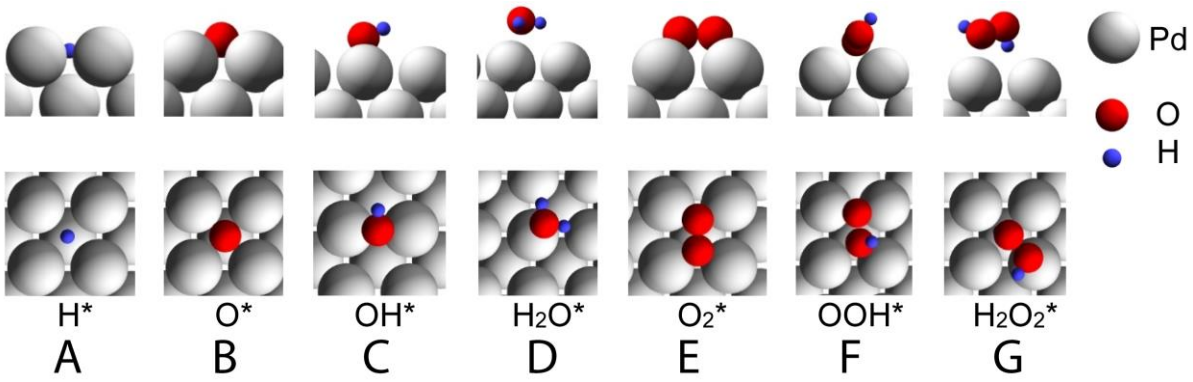

Figure 4.1 (A-G) Side and top-down views of the preferred binding sites for all adsorbates on Pd(100). Blue spheres are hydrogen, red spheres are oxygen, and gray spheres are Pd atoms.

Hydroperoxyl (OOH*) is considered an important intermediate in the DSHP and was identified spectroscopically during the gas-phase reaction of H_2 and O_2 on Au/TiO_2 using inelastic neutron scattering.[150] OOH* binds through its non-hydrogenated oxygen atom to a top site on Pd(111) with the hydroxyl group positioned over an adjacent bridge site and the O-H bond pointing away from the surface; while OOH* binds through its non-hydrogenated oxygen atom to a bridge site on Pd(100) with the hydroxyl group positioned over an adjacent hollow site and the O-H bond pointing away from the surface. The binding energy of OOH* on Pd(100) is -1.28 eV – stronger than its binding energy on Pd(111) by 0.34 eV. However, the site preference for OOH* on Pd(100) and Pd(111) is weak: on Pd(100), OOH* can also bind to top and hollow sites with less than 0.12 eV difference in binding energy from its most stable adsorption site; on Pd(111), OOH* can also bind through its non-hydrogenated oxygen atom to bridge sites with less than 0.03 eV difference in binding energy from its most stable adsorption site.

Molecular oxygen (O_2*) has the largest disparity in binding strength between Pd(111) and Pd(100); the BE on Pd(100) is -1.27 eV, which is 0.77 eV stronger than that on Pd(111). O_2* binds flatly on Pd(100) centered over a hollow site, while on Pd(111) O_2* binds across a hcp site with one O atom at a bridge position and the other at a top position. Interestingly, Long et al[190] used probe molecules and electron spin resonance spectroscopy to show that Pd(100) can more readily

activate O_2 through excitation of ground state triplet O_2 to reactive singlet O_2. This result is in agreement with our calculations; O_2* retains some of its magnetic moment on Pd(111)[55] but a negligible magnetic moment on Pd(100). The strong affinity of Pd(100) for O_2 and O* are reflected in the tendency to reconstruct to a kinetically stable ($\sqrt{5}$x$\sqrt{5}$)*R*27° surface oxide phase under moderate chemical potentials of O_2.[191] The next best adsorption site for O_2 on Pd(100) is a top-top site with a binding energy of -0.85 eV.

The binding energies of H_2O* and H_2O_2* are weak (< 0.4 eV) on both Pd(111) and Pd(100). H_2O* preferentially binds to top sites on both Pd(111) and Pd(100) with the O-H bonds parallel to the Pd surface. The binding energy of H_2O* on Pd(100) is -0.30 eV. H_2O_2* also preferentially binds to top sites and adopts the *trans* configuration on both Pd facets; one oxygen atom is bound to a top site with its hydrogen atom pointing slightly away from the surface plane, and the other oxygen atom is positioned over an adjacent (fcc or hollow) site with its hydrogen atom pointing toward the surface.

Other potential intermediates include aquoxyl (OOHH*, an isomer of H_2O_2* with both hydrogen atoms on the same oxygen atom) and trihydrogen peroxide (HOOHH*). Similar to our findings on Pd(111),[55] neither of these species is stable on Pd(100) – i.e. adsorption of aquoxyl and trihydrogen peroxide structures on Pd(100) results in spontaneous decomposition to (O* + H_2O*) and (OH* + H_2O*), respectively.

Table 4.1 provides the calculated O-O bond lengths for the adsorbed dioxygen species (O_2*, OOH*, and H_2O_2*) and the corresponding values calculated in the gas-phase. There is significant expansion of the O-O bond in both O_2* and OOH* upon adsorption, while the O-O bond length in H_2O_2* remains within 2 % of its calculated gas-phase value. The larger O-O bond expansion on

Pd(100) compared with Pd(111) suggests a weaker O-O bond strength on the more open surface for all the dioxygen species.

4.3.2 Activation energy barriers of elementary steps

The calculated activation energy barriers (E_a) and reaction energies (ΔE) are reported with respect to reactant and product states at infinite separation, unless stated otherwise. Table 4.2 summarizes the results for all elementary steps on Pd(111) and Pd(100). Transition state geometries for the elementary steps are shown in Figure 4.2.

Table 4.2 Energetics of elementary steps considered for the decomposition of H_2O_2. Energetics are reported with respect to either reactants/products at infinite separation (steps 1-11) or co-adsorbed for H-transfer reactions (steps 12-17) because these reactants/products are generally stabilized through hydrogen bonding. Elementary steps are classified as: adsorption/desorption (steps 1-4); O-O scission (steps 5-7); dehydrogenation (steps 8-11); and H-transfer (steps 12-17). E_a and ΔE represent the calculated activation energy and reaction energy in the forward direction. No activation barriers are calculated for adsorption/desorption steps.

#	Elementary step	Pd(111)[a]		Pd(100)	
		E_a / eV	ΔE / eV	E_a / eV	ΔE / eV
(1)	$H_2O_2 + * \leftrightarrow H_2O_2*$	-	-0.32	-	-0.36
(2)	$H_2O* \leftrightarrow H_2O + *$	-	0.22	-	0.30
(3)	$O_2* \leftrightarrow O_2 + *$	-	0.50	-	1.27
(4)	$H* + H* \leftrightarrow H_2 + 2*$	-	1.11	-	1.19
(5)	$H_2O_2* + * \leftrightarrow OH* + OH*$	0.18	-1.53	0.05	-2.29
(6)	$OOH* + * \leftrightarrow O* + OH*$	0.08	-1.50	0.02	-1.83
(7)	$O_2* + * \leftrightarrow O* + O*$	0.85	-1.23	0.30	-0.98
(8)	$OH* + * \leftrightarrow O* + H*$	1.02	0.07	1.03	0.17
(9)	$H_2O* + * \leftrightarrow OH* + H*$	1.10	0.37	0.67	0.00
(10)	$OOH* + * \leftrightarrow O_2* + H*$	0.59	-0.20	0.52	-0.67
(11)	$H_2O_2* + * \leftrightarrow OOH* + H*$	0.62	0.05	0.44	-0.29
(12)	$H_2O* + O* \leftrightarrow OH* + OH*$	0.33	0.33	0.00	-0.51
(13)	$H_2O_2* + O* \leftrightarrow OOH* + OH*$	0.04[b]	-0.44	0.14[b]	-0.87
(14)	$H_2O_2* + OH* \leftrightarrow OOH* + H_2O*$	0.00	-0.16	0.00	-0.17
(15)	$OOH* + O* \leftrightarrow O_2* + OH*$	0.00	-0.27	0.02	-0.81
(16)	$OOH* + OH* \leftrightarrow O_2* + H_2O*$	0.00	-0.38	0.00	-0.13
(17)	$H_2O_2* + O_2* \leftrightarrow OOH* + OOH*$	0.20	-0.02	0.00	0.00

[a]Data for steps 1-12 on Pd(111) are based on reference # [55].
[b]Activation energy corresponds to breaking Pd-O bonds to lift O* from its preferred binding site (fcc or fourfold hollow).

4.3.2.1 O-O bond scission

At least one type of O-O bond scission step can be involved in the decomposition mechanism of H_2O_2. OH* and/or O* fragments are the direct products of O-O bond scission. Both Pd(111) and Pd(100) can readily break the O-O bond in H_2O_2* and OOH*, but there is a significant difference in the ability of these facets to dissociate O_2*.

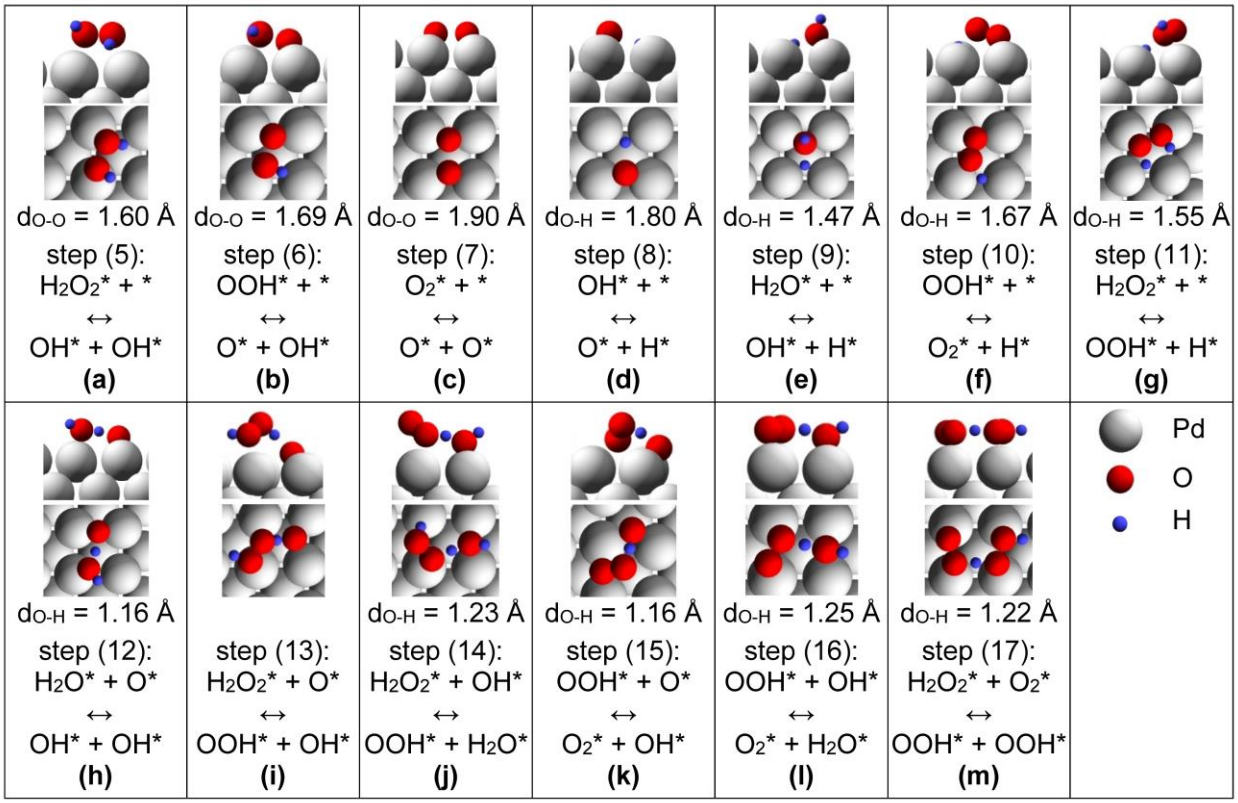

Figure 4.2 Side and top-down views of the transition state geometries for (a-c) O-O bond scission, (d-g) dehydrogenation, and (h-m) H-transfer elementary steps on Pd(100). Blue spheres are hydrogen, red spheres are oxygen, and gray spheres are Pd atoms. Elementary step numbers are in reference to Table 4.2. Bond lengths (d_{x-y}) refer to the bond being broken in the forward reaction, as written. Note that in (i), the transition state for step (13) involves breaking Pd-O bonds to lift O* from its preferred binding site, followed by spontaneous H-transfer from H_2O_2* to O*.

$$H_2O_2^* + * \rightarrow OH^* + OH^*$$

H_2O_2* decomposes to two OH* on Pd(100) with a barrier of 0.05 eV and a reaction energy of -2.29 eV. The corresponding barrier and reaction energy on Pd(111) are 0.18 eV and -1.53 eV. This step occurs through a similar mechanism on both Pd(111) and Pd(100) whereby H_2O_2* rotates

from its most stable position on a top site to the transition state at which the O-O bond is elongated and both OH groups are bound to adjacent Pd atoms across a bridge site. However, at the transition state, the O-H bonds are on the same side of H_2O_2 molecule on Pd(100), while they are on different sides of the molecule on Pd(111). Following O-O bond scission, the two OH* relax to bridge sites in their final co-adsorbed state, stabilized through a hydrogen bond.

$$OOH^* + * \rightarrow O^* + OH^*$$

OOH* decomposition to O* and OH* on Pd(100) is nearly spontaneous with a barrier of 0.02 eV and a reaction energy of -1.83 eV – similar to the energetics on Pd(111). The O-O bond scission occurs over a hollow site on Pd(100) and a hcp site on Pd(111).

$$O_2^* + * \rightarrow O^* + O^*$$

The dissociation of O_2* on Pd(100) occurs over a hollow site, whereby the O-O bond stretches from 1.41 Å in the initial state to 1.90 Å in the transition state. The reaction energy is -0.98 eV and the barrier is 0.30 eV on Pd(100), which is 0.55 eV lower than the corresponding barrier on Pd(111).

The reverse of O_2* dissociation, O* recombination, represents a potential pathway for formation of the O_2 product; this step has been proposed in a number of papers.[31, 192, 193] Our calculations show that O* recombination has prohibitively high barriers – and is thermodynamically unfavorable – on both Pd(111) and Pd(100); the activation barrier exceeds 2 eV on Pd(111) and 1 eV on Pd(100). These results are in agreement with temperature programmed desorption (TPD) experiments for O_2 desorption from Pd(111)[194] and Pd(100)[195], in which the evolution of O_2 from these Pd single crystals after pre-adsorbing O* at near-ambient temperatures is only observed at temperatures exceeding 600 K. Furthermore, in the context of the DSHP, Dissanayake and Lunsford[61] used a mixture of [$^{18}O_2$ + $^{16}O_2$] with H_2 over a Pd/SiO_2 catalyst and

observed that no $H_2{}^{16}O^{18}O$ was formed, indicating that O*/OH* recombination reactions were not relevant to H_2O_2 formation.

4.3.2.2 Dehydrogenation

Because in this study we are only investigating the decomposition of H_2O_2 (Reaction 3) in the absence of H_2 as a reactant, H* can only be derived from dehydrogenation of surface species through O-H bond scission. Barriers for O-H bond scission are generally lower on the more open Pd(100) facet compared with those on Pd(111).

$H_2O_2^* + * \rightarrow OOH^* + H^*$ and $OOH^* + * \rightarrow O_2^* + H^*$

The O-H bonds in H_2O_2* and OOH* are more difficult to break than the O-O bond, based on the activation barriers in Table 4.2. On Pd(100), the O-H bond in H_2O_2* that is pointing toward the surface is cleaved over a bridge site. The activation barrier is 0.44 eV, and the reaction energy is -0.29 eV.

For OOH* on Pd(100), the O-H bond is also broken over a bridge site. This breaking requires rotation of the O-H bond toward the surface, starting from the most stable OOH* geometry. The corresponding activation barrier and reaction energy for O-H bond cleavage in OOH* are 0.52 eV and -0.67 eV on Pd(100).

$H_2O^* + * \rightarrow OH^* + H^*$ and $OH^* + * \rightarrow O^* + H^*$

Dehydrogenations of H_2O* and OH* require a larger activation energy compared with H_2O_2* and OOH* dehydrogenations. On Pd(100), the barrier to break the O-H bond in H_2O* is 0.67 eV, and the reaction is thermoneutral. OH* dehydrogenation is more difficult and has a barrier of 1.03 eV on Pd(100), and the reaction is slightly endothermic. The transition state for O-H cleavage in both H_2O* and OH* occurs over a hollow site on Pd(100).

4.3.2.3 Hydrogen transfer

Formation and cleavage of O-H bonds in which the Pd surface is directly involved have significant activation barriers (> 0.4 eV). Alternatively, the Pd surface can mediate H-transfer between oxygenated intermediates – without involving an explicit H* species. These elementary steps involve nearly spontaneous H-transfer in the exothermic direction on both Pd(111) and Pd(100) (Table 4.2). The activation energy barriers and reaction energies in this section are reported with respect to co-adsorbed reactant and product states, because these states are generally stabilized through hydrogen bonding (ca. 0.1-0.4 eV per hydrogen bond) with respect to the infinitely separated reactants and products.

The hydrogen atom is always transferred between O atoms involved in hydrogen bonding in the most stable co-adsorbed configuration. Importantly, the H-transfer steps represent potential pathways for formation of both the H_2O (H-transfers *to* O*/OH*) and O_2 (H-transfers *from* H_2O_2*/OOH*, retaining the O-O bond) products of H_2O_2 decomposition.

H-transfer to O

H_2O_2*, OOH*, and H_2O* can all directly transfer a H atom to O*; the activation energy barriers for these steps are 0.04, 0.00, and 0.33 eV on Pd(111), with reaction energies of -0.44, -0.27, and 0.33 eV. The corresponding activation energy barriers on Pd(100) are 0.14, 0.02, and 0.00 eV with significantly more exothermic reaction energies of -0.87, -0.81, and -0.51 eV.

H-transfer to OH

H_2O_2* and OOH* can also directly transfer an H atom to OH*. We calculate that these steps proceed with nearly zero activation energy barrier on Pd(111) and Pd(100). The reaction energy for H-transfer from H_2O_2* to OH* is weakly exothermic (-0.16 eV on Pd(111) and -0.17

eV on Pd(100)). The reaction energy for H-transfer from OOH* to OH* is more exothermic on Pd(111) (-0.38 eV) than that on Pd(100) (-0.13 eV).

An additional H-transfer step that was explored is H-transfer from H_2O_2* to O_2*. This reaction is nearly thermoneutral on Pd(111), with a reaction energy of -0.02 eV and an activation energy barrier of 0.20 eV. On Pd(100), the reaction is thermoneutral with negligible barrier.

4.3.3 Catalytic cycles and potential energy surfaces

Based on the elementary steps above, several mechanisms are available to complete the catalytic cycle on *clean* Pd facets, as summarized in Figure 4.3: *O*-assisted*, *OH*-assisted*, *O*+O*-recombination*, and *direct dehydrogenation*. A complete mechanism for *direct dehydrogenation* is not shown for simplicity, as both the DFT calculations and microkinetic modeling results suggest that direct dehydrogenation steps are characterized by much higher barriers and therefore not relevant under the reaction conditions explored in this study. The first step in all other pathways is H_2O_2 adsorption followed by homolytic O-O bond cleavage to form two OH* species. The second H_2O_2* species can also adsorb and directly decompose to two OH*; these OH* species can then disproportionate to form H_2O* and O* – necessitating the recombination of two O* to form O_2* (*O*+O*-recombination* mechanism). Alternatively, two channels exist that bypass the thermodynamically unfavorable and highly activated O* recombination step; both involve consecutive H-transfer steps from the second H_2O_2 molecule to the O*/OH* fragments with retention of the original O-O bond in H_2O_2 (*O*-assisted* and *OH*-assisted* mechanisms).

The potential energy surfaces for all pathways are displayed in Figure 4.4 for both Pd(111) and Pd(100). Based on the DFT calculations alone, the *O*-assisted* and *OH*-assisted* pathways not only provide the most energetically efficient route to form the products, but are also mutually

competitive on both Pd(111) and Pd(100). However, the deep potential wells associated with the strongly bound O*/OH* fragments indicate that there is a strong thermodynamic driving force to populate the surfaces with O*/OH* – especially Pd(100). Therefore, the active surface under reaction conditions may be partially covered by O*/OH*.

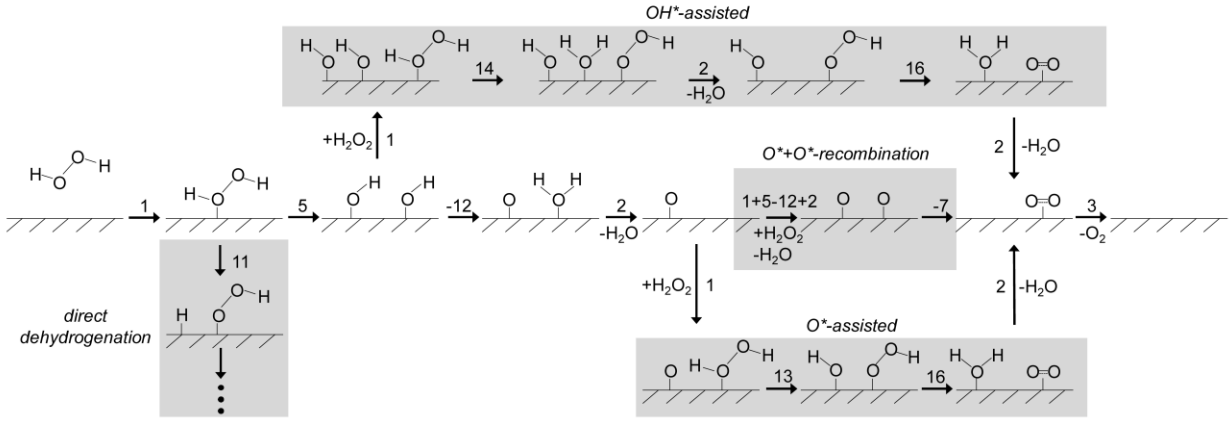

Figure 4.3 Schematic representation of reaction pathways for H_2O_2 decomposition on clean surfaces. The numbers by the black arrows correspond to the elementary steps from Table 4.2. The overall reaction for each of the three mechanisms described in this figure is: 2 H_2O_2 → 2 H_2O + O_2.

Note that on O*/OH*-modified surfaces, there is an increased probability of H-transfer from H_2O_2* prior to O-O bond scission; the required O-O bond scission step may then occur in OOH* rather than in H_2O_2*, slightly altering the succession of elementary steps proposed in Figure 4.3.

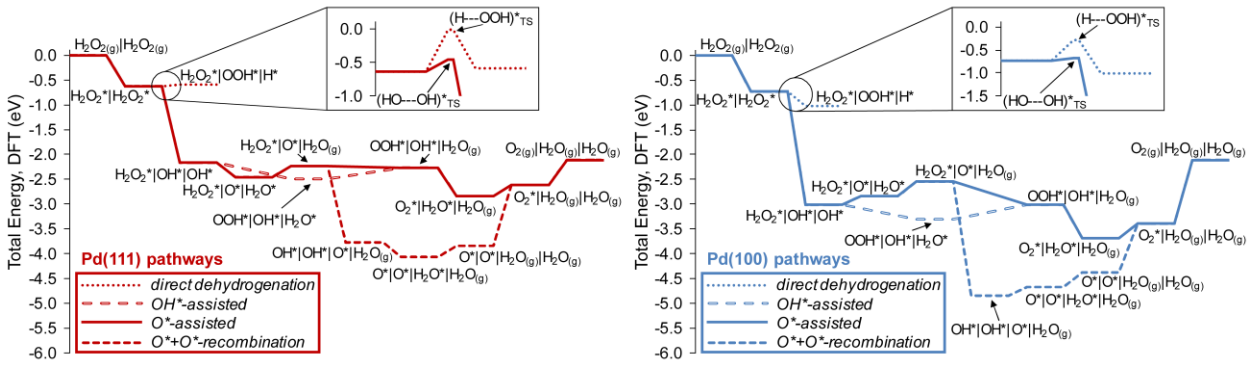

Figure 4.4 Potential energy surfaces (thermochemistry only) for reaction pathways from Figure 4.3 on clean Pd(111) and Pd(100) based on the DFT-derived energetics. Energies are referenced to two H_2O_2 molecules in the gas-phase. The "|" separating two adsorbates denotes infinite separation from each other. Insets compare O-H and O-O bond scission barriers in H_2O_2. "TS" denotes transition state. The x-axis is the reaction coordinate.

4.3.4 Kinetics experiments and microkinetic modeling

The results from our kinetics experiments are shown in Tables 4.3 and 4.4. The experimentally determined activation energy barrier of 53.3 +/- 3.0 kJ mol^{-1} indicates that there is a significant variation in H_2O_2 decomposition rate with reaction temperature under conditions relevant to the DSHP. The nearly first order dependence on concentration of H_2O_2 is in agreement with other experimental studies of H_2O_2 decomposition on Pd under similar conditions of temperature and H_2O_2 concentration.[30, 196] We also observed that the addition of O_2 to the gas phase did not significantly affect the decomposition rate of H_2O_2 up to O_2 partial pressures of at least 37 psi, indicating negligible product inhibition over the conditions studied. This finding is in agreement with the result of Choudhary and Samanta,[59] who observed only a minor difference in the reaction rate for H_2O_2 decomposition over Pd/Al_2O_3 (in the absence of H_2) in a semi-batch reactor when flowing either O_2 or N_2 through the liquid phase.

Table 4.3 Reaction rates obtained from the kinetics experiments on $Pd/spSiO_2$.

Run[a]	Temperature / K	y_{O_2}	$x_{H_2O_2}$	Experimental Rate / mol $molPd_s^{-1}$ s^{-1}
1	307	0.00	0.60	71.8
2	307	0.00	0.30	31.5
3	307	0.00	0.15	17.1
4	307	0.00	0.08	10.5
5	297	0.00	0.15	7.9
6	285	0.00	0.15	3.4
7	307	0.25	0.15	16.7
8	307	0.13	0.15	16.2
9	307	0.06	0.15	16.9

[a]y denotes mole fraction in the gas phase (balance Ar), and x denotes molarity (moles L^{-1}) in the liquid phase at the start of reaction. Pd_s denotes surface Pd atoms determined by CO uptake. Total pressure was 150 psi, and the stir rate was 1200 rpm for all experiments. Reaction rates reported here correspond to the initial rates measured from conversion versus time data at < 15 % conversion, which was approximately linear in this regime. Each reported rate represents the average from at least two repeated sets of conversion versus time data.

Initial estimates for microkinetic model rate parameters are derived from the DFT-calculated energetics. The reactor is simulated as a continuous stirred tank reactor. The turnover frequencies for H_2O_2 decomposition obtained from this model (i.e., the rate of H_2O_2 converted per surface site) are used to calculate reaction orders and apparent activation barrier for comparison with the experimental data.

The rates, reaction orders, and apparent activation barriers predicted by the microkinetic model were initially in poor agreement with the experimental data when using purely DFT-derived parameters from Pd(111) or Pd(100). We subsequently employed sensitivity analysis to identify the sensitive DFT-derived BEs of surface species and transition state energies. We then fit model-predicted reaction rates to experimental rates (such that the residual error is less than 20 %) by modifying sensitive parameters, constraining the adjustment of parameters such that (i) the deviation between DFT-derived BEs and activation barriers on a given Pd facet and the corresponding values from the microkinetic model should be within the ca. 0.1-0.2 eV error bars generally attributed to DFT calculations,[88, 159] and (ii) the adsorbate coverage used in the DFT calculations should be consistent with the coverage predicted by the microkinetic model (that is, the solution should be self-consistent with respect to coverage).

Table 4.4 Experimental and microkinetic model-predicted reaction orders and apparent activation energy barriers (E_{app}). Reported experimental error is the standard error from linear regression.

	Experiment[a]	*O*-coverage solution*	*OH*-coverage solution*
H_2O_2	0.92 ± 0.08	1.00	0.97
O_2	-0.01 ± 0.03	-0.01	0.00
E_{app} / kJ mol^{-1}	53.3 ± 3.0	53.1	56.6

[a]subsequent catalyst batches yielded reaction orders and an apparent barrier within ca. 15 % of the values reported here.

Next we present the results from two model solutions that satisfy the above criteria, but differ in both the coverage and identity of the most abundant surface intermediate, and are denoted as the *O*-coverage solution* and the *OH*-coverage solution*.

4.3.4.1 "O-coverage solution"*

Figure 4.5A shows a parity plot comparing the experimental H_2O_2 decomposition rates with the microkinetic model predictions for the *O*-coverage solution* (initial estimates of parameters are derived from DFT calculations on clean Pd(111), and the supplementary section at the end of this chapter provides details of the parameter adjustments employed to obtain this solution). There is good agreement between model-predicted and experimental reaction rates, and the microkinetic model is able to accurately reproduce the experimental activation barrier and reaction orders (Table 4.4).

The microkinetic model predictions for the surface coverage for the most abundant intermediate, O*, range from 0.13 to 0.16 ML (Figure 4.5B), with the remaining sites being vacant. Marginal changes to the clean surface energetics are expected from adsorbate-adsorbate interactions at such low O* coverage,[197] and furthermore this adjusted parameter set compares well with the DFT-derived parameters on clean Pd(111); the maximum deviation in binding energy or activation barrier is a 0.24 eV destabilization of the binding energy of O_2* on Pd(111). Therefore, a partially O*-covered Pd(111) surface is a plausible representation of the active site for H_2O_2 decomposition.

On the other hand, DFT-derived parameters on Pd(100) deviate significantly (> 0.35 eV for OH*, OOH*, and O_2*) from this *O-coverage solution* parameter set. Pd(100) binds intermediates too strongly, and the low predicted O* coverage is not expected to destabilize intermediates on Pd(100) sufficiently for consistency with the *O*-coverage solution* parameters.

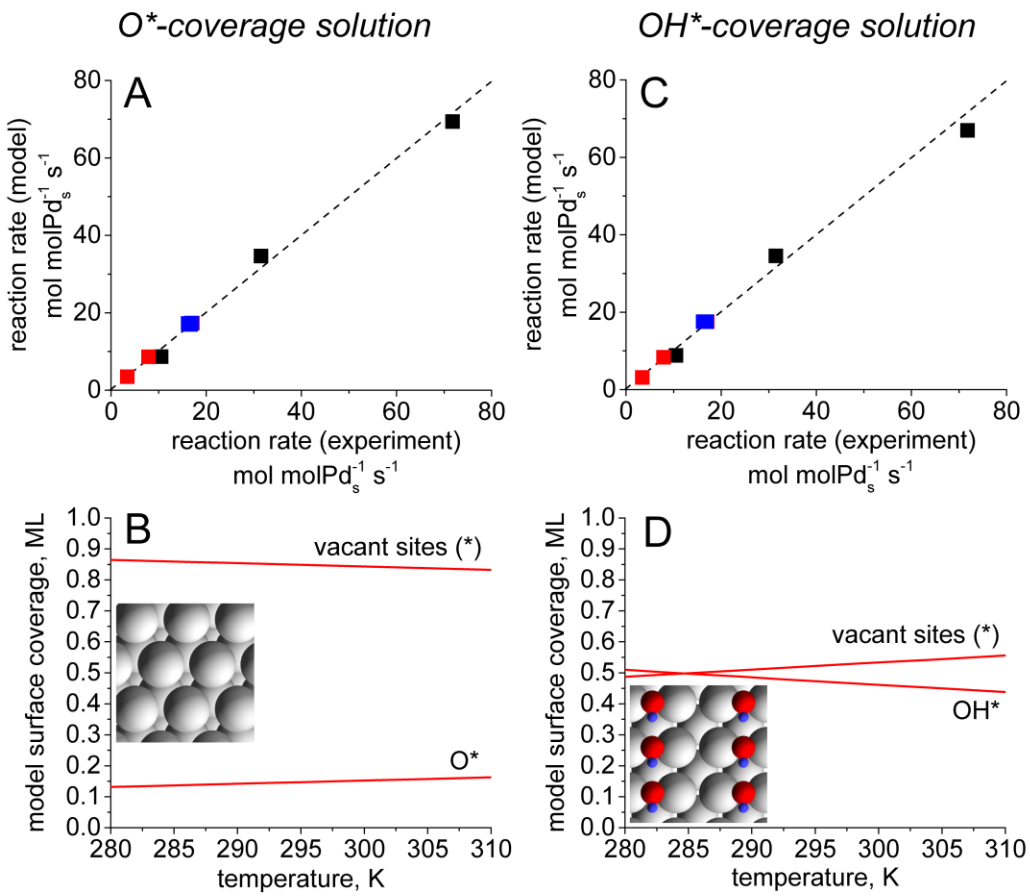

Figure 4.5 (A,C) Parity plots of experimental and model-predicted reaction rates for H_2O_2 decomposition. Refer to Table 4.3 for reaction conditions at each of the points in (A,C). Pd_s denotes surface Pd atoms determined by CO uptake. Red points are varying temperature; blue points are varying O_2 partial pressure; black points are varying feed concentration of H_2O_2. (B,D) Microkinetic model-predicted surface coverages of the most abundant surface intermediates (0.15 M H_2O_2 in H_2O feed with 150 psi Ar in gas-phase). Plots on the left refer to the *O*-coverage solution*, and plots on the right refer to the *OH*-coverage solution* obtained from the microkinetic model. Insets in (B) and (D) provide graphical representations of the nature of the active sites concluded through this study (nearly clean Pd(111) and OH*-modified Pd(100)). Blue spheres are hydrogen, red spheres are oxygen, and gray spheres are Pd atoms.

The *O*-coverage solution* predicts that the dominant reaction pathway is the *O*-assisted* pathway shown in Figure 4.3 (sequence of elementary steps from Table 4.2: 1, 5, -12, 2, 1, 13, 16, 2, 3), with some reaction flux through the parallel *OH*-assisted* pathway (sequence of elementary steps from Table 4.2: 1, 5, 1, 14, 2, 16, 2, 3). The rate of O* recombination to form O_2* is negligible, and dehydrogenation reactions are also inactive (atomic H is only transferred between surface

intermediates). The kinetic relevance of each elementary step was also analyzed using Campbell's degree of rate control:[198, 199]

$$X_{RC,i} = \frac{k_i}{r}\left(\frac{\partial r}{\partial k_i}\right)_{K_{i,eq},k_j}$$

where k_i and $K_{i,eq}$ are the rate constant and equilibrium constant for step i, and r is the overall reaction rate. O-O bond scission in H_2O_2 (step (5) of Table 4.2) carries the highest degree of rate control over the reaction conditions examined, shown in Table 4.5; the remaining rate control is distributed between the subsequent H-transfer reactions.

Table 4.5 Degree of rate control (X_{RC}) calculated for kinetically relevant reaction steps for reaction condition (3) of Table 4.3; X_{RC} is given for both the *O*-coverage solution* and the *OH*-coverage solution* at this experimental condition. Elementary step numbers (#) are in reference to Table 4.2. X_{RC} for the H-transfers is the sum over all steps listed.

#	Elementary step	X_{RC}, *O*-coverage solution*	X_{RC}, *OH*-coverage solution*
(5)	H_2O_2* + * ↔ OH* + OH*	0.59	0.00
(6)	OOH* + * ↔ O* + OH*	0.02	0.55
(13-16)	(H-transfers)	0.40	0.43

4.3.4.2 "OH-coverage solution"*

Using the DFT calculations on clean Pd(100) to derive initial estimates of parameters, a second solution was identified that also gave agreement with the experimental data set (Figure 4.5C and Table 4.4). In this case, the model-predicted surface coverage is ca. 0.5 ML of OH* (Figure 4.5D), and is therefore *not self-consistent* with the clean Pd(111) and Pd(100) surface models used in the DFT calculations. To ensure a solution self-consistent in coverage, we recalculated the binding energies of surface intermediates and the activation energy barriers for steps carrying significant reaction flux (as predicted by the *OH*-coverage solution*) in the presence of 0.5 ML of OH* spectators – i.e. two OH* were added to the unit cell and allowed to relax in the DFT calculations.

Table 4.6 DFT-calculated binding energies (BE) of adsorbed species on Pd(100) in the presence of 0.5 ML of OH*; and comparison with the BEs in the *OH*-coverage solution*.

	Pd(100) + 0.5 ML OH*		*OH*-coverage solution*
Species	Adsorption Site	BE, DFT / eV	BE / eV
H*	hollow	-2.56	-2.56
O*	hollow	-3.16	-2.99
OH*	top-tilted	-1.68	-1.83
OOH*	hollow-upright	-0.61	-0.51
H_2O*	top	-0.26	-0.32
H_2O_2*	top	-0.36	-0.46
O_2*	hollow	-0.14	-0.14

The DFT-derived parameter set on the OH*-modified Pd(100) surface is found to be in close agreement with the adjusted parameter set from the *OH*-coverage solution* (BEs shown in Table 4.6, with further details in supplementary section at the end of this chapter). The DFT calculations show that 0.5 ML of OH* destabilizes most intermediates and transition states investigated on Pd(100) relative to the clean Pd(100) calculations. The binding energies of O*, OH*, O_2*, and OOH* are weakened by > 0.5 eV, while the binding energies of H*, H_2O*, and H_2O_2* are not significantly affected. In addition, the activation energy barriers for O-O bond breaking in OOH* and H_2O_2* increase by 0.39 and 0.56 eV, respectively. Activation energy barriers for H-transfer from H_2O_2* or OOH* to OH* or O* remain small (< 0.2 eV). The maximum deviation in binding energy or activation barrier between the *OH*-coverage* solution and DFT calculations on OH*-modified Pd(100) is a 0.18 eV decrease in the activation barrier for O-O breaking in OOH*. Therefore OH*-modified Pd(100) also appears to be a feasible representation of the active site for H_2O_2 decomposition on Pd.

The dominant reaction pathways predicted for the *OH*-coverage solution* are shown in Figure 4.6. At high OH* coverage, immediate H-transfer from H_2O_2* to OH* is predicted to be nearly quasi-equilibrated (step (14) of Table 4.2). The O-O bond breaks in OOH*, and this step carries the highest degree of rate control (Table 4.5). Hydrogen transfers from OOH* to OH* (step

(16) of Table 4.2) and from OOH* to O* (step (15) of Table 4.2) carry the remaining reaction flux to form O_2* and H_2O*; hydrogen transfer from H_2O* to O* (step (12) of Table 4.2) is also nearly quasi-equilibrated.

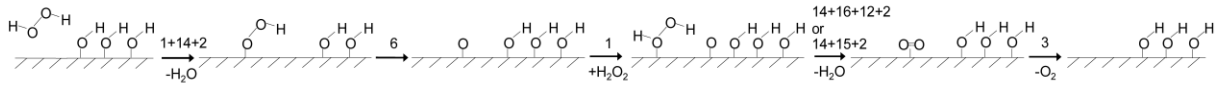

Figure 4.6 Dominant reaction pathways predicted by the microkinetic model for the *OH*-coverage solution*. The numbers by the black arrows correspond to the elementary steps numbers given in Table 4.2.

4.4 Discussion

The microkinetic modeling results suggest that both the close-packed Pd(111) and more open Pd(100) facets can contribute to the total H_2O_2 decomposition activity. Furthermore, on both Pd facets all reaction flux is predicted to go through an O-O bond breaking step (in either H_2O_2* or OOH*), followed by successive H-transfer steps to O*/OH* adsorbates. The relevant surface coverage of O*/OH* is then a function of the ability of the Pd surfaces to generate the O*/OH* fragments through O-O bond breaking (which can vary strongly with surface coverage, as seen from calculations on the OH*-modified Pd(100)), and the availability of H-donating species (H_2O_2* and OOH*) to reduce O*/OH* to H_2O* through the rapid H-transfer reactions. This mechanism is comparable to the redox mechanism discussed in references # [196] and [42]. The *direct dehydrogenation* and *O*+O*-recombination* pathways (Figure 4.3) are predicted to be inactive over all experimental conditions examined.

Although H-transfer steps carry some degree of rate control in the microkinetic model solutions, the DFT calculations show that the activation barriers for these steps are nearly insensitive to the surface structure of the Pd substrate. Interestingly, experimentally measured activation energy barriers for the gas phase H-transfer reactions of H_2O_2 or OOH• to OH• or O• radicals are also readily accessible (< 0.2 eV) around room temperature.[200] The action of the metal

substrate is then to generate the O*/OH* species through O-O bond breaking, and localize the H-transfer event to the surface. H_2O_2*, OOH*, and H_2O* are mobile on both Pd(111) and Pd(100) based on the small differences in binding energies among the available binding sites and therefore can diffuse across the Pd surface to find – and react with – the O*/OH* fragments. Additionally, we note that O* strongly prefers the threefold and fourfold hollow sites on Pd(111) and Pd(100), respectively; and O* must be lifted slightly from its preferred binding site to accept a H atom. This behavior is reflected in the low activation energy barrier generally calculated for H-transfers to O*, compared with the virtually zero barrier calculated for H-transfers to OH* – which is more accessible at its most favorable binding site (bridge site) on Pd(111) and Pd(100).

Breaking of the O-O bond in either H_2O_2* or OOH* carries the majority of rate control – suggesting that strategies to reduce H_2O_2 decomposition activity must focus on tuning surface reactivity toward the O-O bond. Retention of the O-O bond in dioxygen species is generally acknowledged to be a key factor in the selective synthesis of H_2O_2 by the DSHP both in theoretical[52, 55, 56, 133] and experimental literature,[24, 26, 61, 66] and our results here quantitatively highlight this as the central parameter governing the subsequent H_2O_2 decomposition activity on the Pd surface.

In view of the aforementioned findings, reduced Pd nanoparticles would be expected to be an ineffective catalyst for the DSHP due to high activity of Pd for O-O bond breaking (0.18 eV and 0.05 eV barriers to break O-O bond in H_2O_2 on clean Pd(111) and Pd(100), respectively). Extensive surface poisoning may be necessary to inhibit H_2O_2 decomposition on Pd, which our results suggest can readily occur on surface facets of supported Pd nanoparticles that are generally in high abundance (the (111) and (100) facets). Indeed, the experimentally measured H_2O_2 decomposition activity of supported Pd nanoparticles can be effectively quenched upon adding

halides (along with acids, whose role may partly be to facilitate halide adsorption) to the reaction medium, often at Pd:halide atomic ratios close to or exceeding 1:1.[59, 66, 201-203] Unfortunately, there are limited fundamental studies that examine the halide coverage necessary to achieve this effect.

Some of the most successful experimental catalysts to-date for the DSHP are based on alloys of Pd with Au, on which the subsequent decomposition reactions of H_2O_2 are partially or completely inhibited. DFT calculations indicate that dilution of Pd surfaces with Au significantly increases barriers for O-O bond scission.[54] However, experiments demonstrate that Au itself is generally an ineffective catalyst for the DSHP and gives slow rates,[33, 35] likely due to the significant activation energy barrier required to dissociate H_2 on Au[204] and weak adsorption of O_2 (Table 3.2 of Chapter 3). Promising search directions for improved DSHP catalysts may include bimetallic systems in which an active component (e.g. Pd) is effectively isolated in a relatively inert component (e.g. Au) resulting in reduced O-O bond breaking capacity but retention of H_2 dissociation[205] capacity; similar catalysts have proven very effective for the electrocatalytic synthesis of H_2O_2.[206, 207]

Lastly, the presence of H_2 in the reactor feed (not considered in the present work) has been shown to enhance the overall H_2O_2 decomposition activity over Pd-based catalysts.[36, 59] Choudhary and Samanta[31] observed that on unmodified Pd, H_2 both increases the H_2O_2 decomposition rate and consumes H_2O_2 through complete hydrogenation to H_2O (Reaction 4). Moreover, although adding chloride or bromide to an acidified reaction medium can quench H_2O_2 decomposition on Pd, H_2O_2 hydrogenation activity remains;[59] this observation may indicate significant differences in the active site(s) and rate controlling step(s) responsible for H_2O_2 decomposition versus H_2O_2 hydrogenation – although O-O bond breaking is required in both reactions. Tentative explanations addressing the role of H_2 have been proposed, such as maintaining the Pd surface in the reduced

state[192] for facile O-O bond breaking. Additionally, direct hydrogenation of H_2O_2 was shown to be a highly activated step using DFT calculations.[208] The influence of subsurface hydrogen or even Pd-hydrides may also be relevant.[53] In Chapter 8, we utilize DFT calculations to explore how saturation of Pd with hydrogen (surface, subsurface, and bulk) modifies its reactivity toward H_2O_2 decomposition.

4.5 Conclusions

Both the close-packed (111) and more open (100) facets can represent the active site for SiO_2-supported Pd nanoparticles. The DFT results show that O-O bond scission is facile on both Pd facets, such that O* and OH* intermediates are readily produced. Furthermore, H_2O_2* and OOH* can reduce O* and OH* to H_2O through thermodynamically driven H-transfer reactions, liberating O_2. The alternative step to produce O_2 (recombination of O*) is both thermodynamically and kinetically unfavorable. In addition, steps involving dehydrogenation through direct O-H bond cleavage over Pd are less favored than the H-transfer steps.

Microkinetic models based on two parameter sets are able to describe the experimental data for a SiO_2-supported Pd catalyst: the first set corresponds to a Pd surface partially covered in < 0.2 ML of O*, and these adjusted parameters are consistent with the DFT-derived parameters on clean Pd(111); the second set corresponds to a Pd surface covered in ca. 0.5 ML of OH*, and these adjusted parameters are consistent with the DFT-derived parameters on a Pd(100) surface with OH* spectators. Therefore, the microkinetic model suggests that both Pd(111) and Pd(100) can contribute to H_2O_2 decomposition activity. Experimental identification of dominant surface species during H_2O_2 decomposition on Pd might be realized by *in situ* X-ray photoelectron spectroscopy measurements in a similar manner to work performed on Pt for the oxygen reduction reaction.[164]

Consistent with the insights from DFT calculations, the dominant reaction pathways involve O-O bond breaking in either H_2O_2* or OOH* followed by H-transfer reactions between various reaction intermediates. Breaking of the O-O bond is identified as the key parameter governing H_2O_2 decomposition activity, because this step carries the highest degree of rate control.

Supplementary Figures, Tables, and Methods for Chapter 4

Microkinetic model formulation

In the microkinetic model simulation, the reactor is operated as a transient continuous stirred tank reactor (CSTR) and evolved to steady-state as described in reference # [209]. The CSTR model provides a good approximation to the experimental setup (a constant volume batch reactor) at low reactant conversion (H_2O_2 conversion was kept below 15 % for all experimental rate measurements) and negligible product inhibition (apparent reaction order with respect to P_{O2} was ca. 0 over the range of conditions studied, Table 4.4).

The proposed elementary steps (Table 4.2) correspond to a Langmuir-Hinshelwood process. The adsorption/desorption steps are assumed to be quasi-equilibrated. An aqueous H_2O_2 solution is used in the experiments, and the following procedure is implemented to reflect adsorption from the aqueous H_2O_2 solutions at each feed condition: (i) an experimentally derived Henry's law constant[210] for dilute aqueous H_2O_2 solutions (obtained at similar temperature/concentration conditions to our experimental conditions) is used to calculate the equilibrium vapor pressure of H_2O_2; (ii) an ideal mixture is assumed to be formed between H_2O_2 and H_2O (Raoult's law holds), using Antoine equation parameters for H_2O taken from the National Institute of Standards and Technology (NIST),[62] the equilibrium vapor pressure of H_2O is calculated; and (iii) the DFT-derived gas-phase adsorption equilibrium constants for H_2O_2 and H_2O are used to determine their respective Pd surface concentrations. Note that because no corrections are made to the energetics of the surface-bound species to reflect potential interactions at the liquid-solid interface, this treatment only considers the aqueous phase as a reservoir for H_2O_2 and H_2O.

The initial estimates of parameters for the *O*-coverage solution* are derived from the DFT calculations on clean Pd(111). Activation barriers are constrained (≥ 0) for exothermic steps and (≥ reaction energy) for endothermic steps in the microkinetic model. Pre-exponential factors for elementary steps are calculated from transition state theory;[85] a pre-exponential factor of $k_BT\ h^{-1}$ is assumed for steps in which no transition state is identified in the DFT calculations. The Shomate parameters are calculated from the DFT-derived vibrational frequencies on Pd(111)[83] to describe the temperature-dependence of entropies and enthalpies for surface species and transition states; these values are presented in Table S4.1. The final Shomate parameter values corresponding to the *O*-coverage solution* are obtained by adjusting only the Shomate parameter F (adjusting F corresponds directly to adjusting binding energies and transition state energies).

Shomate equation according to NIST:[62]

$$t = T[K]/1000$$

$$C_p°[J\ mol^{-1}\ K^{-1}] = A + Bt + Ct^2 + Dt^3 + E/t^2$$

$$H° - H°_{T0}[kJ\ mol^{-1}] = At + Bt^2/2 + Ct^3/3 + Dt^4/4 - E/t + F - H$$

$$S°[J\ mol^{-1}\ K^{-1}] = A\ln(t) + Bt + Ct^2/2 + Dt^3/3 - E/(2t^2) + G$$

Analogously, the initial estimates of parameters for the *OH*-coverage solution* are derived from the DFT calculations on clean Pd(100). The Shomate parameters are calculated from the DFT-derived vibrational frequencies on clean Pd(100)[83] to describe the temperature-dependence of entropies and enthalpies; these values are presented in Table S4.2. The final Shomate parameter values corresponding to the *OH*-coverage solution* are obtained by adjusting only the Shomate parameter F (adjusting F corresponds directly to adjusting binding energies and transition state energies).

Microkinetic model limitations

*Solvent and pH effect*s

The experimental measurements were performed in a three-phase system (gaseous product, liquid reactant and product, and solid catalyst) using conditions relevant to a DSHP process. Water has been shown to interact weakly with noble metal surfaces,[211] but can potentially solvate adsorbates and transition states.[212] The influence of solvation is expected to be most pronounced for weakly-bound adsorbates, whose chemisorption energies are comparable to the intermolecular interactions in water. Such effects are challenging to account for in DFT calculations for a number of reasons, including: the structure of water at metal interfaces remains a subject of intense study;[213] there are inadequacies in the DFT-description of water;[214] and it is computationally expensive to explicitly treat solvent models in DFT calculations. As a first approximation to the H_2O_2 decomposition chemistry, experimentally carried out in the aqueous phase over a supported Pd catalyst, we neglect solvent effects in the DFT calculations. The validity of this approximation will depend on the degree of solvation of surface species in the kinetically significant steps.

The solution pH has also been shown to significantly affect the rate of Pd-catalyzed H_2O_2 decomposition.[26] One beneficial role of protons (for inhibiting H_2O_2 decomposition) has been proposed to be through decreasing adsorption of H_2O_2 onto the catalyst.[169] In the absence of any direct role of protons in the reaction mechanism, the influence of pH could then potentially be incorporated in the adsorption equilibrium constant for H_2O_2. In addition, the counter-anion strongly influences the H_2O_2 decomposition rate; coordinating anions like Cl^- and Br^- were shown to be effective inhibitors of H_2O_2 decomposition in the presence of acids (which, in part, may act to facilitate anion adsorption on Pd), while oxyacids like sulfuric and acetic acid are less

effective.[169] However, the effect of pH and other additives was not investigated in this work. All H_2O_2 feed solutions in our experiments were prepared using ultra-pure water.

Comparison of binding energies and activation barriers from the *O*-coverage solution* and *OH*-coverage solution* with the DFT-derived values at 0 K

The adjustments ("Δ") to the DFT-calculated binding energies and activation barriers on Pd(111) needed to obtain the *O*-coverage solution* are shown in Table S4.3. The Δ value for the binding energy of a surface species is equivalent to the difference between the DFT-derived Shomate parameter F for that species and its F parameter corresponding to the *O*-coverage solution* (Table S4.1). The Δ for the activation barrier of an elementary step is equivalent to the difference between the DFT-derived Shomate parameter F for that transition state and its F parameter corresponding to the *O*-coverage solution*, subtracting the change in the F parameter for the initial state of the elementary step (Table S4.1); for example, for step (5) there is a 0.06 eV *increase* in the transition state F parameter for the *O*-coverage solution* with respect to the F parameter on clean Pd(111), and a 0.05 eV *decrease* in the F parameter for the initial state H_2O_2* – resulting in an overall adjustment in the activation barrier for step (5) of [+0.06 – (-0.05) = +0.11] eV.

The maximum adjustment Δ of binding energies and activation barriers in Table S4.3 is a 0.24 eV destabilization of the binding energy of O_2* on Pd(111).

The adjustments ("Δ") to the clean Pd(100) DFT-calculated binding energies and activation barriers (for elementary steps that carry the majority of reaction flux, as predicted by the *OH*-coverage solution*) needed to obtain the *OH*-coverage solution* are shown in Table S4.4. The Δ for the binding energy of a surface species is equivalent to the difference between the DFT-derived

Shomate parameter F for that species and its F parameter corresponding to the *OH*-coverage solution* (Table S4.2). The Δ for the activation barrier of an elementary step is equivalent to the difference between the DFT-derived Shomate parameter F for that transition state and its F parameter corresponding to the *OH*-coverage solution*, subtracting the change in the F parameter for the initial state of the elementary step (Table S4.2); for example, for step (6) there is a 0.974 eV *increase* in the transition state F parameter for the *OH*-coverage solution* with respect to the F parameter on clean Pd(100), and a 0.767 eV *increase* in the F parameter for the initial state OOH* – resulting in an overall adjustment in the activation barrier for step (6) of [+0.974 – (+0.767) = +0.21] eV from its value on clean Pd(100).

Adjustments Δ of binding energies on clean Pd(100) and those corresponding to the *OH*-coverage solution* are large (> 0.5 eV for the binding energies of O*, OH*, O_2*, and OOH*). However, the *OH*-coverage solution* predicts a surface covered in 0.44-0.51 ML of hydroxyl over the range of experimental conditions studied, with the remainder of the surface essentially vacant (the next highest adsorbate coverage is < 0.01 ML). Therefore we recalculated these binding energies and activation barriers using DFT by including two OH* in the (2 × 2) unit cell for Pd(100) and allowing these OH* spectators to relax during calculations. The resulting binding energies and activation barriers are in agreement with the values from the *OH*-coverage solution*, as shown in Table S4.4 (maximum deviation is a 0.18 eV decrease in the activation barrier for O-O scission in OOH*).

Analysis of the model-predicted apparent activation barrier

The contributions to the apparent activation barrier for the *O*-coverage solution*, which predicts a mostly vacant surface, can be extracted from the enthalpy surface in Figure S4.1. The van‘t Hoff equation was utilized to estimate the enthalpy of H_2O_2 dissolution (-65.9 kJ/mol) from

the experimental Henry's law constant.[210] The apparent activation barrier calculated in the microkinetic model can therefore be approximated by the sum of (i) the energy required to remove H_2O_2 from its aqueous solvation shell and bind it to the Pd surface; and (ii) the activation energy barrier for O-O bond scission in H_2O_2. Accordingly, the microkinetic model predicts that the activation barrier for O-O bond scission carries the highest degree of rate control compared with subsequent steps.

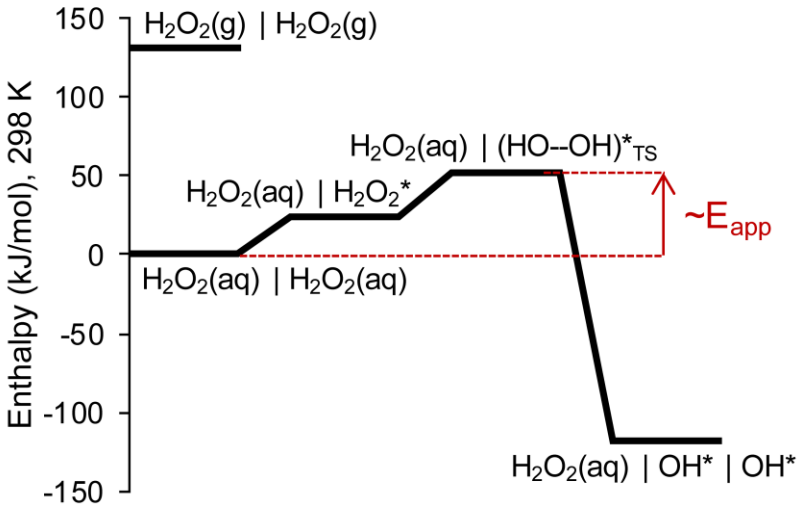

Figure S4.1 Enthalpy surface for adsorption and O-O bond scission in H_2O_2 corresponding to the *O*-coverage solution* parameters. The reference state is aqueous H_2O_2. The "|" separating two adsorbates denotes infinite separation from each other, "(g)" denotes a gas-phase species, "*" denotes a surface-adsorbed species, and "TS" denotes a transition state.

Table S4.1 Shomate parameters (A to G) for T = 100-400 K on clean Pd(111), where the Shomate parameter H has been set to the reference enthalpy $H°_{T0}$. Co-adsorbed reactants/products that can be stabilized through hydrogen bonding are treated as separate species in the microkinetic model that form from the infinitely separated reactants with no activation barrier and react through the H-transfer steps (e.g., the two steps for formation and reaction of co-adsorbed hydrogen peroxide and atomic oxygen: $H_2O_2^* + O^* \rightarrow [H_2O_2^* + O^*]$, followed by H-transfer reaction $[H_2O_2^* + O^*] \rightarrow [OOH^* + OH^*]$. The "[ ]" in this table denotes the co-adsorbed species, which occupy two surface sites). Any contributions to rate control from the co-adsorbate formation steps has been included in the sum over H-transfer steps in Table 4.5. Both co-adsorbed species $[OOH^* + O^*]$ and $[O_2^* + OH^*]$ are found to have a destabilizing interaction with respect to infinite separation based on DFT calculations on both clean Pd(111) and Pd(100), and are therefore not included as co-adsorbed species in the microkinetic model. Only the Shomate parameter F is adjustable in the microkinetic model because this corresponds directly to adjusting binding energies and transition state energies. The final adjusted value of F corresponding to the *O*-coverage solution* is provided in the last column. The ca. 0.13-0.16 ML of atomic oxygen coverage predicted in the *O*-coverage solution* refers to the individual O* surface species.

Species	A	B	C	D	E	F	G	F (O*-coverage solution)
Individual surface species								
H^*	−1.2379	−31.0614	274.9744	−301.1067	0.0230	−1,572.20	0.1131	−1,572.20
O^*	3.5819	40.1962	156.2183	−376.4105	−0.0709	−42,077.10	0.7089	−42,079.50
OH^*	4.8344	121.4179	−60.9688	−136.1449	−0.0267	−43,653.89	8.8485	−43,653.89
OOH^*	13.8608	172.3887	−231.4055	107.4082	−0.0458	−85,580.19	28.9736	−85,570.09
H_2O^*	13.0211	157.7417	−338.6789	278.7604	−0.0575	−45,267.04	25.9167	−45,267.04
$H_2O_2^*$	26.5334	173.8183	−326.9946	307.0207	−0.0798	−87,162.06	63.5197	−87,167.26
O_2^*	12.3129	170.8770	−350.4969	286.8124	−0.0532	−84,026.41	36.2718	−84,002.91
Coadsorbed surface species								
$[H_2O_2^* + O^*]$	−10.00	528.76	−1,147.58	1,000.37	−0.0689	−129,243.19	−63.32	−129,239.19
$[H_2O_2^* + OH^*]$	18.78	201.08	−131.12	19.37	−0.0901	−130,887.40	35.79	−130,887.40
$[OOH^* + OH^*]$	16.93	212.17	−126.11	−63.43	−0.1282	−129,291.72	23.32	−129,291.72
$[O_2^* + H_2O^*]$	3.59	406.90	−737.38	545.40	−0.0667	−129,322.19	−16.70	−129,298.69
$[OOH^* + H_2O^*]$	11.49	329.61	−418.95	203.31	−0.0705	−130,900.76	10.82	−130,890.76
$[OH^* + OH^*]$	−10.73	355.60	−531.46	283.50	−0.0238	−87,315.31	−52.20	−87,315.31
$[H_2O^* + O^*]$	−14.32	521.47	−1,229.11	1,089.45	−0.0533	−87,350.36	−74.03	−87,350.36
$[H_2O_2^* + O_2^*]$	16.70	369.93	−571.72	388.33	−0.1296	−171,223.92	16.16	−171,200.42
$[OOH^* + OOH^*]$	−1.04	400.60	−555.99	379.77	−0.0611	−171,219.15	−29.52	−171,214.15
Transition states								
(5) $H_2O_2^* + * \leftrightarrow [OH^* + OH^*]$	19.1038	217.2597	−433.2384	374.5711	−0.0718	−87,143.93	42.1829	−87,138.13
(6) $OOH^* + * \leftrightarrow O^* + OH^*$	10.2082	157.9428	−118.689	−94.1579	−0.0886	−85,576.35	11.2061	−85,551.35
(7) $O_2^* + * \leftrightarrow O^* + O^*$	−11.4069	327.403	−796.6204	705.6756	−0.016	−83,940.97	−50.7924	−83,917.47
(8) $OH^* + * \leftrightarrow O^* + H^*$	3.3211	104.2105	−1.4067	−190.3628	−0.0481	−43,557.19	0.4708	−43,557.19
(9) $H_2O^* + * \leftrightarrow OH^* + H^*$	6.4144	107.4376	28.2296	−186.3454	−0.0378	−45,159.27	11.5313	−45,159.27
(10) $OOH^* + * \leftrightarrow O_2^* + H^*$	11.3126	145.9346	−50.2891	−141.1647	−0.0687	−85,525.28	18.297	−85,515.18
(11) $H_2O_2^* + * \leftrightarrow OOH^* + H^*$	14.9553	176.278	−148.4772	6.5883	−0.0585	−87,099.96	30.1399	−87,104.96
(12) $[H_2O^* + O^*] \leftrightarrow [OH^* + OH^*]$	Nearly spontaneous, transition state could not be isolated within the accuracy of the DFT parameters.							
(13) $[H_2O_2^* + O^*] \leftrightarrow [OOH^* + OH^*]$	14.2811	285.1948	−435.9657	307.4847	−0.095	−129,242.16	18.8832	−129,222.26
(14) $[H_2O_2^* + OH^*] \leftrightarrow [OOH^* + H_2O^*]$	Nearly spontaneous, transition state could not be isolated within the accuracy of the DFT parameters.							
(15) $OOH^* + O^* \leftrightarrow O_2^* + OH^*$	17.1135	202.604	−304.3029	233.8313	−0.0931	−127,649.63	34.4015	−127,633.63
(16) $[OOH^* + OH^*] \leftrightarrow [O_2^* + H_2O^*]$	13.1863	198.5609	−22.739	−224.1188	−0.091	−129,295.76	18.5607	−129,295.76
(17) $[H_2O_2^* + O_2^*] \leftrightarrow [OOH^* + OOH^*]$	17.0212	279.2991	−275.2226	107.3011	−0.0951	−171,201.20	27.3271	−171,177.70
Gas-phase species								
$H_2(g)$	28.60	4.79	−16.29	18.74	0.00185	−3,041.56	168.41	
$O_2(g)$	28.93	2.86	−20.27	50.84	0.00040	−83,972.46	235.00	
$H_2O(g)$	33.75	−3.43	1.06	26.34	−0.00204	−45,239.60	236.46	
$H_2O_2(g)$	31.01	36.28	53.24	−75.24	−0.00409	−87,123.43	259.82	

Table S4.2 Shomate parameters (A to G) for T = 100-400 K on clean Pd(100), where the Shomate parameter H has been set to the reference enthalpy $H°_{T0}$. Co-adsorbed reactants/products that can be stabilized through hydrogen bonding are treated as separate species in the microkinetic model that form from the infinitely separated reactants with no activation barrier and react through the H-transfer steps (e.g., the two steps for formation and reaction of co-adsorbed hydrogen peroxide and atomic oxygen: H_2O_2* + O* → [H_2O_2* + O*], followed by H-transfer reaction [H_2O_2* + O*] → [OOH* + OH*]. The "[ ]" in this table denotes the co-adsorbed species, which occupy two surface sites). Any contributions to rate control from the co-adsorbate formation steps has been included in the sum over H-transfer steps in Table 4.5. Both co-adsorbed species [OOH* + O*] and [O_2* + OH*] are found to have a destabilizing interaction with respect to infinite separation based on DFT calculations on both clean Pd(111) and Pd(100), and are therefore not included as co-adsorbed species in the microkinetic model. Only the Shomate parameter F is adjustable in the microkinetic model because this corresponds directly to adjusting binding energies and transition state energies. The final adjusted value of F corresponding to the *OH*-coverage solution* is provided in the last column. The ca. 0.5 ML of hydroxyl coverage predicted in the *OH*-coverage solution* refers to the co-adsorbed surface species [OH* + OH*], which occupies two surface sites (i.e., 0.5 ML of total hydroxyl coverage is 0.25 ML of [OH* + OH*]).

Species	A	B	C	D	E	F	G	F (OH*-coverage solution)
Individual surface species								
H*	2.4742	78.1496	−29.9400	−119.8483	−0.0583	−1,584.14	−3.4570	−1,567.14
O*	7.1819	94.1544	−171.5667	89.7288	−0.0814	−42,102.80	6.2529	−42,014.80
OH*	2.5023	102.0164	55.4286	−293.2032	−0.0424	−43,693.80	−2.0461	−43,635.71
OOH*	16.1481	186.9070	−287.8807	153.4456	−0.1135	−85,619.16	23.6466	−85,545.13
H_2O*	14.1861	209.8581	−497.7306	456.2954	−0.0045	−45,268.60	50.6399	−45,270.60
H_2O_2*	19.1131	199.2745	−325.1658	243.3293	−0.1187	−87,169.72	31.2071	−87,179.32
O_2*	−17.8817	366.1298	−814.9159	680.9070	−0.0067	−84,094.93	−70.4549	−83,985.93
Coadsorbed surface species†								
[H_2O_2* + O*]	9.71	393.72	−810.69	702.04	−0.103	−129,265.65	−2.74	−129,200.65
[H_2O_2* + OH*]	14.85	297.49	−393.35	258.50	−0.112	−130,907.08	15.55	−130,827.08
[OOH* + OH*]	0.35	357.22	−601.84	468.72	−0.067	−129,345.95	−19.13	−129,204.95
[O_2* + H_2O*]	−5.50	558.20	−1,316.93	1,175.29	−0.062	−129,358.13	−44.30	−129,258.13
[OOH* + H_2O*]	−0.10	459.54	−836.91	646.44	−0.060	−130,917.92	−27.76	−130,836.92
[OH* + OH*]	9.33	148.28	102.13	−367.59	−0.092	−87,420.45	8.56	−87,332.07
[H_2O* + O*]	−19.09	528.39	−1,224.49	1,080.39	−0.044	−87,365.85	−86.87	−87,315.85
[H_2O_2* + O_2*]	−11.80	552.31	−1,129.58	1,011.99	−0.070	−171,283.27	−68.30	−171,213.27
[OOH* + OOH*]	−14.91	570.57	−1,181.29	1,067.56	−0.070	−171,283.08	−79.10	−171,098.08
Transition states								
(5) H_2O_2* + * ↔ [OH* + OH*]	15.8130	182.5407	−253.3928	149.6250	−0.0630	−87,159.17	32.2389	−87,118.17
(6) OOH* + * ↔ O* + OH*	−7.1496	351.0642	−810.0315	711.7780	−0.0499	−85,610.65	−43.9678	−85,516.70
(7) O_2* + * ↔ O* + O*	5.8195	69.2012	243.6839	−597.6716	−0.1060	−84,076.08	1.8144	−83,931.08
(8) OH* + * ↔ O* + H*	−0.6430	54.3148	216.6492	−426.8104	−0.0269	−43,592.42	−7.7810	−43,512.42
(9) H_2O* + * ↔ OH* + H*	−27.6558	435.1438	−919.8486	737.9061	0.0165	−45,201.22	−99.2842	−45,201.22
(10) OOH* + * ↔ O_2* + H*	10.3419	130.5716	−63.5579	−69.7197	−0.0917	−85,567.26	12.2305	−85,487.26
(11) H_2O_2* + * ↔ OOH* + H*	12.0433	165.3644	−11.8770	−220.3537	−0.0918	−87,124.60	14.9198	−87,124.60
(12) [H_2O* + O*] ↔ [OH* + OH*]	−22.7796	423.6000	−820.7693	652.6636	0.0086	−87,366.18	−85.3674	−87,281.18
(13) [H_2O_2* + O*] ↔ [OOH* + OH*]	−3.0431	373.9495	−677.1616	525.9745	−0.0446	−129,246.02	−31.9938	−129,170.02
(14) [H_2O_2* + OH*] ↔ [OOH* + H_2O*]	17.4539	229.3678	−137.8705	−45.9880	−0.0810	−130,910.53	33.0865	−130,822.53
(15) OOH* + O* ↔ O_2* + OH*	−2.0505	346.9272	−671.5379	564.6279	−0.0671	−127,672.98	−30.9511	−127,672.98
(16) [OOH* + OH*] ↔ [O_2* + H_2O*]	−6.9963	372.1790	−577.7797	389.5662	−0.0170	−129,348.30	−29.3073	−129,348.30
(17) [H_2O_2* + O_2*] ↔ [OOH* + OOH*]	−21.6571	572.7990	−1,126.8435	965.9686	−0.0254	−171,284.89	−91.5796	−171,284.89

Table S4.3 Adjustments ("Δ") to the DFT-calculated binding energies (BE) and activation barriers (E_a) on clean Pd(111) needed to obtain the *O*-coverage solution*. Elementary step numbers (#) are in reference to Table 4.2. Activation barriers for steps (5-11) are with respect to infinitely separated reactants, while activation barriers for H-transfer steps (12-17) are in reference to the co-adsorbed reactants.

Parameter	Pd(111), DFT (eV)	*O*-coverage solution* (eV)	Δ (eV)
BE, H*	-2.70	-2.70	0.00
BE, O*	**-3.64**	**-3.66**	**-0.02**
BE, OH*	-2.03	-2.03	0.00
BE, OOH*	**-0.94**	**-0.84**	**+0.10**
BE, H_2O*	-0.22	-0.22	0.00
BE, H_2O_2*	**-0.32**	**-0.37**	**-0.05**
BE, O_2*	**-0.50**	**-0.26**	**+0.24**
E_a, (5) H_2O_2* + * ↔ OH* + OH*	**0.18**	**0.29**	**+0.11**
E_a, (6) OOH* + * ↔ O* + OH*	**0.08**	**0.23**	**+0.15**
E_a, (7) O_2* + * ↔ O* + O*	0.85	0.85	0.00
E_a, (8) OH* + * ↔ O* + H*	1.02	1.02	0.00
E_a, (9) H_2O* + * ↔ OH* + H*	1.10	1.10	0.00
E_a, (10) OOH* + * ↔ O_2* + H*	0.59	0.59	0.00
E_a, (11) H_2O_2* + * ↔ OOH* + H*	0.62	0.62	0.00
E_a, (12) H_2O* + O* ↔ OH* + OH*	0.33	0.33	0.00
E_a, (13) H_2O_2* + O* ↔ OOH* + OH*	**0.04**	**0.20**	**+0.16**
E_a, (14) H_2O_2* + OH* ↔ OOH* + H_2O*	0.00	0.00	0.00
E_a, (15) OOH* + O* ↔ O_2* + OH*	**0.00**	**0.17**	**+0.17**[a]
E_a, (16) OOH* + OH* ↔ O_2* + H_2O*	0.00	0.00	0.00
E_a, (17) H_2O_2* + O_2* ↔ OOH* + OOH*	0.20	0.20	0.00

[a]The adjustment Δ reported here only includes the change in transition state energy for this step between the clean Pd(111) value and that for the OH*-coverage solution, as the initial state of OOH* + O* was not treated as a separate co-adsorbed state in the microkinetic model (described in caption of Table S4.1).

Table S4.4 Adjustments ("Δ") to the DFT-calculated binding energies (BE) and activation barriers (E_a) on clean Pd(100) needed to obtain the *OH*-coverage solution*. Only the steps which carry the majority of the reaction flux are shown, as predicted by the *OH*-coverage solution*. The last column shows the DFT values for the binding energies and activation barriers re-calculated on Pd(100) modified with 0.5 ML of OH* spectators. Elementary step numbers (#) are in reference to Table 4.2. Activation barriers for H-transfer steps are in reference to the co-adsorbed reactants.

Parameter	clean Pd(100), DFT (eV)	*OH*-coverage solution* (eV)	Δ (eV)	OH-modified Pd(100), DFT (eV)
BE, H*	-2.74	-2.56	+0.18	-2.56
BE, O*	-3.90	-2.99	+0.91	-3.16
BE, OH*	-2.43	-1.83	+0.60	-1.68
BE, OOH*	-1.28	-0.51	+0.77	-0.61
BE, H_2O*	-0.30	-0.32	-0.02	-0.26
BE, H_2O_2*	-0.36	-0.46	-0.10	-0.36
BE, O_2*	-1.27	-0.14	+1.13	-0.14
E_a, (6) OOH* + * ↔ O* + OH*	0.02	0.23	+0.21	0.41
E_a, (12) H_2O* + O* ↔ OH* + OH*	0.00	0.36	+0.36	0.41
E_a, (14) H_2O_2* + OH* ↔ OOH* + H_2O*	0.00	0.08	+0.08	0.00
E_a, (15) OOH* + O* ↔ O_2* + OH*	0.02	0.02	0.00[a]	0.00[b]
E_a, (16) OOH* + OH* ↔ O_2* + H_2O*	0.00	0.00	0.00	0.00

[a]The adjustment Δ reported here only includes the change in transition state energy for this step between the clean Pd(111) value and that for the OH*-coverage solution, as the initial state of OOH* + O* was not treated as a separate co-adsorbed state in the microkinetic model (described in caption of Table S4.2).

[b]Spontaneous in forward direction; transition state could not be isolated within the accuracy of our DFT parameters.

Chapter 5: Understanding the Role of Co-Adsorbed Halides on Pd(111)

5.1 Introduction

The previous two chapters provide mechanistic evidence for why monometallic Pd catalysts are not substantially selective for H_2O_2 and are highly active for its decomposition in the absence of promoters. In particular, our DFT calculations suggest that direct H_2O_2 formation is difficult on unmodified Pd because the O_2* and OOH* intermediates can readily dissociate, with the O-O bond in these intermediates decreasing in stability as the coordinative saturation of the metal surface atoms decreases (e.g., moving from Pd(111) to Pd(100)). H_2O_2 itself can also readily decompose on Pd because of its low O-O bond dissociation barrier and the subsequent facile hydrogen-transfer steps that carry the reaction flux. Our microkinetic modeling results from Chapter 4 suggest that the primary means to prevent H_2O_2 decomposition on Pd are to (i) raise the kinetic barrier for breaking its O-O bond and/or (ii) destabilize the adsorbed state of H_2O_2 (see Figure S4.1).

A key experimental observation continues to drive research on Pd-based materials: the undesirable side reactions can be reduced or even eliminated,[35, 172] while maintaining active production of H_2O_2, by adding acids and halides to the reaction medium and/or modifying Pd with appropriate secondary metals. There is a growing body of theoretical literature that examines how secondary metals such as Au modify Pd's reactivity toward the DSHP,[53, 54, 134, 206, 208, 215-218] while significantly less theoretical literature exists concerning other promoters.[57] In this chapter, we utilize DFT calculations to investigate the effect of adsorbed halides on the DSHP surface chemistry.

Halides are an undesirable additive for the DSHP from a processing standpoint (e.g., their presence can promote metal corrosion/leaching and may necessitate additional H_2O_2 purification steps depending on the downstream application), but it is valuable to understand their interaction with Pd so that we can refine approaches to catalyst synthesis and DSHP operational conditions. The early work of Pospelova highlights the importance of strongly adsorbing anions such as halides – in addition to protons – in the reaction medium for monometallic Pd catalysts; no H_2O_2 is produced in their absence.[30] Halides are most effective toward inhibiting H_2O_2 decomposition at low pH, and it has been proposed that protons facilitate halide adsorption onto the catalyst.[48, 68, 170] Post-mortem characterization substantiates halide adsorption to supported Pd catalysts,[170] and adsorption studies[48, 219] demonstrate an increased halide uptake by Pd catalysts with decreasing solution pH. Cations other than protons have little to no effect on the DSHP reactions.[59, 66]

Halides can modulate the reactivity of Pd toward all reaction pathways. A number of experimental studies examine the effect of halide concentration in the liquid phase on direct H_2O_2 synthesis and decomposition over supported Pd catalysts.[29, 31, 47-49, 66, 68, 220] In general, H_2O_2 decomposition rates (and H_2 conversion rates for the synthesis reaction) decrease monotonically

with increasing concentration of halide (Cl^-, Br^-, or I^-).[29, 31, 49, 68] The presence of halides can also inhibit direct H_2O formation with respect to direct H_2O_2 formation, and there generally exists an optimal halide concentration that results in the highest yield and selectivity to H_2O_2 in the direct synthesis reaction.[31, 66, 68] Br^- and Cl^- are the most effective halides for improving selectivity to H_2O_2, while I^- tends to completely poison the catalyst toward both H_2O_2 synthesis and decomposition, and F^- has the weakest effect on reactivity.

The model we use to better understand these behaviors is halides co-adsorbed with DSHP intermediates on the close-packed Pd(111) surface. One prevailing hypothesis is that halides modify the interactions of Pd atoms with adsorbed species – particularly to stabilize the adsorbed-dioxygen molecules (O_2*, OOH*, and H_2O_2*)[29, 66, 68, 170] with respect to their O-O bond dissociation reactions to O* and OH* fragments, which are strongly exothermic on unmodified Pd as shown in the previous chapters and lead to H_2O formation. We evaluate this hypothesis along with other potential effects induced by the co-adsorption of halides. The insights from this study are also relevant to the electrocatalytic oxygen reduction reaction, wherein Pt-based materials are often used as catalysts and the presence of halides or other anions are inherent in these systems.[221]

An additional, but not necessarily exclusive, hypothesis on the roles of halides is the selective blocking of active sites that are responsible for H_2O formation and H_2O_2 decomposition.[57, 59, 66, 68, 222] In particular, Deguchi, Yamano, and Iwamoto[47, 48, 57] provide evidence that multiple types of Pd sites may be active during reaction – sites including corners and edges that have a high degree of coordinative undersaturation and are responsible for forming H_2O and decomposing H_2O_2, and more coordinatively saturated sites that favor direct H_2O_2 formation, consistent with prior reports in the literature.[223, 224] The stronger adsorption strength of a H^+ and Br^- pair calculated at the more coordinatively undersaturated Pd sites suggests that these sites can

be preferentially blocked[57]; we will consider halide adsorption on more coordinatively undersaturated features of Pd nanoparticles in Chapter 6. Another hypothesis is that halides induce phase modifications[72, 225] and/or nanoparticle sintering and reconstruction[73] that expose desirable Pd ensembles. We do not explicitly address this latter hypothesis in our DFT calculations.

5.2 Computational Methods

All DFT calculations in this chapter were performed using the Vienna *Ab Initio* Simulation Package (VASP)[137, 226] in the generalized gradient approximation (GGA-PW91).[109] The projector augmented wave (PAW)[227, 228] method was used to describe the electron-ion interactions, and the electron wave functions were expanded using plane waves with an energy cutoff of 400 eV. The convergence criterion for geometric relaxations was 0.02 eV $Å^{-1}$. The Pd(111) substrate was represented by a periodically repeated (3 × 3) unit cell with four atomic layers. This slab was separated in the z-direction from its successive image by a vacuum layer of at least 12 Å. The top slab layer was allowed to relax, and the bottom three slab layers were fixed at their bulk lattice positions. The calculated lattice constant for bulk Pd, 3.96 Å, is in good agreement with the experimentally measured value of 3.89 Å.[141] Calculations involving molecular oxygen were performed spin-polarized. The first Brillouin zone was sampled with a (4 × 4 × 1) Monkhorst-Pack k-point mesh.[143] For cases where a (2 × 2) unit cell was used, a (6 × 6 × 1) Monkhorst-Pack k-point mesh was used with all other parameters held the same as for the (3 × 3) unit cell.

Adsorption was modeled by placing adsorbates on one side of the slab, with the electrostatic potential adjusted accordingly.[139, 140] The DSHP is generally performed in a liquid solvent[18], but none of the energetics presented here were corrected to reflect interactions of adsorbed species with the solvent phase. This simplified model was used to elucidate trends in the binding of intermediates and transition states as a function of halogen identity and coverage. We

note that we will refer to “halogen” species in the context of our DFT model, but refer to “halide” species when discussing experiments in which the halogens were introduced to the reaction medium as the corresponding halide salt or hydrogen halide.

Binding energies of intermediates were referenced to the corresponding gas-phase species and either the clean Pd(111) slab:

$$BE = E_{adsorbate+slab} - E_{gas\text{-}phase\ adsorbate} - E_{slab}$$

or halogen-covered Pd(111) slab:

$$BE = E_{adsorbate+halogens+slab} - E_{gas\text{-}phase\ adsorbate} - E_{halogens+slab}$$

where $E_{adsorbate+slab}$ is the total energy of the clean slab with adsorbate, $E_{gas\text{-}phase\ adsorbate}$ is the total energy of the adsorbate in the gas-phase, E_{slab} is the total energy of the clean slab, $E_{adsorbate+halogens+slab}$ is the total energy of the slab with halogen(s) and adsorbate co-adsorbed, and $E_{halogens+slab}$ is the total energy of the slab with halogens adsorbed in their most stable configuration. Binding energies were verified to be within 0.1 eV (referenced to the BEs calculated using the parameters stated above) upon increasing the k-point set to (6 × 6 × 1), increasing the energy cutoff to 500 eV, or relaxing the second metal layer for the (3 × 3) unit cell. Unless otherwise stated, only the minimum energy structures found through rigorous permutation of co-adsorbates among the available binding sites on the Pd(111) slab are reported. We observed no reconstruction of the top layer of the Pd(111) slab in any of our calculations.

The minimum energy paths for elementary steps were calculated using the climbing image nudged elastic band method (CI-NEB[112, 115]) with seven interpolated images. Transition states for non-spontaneous steps were verified by identification of a single imaginary frequency along the reaction coordinate.

5.3 Results

The results are organized as follows: First, we present binding properties of the halogens on Pd(111) including binding energies, diffusion barriers, and adsorption phases. Next, we introduce intermediates and the reaction network for H_2O_2 synthesis and decomposition mechanisms, and we investigate the stability of intermediates and transition states for key elementary steps in the presence of co-adsorbed halogens. Finally, we consider direct participation of halogens in elementary steps using a single co-adsorbed halogen atom in the unit cell.

5.3.1 Halogen binding on Pd(111)

Halogen interactions with transition metal surfaces are the subject of a number of computational studies in the literature, and the reader is referred to those works for more detailed discussions.[229-234] A comprehensive review of both experiments and theoretical models for anion adlayers on transition metal surfaces can also be found in reference # [235]. Here we present only the properties of halogens on Pd(111) that are relevant to our discussion.

5.3.1.1 Preferred binding sites, binding energies, and subsurface sorption

All halogens prefer binding to the threefold fcc site at 1/9 monolayer (ML) coverage on Pd(111). The binding energies (Table 5.1) are in close agreement with those calculated in other works.[229, 231] F* binds most strongly to Pd(111) with a BE of -3.44 eV, while Br* and I* bind most weakly with BEs of -3.04 eV and -3.05 eV, respectively.

The next most stable binding site for all halogens is the threefold hcp site. The activation barrier for halogen diffusion from the fcc to hcp site over a bridge site is less than 0.2 eV – indicating high mobility of these species on Pd(111) under conditions relevant to the DSHP[19] (Table 5.1, with diffusion pathway depicted in Figure 5.1). The top site is the least stable high-

symmetry binding site. F* is less stable on the top site by 0.24 eV compared with its binding energy on the fcc site, while for Cl*, Br*, and I* the energy difference between the top and fcc sites is greater than 0.5 eV. We note that the x- and y-coordinates for Cl*, Br*, and I* are fixed directly above a top site for these calculations, while only the z-coordinate is allowed to relax, because otherwise the top binding site is unstable and results in spontaneous relaxation of Cl*, Br*, and I* to a neighboring threefold site.

Table 5.1 Surface adsorption energies (BE), geometric parameters (ΔZ_{Pd}, $Z_{X\text{-}Pd}$, and $d_{Pd\text{-}Pd}$), surface diffusion activation energies (E_a), and subsurface sorption energies (ΔE) of halogens on Pd(111); coverage is 1/9 ML.

Species	Binding Site	BE / eV	ΔZ_{Pd} / Å	$Z_{X\text{-}Pd}$ / Å	$d_{Pd\text{-}Pd}$ / Å	E_a / eV diffusion *fcc to hcp*	ΔE / eV diffusion *fcc to hcp*	ΔE / eV subsurface[a] *fcc to O_h under fcc*
F*	fcc	-3.44	-0.01	1.50	2.93	0.15[b]	0.15	unstable[c]
Cl*	fcc	-3.17	0.02	1.76	2.93	0.17	0.12	3.54
Br*	fcc	-3.04	0.01	1.91	2.92	0.16	0.09	3.63
I*	fcc	-3.05	0.02	2.04	2.93	0.16	0.07	3.21

[a]O_h denotes an octahedrally coordinated subsurface site in the first subsurface layer
[b]no transition state identified; activation barrier is equal to reaction energy
[c]F spontaneously relaxes to the surface fcc site
See Figure 5.1 for definitions of the geometric parameters.

We also investigate halogen penetration into the first subsurface layer, but find absorption to subsurface sites to be highly endothermic with respect to adsorption on the surface fcc site (greater than 3 eV energy difference for Cl*, Br*, and I*). Allowing the second and third Pd slab layers to relax during these subsurface calculations yields similar energetics. No stable subsurface absorption state is identified for F*, which spontaneously relaxes to the Pd surface irrespective of its subsurface placement prior to geometry optimization. Halogen adsorption is therefore restricted to the surface layer in all subsequent calculations. Nonetheless it is important to mention that corrosion and leaching of supported Pd nanoparticles has been observed in the presence of acid and halide during direct H_2O_2 synthesis experiments.[73, 203, 225, 236] Recent *in situ* X-ray absorption

fine structure (XAFS) experiments performed by Centomo et al[225] also provide evidence that Br^- can promote the leaching of PdO and apparent reduction of Pd – which may contribute to the formation of Pd surface structures that are desirable for selective H_2O_2 synthesis. We do not attempt to explore mechanisms for halide-induced corrosion[237] or reconstruction of the Pd surface in this chapter.

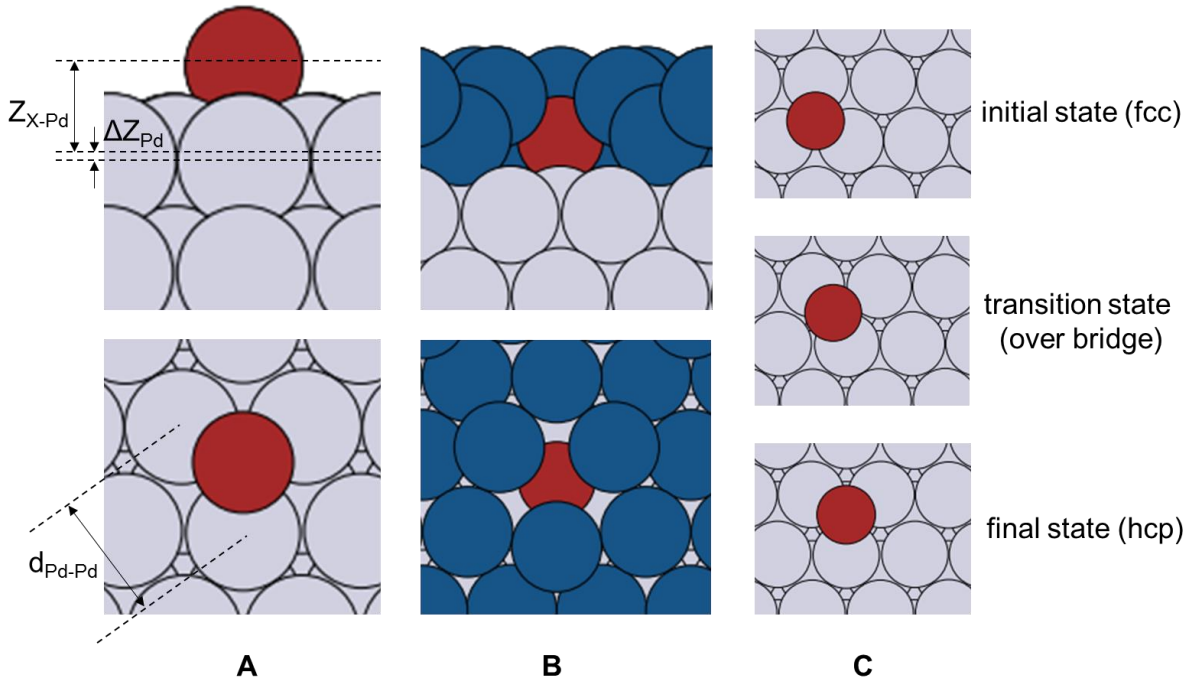

Figure 5.1 (A) Side and top-down views of Br* at its preferred binding site (fcc) on Pd(111). (B) Side and top-down views of Br* absorbed in the first subsurface layer of Pd(111) at the octahedrally coordinated site; the top layer of Pd atoms is colored in blue. (C) Top-down views of the fcc to hcp diffusion path. The transition state occurs over a bridge site for Cl*, Br*, and I*; no transition state is identified for F* diffusion along this pathway. Geometric parameters: $Z_{X\text{-}Pd}$ is the vertical distance between the adsorbed halogen and the plane containing the three Pd atoms directly bound to it; ΔZ_{Pd} is the vertical displacement of the plane of Pd atoms in contact with the halogen adsorbate and the plane of Pd atoms on the top layer of the clean relaxed surface; and $d_{Pd\text{-}Pd}$ is the average of the bond lengths between the three Pd atoms directly bound to the halogen adsorbate (the corresponding value on the relaxed clean surface is 2.80 Å). Atom colors: halogen (dark red), Pd (gray or dark blue).

5.3.1.2 Adlayer structures and saturation coverages

Both the identity of the halogen and its surface coverage of Pd are important parameters that can affect reactivity. We evaluate the relevance of higher coverage adlayers by first calculating the minimum energy structures for halogen adsorption on Pd(111) in the (2 × 2) and (3 × 3) unit

cells up to 1/2 ML coverage. The results are presented in Figure 5.2. F*, Cl*, Br*, and I* adopt the same adlayer structures at 1/9, 2/9, 1/4, and 1/3 ML. The halogens populate only the threefold fcc sites for these coverages, and the average binding energy per halogen does not vary significantly. Cl*, Br*, and I* adlayers rapidly decrease in stability above 1/3 ML, and these halogens begin to occupy the less stable (bridge and top) sites. The average binding energy per F* atom only decreases by ca. 0.2 eV even up to 1/2 ML coverage – and F* adopts a different (linear) structure than the other halogens at 1/2 ML.

Employing an approach similar to that of Gossenberger et al,[231] we then construct *ab initio* phase diagrams[144] to analyze trends in adlayer stability (considering the structures in Figure 5.2) for an aqueous DSHP process that uses the hydrogen halides as promoters. We refer to gas-phase reservoirs of the respective hydrogen halide species to define the chemical potential driving force for halide adsorption onto Pd(111), which we subsequently relate to the aqueous-phase hydrogen halide reservoirs that would be in equilibrium with the gas-phase (equivalence of chemical potentials) through experimental equilibrium expressions. Details of phase diagram development can be found in the supplementary section at the end of this chapter.

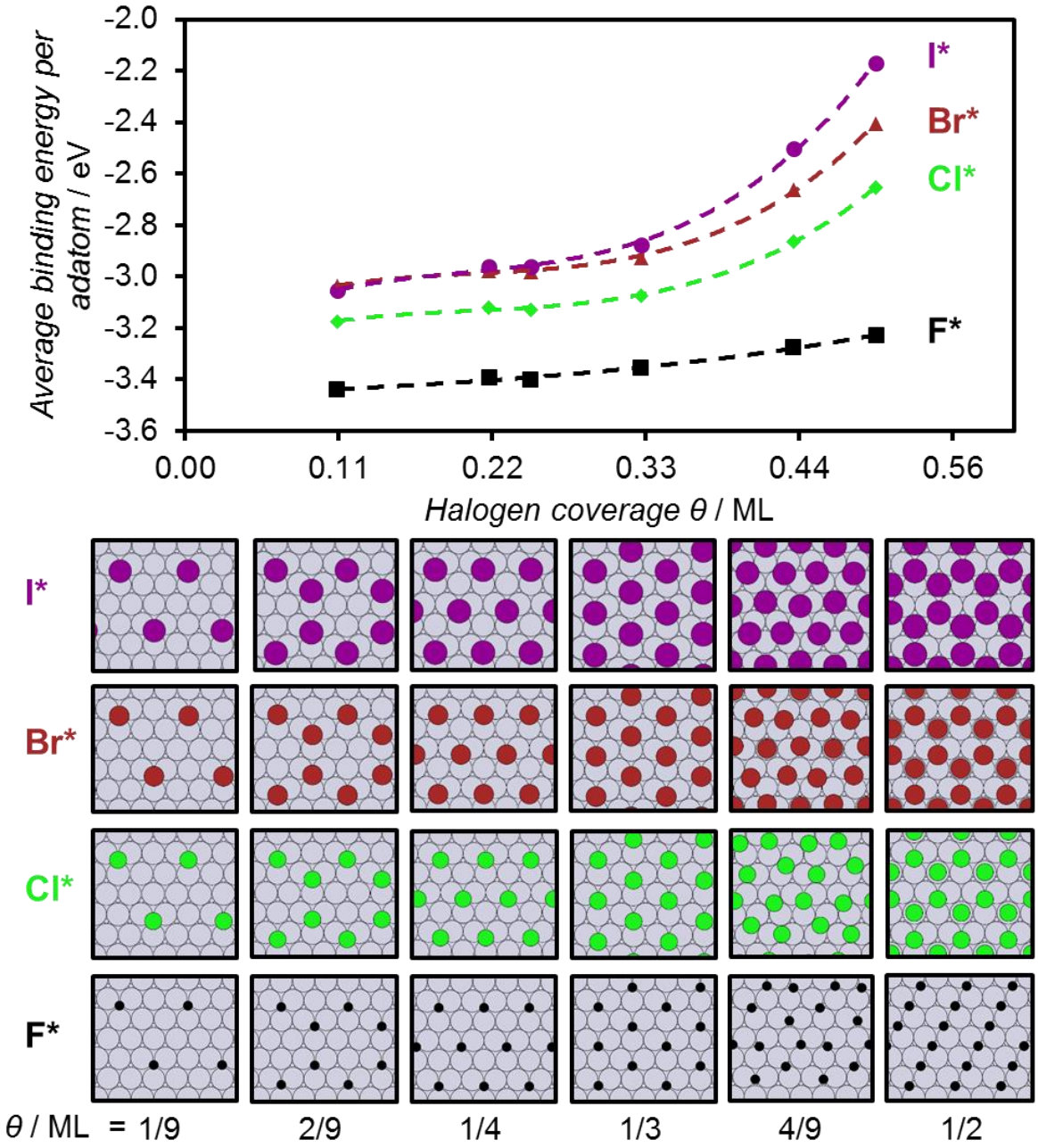

Figure 5.2 Average binding energy per halogen adatom as a function of coverage on Pd(111), with corresponding top-down views of the most stable relaxed structures at each coverage. Dashed lines are to guide the eye. Atom colors: I (purple), Br (dark red), Cl (green), F (black), and Pd (gray).

The phase diagrams (Figure 5.3) predict 1/3 ML of Cl*, Br*, or I* to be the saturation coverage at aqueous hydrogen halide concentrations as high as 1 molal – generally much higher than concentrations used in the experimental literature to promote direct H_2O_2 synthesis on Pd. Cl*, Br*, and I* adopt the commensurate $(\sqrt{3} \times \sqrt{3})R30°$ structure depicted in Figure 5.2 at 1/3

ML coverage. This structure has been experimentally identified for Cl*, Br*, and I* on Pd(111) single crystals after exposure to gas-phase halogens[238-241] and to aqueous halide solutions in electrochemical environments.[242-245] Furthermore, Carrasquillo et al[242] found that the interaction strength between aqueous halide and a Pd(111) single-crystal electrode is in the order $Cl^- < Br^- < I^-$; this result is in qualitative agreement with our phase diagrams, wherein the transition from clean to halogen-covered Pd(111) is predicted to occur most rapidly for increasing concentrations of HI, followed by HBr and then HCl.

We anticipate F* to have negligible coverage on Pd(111) even at relatively high concentrations of HF (Figure 5.3). The H-F bond is the strongest of the hydrogen halides, and we calculate the dissociative adsorption of HF onto Pd(111) to be nearly thermoneutral (-0.12 eV reaction energy), while the dissociative adsorptions of HCl, HBr, and HI are highly exothermic (by greater than 1.4 eV, Table S5.1 and Figure S5.1); solvation of HF in an aqueous environment is favored to its dissociative adsorption on Pd(111). Moreover, electrochemical analyses of transition metal electrodes in aqueous solutions of fluoride indicate that fluoride is a nonspecifically adsorbing species – unlike chloride, bromide, and iodide, which are all specifically adsorbing anions that can form ordered adlayer structures such as that described above.[235]

Based on these results, we choose to quantify the effect of co-adsorbed Cl*, Br*, and I* on the energetics of H_2O_2 synthesis and decomposition mechanisms up to a halogen surface coverage 1/3 ML in the (3 × 3) Pd(111) unit cell. We examine only the case of 1/9 ML coverage for F* to probe its low-coverage effects.

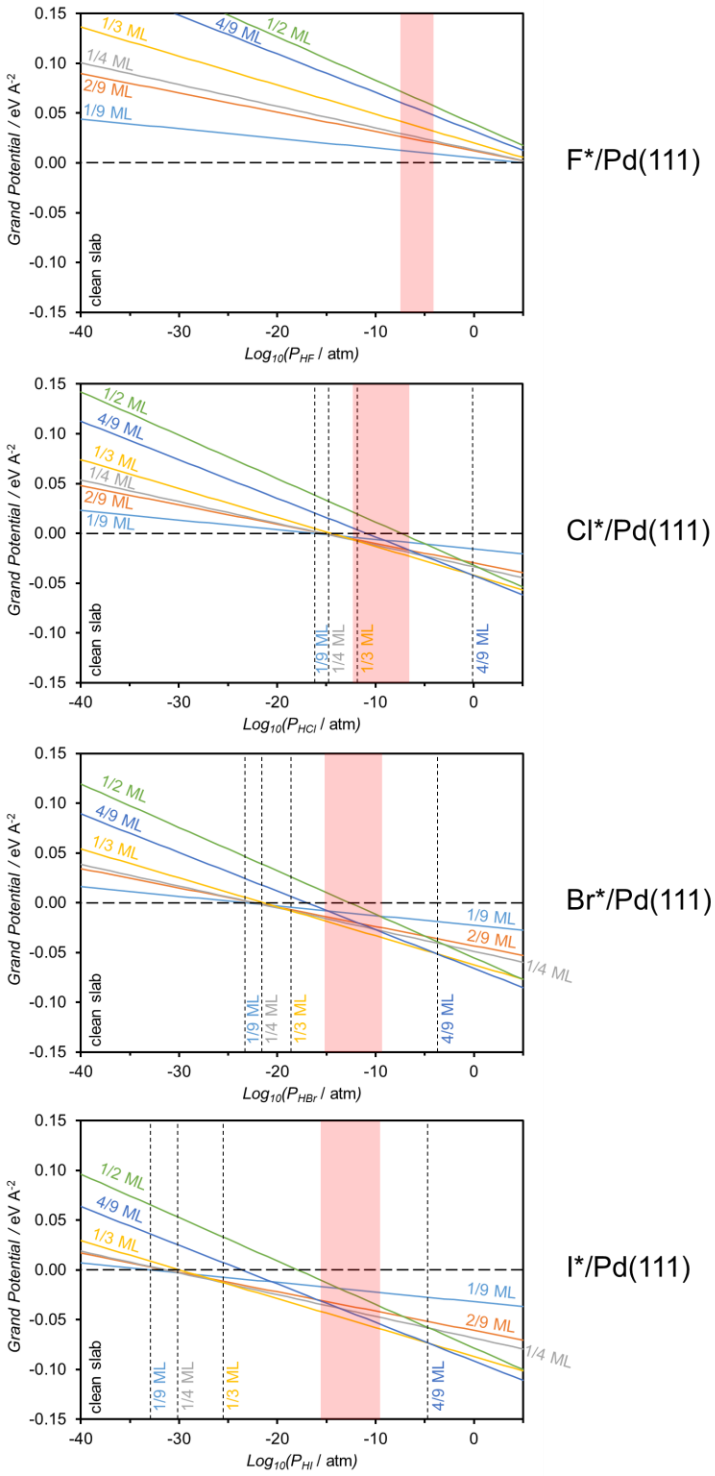

Figure 5.3 Phase diagram for F*, Cl*, Br*, and I* on Pd(111) as a function of the partial pressure of the corresponding hydrogen halide at 298 K. The phase with the most negative grand potential at a given partial pressure of hydrogen halide is the most thermodynamically stable phase of those considered. The horizontal dotted black line at a grand potential of zero indicates the clean slab. The vertical dotted black lines are used to indicate a new stable phase moving left to right on the diagram. The shaded red region shows the molal concentration of aqueous hydrogen halide (0.001 – 1 molal spanned by the shaded red region) that would be in equilibrium with the corresponding hydrogen halide partial pressure – calculated using experimental equilibrium expressions.[246]

5.3.2 Energetics for H_2O_2 synthesis and decomposition mechanisms on Pd(111)

We recompile the networks of elementary steps proposed in the previous two chapters to describe the H_2O_2 synthesis and decomposition mechanisms (Scheme 5.1), which comprise hydrogenation, O-O and H-H bond dissociation, hydrogen transfer, and adsorption/desorption steps.

In the context of Scheme 5.1 and in accord with previous DSHP literature, direct H_2O_2 formation proceeds through sequential hydrogenation of O_2* to OOH* (step 5) and then to H_2O_2* (step 6), maintaining the O-O bond. O-O dissociation steps (steps 9-11) form O*/OH* fragments that can be hydrogenated directly to H_2O* (steps 7 and 8). Hydrogen transfer steps from OH*, OOH*, or H_2O_2* to O* or OH* (steps 12-16) can also form H_2O*. Moreover, these hydrogen transfer steps may be integral to the H_2O_2 decomposition mechanism on Pd in the absence of co-fed H_2 (Chapter 4). The elementary mechanism by which H_2 hydrogenates H_2O_2 to H_2O remains uncertain, although DFT computations suggest the absence of direct hydrogenation of H_2O_2* by H* due to a large kinetic barrier.[208]

Adsorption/Desorption

1. $O_2 + * \leftrightarrow O_2*$
2. $H_2 + 2* \leftrightarrow 2H*$
   - 2a. $H_2 + * \leftrightarrow H_2*$
   - 2b. $H_2* + * \leftrightarrow H* + H*$
3. $H_2O_2 + * \leftrightarrow H_2O_2*$
4. $H_2O + * \leftrightarrow H_2O*$

Hydrogenation

5. $H* + O_2* \leftrightarrow OOH* + *$
6. $H* + OOH* \leftrightarrow H_2O_2* + *$
7. $H* + OH* \leftrightarrow H_2O* + *$
8. $H* + O* \leftrightarrow OH* + *$

O-O Dissociation

9. $O_2* + * \leftrightarrow O* + O*$
10. $OOH* + * \leftrightarrow O* + OH*$
11. $H_2O_2* + * \leftrightarrow OH* + OH*$

Hydrogen Transfer

12. $H_2O* + O* \leftrightarrow OH* + OH*$
13. $OOH* + O* \leftrightarrow O_2* + OH*$
14. $H_2O_2* + O* \leftrightarrow OOH* + OH*$
15. $OOH* + OH* \leftrightarrow O_2* + H_2O*$
16. $H_2O_2* + OH* \leftrightarrow OOH* + H_2O*$
17. $OOH* + OOH* \leftrightarrow H_2O_2* + O_2*$

Scheme 5.1. The proposed elementary reaction steps encompassing H_2O_2 synthesis, H_2O synthesis, and H_2O_2 decomposition. The steps in green are the pathway for sequential hydrogenation of O_2 to H_2O_2; the steps in red are the O-O bond dissociation steps that represent bifurcation points along the H_2O_2 synthesis pathway and generate the O*/OH* precursors to H_2O synthesis. H_2 dissociation can occur directly from the gas-phase (step 2) or through a molecular H_2* precursor (steps 2a-b).

5.3.2.1 Stability of surface intermediates

Table 5.2 provides the binding energies of intermediates on clean Pd(111) along with preferred adsorption sites. All intermediates bind more weakly to clean Pd(111) than do the halogens (Table 5.1) with the exception of atomic oxygen.

Most intermediates exhibit repulsive interactions with 1/9 ML of co-adsorbed Cl*, Br,* or I* and tend to maximize their lateral separation from the halogen. Destabilizations in binding energies due to the co-adsorbed halogen are on the order of 0.1 eV with respect to binding on the clean Pd(111) slab, do not depend strongly on the halogen identity, and are mainly due to lateral strain in the Pd surface induced by the co-adsorbates (Figure S5.2 and Tables S5.2 to S5.3). All intermediates, including the co-adsorbed halogen, remain in their most stable clean-surface adsorption sites; the only exception is the co-adsorption of Cl* and OOH*, in which OOH* adopts a top-top binding configuration to form a hydrogen bond with Cl*. H_2O_2* and H_2O* also form hydrogen bonds with Cl*, Br*, and I* – but any stabilization due to hydrogen bonding with these halogens is weak (< 0.1 eV stabilization with respect to binding on the clean Pd(111) slab). These calculations show that low coverages of Cl*, Br*, and I* may not significantly affect the reactivity of Pd(111), with the halogens mainly acting as site blockers to reduce the total number of available Pd sites. In addition, the weak interaction of H_2O* with Cl*, Br*, and I* suggests these halogens may be only weakly solvated when bound to the Pd surface.[247]

1/9 ML of co-adsorbed F* similarly destabilizes O*, H*, O_2*, and H_2*. However, F* forms particularly strong hydrogen bonds with OH-containing intermediates. Figure 5.4 provides the interaction energies and geometric parameters for the hydrogen-bonded configurations of H_2O_2*, OOH*, H_2O*, and OH* with F*. In all cases F* moves to a Pd top site (its least stable binding site on clean Pd(111)) to maximize the hydrogen-bonding interaction and minimize any screening

effects from surrounding Pd atoms that may result from adsorption in the deeper threefold sites. The O-H bond participating in the hydrogen bond with F* increases in length in the order OH* < H_2O* < H_2O_2* < OOH*, which is the same order as the increasing strength of hydrogen bonding stabilization. In fact, there is nearly complete transfer of hydrogen to F* from H_2O_2* and OOH* (both of which have much weaker O-H bonds in the gas-phase when compared with those in OH and H_2O). F* and OOH* or H_2O_2* spontaneously form these same co-adsorption states even when they are placed in next nearest-neighbor binding sites in the initial configuration before geometry optimization. The strong hydrogen bonding between F* and H_2O* is in agreement with the observation that aqueous fluoride ions generally exhibit nonspecific adsorption on transition metal surfaces, maintaining significant solvation shells.[235]

Table 5.2 Binding energies (eV) and adsorption sites for reaction intermediates on clean and halogen-covered Pd(111). The reference energy is the gas-phase intermediate infinitely separated from the clean or halogen-covered slab. Bolded values indicate that the adsorbate and/or halogen adlayer are displaced from their preferred clean-surface adsorption configurations. N/A indicates that adsorption is endothermic. Values in parenthesis for H_2O_2 and H_2O indicate physisorption states in which the adsorbate sits above the halogen atoms (and does not form a bond with Pd), stabilized by a hydrogen bond with an adsorbed halogen. These physisorption states above the halogen adlayer are denoted by a "$^{(p)}$" in the text, and the adsorbed states directly bound to Pd atom(s) are denoted by the conventional "*".

species	1/9 ML halogen/Pd(111)			2/9 ML halogen/Pd(111)			1/3 ML halogen/Pd111			clean
	Cl	Br	I	Cl	Br	I	Cl	Br	I	Pd(111)
O	-4.49 fcc	-4.48 fcc	-4.47 fcc	-4.35 fcc	-4.35 fcc	-4.34 fcc	**-3.71** **fcc**	**-3.62** **fcc**	**-3.40** **fcc**	-4.58 fcc
H	-2.87 fcc	-2.88 fcc	-2.89 fcc	-2.83 fcc	-2.84 fcc	-2.85 fcc	-2.61 fcc	-2.59 fcc	-2.53 fcc	-2.93 fcc
OH	-2.54 fcc	-2.53 fcc	-2.50 fcc	-2.45 br	-2.44 br	-2.41 br	**-1.99** **br**	**-1.87** **br**	**-1.62** **top**	-2.63 fcc
O_2	-0.93 top-br	-0.93 top-br	-0.92 top-br	-0.84 top-br	-0.84 top-br	-0.82 top-br	**-0.24** **top-top**	**-0.12** **top-top**	**N/A**	-0.99 top-br
H_2	-0.23 top	-0.21 top	-0.19 top	-0.17 top	-0.15 top	-0.09 top	**N/A**	**N/A**	**N/A**	-0.29 top
H_2O_2	-0.36 top	-0.33 top	-0.32 top	-0.33 top	-0.30 top	-0.31 top	**-0.12** **top**	**N/A** **(-0.10)**	**N/A** **(-0.12)**	-0.33 top
OOH	**-1.30** **top-top**	-1.29 top-br	-1.27 top-br	**-1.24** **top-top**	**-1.23** **top-top**	**-1.21** **top-top**	**-0.84** **top-top**	**-0.73** **top**	**-0.47** **top**	-1.38 top-br
H_2O	-0.32 top	-0.28 top	-0.25 top	-0.34 top	-0.29 top	-0.23 top	**-0.14** **top**	**N/A** **(-0.08)**	**N/A** **(-0.09)**	-0.28 top

Increasing the coverage of co-adsorbed Cl*, Br*, or I* to 2/9 ML further destabilizes all intermediates except for H_2O* on 2/9 Cl*-covered Pd(111), and H_2O_2* and H_2O* on 2/9 Cl*- and Br*-covered Pd(111), which are weakly stabilized via hydrogen bonding (Table 5.2). The magnitude of destabilization is again nearly independent of halogen identity, similar to the case for 1/9 ML of Cl*, Br*, or I*, with the maximum reduction in binding strength being 0.24 eV for O* on 2/9 ML I*-covered Pd(111). Most intermediates retain their preferred binding site/geometry as that on the clean Pd(111) slab, and no Pd atoms are shared between the intermediates and co-adsorbed halogens in their most stable configurations. The 2/9 ML Cl*, Br*, and I* adlayer structure remains intact after adsorption of any intermediate, with all halogens binding at fcc sites.

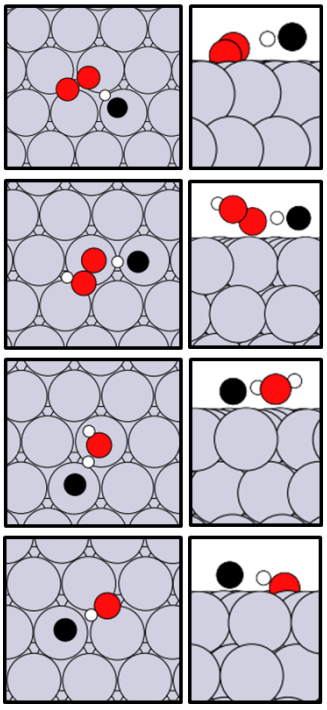

Species	$d_{O\text{-}H}$ / Å	$d_{F\text{-}H}$ / Å	$<_{O\text{-}H\text{-}F}$ / °	ΔE / eV
OOH	1.451 (0.984)	1.017	169.0	-0.53
H_2O_2	1.282 (0.984)	1.097	170.7	-0.49
H_2O	1.053 (0.978)	1.399	168.8	-0.40
OH	1.034 (0.974)	1.516	160.4	-0.08

Figure 5.4 Top-down and side views of the hydrogen-bonded states corresponding to 1/9 ML F* co-adsorbed with OH*, H_2O*, OOH*, and H_2O_2* on Pd(111). $d_{X\text{-}H}$ is the distance between the hydrogen atom shared in the hydrogen bond and the participating F or O atom. The values of $d_{O\text{-}H}$ in parenthesis are the corresponding O-H bond lengths on the clean slab. ΔE is the difference in total energy between the configurations of both species co-adsorbed and infinitely separated on Pd(111) (a negative value indicates that the co-adsorbed configuration is stabilized with respect to infinite separation). Atom colors: F (black), H (white), O (light red), and Pd (gray).

1/3 ML of halogen on Pd(111) represents a critical coverage at which the disparity between Cl*, Br*, and I*'s ability to destabilize intermediates – and the magnitude of the destabilizations – increases drastically (Table 5.2). All Pd atoms are coordinated to one halogen atom in the minimum energy $(\sqrt{3} \times \sqrt{3})R30°$ structure that Cl*, Br*, and I* adopt on Pd(111) (Figure 5.2). Co-adsorption of intermediates then requires either disruption of the halogen adlayer to accommodate binding and/or sharing Pd atoms with the halogens. The general trend in destabilization is Cl* < Br* < I*, and the maximum reduction in binding strength with respect to clean-slab binding is 1.18 eV for O* on 1/3 ML I*-covered Pd(111).

Of the open-shell intermediates, only OH* and OOH* adopt different binding geometries on 1/3 ML halogen-covered Pd(111) compared with those on the clean slab. O* remains at its preferred fcc site in the presence of 1/3 ML of Cl*, Br*, or I*, but O* displaces all co-adsorbed halogens out of their fcc sites toward bridge sites. H* also remains at its preferred fcc site, and the $(\sqrt{3} \times \sqrt{3})R30°$ halogen adlayer structure remains intact with all halogens bound to fcc sites. The binding energy of H* also varies the least among the open-shell intermediates on 1/3 ML halogen-covered Pd(111), ranging from -2.53 eV for I*-covered Pd(111) to -2.61 eV for Cl*-covered Pd(111) (the corresponding clean-surface binding energy for H* is -2.93 eV); the energy difference between OH*, OOH*, or O* binding to I*-covered Pd(111) versus Cl*-covered Pd(111) is greater than 0.3 eV.

The closed-shell reactants and products (H_2O, H_2O_2, and H_2), aside from molecular oxygen, interact weakly with clean Pd(111) and prefer binding at top sites. All top sites in the $(\sqrt{3} \times \sqrt{3})R30°$ halogen adlayer are adjacent to a halogen-occupied fcc site, and the energy penalty to share the Pd atom or displace the halogen to accommodate top-site adsorption in some cases cannot be fully compensated by the binding energy of the closed-shell species to Pd. The result is endothermic

binding with respect to the gas-phase species – or weakly exothermic physisorption above the halogen adlayer (denoted by a "$^{(p)}$" appended to the species) with no direct bond to any Pd atoms.

Perturbing the $(\sqrt{3} \times \sqrt{3})R30°$ adlayer to accommodate H_2* binding at a top site is endothermic on halogen-covered Pd(111) by up to ca. 0.5 eV for the case of I*. O_2* binds exothermically in the presence of the Cl* and Br* adlayers, but its binding energy is destabilized from the clean-surface value by over 0.7 eV. The 1/3 ML I* adlayer destabilizes binding such that O_2* prefers desorption by 0.11 eV. Moreover, on clean Pd(111) O_2* retains only a small fraction (ca. 6 %) of its gas-phase magnetic moment, while on all the 1/3 ML halogen-covered surface models O_2* retains over 60 % of its gas-phase magnetic moment – suggesting that the presence of the co-adsorbed halogens might reduce the ability of Pd to activate the O-O bond in O_2*.

H_2O_2* and H_2O* adsorptions to a Pd top site are favorable on 1/3 ML Cl*-covered Pd(111) by ca. 0.1 eV with respect to the gas-phase species. This is not the case for 1/3 ML Br*- and I*-covered Pd(111); H_2O_2 and H_2O prefer to physisorb (denoted by a "^{p}") above these $(\sqrt{3} \times \sqrt{3})R30°$ adlayers, forming weak hydrogen bonds with a single adsorbed halogen that stabilize $H_2O_2^{(p)}$ and $H_2O^{(p)}$ by ca. 0.1 eV with respect to their infinite separation from the halogen-covered slab (Figure S5.3). Rearranging the $(\sqrt{3} \times \sqrt{3})R30°$ adlayer to permit H_2O_2* or H_2O* binding to a Pd top site is nearly thermoneutral on the Br*-covered slab but endothermic by ca. 0.3 eV on the I*-covered slab.

The calculations described in this section demonstrate that co-adsorbed halogens can have a significant impact on the stability of reaction intermediates, particularly when the halogen coverage increases to 1/3 ML. These interactions are mainly repulsive for Cl*, Br*, and I* and will result in modifications to reaction thermochemistry and the stability of transition states, as discussed in the following sections.

5.3.2.2 Surface reaction energies

The surface reactions that we use to describe the H_2O_2 synthesis and decomposition mechanisms (as written in Scheme 5.1) can be classified as: bond-forming (hydrogenation), bond-breaking (H-H and O-O bond dissociations), and bond-transfer (hydrogen transfer). The thermochemistry of these reactions on halogen-covered Pd(111) depends on the reaction class, identity of co-adsorbed halogen, and degree of halogen coverage. All reaction energies are reported with respect to infinitely separated reactants and products on the clean or halogen-covered Pd(111) surfaces.

Hydrogenations of O* and OH* (O_2* and OOH*) are bond-forming reactions that lead to H_2O* (H_2O_2*) production. Figure 5.5 demonstrates that the exothermicity of these reactions generally increases with increasing halogen coverage on Pd(111). There is no uniform trend in the reaction energies as a function of halogen identity; the differences in reaction energy for a specific hydrogenation reaction and halogen coverage are small (< 0.1 eV) among Cl*-, Br*-, and I*-covered Pd(111).

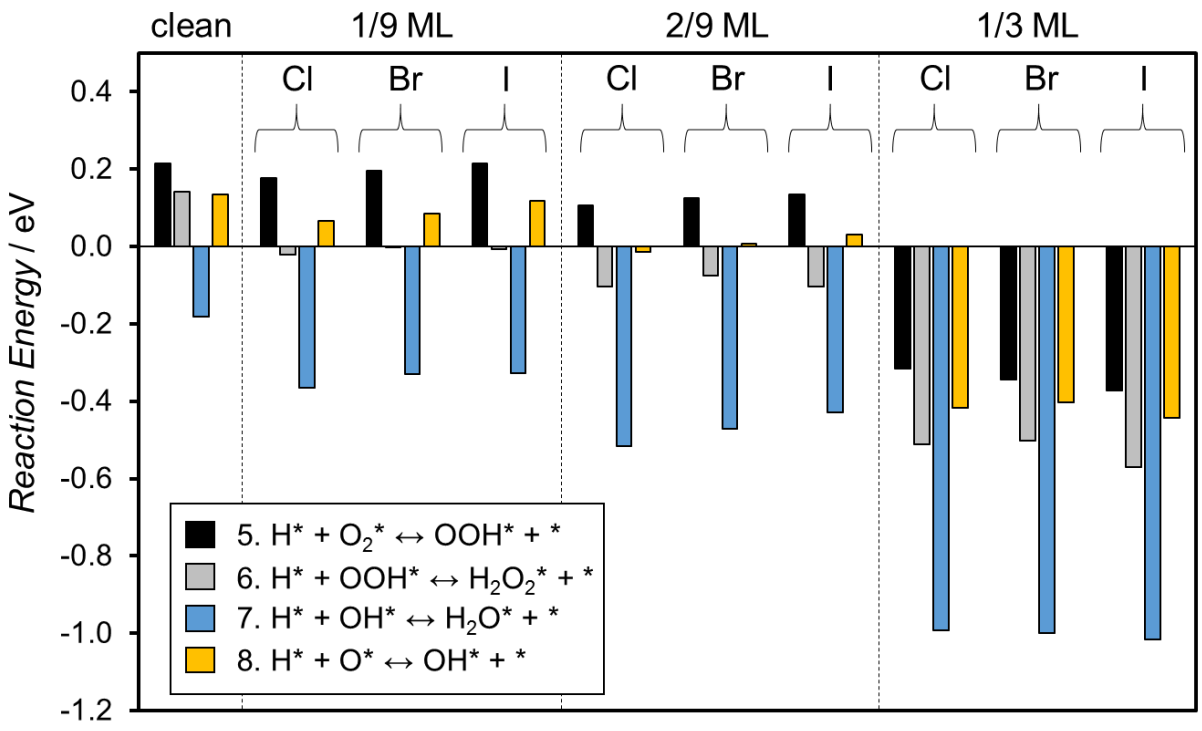

Figure 5.5 Reaction energies for hydrogenations on clean and halogen-covered Pd(111). Energies are reported with respect to infinitely separated reactants and products on the clean or halogen-covered slabs. Data for this figure is tabulated in Table S5.4.

O-O dissociations in O_2*, OOH*, and H_2O_2* are bond-breaking reactions that divert reaction flux away from direct H_2O_2 synthesis. O-O dissociation is also involved in H_2O_2 decomposition to H_2O. Reaction exothermicity decreases monotonically with increasing halogen coverage (Figure 5.6). All O-O dissociation reactions remain considerably exothermic, and thus recombination of the O* and OH* fragments as a pathway to form H_2O_2* is unlikely even on 1/3 ML halogen-covered Pd(111). This is in agreement with isotopic DSHP experiments using a mixture of $^{16}O_2$ and $^{18}O_2$ over a Pd/SiO_2 catalyst in 1 M HCl, in which all H_2O_2 formed from non-dissociated O_2 (no formation of $H_2{}^{16}O^{18}O$).[61]

H_2* dissociation is another bond-breaking reaction that is essential for high catalytic turnover. The reaction energy for H_2* dissociation does not vary significantly in the presence of halogens and remains exothermic over all halogen coverages considered (Figure 5.6).

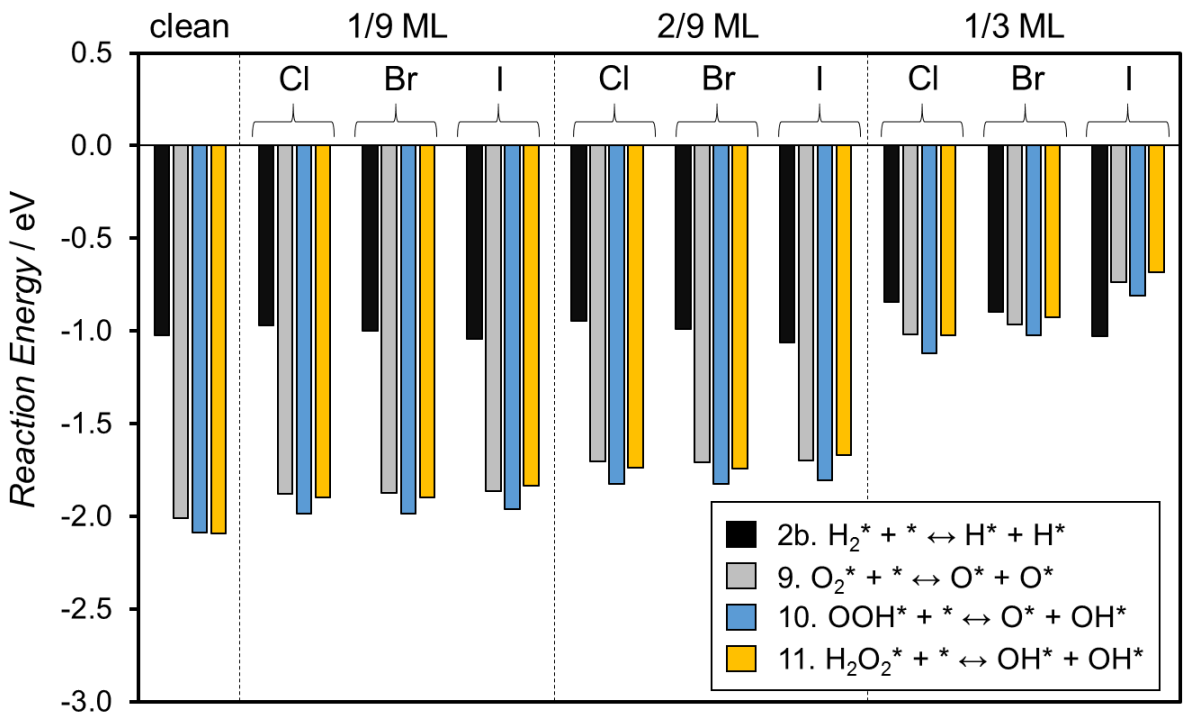

Figure 5.6 Reaction energies for O-O and H-H bond dissociations on clean and halogen-covered Pd(111). Energies are reported with respect to infinitely separated reactants and products on the clean or halogen-covered slabs. Data for this figure is tabulated in Table S5.4.

The final class of surface reaction, bond-transfer (Figure 5.7), does not explicitly involve Pd atoms in the bond breaking/forming event. Rather, the Pd surface acts as a two-dimensional template for the hydrogen-transfer between reactants. Our previous DFT calculations demonstrate that the transfer of a hydrogen atom between O/OH-containing intermediates proceeds nearly spontaneously in the exothermic direction on both the clean Pd(111) and Pd(100) surfaces, and microkinetic modeling results also suggested that these hydrogen-transfer reactions are key flux-carrying steps for the decomposition of H_2O_2 to O_2 and H_2O on Pd (Chapter 4). Figure 5.7 shows that the reaction energies for all hydrogen transfer steps are less sensitive to the presence of co-adsorbed halogens compared with reaction energies for the bond-forming and bond-breaking steps. All deviations from the clean-surface values are within 0.3 eV, and most hydrogen transfer reactions that are exothermic (endothermic) on clean Pd(111) remain exothermic (endothermic) on halogen-covered Pd(111). Bond-forming and bond-breaking reactions discussed above

generally exhibit much larger deviations from the clean surface reaction energies in the presence of halogens (as large as 1.4 eV).

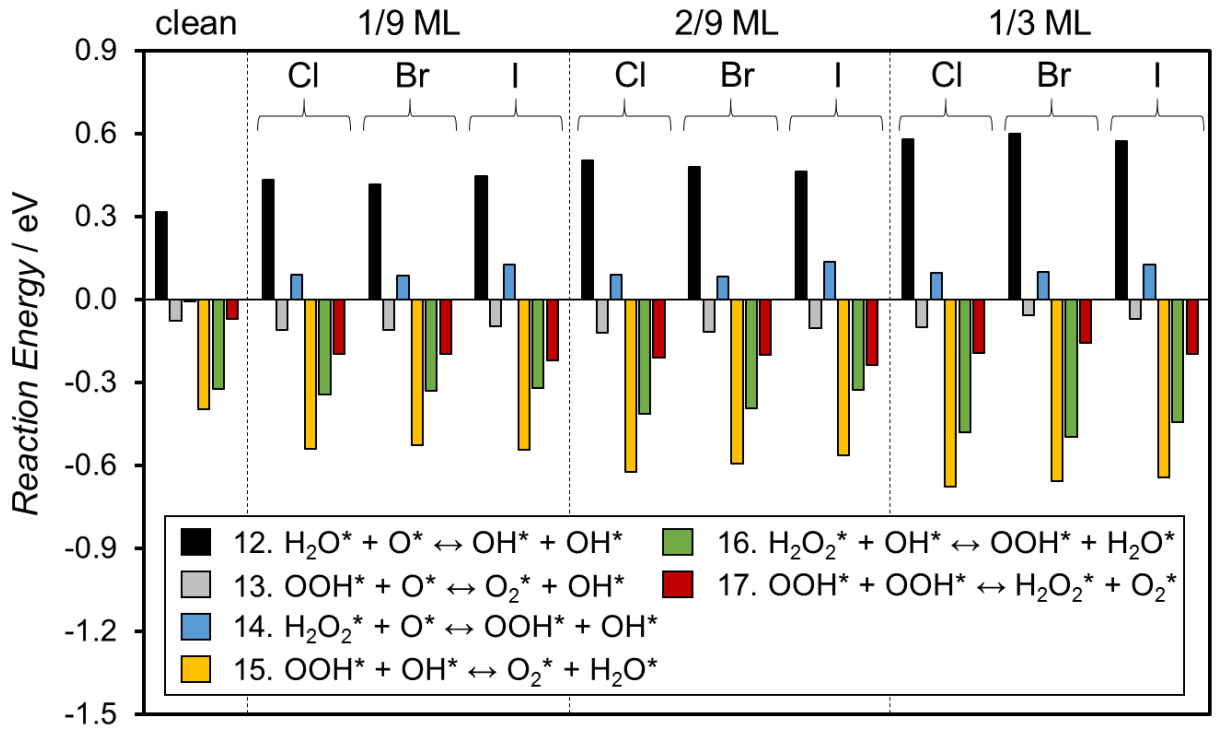

Figure 5.7 Reaction energies for hydrogen transfers on clean and halogen-covered Pd(111). Energies are reported with respect to infinitely separated reactants and products on the clean or halogen-covered slabs. Data for this figure is tabulated in Table S5.4.

5.3.2.3 Activation energy barriers for O-O and H-H bond dissociation

So far we have only discussed the thermochemistry of H_2O_2 synthesis and decomposition mechanisms in the presence of halogens. Rather than quantify all activation energy barriers, we focus on a subset crucial to the selective synthesis – and preservation – of H_2O_2: the O-O bond dissociations. Wilson and Flaherty recently concluded that these steps are kinetically relevant to direct H_2O formation over supported Pd catalysts through an experimentally-consistent kinetic model,[58] and we also find these steps to be kinetically relevant to H_2O_2 decomposition in Chapter 4. The halogens reduce the thermodynamic favorability of O-O dissociations (Figure 5.6), yet all these steps remain significantly exothermic even at 1/3 ML of halogen coverage. We can then

consider that another potential role of co-adsorbed halogens is to kinetically hinder these steps (by destabilizing transition states) on Pd(111), as has been suggested in the experimental literature.[26] Although it is desirable for the halogens to render the Pd surface inactive toward O-O bond dissociation reactions, the Pd surface must not be so passive as to be unable to dissociate H_2 such that catalyst activity suffers. Therefore, we also calculate the activation energy barriers for H_2 dissociation on halogen-covered Pd(111).

The activation energy barriers for O-O and H-H dissociation reactions are presented in Table 5.3, with the corresponding transition state geometries in Figure S5.4, for clean Pd(111) and Pd(111) covered with 1/3 ML of Cl*, Br*, and I*. The transition state for O_2* dissociation on the clean surface occurs over an hcp site with the O atoms positioned on neighboring bridge sites. We identify an analogous transition state structure on halogen-covered Pd(111), and the halogen adlayer configurations are also similar at this transition state. The activation energy barrier increases from 0.56 eV on clean Pd(111) to 0.89, 0.90, and 0.97 eV on 1/3 ML Cl*-, Br*-, and I*-covered Pd(111), respectively.

Table 5.3 Activation energy barriers (eV) for O-O and H-H bond dissociation steps on clean and 1/3 ML halogen-covered Pd(111). Step numbers are in reference to Scheme 5.1.

#	Reaction	clean Pd(111)	1/3 ML halogen-covered Pd(111)		
			Cl	Br	I
2b.	H_2* + * ↔ H* + H*	0.04[a]	0.04[a]	0.03[a]	0.01[a]
9.	O_2* + * ↔ O* + O*	0.56	0.89	0.90	0.97
10.	OOH* + * ↔ O* + OH*	0.00[a]	0.44	0.44	0.30
11.	H_2O_2* + * ↔ OH* + OH*	0.24	0.20[a]	0.17[a]	0.25[a]

[a]transition state structure could not be verified within the precision of our calculations (i.e. no single imaginary frequency is identified along the reaction coordinate). The reported barrier is calculated using the highest energy image in the converged CI-NEB calculation.

OOH* is very unstable on clean Pd(111), and its decomposition to O* and OH* proceeds spontaneously over an fcc site. We calculate significant – but still accessible under typical DSHP conditions[19] – activation barriers of 0.44, 0.44, and 0.30 eV for this step on the 1/3 ML Cl*-, Br*-,

and I*-covered Pd(111) surfaces, respectively. The transition state structure on Cl*-covered Pd(111) resembles that on the clean Pd(111) surface, while the O-O dissociation takes place over a bridge site on Br*- and I*-covered Pd(111). For the latter pathways, the final state structure of the NEB calculation contains O* bound to both a Pd top site and a Br* or I* atom, and OH* is bound to a Pd top site (Figure S5.5). This pathway is also available on Cl*-covered Pd(111), but its transition state energy is higher than that for the pathway involving OOH* decomposition over the fcc site.

Interestingly, at the level of our calculations Pd(111) retains its ability to decompose H_2O_2* into two OH* even on the halogen covered surfaces; all activation energy barriers are ca. 0.2 eV despite a large reduction in the reaction exothermicity induced by 1/3 ML of halogens (Figure 5.6). The transition state geometries are nearly identical on the halogen-covered surfaces, with the O-O dissociation occurring over a bridge site and the two OH groups over neighboring top sites.

The dissociation of H_2 supplies hydrogen for steps 5-8 of Scheme 5.1. H_2 dissociation can occur through multiple pathways on Pd(111): dissociative H_2 adsorption (step 2 of Scheme 5.1) or a molecular H_2* precursor (steps 2a-b of Scheme 5.1).[146] Both of these pathways are nearly spontaneous on the clean surface. We are not able to identify dissociative adsorption pathways on 1/3 ML halogen-covered Pd(111); all pathways proceed through the molecular H_2* precursor, which requires a Pd top site for adsorption. However, the dissociation of H_2* from this precursor state is nearly spontaneous on the halogen-covered surface as on clean Pd(111).

The calculations in this section demonstrate that the intrinsic activation energy barriers for H_2* and H_2O_2* dissociations on Pd(111) are virtually unaffected by the presence of 1/3 ML of Cl*, Br*, or I*, while these adsorbed halogens can kinetically inhibit O_2* and OOH* dissociations.

5.3.2.4 Direct participation of halogens

Adsorbed halogens not only modify the energetics of surface reactions through adsorbate-adsorbate interactions as reported above, but they can also potentially participate in elementary steps. Similar to the hydrogen transfer steps between O/OH-containing intermediates shown in Scheme 5.1, adsorbed halogens may act as hydrogen acceptors and donors. We analyze these elementary steps at 1/9 ML halogen coverage. Figure 5.8 shows the reaction energies for the transfer of a hydrogen atom to a halogen – plotted against the experimentally measured gas-phase proton affinities of the corresponding halides.[248] We first observe that hydrogen transfer from any OH-containing intermediate (or H*) to Cl*, Br*, or I* is highly endothermic (> 1 eV), and so hydrogen transfer to form HCl*, HBr*, or HI* is unlikely at low halogen coverage (these hydrogen halides remain dissociated on Pd(111)). Conversely, the reaction energies for hydrogen transfer to F* range from -0.25 eV when the hydrogen comes from OOH* to 0.14 eV when the hydrogen comes from H_2O*, suggesting that F* can facilitate hydrogen transfer between intermediates. There is an approximately linear correlation between these reaction energies and the experimental gas-phase proton affinities of the corresponding halide species, and the magnitude of the slope is slightly less than unity (ca. 0.8). That is, the halides' relative propensities for hydrogen in the gas phase are only slightly dampened by their adsorption on Pd(111).

O* and OH* fragments can also potentially oxidize adsorbed halogens to XO* or XOH*, where X = F, Br, Cl, or I. The surface reactions to form these species are highly endothermic at 1/9 ML halogen surface coverage. Formation of IOH* from I* and OH* is least endothermic with a reaction energy of 1.17 eV. All other oxidations of the halogens by O* or OH* are endothermic by more than 1.5 eV. The oxidation of adsorbed halogens is likely irrelevant at low halogen

coverage; however, we note that we find evidence for these species during the NEB calculations at 1/3 ML halogen coverage as described in the previous section.

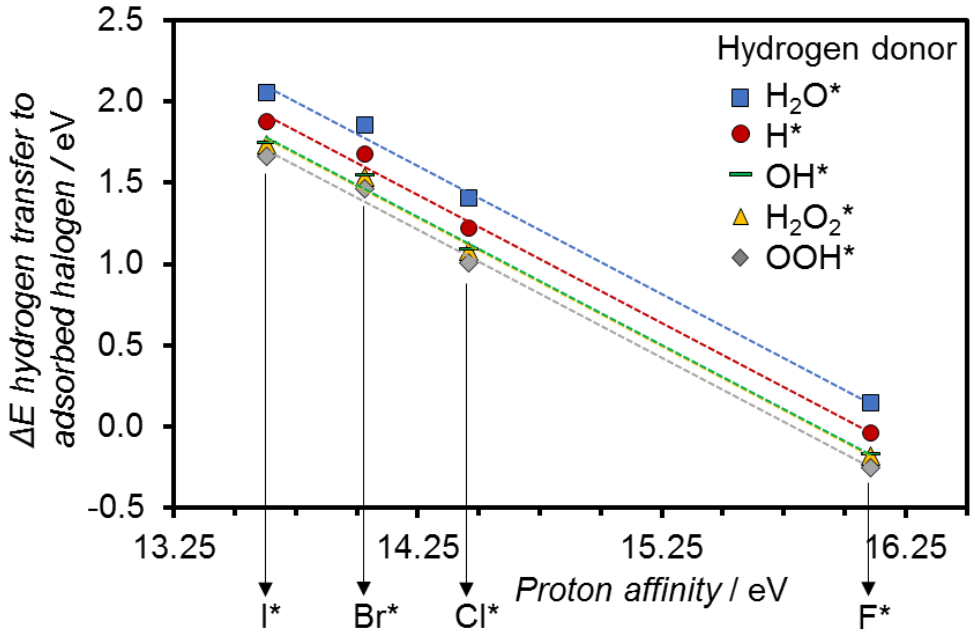

Figure 5.8 Surface reaction energies for hydrogen transfer from DSHP reaction intermediates to adsorbed halogens on clean Pd(111) at 1/9 ML halogen coverage (e.g., ΔE = 2.06 eV for the reaction $H_2O^* + I^* \leftrightarrow OH^* + HI^*$), plotted as a function of the experimental proton affinity of the corresponding gas-phase halide.[248] The slope for all trend lines (dotted lines) is -0.79.

5.4 Discussion

5.4.1 Anticipated effects on activity and selectivity

Consolidation of the results yields three major features of halogen-covered Pd(111) – in addition to the concomitant decrease in the number of available Pd sites due to adsorbed halogens – that are expected to translate into experimentally observable changes to catalytic activity and selectivity in the DSHP.

5.4.1.1 Hindered uptake of reactants and re-adsorption of products

Sufficient coverage of Cl*, Br*, or I* (1/3 ML with respect to the (3 × 3) Pd(111) unit cell used in this chapter) inhibits the adsorption and dissociation of reactants. Figure 5.9 shows the

potential energy surfaces (PESs) for H_2, O_2, and H_2O_2 adsorption and dissociation on clean and 1/3 ML halogen-covered Pd(111). The transition state for O_2* dissociation on clean Pd(111) is lower in energy than the desorbed state of O_2(g), but on 1/3 ML halogen-covered Pd(111) the transition state exceeds the desorbed O_2(g) state by over 0.6 eV (due to contributions from both the halogen-induced destabilization of O_2* and increase in O-O activation energy barrier). This indicates that direct H_2O formation on halogen-covered Pd(111) is unlikely to proceed through O-O bond dissociation in O_2*.

The potential energy surface for H_2 adsorption and dissociation also exhibits an increase in the transition state energy for H-H dissociation relative to H_2(g), despite no major change to the intrinsic activation barrier for dissociation of the molecular precursor H_2* in the presence of halogens (Figure 5.9B). Our calculated increase in the transition state energy for H_2 dissociation on halogen-covered Pd(111) could indicate this step becoming kinetically limiting when halides sufficiently cover the catalyst surface.

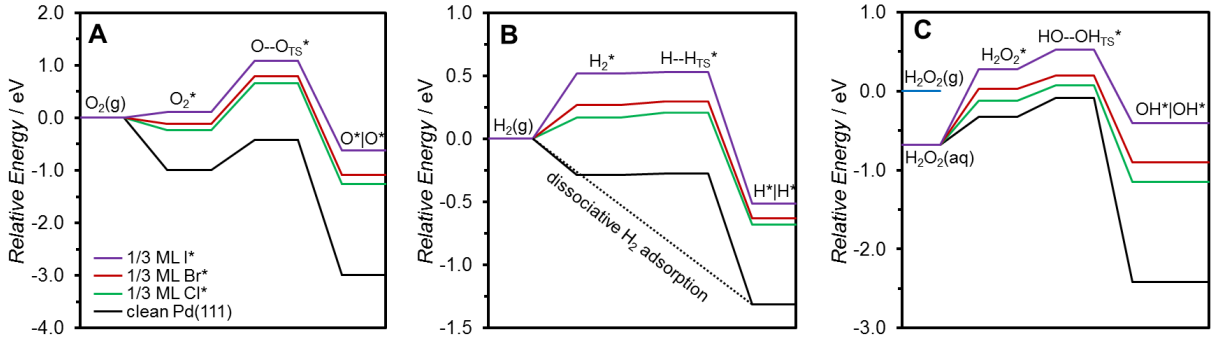

Figure 5.9 Potential energy surfaces for adsorption and dissociation of (A) O_2, (B) H_2, and (C) H_2O_2 on clean and 1/3 ML halogen-covered Pd(111). The reference state is the gas-phase molecule infinitely separated from the surface. The dotted black line in (B) represents the dissociative adsorption of H_2(g) on clean Pd(111), which is nearly spontaneous; all H_2(g) dissociation pathways on 1/3 ML halogen-covered Pd(111) are found to proceed through the H_2* molecular precursor. "(g)" denotes a gas-phase species; "|" denotes infinite separation of the species on the surface; "TS" denotes a transition state; and "(aq)" denotes an aqueous-phase species [the energy for H_2O_2(aq) with respect to the DFT-gas phase energy for H_2O_2(g) is approximated using an experimental Henry's Law coefficient[210]]. The x-axis is the reaction coordinate.

The destabilization of H_2O_2* on halogen-covered Pd(111) has consequences for both the selective direct synthesis and subsequent decomposition of H_2O_2. The dissolution enthalpy of H_2O_2 in H_2O is derived from an experimental Henry's Law constant[210] and is included in the potential energy surface (Figure 5.9C) to approximate the energy of H_2O_2(aq), because this state represents the thermodynamic reservoir for H_2O_2 in aqueous DSHP systems. Desorption of H_2O_2* with respect to its dissociation to two OH* on halogen-covered Pd(111) increases in favorability in the order Cl* < Br* < I*. In fact, on 1/3 ML I*-covered Pd(111) the dissociated state of two OH* is higher in energy than the desorbed state of H_2O_2(aq). Direct H_2O formation through H_2O_2* as an intermediate is consequently less favorable on halogen-covered Pd(111) compared with the clean surface. Qualitatively similar results have been calculated using a Pt cluster model with co-adsorbed Cl* in the context of the electrochemical oxygen reduction reaction.[249]

In connection to the H_2O_2 re-adsorption and decomposition reactions, if we assume a similar mechanism to the one we proposed in Chapter 4, then the O-O dissociation step in H_2O_2* is the most kinetically significant step for H_2O_2 decomposition in the absence of co-fed H_2. Our microkinetic model further suggested that the apparent activation barrier can be well-approximated by the relative energy of the transition state for O-O bond dissociation in H_2O_2* with respect to the state of H_2O_2(aq) (Figure S4.1). Therefore, we anticipate that the apparent activation energy barrier for H_2O_2(aq) decomposition measured on a halogen-covered Pd catalyst will increase in the order Cl* < Br* < I* at a fixed halogen coverage (despite no significant change to the intrinsic O-O bond dissociation barrier in H_2O_2*), with the major contribution being from restricted H_2O_2 re-adsorption. A similar function has been proposed for adsorbed anions on Pt[249] and Au[250] catalysts for the electrocatalytic oxidation and reduction of H_2O_2. The remaining mechanism to close the catalytic cycle once H_2O_2 dissociates to OH* will likely be similar to the one that we

described in Chapter 4 because it involves only the thermodynamically driven hydrogen transfer steps – and the corresponding reaction energies are relatively insensitive to the presence of co-adsorbed halogens (Figure 5.7).

5.4.1.2 Increased favorability of hydrogenation with respect to O-O bond dissociation

A second consequence of Cl*, Br*, or I* coverage on Pd(111) is increased favorability of hydrogenation reactions with respect to O-O bond dissociation, suggesting improved selectivity toward direct H_2O_2 formation on halogen-modified Pd(111). This manifests itself both in the increasingly competitive thermochemistry for hydrogenations of O_2* and OOH* versus their decompositions to O* and OH* (Figure 5.10) and larger activation barriers for O-O bond dissociations (Table 5.3). Direct H_2O formation through O-O bond dissociation is expected to dominate at low halogen coverage (< 1/3 ML with respect to our surface model), particularly through the decomposition of the OOH* intermediate.

Importantly, in this chapter we did not calculate the effect of halogens on activation energy barriers for the hydrogenation reactions that compete with the O-O bond dissociations. This information is critical to the prediction of selectivity toward H_2O_2 versus H_2O. However, as we discussed in the Chapter 1, there is a growing body of literature proposing direct solvent participation in these hydrogenation steps when the DSHP is performed in the liquid phase; a comprehensive theoretical assessment of the mechanistic details for O_2* and OOH* hydrogenations will provide a strong supplement to the DSHP literature. Our calculations in this thesis have considered only the direct reaction between H* and oxygenated intermediates at the gas-solid interface (Chapter 3).

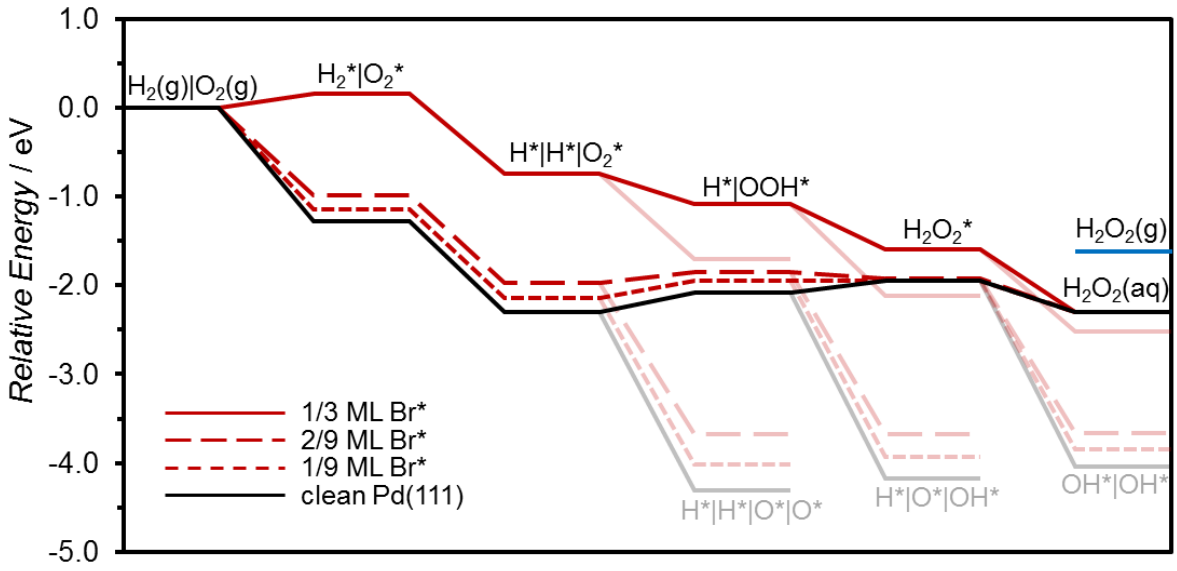

Figure 5.10 Potential energy surface for direct H_2O_2 formation on clean and 1/9, 2/9, and 1/3 ML Br*-covered Pd(111) (thermochemistry only, analogous plots for Cl*- and I*-covered Pd(111) are in Figures S5.6 and S5.7). The reference state is gas-phase H_2 and O_2 infinitely separated from the surface. The faded pathways represent the O-O bond dissociation steps that form O* and OH* and lead to direct H_2O synthesis. The x-axis is the reaction coordinate.

5.4.1.3 Attractive adsorbate-adsorbate interactions (hydrogen-bonding)

Hydrogen bonding interactions between OH-containing intermediates and the adsorbed halogens are weak for Br*, Cl*, and I* (< 0.1 eV stabilization), but significant for F* (ca. 0.1-0.5 eV stabilization). F* is not likely to populate Pd to a significant degree, but even small amounts of F* may affect reactivity due to these strong hydrogen bonds. For example, F* can facilitate the coupling of OH-containing intermediates for the hydrogen transfer reactions (steps 12-17 of Scheme 5.1). F* can also assist in H_2O_2 adsorption, readily abstracting hydrogen from H_2O_2* (and even OOH*) and donating hydrogen to OH* to form H_2O* (Figure 5.8). These functions may help to explain why the rate of H_2O_2* decomposition on supported Pd catalysts can increase when fluoride is added to the reaction medium.[59, 68]

5.4.2 Reactivity trends and scaling on halogen-modified Pd(111)

Experiments demonstrate that there is an optimal halide concentration in the DSHP reaction medium that maximizes H_2O_2 yield, which differs based on the halide employed[170, 203]

(generally, $[I^-] < [Br^-] < [Cl^-]$ at their respective optima). Increasing the halide concentration beyond the optimum continuously decreases catalytic activity (decreased rate of H_2 conversion) and can also reduce selectivity toward H_2O_2. Assuming a single type of active site, these trends suggest a volcano-type relationship[87, 251] between the surface concentration of adsorbed halide and the relative rates of the various reaction pathways. We present a simple analysis of the thermochemistry for the standard direct H_2O_2 formation pathway (sequence of steps from Scheme 5.1: 1, 2, 5, 6, and reverse of reaction 3) to provide further insight into these experimental observations in the context of our DFT calculations on halogen-modified Pd(111).

First we recall the Sabatier principle, which posits that an optimal catalyst binds species with moderate strength such that reactant bonds are readily activated and products are easily released; a straight line from reactants to products would represent this hypothetical behavior on the thermochemical PES for direct H_2O_2 formation (Figure 5.11A). Positive deviations from this straight line (1/3 ML halogen-covered Pd(111)) indicate that binding is too weak, while negative deviations (clean, 1/9, and 2/9 ML halogen-covered Pd(111)) indicate that binding is too strong. Figure 5.11A then shows that a halogen coverage between 2/9 and 1/3 ML modulates binding on Pd(111) to provide the closest approach to this hypothetical optimal PES. Increasing halogen coverage above 1/3 ML may continuously decrease the rate of H_2O_2 decomposition by restricting H_2O_2 re-adsorption (Figure 5.9C), but at the expense of diminishing H_2 and O_2 uptake.

The halogens (at a fixed coverage) generally destabilize intermediates to a greater extent in the order Cl* < Br* < I* (Table 5.2). Therefore we anticipate that a lower coverage of I* compared with that of Br* or Cl* is necessary to upshift the clean Pd(111) PES toward the hypothetical optimal PES. In this context we can rationalize why iodide, which also has the strongest propensity among the halogens to populate Pd(111) (Figure 5.3), can quickly render Pd

inactive toward all DSHP pathways when its solution-phase concentration is increased compared with bromide and chloride.[170]

A more quantitative analysis requires the explicit calculation of all kinetic parameters to best compare the competing reaction pathways. However, the predictive power of such an analysis is limited by the simplified DFT model employed in this work. Improved models should focus primarily on corrections for solvation of surface species and transition states[212] and van der Waals interactions (which may be particularly significant at high surface coverages and affect energetics for Cl*, Br*, and I* to different degrees).[252] Experimental insight into the steady-state surface coverage of halides on Pd catalysts as a function of reaction conditions is ultimately desirable for comparison.

Finally we show that linear scaling relations[253] can well-approximate the binding energies of open-shell intermediates (Figure 5.11B) as a function of the binding energy of O*, which has been suggested as a reactivity descriptor for the DSHP in the computational literature.[55, 56, 133] These scaling relations are developed from the binding energy data in Table 5.2 on clean and Cl*-, Br*-, and I*-covered Pd(111). We note that the halogen coverages considered are relatively dilute with respect to full monolayer coverage, and so the validity of this scaling at higher halogen coverages may be limited. Nonetheless, the existence of linear scaling up to 1/3 ML halogen coverage suggests a constraint on the ability of Cl*, Br*, and I* to modulate thermochemistry on Pd(111). Further development of these scaling relations for transition state energies[254] (Figure S5.8) could potentially be utilized to better analyze competing pathways and approximate the maximum theoretical selectivity toward H_2O_2 when the energetics are strictly constrained to these scaling relations.

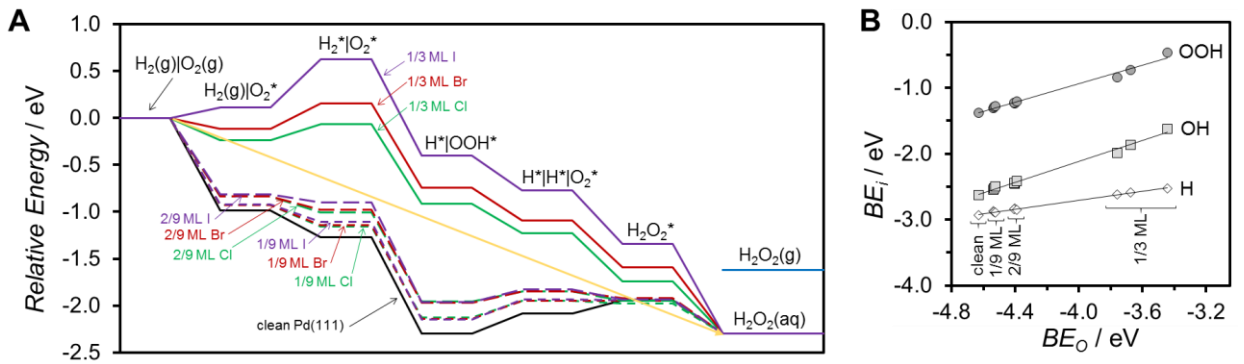

Figure 5.11 (A) Potential energy surfaces (PESs) for the thermochemistry of direct H_2O_2 formation. The DFT-calculated potential energy surfaces for clean and halogen-covered Pd(111) are labeled in the figure [solid lines: 1/3 ML I* (purple), Br* (red), and Cl* (green), and clean Pd(111) (black); dashed lines: 2/9 ML halogen; dotted lines: 1/9 ML halogen]. The hypothetical optimal potential energy surface suggested by the Sabatier principle is a straight line from reactants to products (orange line). "(g)" denotes a gas-phase species; "|" denotes infinite separation of the species on the surface; and "(aq)" denotes an aqueous-phase species (energy for H_2O_2(aq) with respect to the DFT-gas phase energy for H_2O_2(g) is approximated using an experimental Henry's Law coefficient[210]). The x-axis is the reaction coordinate. (B) Linear scaling relations between the binding energy of atomic oxygen (BE_O) and the binding energies of the other open-shell intermediates (BE_i) using the energetics from Table 5.2. The labels below the data points indicate the corresponding halogen coverage. We calculate mean and maximum absolute errors of 0.02 eV and 0.08 eV, respectively, between the linear scaling predictions and all DFT-derived data in (B).

5.5 Conclusions

In this chapter we performed detailed plane-wave DFT calculations to determine the effect of co-adsorbed halogens (F*, Cl*, Br*, and I*) on the energetics for direct H_2O_2 synthesis and decomposition mechanisms on Pd(111). Our results suggest that the primary role of co-adsorbed Cl*, Br*, or I* is to weaken the interaction of Pd with DSHP intermediates, and this is expected to improve selectivity toward direct H_2O_2 formation and limit its subsequent decomposition by: restricting re-adsorption of H_2O_2, decreasing the exothermicity of O-O bond dissociation reactions in O_2* and OOH* with respect to their hydrogenations, and increasing kinetic barriers for O-O bond dissociation in O_2* and OOH*. All of these functions are most effective at higher halogen coverage, but increasing halogen coverage can also limit O_2 and H_2 uptake; this is anticipated to result in an optimal halogen coverage on Pd(111) that sufficiently inhibits H_2O_2 re-adsorption and decomposition but retains activity for direct H_2O_2 formation.

It is desirable to identify a Pd catalyst that can operate effectively in the absence of halide promoters, and these insights may potentially be utilized to identify alternative promoter species (e.g., co-solvents exhibiting strong interactions with the Pd surface[255]) that perform similar functions as adsorbed halogens but would be less detrimental to the operation of a DSHP process. In the next chapter, we evaluate if these conclusions are sensitive to the structure of the Pd substrate.

Supplementary Figures, Tables, and Methods for Chapter 5

Phase diagram formulation

We use an approach similar to that of Gossenberger et al[231] to construct *ab initio* phase diagrams with simplifying, albeit some severe, assumptions. These diagrams are used to evaluate the relative stabilities of the adlayer structures detailed in Figure 5.2. Unlike for the electrochemical system,[231] a solvated halide whose (electro)chemical potential is a function of the electrode potential is not an appropriate reference state. Instead, we first consider an infinite reservoir of the gas-phase hydrogen halide – whose ideal gas chemical potential (μ) is well-defined – to provide the driving force for halide adsorption:

$$\mu_{HX(g)}(P,T) = E_{HX(g)} + \mu_{0,HX(g)}(P_0,T) + k_B \times T \times \ln(P\ P_0^{-1}) \qquad \textbf{[Equation S5.1]}$$

where $\mu_{HX(g)}$ is the ideal gas chemical potential of the hydrogen halide (X = F, Cl, Br, or I) at the specified temperature and pressure, $E_{HX(g)}$ is the total energy (DFT) of the hydrogen halide molecule in the gas phase, $\mu_{0,HX(g)}(P_0,T)$ is the difference in chemical potential of the gaseous hydrogen halide between 0 K and the specified temperature at 1 atm, and k_B is the Boltzmann constant. $\mu_{0,HX(g)}(P_0,T)$ is calculated from the *NIST-JANAF Thermochemical Tables*.[62] The hydrogen halide is assumed to adsorb dissociatively on Pd(111) as in reference # [57], e.g. HBr(g) + 2* ↔ H* + Br*. The grand potential (Ω) for each halogen adlayer is then expressed as:

$$\Omega(P,T) = A^{-1} \times [E_{X/slab} - E_{slab} + N_X \times (E_{H/slab} - E_{slab}) - N_X \times \mu_{HX(g)}(P,T)] \qquad \textbf{[Equation S5.2]}$$

where $E_{X/slab}$ is the total energy the halogens and slab in the unit cell, N_X is the number of halogen atoms in the unit cell, $E_{H/slab}$ is the total energy of atomic hydrogen at 1/9 ML coverage on the clean slab, E_{slab} is the total energy of the clean slab, and A is the surface area of the unit cell.

In our formulation of Equation S5.2, we neglect the following: (i) changes in zero-point energies upon adsorption and the surface entropy of adsorbed halogens, (ii) the aqueous environment of adsorbed species, and (iii) the effect of other co-adsorbed reaction intermediates on the energetics of adsorption.[231] Equation S5.2 also takes a constant value for the binding energy of atomic H*; i.e. the assumption is that there is an infinite reservoir of H* with constant chemical potential, and the halogen-halogen interactions as their surface coverage increases will dominate their phase behavior.

The phase that minimizes $\Omega(P,T)$ at a given temperature and partial pressure of HX(g) is the most stable (Figure 5.3). The final step is to relate the partial pressure of HX(g) to the aqueous-phase concentration that would be in equilibrium with the gas-phase (equivalence of chemical potentials), which is readily implemented using experimental equilibrium expressions.[246] These diagrams allow us to predict which halogen adlayers in Figure 5.2 are the most stable as a function of the aqueous concentration of hydrogen halide and temperature.

Hydrogen halide binding on Pd(111)

Table S5.1 Surface adsorption energies, dissociation energies, and geometric parameters for the hydrogen halides on clean Pd(111). Corresponding images of the adsorbed hydrogen halides are in Figure S5.1

Species	Binding Site	Binding Energy / eV	d_{X-H} / Å			$<_{H-X-surface\ normal}$ / degrees	Dissociation Energy[a] / eV
			adsorbed (DFT)	gas-phase (DFT)	gas-phase (experimental)[62]		
HF	fcc	-0.16	0.958	0.938	0.917	168.8	0.04
HCl	top-top	-0.22	1.464	1.287	1.275	126.0	-1.22
HBr	top	-0.23	1.442	1.432	1.414	80.6	-1.67
HI	fcc	-0.62	1.692	1.625	1.609	73.9	-1.87

[a]HX* + * → H* + X*, where X = F, Cl, Br, or I

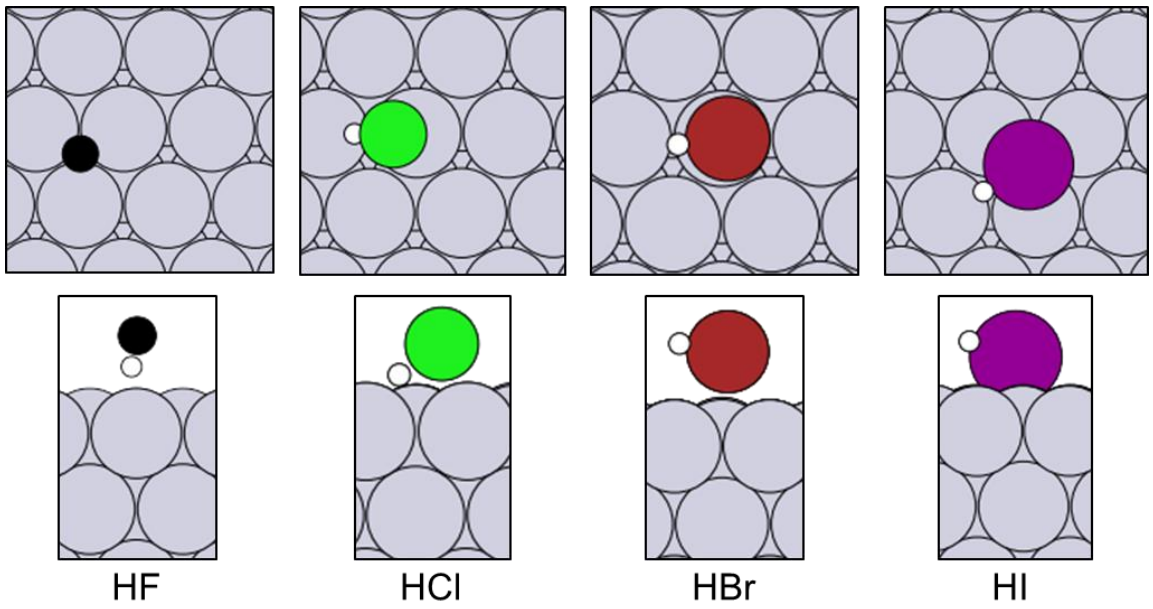

Figure S5.1 Top-down and side views of the preferred binding geometries for the hydrogen halides on clean Pd(111). Atom colors: I (purple), Br (dark red), Cl (green), F (black), H (white), and Pd (gray).

Energy decomposition for co-adsorption of DSHP intermediates with the halogens

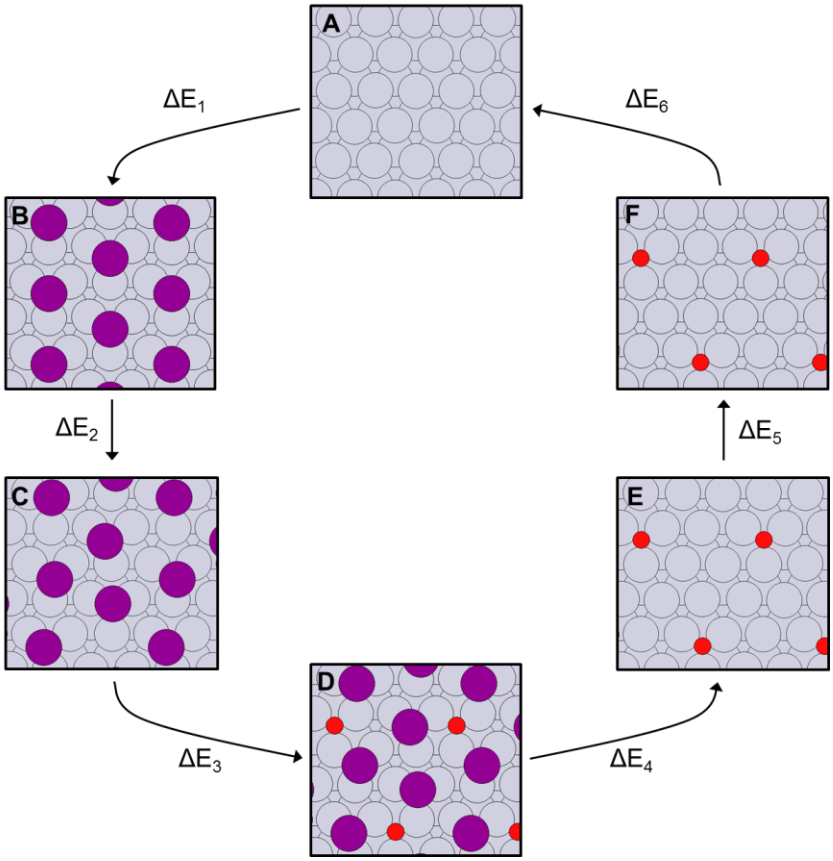

Figure S5.2 Thermodynamic cycle for co-adsorption of DSHP intermediates with the halogens. This example shows the energy cycle for the co-adsorption of O and 3I. Atom colors: I (purple), O (red), and Pd (gray). (A-F) are states with total DFT energies ((3 × 3) surface unit cell) of**:**

A: clean relaxed Pd(111) slab + gas phase energy of O(g) + three times the gas phase energy of I(g)
B: most stable relaxed configuration of three I* (1/3 ML total I* coverage) + gas phase energy of O(g)
C: three I* fixed in their configuration from state **D** + gas phase energy of O(g)
D: most stable relaxed configuration of three I* co-adsorbed with one O*
E: one O* fixed in its configuration from state **D** + three times the gas phase energy of I(g)
F: most stable relaxed configuration of one O* + three times the gas phase energy of I(g)

Based on these definitions:
$\mathbf{-\Delta E_6}$ is the binding energy of O* on clean Pd(111);
$\mathbf{(\Delta E_2 + \Delta E_3)}$ is the binding energy of O* on the 1/3 ML I*-covered slab;
$\mathbf{(\Delta E_2 + \Delta E_3 + \Delta E_6)}$ is the difference between the binding energy of O* on the clean slab and the 1/3 ML I*-covered slab.
The contributions to this difference can be summarized as:
$\mathbf{\Delta E_2}$ is the energy needed to perturb the 1/3 ML I* adlayer from its most stable relaxed configuration to accommodate co-adsorption with O*;
$\mathbf{-\Delta E_5}$ is the energy needed to perturb O* from its most stable relaxed configuration to accommodate co-adsorption with 3I*;
$\mathbf{(\Delta E_3 + \Delta E_5 + \Delta E_6)}$, or equivalently $\mathbf{-(\Delta E_1 + \Delta E_2 + \Delta E_4)}$, is the remaining O*-I* interaction energy that comprises (1) perturbation of Pd's electronic structure, (2) electrostatic (dipole-dipole) interactions, and (3) Pauli repulsion. These values are provided in Tables S5.2 and S5.3 for O* on 1/9 and 1/3 ML halogen-covered Pd(111).

Table S5.2 Contributions to the destabilization of O* induced by co-adsorption with 1/9 ML I*.

Energy[a]	Definition[a]	1/9 ML I
$-\Delta E_6$	BE of O* on clean Pd(111)	-4.58
$\Delta E_2 + \Delta E_3$	BE of O* on halogen-covered Pd(111)	-4.47
$\Delta E_2 + \Delta E_3 + \Delta E_6$	**total destabilization of O***	**0.11**
ΔE_2	contribution from perturbation of halogen adlayer to accommodate O*	0.10
$-\Delta E_5$	contribution from perturbation of O* to accommodate halogen adlayer	0.08
$-(\Delta E_1 + \Delta E_2 + \Delta E_4)$	remaining contribution from O*-halogen interactions	-0.08

[a]see Figure S5.2 and its caption for details

Table S5.3 Contributions to the destabilization of O* induced by co-adsorption with 1/3 ML of Cl*, Br*, and I*.

Energy[a]	Definition[a]	1/3 ML halogen		
		Cl	Br	I
$-\Delta E_6$	BE of O* on clean Pd(111)	-4.58	-4.58	-4.58
$\Delta E_2 + \Delta E_3$	BE of O* on halogen-covered Pd(111)	-3.71	-3.62	-3.40
$\Delta E_2 + \Delta E_3 + \Delta E_6$	**total destabilization of O***	**0.87**	**0.96**	**1.18**
ΔE_2	contribution from perturbation of halogen adlayer to accommodate O*	0.41	0.42	0.45
$-\Delta E_5$	contribution from perturbation of O* to accommodate halogen adlayer	0.07	0.07	0.07
$-(\Delta E_1 + \Delta E_2 + \Delta E_4)$	remaining contribution from O*-halogen interactions	0.39	0.47	0.66

[a]see Figure S5.2 and its caption for details

Binding geometries of $H_2O^{(p)}$ and $H_2O_2^{(p)}$ on 1/3 ML Br*-covered Pd(111)

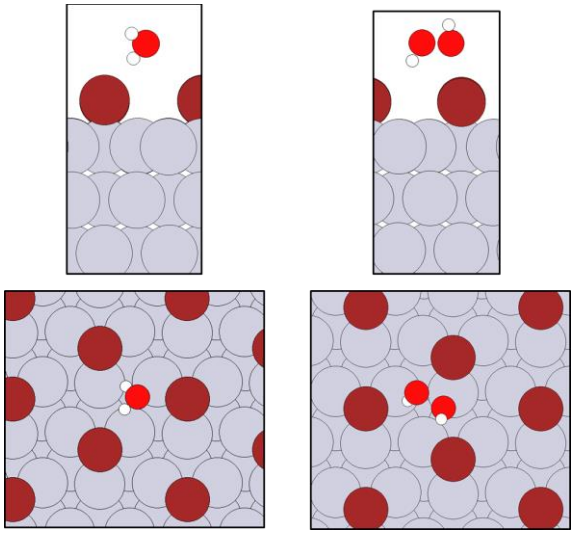

Figure S5.3 Top-down and side views of (left) $H_2O^{(p)}$ and (right) $H_2O_2^{(p)}$ binding geometries on 1/3 ML Br*-covered Pd(111). $H_2O^{(p)}$ and $H_2O_2^{(p)}$ do not disrupt the $(\sqrt{3} \times \sqrt{3})R30°$adlayer, but instead sit above the adlayer and form a (weak) hydrogen bond with an adsorbed bromine atom. The structures of these physisorbed states on 1/3 ML I*-covered Pd(111) are analogous. Atom colors: Br (dark red), O (light red), H (white), and Pd (gray).

Tabulated reaction energies

Table S5.4 Reaction energies on halogen-covered Pd(111) (in eV), corresponding to Figures 5.5 to 5.7. Gray rows (5-8) correspond to bond-making (Figure 5.5), blue rows (2b, 9-11) correspond to bond-breaking (Figure 5.6), and green rows (12-17) correspond to bond-transfer (Figure 5.7), for the reactions as written in the forward direction.

Reaction	clean Pd(111)	1/9 ML halogen/Pd(111)			2/9 ML halogen/Pd(111)			1/3 ML halogen/Pd(111)		
		Cl	Br	I	Cl	Br	I	Cl	Br	I
5. H* + O_2* ↔ OOH* + *	0.21	0.18	0.20	0.21	0.11	0.12	0.14	-0.32	-0.34	-0.37
6. H* + OOH* ↔ H_2O_2* + *	0.14	-0.02	0.00	-0.01	-0.10	-0.08	-0.10	-0.51	-0.50	-0.57
7. H* + OH* ↔ H_2O* + *	-0.18	-0.36	-0.33	-0.33	-0.52	-0.47	-0.43	-0.99	-1.00	-1.02
8. H* + O* ↔ OH* + *	0.13	0.07	0.09	0.12	-0.01	0.01	0.03	-0.42	-0.40	-0.44
2b. H_2* + * ↔ H* + H*	-1.31	-1.20	-1.20	-1.21	-1.23	-1.12	-1.14	-1.15	-0.68	-0.63
9. O_2* + * ↔ O* + O*	-2.01	-1.88	-1.87	-1.86	-1.70	-1.71	-1.70	-1.02	-0.96	-0.74
10. OOH* + * ↔ O* + OH*	-2.09	-1.98	-1.98	-1.96	-1.83	-1.83	-1.80	-1.12	-1.02	-0.81
11. H_2O_2* + * ↔ OH* + OH*	-2.09	-1.90	-1.90	-1.84	-1.74	-1.74	-1.67	-1.02	-0.92	-0.68
12. H_2O* + O* ↔ OH* + OH*	0.32	0.43	0.42	0.45	0.50	0.48	0.46	0.58	0.60	0.57
13. OOH* + O* ↔ O_2* + OH*	-0.08	-0.11	-0.11	-0.10	-0.12	-0.12	-0.10	-0.10	-0.06	-0.07
14. H_2O_2* + O* ↔ OOH* + OH*	-0.01	0.09	0.09	0.12	0.09	0.08	0.13	0.10	0.10	0.13
15. OOH* + OH* ↔ O_2* + H_2O*	-0.40	-0.54	-0.53	-0.54	-0.62	-0.60	-0.57	-0.68	-0.66	-0.64
16. H_2O_2* + OH* ↔ OOH* + H_2O*	-0.32	-0.34	-0.33	-0.32	-0.41	-0.39	-0.33	-0.48	-0.50	-0.45
17. OOH* + OOH* ↔ H_2O_2* + O_2*	-0.07	-0.20	-0.20	-0.22	-0.21	-0.20	-0.24	-0.20	-0.16	-0.20

Transition state geometries for O-O and H-H bond dissociation

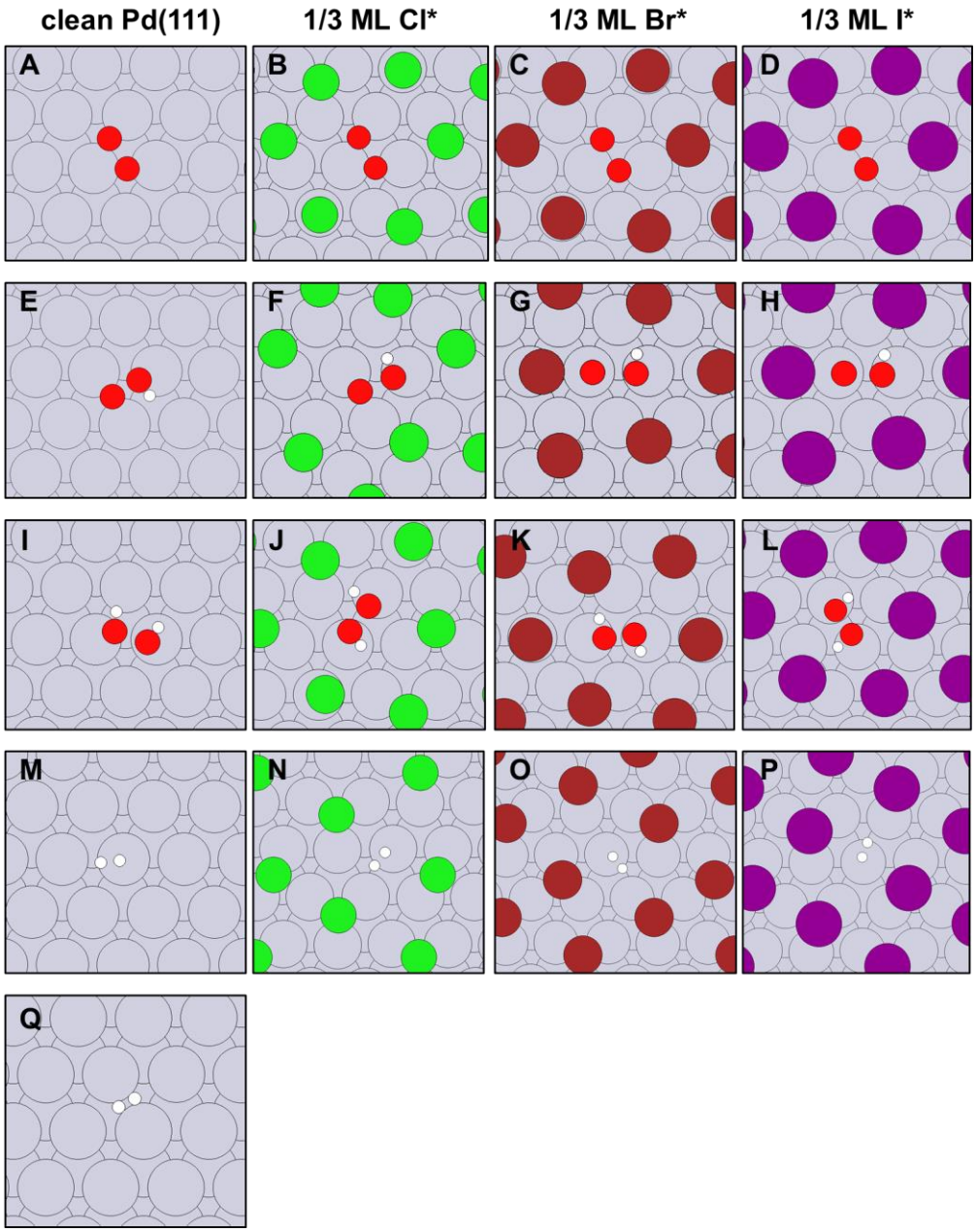

Figure S5.4 Top-down views of the transition state structures for O-O bond dissociation in (A-D) O_2*; (E-H) OOH*; and (I-L) H_2O_2*; and for H-H bond dissociation in (M-P) H_2* on clean and 1/3 ML halogen-covered Pd(111). (Q) is the transition state corresponding to dissociative H_2 adsorption on clean Pd(111) (no molecular H_2* precursor). Note that for the transition state structures in (J-L) and (M-Q), no imaginary frequency is identified along the reaction coordinate within the precision of our calculations; the structure included above represents that of the highest energy image in the converged CI-NEB calculation. OOH* dissociation on clean Pd(111) is spontaneous, and (E) corresponds to the initial state image, which is the highest energy structure in that CI-NEB calculation. Atom colors: I (purple), Br (dark red), Cl (green), O (light red), H (white), and Pd (gray).

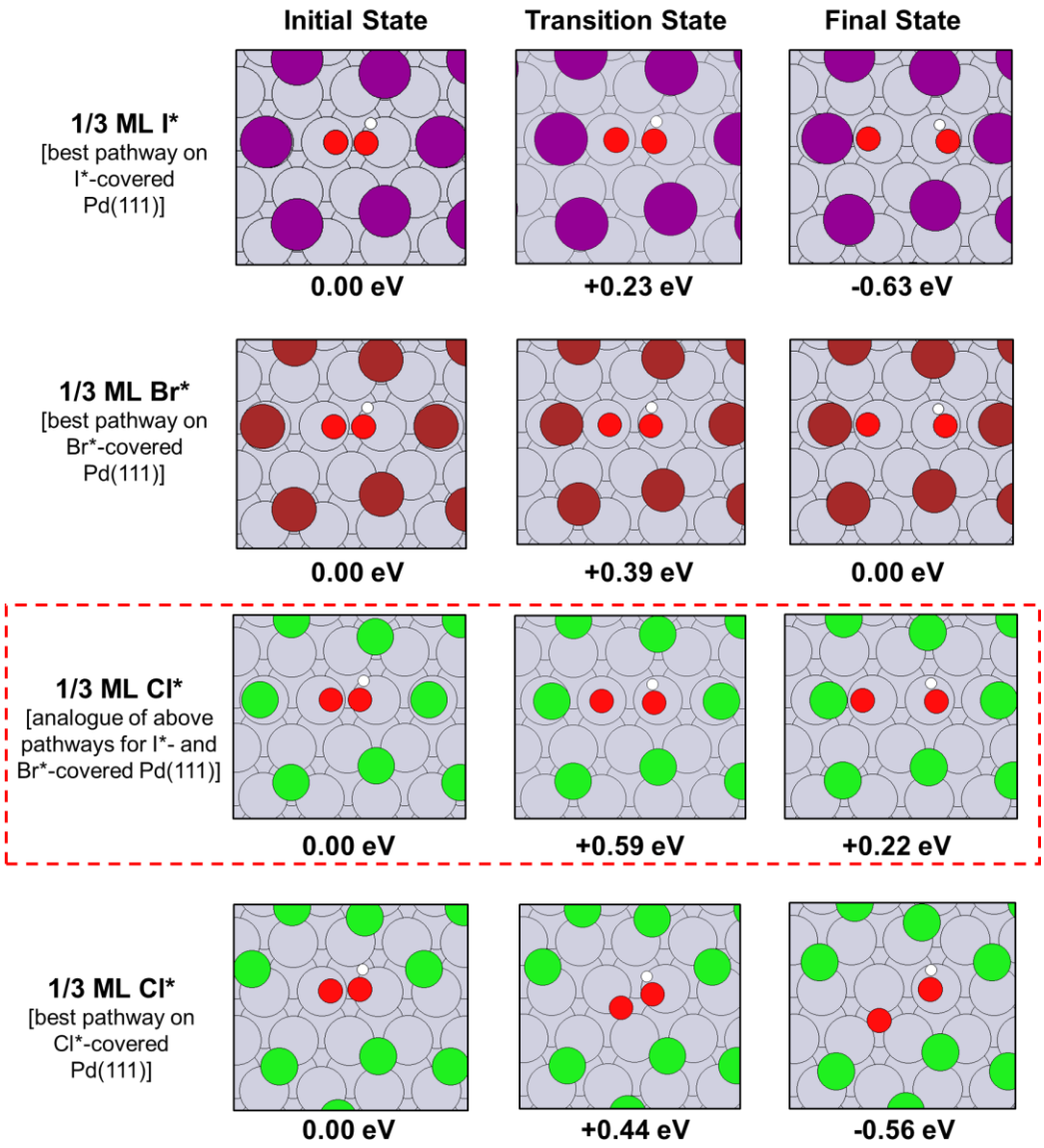

Figure S5.5 Top-down views of the initial, transition, and final states in the minimum energy CI-NEB pathways for O-O dissociation in OOH* on 1/3 ML halogen-covered Pd(111). The initial state for each pathway is taken as the energy reference. On I*- and Br*-covered Pd(111), the final state involves the O* fragment forming a bond with both a Pd atom (at a top site) and a halogen atom. A similar pathway is available on Cl*-covered Pd(111), but this is higher in absolute energy by 0.21 eV at the transition state (dotted red box) compared with the lowest energy OOH* dissociation pathway on 1/3 ML Cl*-covered Pd(111). Values below the images are the energies with respect to the initial state of the CI-NEB pathway. Atom colors: I (purple), Br (dark red), Cl (green), O (light red), H (white), and Pd (gray).

Potential energy surfaces on 1/9, 2/9, and 1/3 ML Cl*- and I*-covered Pd(111)

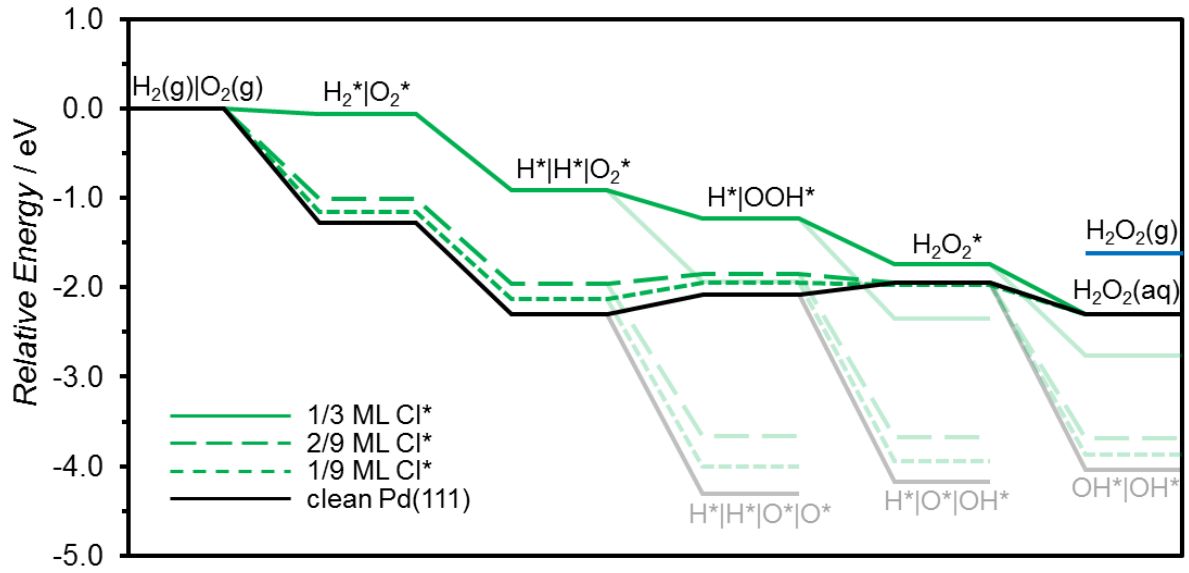

Figure S5.6 Potential energy surface for direct H_2O_2 formation on clean and 1/9, 2/9, and 1/3 ML Cl*-covered Pd(111) (thermochemistry only). The reference state is gas-phase H_2 and O_2 infinitely separated from the surface. The faded pathways represent the O-O bond dissociation steps that form O* and OH* and lead to direct H_2O synthesis. The x-axis is the reaction coordinate.

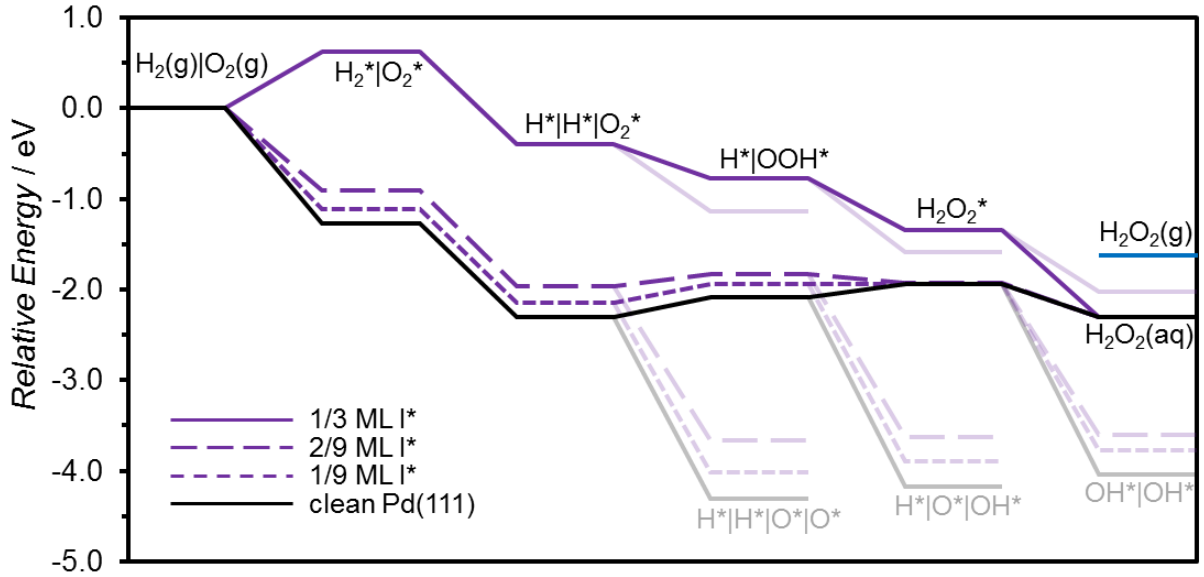

Figure S5.7 Potential energy surface for direct H_2O_2 formation on clean and 1/9, 2/9, and 1/3 ML I*-covered Pd(111) (thermochemistry only). The reference state is gas-phase H_2 and O_2 infinitely separated from the surface. The faded pathways represent the O-O bond dissociation steps that form O* and OH* and lead to direct H_2O synthesis. The x-axis is the reaction coordinate.

Transition state scaling relations for H-H and O-O bond dissociations

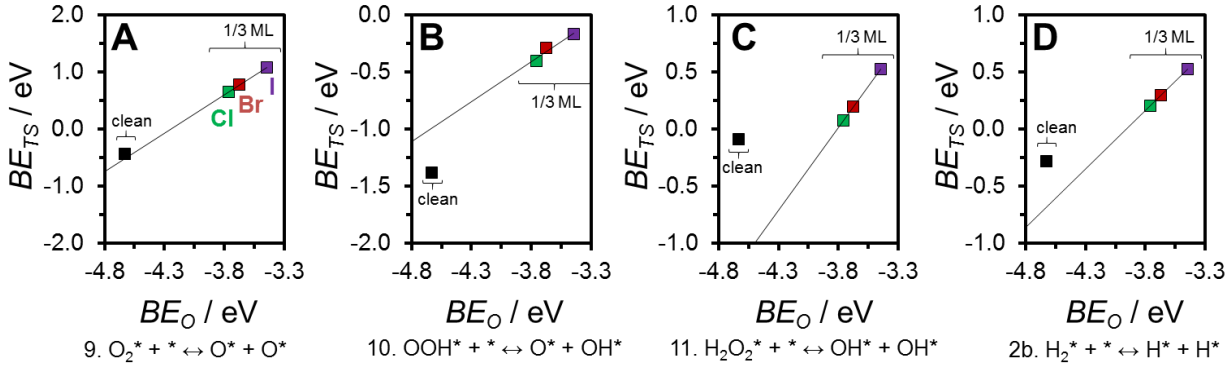

Figure S5.8 Transition state energies (BE_{TS}) plotted against the binding energy of O* for O-O bond dissociations in (A) O_2*, (B) OOH*, and (C) H_2O_2*; and H-H bond dissociation in (D) H_2*. The transition state energy is calculated with respect to the corresponding gas-phase species being dissociated. Step numbers are in reference to Scheme 5.1. Black, green, dark red, and purple points correspond to clean and 1/3 ML Cl*-, Br*-, and I*-covered Pd(111), respectively. The scaling between these transition state energies and the binding energy of O* is approximately linear for the three halogens at 1/3 ML coverage (black line), but the clean surface transition state energy deviates significantly from this trendline for OOH*, H_2O_2*, and H_2* dissociations.

Chapter 6: The Impact of Metal Surface Structure on Halide-Modified Pd Catalysts

6.1 Introduction

In Chapter 5 we used density functional theory calculations to determine how adsorbed halides modify the reactivity of Pd(111), and we discussed why our results may help to explain the experimental observations of increased selectivity toward H_2O_2 and inhibited H_2O_2 decomposition when the appropriate halide concentration is added to the reaction medium. Recent experimental literature also indicates that the reactions involved in the DSHP are structure sensitive, wherein more coordinatively undersaturated Pd features are suggested to be most active for H_2O formation;[58, 224, 256, 257] accordingly, these experiments show that small Pd nanoparticles are less selective toward H_2O_2 than large Pd nanoparticles. The effect of promoters such as halides may also be sensitive to Pd surface structure,[18, 48, 57] and therefore in this chapter we explore how well our analysis from Chapter 5 can be generalized to more coordinatively undersaturated features of Pd.

We have two objectives: first, we desire to elucidate the binding trends of halides on different Pd facets because their relevant surface concentrations may vary substantially with halide identity and the coordinative saturation of the Pd surface atoms. Second, we want to quantify the extent to which the promotional effects identified in Chapter 5 (i.e., decreased exothermicity of O-O bond dissociation, increased kinetic barriers for O-O bond dissociation, and blocked H_2O_2 adsorption at high halide coverage) depend on the coordinative saturation of Pd.

6.2 Computational Methods

The DFT calculations in this chapter were performed using the Vienna *Ab Initio* Simulation Package[137, 226] (VASP) with the generalized gradient approximation (GGA-PW91[109]) to describe the exchange-correlation energy and potential. Electron-ion interactions were described using the projector augmented wave (PAW) potentials,[227, 228] and electron wave functions were expanded using plane waves with an energy cutoff of 400 eV. The Pd(100) slab was represented by a periodically repeated $(2\sqrt{2} \times 2\sqrt{2})R45°$ unit cell with four atomic layers. This unit cell corresponds to a 1/8 monolayer (ML, number of adsorbates per number of surface Pd atoms) surface coverage for a single adsorbate added to the slab. The top two layers were allowed to relax in geometry optimizations, while the bottom two layers were fixed at their bulk lattice positions, where our calculated bulk Pd lattice constant of 3.96 Å is in good agreement with the experimentally determined value of 3.89 Å.[141] The Pd(533) slab was represented by a (1 × 2) unit cell for two atoms along the step edge (and a (1 × 3) unit cell for three atoms along the step edge) with sixteen atomic layers, corresponding to a terrace that is four atoms wide and four atoms deep. Coverage in ML for the Pd(533) slab is defined as the number of adsorbates coordinated to step edge atoms divided by the total number of step edge atoms in the unit cell. Both the Pd(100) and Pd(533) slabs were separated from their periodic images in the z-direction by a vacuum layer of at least 12 Å.

The first Brillouin zone was sampled with a (4 × 4 × 1) Monkhorst-Pack[143] k-point mesh for both the Pd(100) slab and the (1 × 3) Pd(533) slab, and a (4 × 6 × 1) Monkhorst-Pack k-point mesh for the (1 × 2) Pd(533) slab. Results for the Pd(111) slab were taken from Chapter 5, where the calculations were performed using analogous computational parameters and a (3 × 3) unit cell.

The $(2\sqrt{2} \times 2\sqrt{2})R45°$ unit cell for Pd(100), rather than a (3 × 3) unit cell as used for Pd(111), was chosen to enable reproduction of experimentally characterized adlayers for Cl*, Br*, and I* on Pd(100).[235, 242, 243, 258, 259] Furthermore, the total surface area in this Pd(100) unit cell is within 3 % of the total surface area in the (3 × 3) Pd(111) unit cell. This means that for each halogen atom added to the Pd(100) and Pd(111) slab models, the halogen surface coverage per unit surface area is nearly equivalent despite only having eight Pd atoms in the surface of the Pd(100) unit cell and nine Pd atoms in the surface of the Pd(111) unit cell.

Adsorption was modeled by adding adsorbates to one side of the slab, and the electrostatic potential was adjusted accordingly.[139, 140] We note that all DFT calculations in this chapter represent gas-phase calculations, despite the direct synthesis reaction being performed primarily in a liquid solvent and less frequently with all reactants and products in the gas-phase. [As in Chapter 5] although we made no corrections to the DFT-derived energetics to reflect any potential interactions of adsorbed species with a liquid solvent, we believe that our model should reasonably capture the qualitative behavior induced by changes in halogen surface coverage, halogen identity, and Pd surface structure. We refer to "halogens" in the context of our DFT model and "halides" when referencing experimental results in which halogens were introduced to the reaction medium as the hydrogen halide or halide salts. Binding energies (BE) for reaction intermediates on the clean Pd slabs were calculated according to:

$$BE = E_{adsorbate+slab} - E_{slab} - E_{gas\text{-}phase\ adsorbate},$$

where $E_{adsorbate+slab}$ is the total energy of the metal slab with adsorbate on it, E_{slab} is the total energy of the clean slab, and $E_{gas\text{-}phase\ adsorbate}$ is the total energy of the isolated adsorbate in the gas-phase; and for the halogen-covered slabs:

$$BE = E_{adsorbate+halogens+slab} - E_{halogens+slab} - E_{gas\text{-}phase\ adsorbate},$$

where $E_{adsorbate+halogens+slab}$ is the total energy of the slab with halogens and adsorbate co-adsorbed, and $E_{halogens+slab}$ is the total energy of the slab with halogens adsorbed in their most stable configuration. Only the most stable minimum energy structure for each combination (adsorbate + halogens + slab) is reported in binding energy calculations, which was identified by rigorously permuting all surface species among the available high-symmetry binding sites (e.g., top, bridge, and fourfold hollow sites on Pd(100)) to generate initial configurational guesses; the subsequent geometry optimizations for each configuration were performed until the Hellmann-Feynman forces on atoms were less than 0.02 eV $Å^{-1}$. Referencing the DFT parameters above, the convergence of BEs with respect to increasing k-points or energy cutoff was verified to be within 0.1 eV. We observed no long-range surface reconstructions on Pd(100) or Pd(533) induced by adsorption of halogens or reaction intermediates.

Reaction barriers and minimum energy pathways were determined using the climbing image nudged elastic band (CI-NEB) method[112, 115] with seven interpolated images and a convergence criterion of the forces on all images being below 0.1 eV $Å^{-1}$. All reaction energies and barriers are reported with respect to the intermediates composing the initial and final states at infinite separation from each other with respect to the clean (or halogen-covered) Pd slabs. The transition states were verified by identifying a single imaginary vibrational mode along the reaction coordinate.

6.3 Results and Discussion

We first discuss the adsorption of Cl*, Br*, and I* to various surface features of Pd that are expected to be present on typical supported Pd catalysts. Then, we utilize a Pd(100) model to investigate the impact of Pd surface structure on the thermochemistry for adsorption and reaction of intermediates when halogens are co-adsorbed, comparing to calculations from Chapter 5 on halogen-covered Pd(111). The proposed reaction network is the same as that in Chapter 5 (Scheme 5.1). We construct a potential energy surface (PES) to demonstrate trends in reaction energetics for the direct pathway toward H_2O_2, which comprises the sequential hydrogenation of O_2* followed by H_2O_2* desorption (sequence of elementary steps: 5 → 6 → -3 from Scheme 5.1). We also evaluate the thermochemical trends at the three bifurcation points along the direct pathway toward H_2O_2, which are defined by steps in which the O-O bond dissociates to form O*/OH* fragments, diverting flux toward H_2O (steps 9 to 11 from Scheme 5.1). Finally, we compare kinetic barriers for these selectivity-determining O-O bond dissociation steps on clean and halogen-covered Pd(100) to the corresponding values on Pd(111).

6.3.1 Halogen binding, diffusion, and saturation coverage

The adsorption properties of halogens on Pd can show a significant dependence on Pd surface structure. Isolated Pd nanoparticles that are larger than 3-5 nm are expected to exhibit an abundance of planar facets (primarily, the close-packed (111) facet and more open (100) facet) – in addition to defect sites including corners and edges.[176, 177] Figure 6.1 presents relative binding energies and diffusion barriers on these surface features, where we employ the (533) step edge as a surrogate model for nanoparticle defect sites.

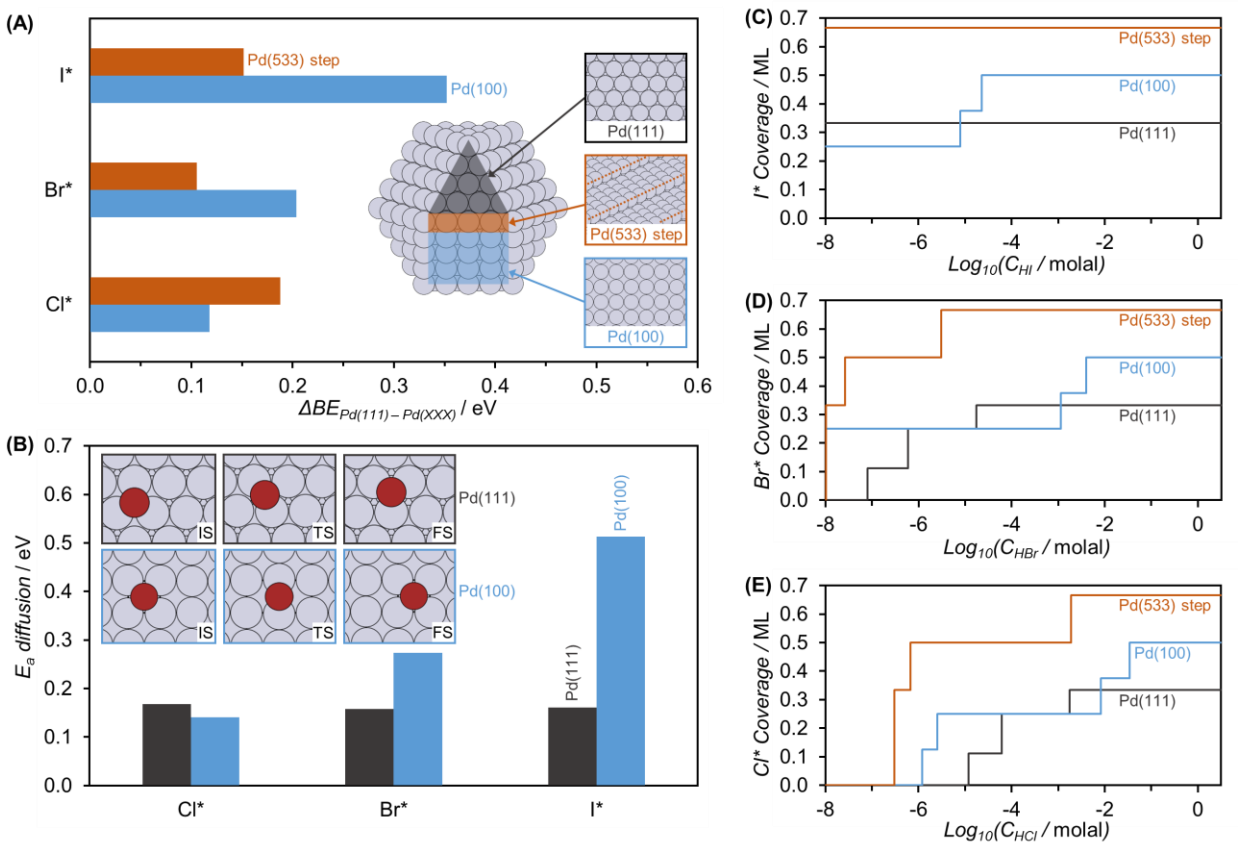

Figure 6.1 (A) The difference in halogen binding energy (*ΔBE*) between its value on Pd(111) and its value on Pd(100) and Pd(533). A positive number represents stronger binding compared with Pd(111). The inset provides a pictorial representation of each surface, and the dotted orange line in the image for Pd(533) denotes the step edge. (B) The surface diffusion activation energy (E_a *diffusion*) for each halogen on Pd(111) and Pd(100). The diffusion pathway on Pd(111) is from a fcc to an adjacent hcp site, and the diffusion pathway on Pd(100) is from a fourfold hollow site to an adjacent fourfold hollow site; both pathways have transition states over a bridge site (insets). Atom colors: halogen (dark red) and Pd (gray). "IS", "TS", and "FS" denote the initial state, transition state, and final state of the surface diffusion NEB pathways. For (A) and (B), the energies are calculated with a single halogen in the unit cell, which corresponds to coverages of 1/9 ML, 1/8 ML, and 1/3 ML for Pd(111), Pd(100), and Pd(533), respectively. (C-E) Halogen coverage on Pd(111), Pd(100), and Pd(533) predicted as a function of the aqueous-phase concentration of the corresponding hydrogen halide at 298 K.

The order of binding preference for Br* and I* on clean Pd surfaces is Pd(111) < Pd(533) step edge < Pd(100), while for Cl* it is Pd(111) < Pd(100) < Pd(533) step edge (Figure 6.1A). Similar to their preference for the threefold fcc site on Pd(111), these halogens also bind most stably to the multifold adsorption site (fourfold hollow) on Pd(100), in agreement with previous DFT calculations.[229] At the (533) step edge, Br* and Cl* adopt a bridge binding configuration that is coordinated to two step edge atoms, while I* prefers the fourfold site along the step edge. The

diffusion properties of the halogens on the planar Pd facets also depend on surface structure (Figure 6.1B). All diffusion barriers on Pd(111) are small (< 0.2 eV) and approximately independent of halogen identity, varying by only ca. 0.01 eV. The diffusion barriers on Pd(100) can be much larger and increase from 0.14 eV to 0.27 eV to 0.51 eV when changing from Cl* to Br* to I*. The strong binding of I* to Pd(100) – which is the strongest among all of these halogens to any of these Pd facets – coupled with I*'s significant diffusion barrier across Pd(100) may suggest both thermochemical and kinetic limitations to displacing I* adatoms from the (100) facet, for example to accommodate reaction intermediates or transition states.

We then examine the stability of higher coverage halogen adlayers. Figure 6.2 contains the average halogen binding energy and preferred structure for the most stable adlayers of Cl*, Br*, and I* up to 5/8 ML on Pd(100). Br* and I* adopt commensurate adlayer structures at these coverages, exclusively occupying the fourfold hollow sites from 1/8 to 1/2 ML, while Cl* starts to adopt bridge binding sites at 3/8 ML coverage. (We note that the most stable Cl* structures we identify at 3/8 and 1/2 ML, where some Cl* occupy bridge sites, appear to differ from those identified in low-energy electron diffraction experiments that show Cl* only occupying fourfold hollow sites.[259] We calculate an energy difference of ca. 0.1 eV between our most stable structures reported here and the structures with all Cl* at fourfold hollow sites.) The average binding energy per halogen atom decreases with increasing halogen coverage in all cases. We perform similar calculations for halogen binding up to 2/3 ML on the Pd(533) step edge and up to 5/9 ML on Pd(111).

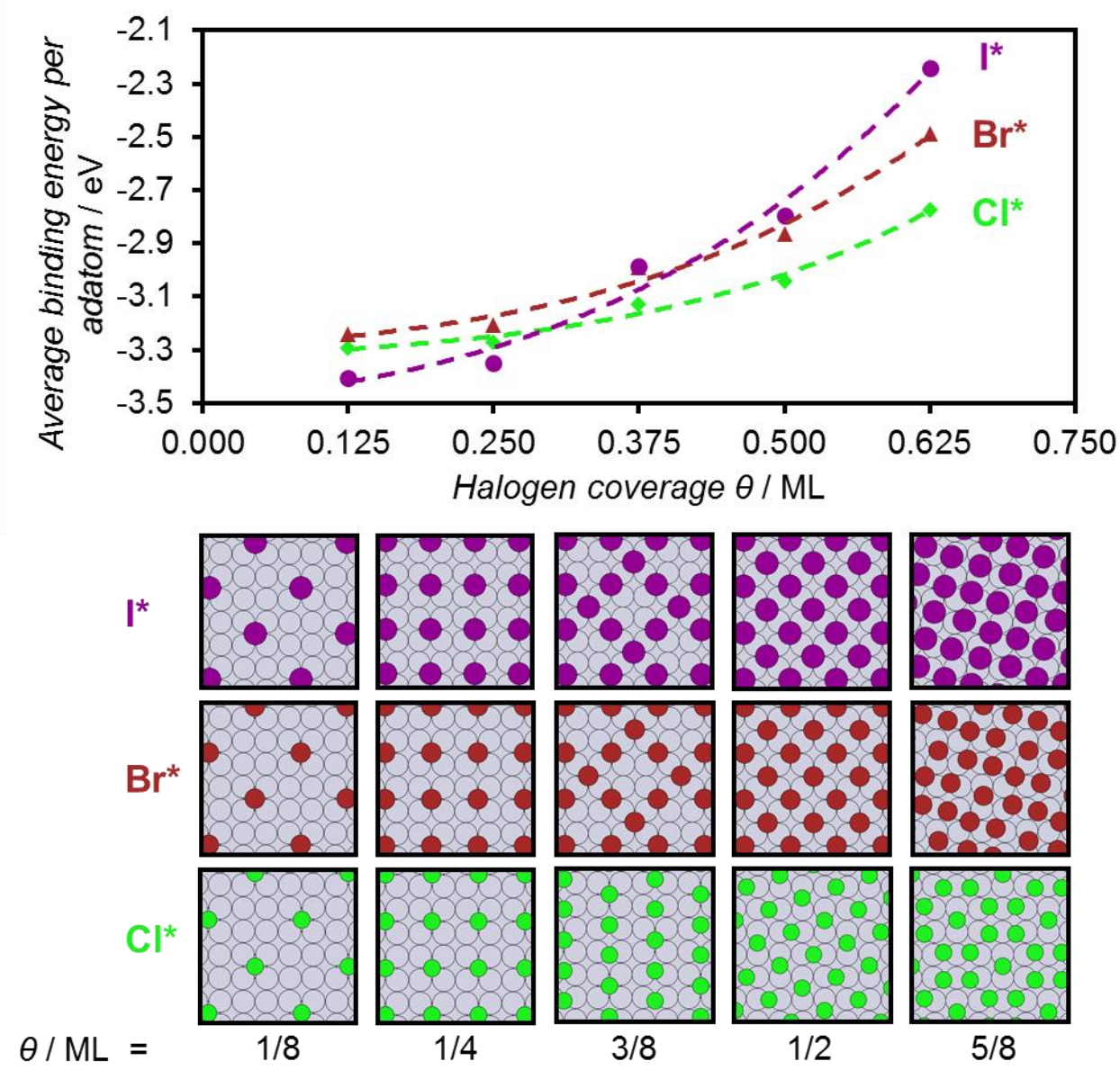

Figure 6.2 Average binding energy per halogen adatom as a function of coverage on Pd(100), with corresponding top-down views of the most stable adlayer structure at each coverage. Dashed lines are to guide the eye. Atom colors: I (purple), Br (dark red), Cl (green), and Pd (gray).

The appreciable differences in halogen binding energies across the Pd facets lead us to anticipate that halogens may populate Pd nanoparticles non-uniformly. We desire to assess qualitative trends in halogen coverage by relating the thermochemical stability of halogen adlayers to experimental conditions, i.e., a liquid-phase direct H_2O_2 synthesis process. We adopt the following procedure for that purpose, with more details provided in Figure S6.1. First, we consider

that halogens are experimentally introduced to the reaction media in a number of forms that primarily include dissolved halide salts[66, 170, 203] and hydrogen halide.[29, 222, 260] Here we choose an aqueous reservoir of the latter to calculate the chemical potential driving force for halogen adsorption on Pd. Next, we need a way to relate this reservoir to our DFT calculations, which are performed in the gas-phase. This is accomplished by defining a second reservoir of gas-phase hydrogen halide that is in equilibrium with the aqueous hydrogen halide reservoir (equivalence of chemical potentials), wherein we use gas-liquid equilibrium relations from the experimental literature.[246] The chemical potential of this second gas-phase reservoir, under the ideal gas assumption, is a well-defined function of temperature and pressure and provides the link to our DFT-calculated gas-phase binding energies of the halogen adlayers. Collectively, this procedure enables the construction of *ab initio* phase diagrams for halogen adsorption onto the different Pd facets as a function of temperature and aqueous hydrogen halide concentration, and the results are summarized in Figure 6.1C-E.

Although we make some approximations (described in Figure S6.1) to build these *ab initio* phase diagrams, we can compare the predicted trends with available experimental data. First, we predict that I* populates Pd the most rapidly, followed by Br* and then Cl*, as a function of increasing aqueous-phase concentration. This is consistent with aqueous-phase experimental measurements on both Pd(111) and Pd(100) electrodes in which the strength of adsorption is inferred to be chloride < bromide < iodide based on the spontaneous displacement of adsorbed chloride by bromide, and adsorbed bromide by iodide.[242] Second, we predict that the 1/4 and 1/2 ML adlayer structures are stable over wide concentration ranges on Pd(100) for all halogens, and the 1/2 ML adlayer structure on Pd(100) and 1/3 ML adlayer structure on Pd(111) are the saturation limits at room temperature up to 1 molal of hydrogen halide (which is significantly higher than the

concentrations of hydrogen halides generally employed for the DSHP in literature and patents); these results are consistent with experimentally characterized halogen saturation coverages on Pd(111) and Pd(100) in gas-phase and aqueous environments.[235, 238-240, 242-244, 258, 259]

The phase diagrams also predict that the Pd(533) step edge tends to saturate more rapidly with halogens than the Pd(111) and Pd(100) planar facets, suggesting that defect sites on Pd nanoparticles might be expected to be the first sites to become blocked under reaction conditions (in agreement with other theoretical literature[57]), while Pd(111) and Pd(100) may remain less obstructed by halogens. We next consider the reactivity of halogen-covered Pd(100) toward reaction intermediates in order to elucidate if the effects of halogen co-adsorption that we previously identified on Pd(111) are structure sensitive.

6.3.2 Co-adsorption of reaction intermediates with halogens on Pd(100)

We first examine the case of the 1/2 ML halogen-covered Pd(100) slab – the saturation limit identified in the previous section. We find that 1/2 ML of Cl*, Br*, or I* effectively passivates Pd(100) toward adsorption of the O_2 reactant (Figure 6.3). The binding energy of O_2* is -1.53 eV on clean Pd(100), much larger than the binding energy of -0.99 eV on clean Pd(111), but the O_2* binding energy is no longer exothermic on 1/2 ML halogen-covered Pd(100). There is large energy penalty required to rearrange the 1/2 ML halogen adlayers to accommodate O_2* adsorption that is not compensated by formation of Pd-O bonds, causing the bound state of O_2* to be less stable than the gas-phase desorbed state of O_2. This energy difference can exceed 1 eV for the case of 1/2 ML I*-covered Pd(100). In addition, the O-O bond length in O_2* shortens by about 4 % on the 1/2 ML halogen-covered slabs compared with its value on clean Pd(100) (Table 5.1). This suggests that the internal O-O bond is stronger – more resistant to direct dissociation – on the halogen-covered slabs with respect to clean Pd(100).

Not only can 1/2 ML of adsorbed halogens restrict O_2 uptake, but it can also prevent re-adsorption of H_2O_2. In Chapter 5, we calculated that 1/3 ML of Br* or I* is sufficient to block H_2O_2* adsorption to Pd atoms on Pd(111), and proposed that this could be a key factor in explaining the experimental observation that halogens retard H_2O_2 decomposition on Pd catalysts. As for O_2*, rearrangement of the 1/2 ML halogen adlayer on Pd(100) is required to accommodate H_2O_2*, and this is evidenced by a substantial increase – about 14 % for I* and Br* adlayers – in the average z-coordinate of the halogen adlayer above the top Pd layer, compared to the most stable 1/2 ML halogen adlayer structure (halogens are displaced from fourfold hollow sites to the less stable bridge and top sites). We note that a physisorption state for H_2O_2, denoted as $H_2O_2^{(p)}$, is available in which H_2O_2 neither binds directly to Pd surface atoms nor disrupts the preferred 1/2 ML halogen adlayer structure, but instead sits above the halogen atoms and forms a hydrogen bond with one adsorbed halogen atom (Figure 6.3). The stabilization of $H_2O_2^{(p)}$ is weak, only about 0.1 eV, with respect to H_2O_2 infinitely separated from 1/2 ML halogen-covered Pd(100). We identified a similar $H_2O_2^{(p)}$ binding state on 1/3 ML halogen-covered Pd(111) in Chapter 5.

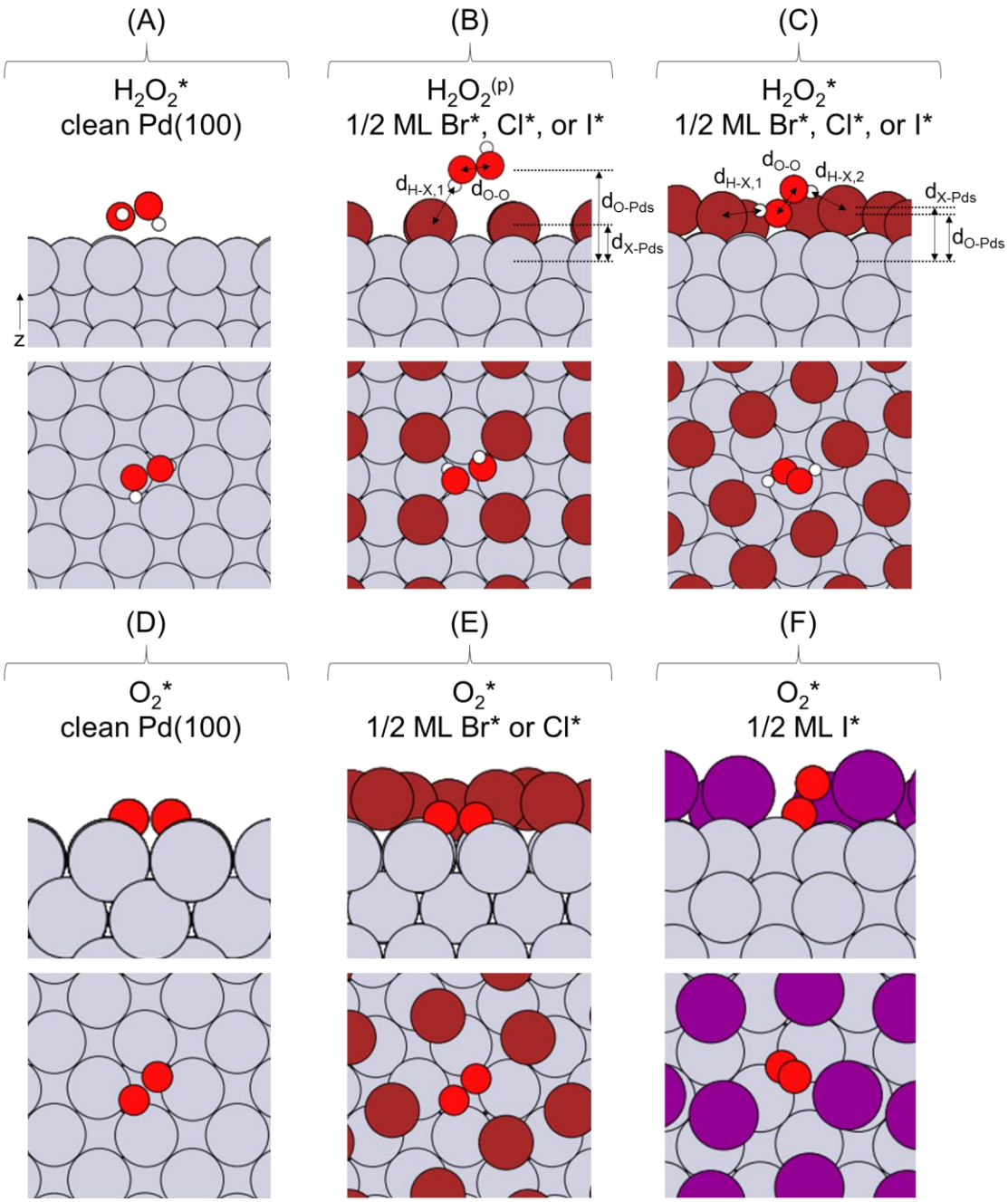

Figure 6.3 Side and top-down views of (A-C) H_2O_2 and (D-F) O_2 adsorption on clean and 1/2 ML halogen-covered Pd(100). Atom colors: I (purple), Br (dark red), H (white), O (light red), and Pd (gray). The two-sided arrows in (B) and (C) define the geometric parameters: $d_{H-X,1}$ and $d_{H-X,2}$ are the distances between hydrogen atoms in H_2O_2 and halogen atoms that participate in hydrogen bonding, d_{O-O} is the intramolecular O-O bond length, d_{X-Pds} is the distance between the average z-coordinate of all halogen atoms and the average z-coordinate of the top layer of Pd atoms, and d_{O-Pds} is the distance between the z-coordinate of the O atom in H_2O_2 closest to the surface and the average z-coordinate of the top layer of Pd atoms. The values for these geometric parameters are provided in Table 6.1. The "*" denotes an adsorbed state in which H_2O_2 (or O_2) binds directly to the Pd surface atom(s), and the "$^{(p)}$" denotes a physisorbed state in which H_2O_2 sits above the halogen atoms (and does not form a bond with Pd), stabilized by a hydrogen bond with an adsorbed halogen. In (B) and (C) only a graphical representation for 1/2 ML of Br* is provided, but the adsorption structure is analogous for the case of 1/2 ML of Cl* or I*.

These calculations suggest that Pd(100) will be inactive toward both H_2O_2 direct synthesis and its subsequent decomposition if the chemical potential of halogens in the reaction medium provides a sufficient driving force to populate Pd acutely with halogens – characterized by at least 1/2 ML of adsorbed halogens based on our model. (We calculate exothermic binding energies for O_2* and H_2O_2* at lower halogen coverages on Pd(100).) On Pd(111), we find that halogen coverages as low as 1/3 ML can be enough to restrict adsorption of reactants. Furthermore, our predictions in Figure 6.1 indicate that I* populates all Pd facets the most rapidly at a given solution-phase concentration of the corresponding hydrogen halide. Collectively these results qualitatively agree with experimental observations wherein iodide can completely deactivate Pd catalysts at significantly lower liquid-phase concentrations compared to bromide and chloride[170].

Table 6.1 Geometric parameters (defined in Figure 6.3) and binding energies for H_2O_2 and O_2 adsorption to 1/2 ML halogen-covered Pd(100). The DFT-calculated O-O bond lengths in gas-phase H_2O_2 and O_2 are 1.47 Å and 1.24 Å, respectively. Positive binding energies result from a greater energy requirement to rearrange the halogen adlayer (to accommodate H_2O_2 or O_2 on the surface) than is compensated by adsorbing H_2O_2 or O_2 to Pd.

Parameter	**clean**	**1/2 ML Cl***		**1/2 ML Br***		**1/2 ML I***	
	H_2O_2*	**$H_2O_2^{(p)}$**	**H_2O_2***	**$H_2O_2^{(p)}$**	**H_2O_2***	**$H_2O_2^{(p)}$**	**H_2O_2***
$d_{H\text{-}X,1}$ / Å	N/A	2.58	2.18	2.64	2.21	2.77	2.55
$d_{H\text{-}X,2}$ / Å	N/A	N/A	1.91	N/A	2.17	N/A	2.47
$d_{O\text{-}O}$ / Å	1.48	1.47	1.46	1.47	1.47	1.47	1.47
$d_{O\text{-}Pds}$ / Å	2.37	4.56	2.24	4.49	2.26	4.37	2.50
$d_{X\text{-}Pds}$ / Å	N/A	1.87	1.94	1.79	2.05	1.90	2.16
BE / eV	-0.35	-0.10	+0.04	-0.10	+0.46	-0.11	+1.30
	O_2*	**O_2***		**O_2***		**O_2***	
$d_{O\text{-}O}$ / Å	1.42	1.36		1.36		1.37	
BE / eV	-1.53	+0.20		+0.58		+1.02	

For the remainder of this study we restrict the halogen coverage on Pd(100) to under 1/2 ML, considering models with 1/8, 1/4, and 3/8 ML of co-adsorbed halogens in the Pd(100) unit cell; these halogen-covered Pd(100) models are compared directly to the 1/9, 2/9, and 1/3 ML halogen-covered Pd(111) models that we previously investigated. Moreover, halogen coverages

that are under 1/2 ML on Pd(100) should be more representative of an active state of halogen-modified Pd(100) wherein reactant adsorption is not completely blocked.

Figure 6.4 provides the binding energies for all intermediates (H*, O*, OH*, OOH*, O_2*, H_2*, H_2O_2*, and H_2O*) as a function of Br* coverage on Pd(111) and Pd(100). The binding energy data for Cl*- and I*-covered Pd(111) and Pd(100) exhibit similar trends, and all binding energies are tabulated in Table S6.1. A single adsorbed halogen in the unit cell does not significantly affect the BEs of other intermediates on both Pd(100) and Pd(111) (differences are < 0.1 eV compared to the clean-surface binding energies, and do not strongly depend on halogen identity). The largest step change in binding energies on Pd(100) occurs when the halogen coverage increases from 1/8 ML to 1/4 ML. 1/4 of co-adsorbed halogens significantly destabilizes all intermediates with the following exceptions: the binding energy of H* on Cl*-, Br*-, and I*-covered Pd(100) remains within 0.1 eV of its clean-surface value; and the binding energies of H_2O* and H_2O_2* can be slightly stabilized on Cl*-covered Pd(100) due to hydrogen-bonding with Cl*. I* generally induces the largest destabilizations in binding energy with respect to the clean-surface values, followed by Br* and then Cl*; the effectiveness of these halogens at weakening binding strengths takes the same order on Pd(111).

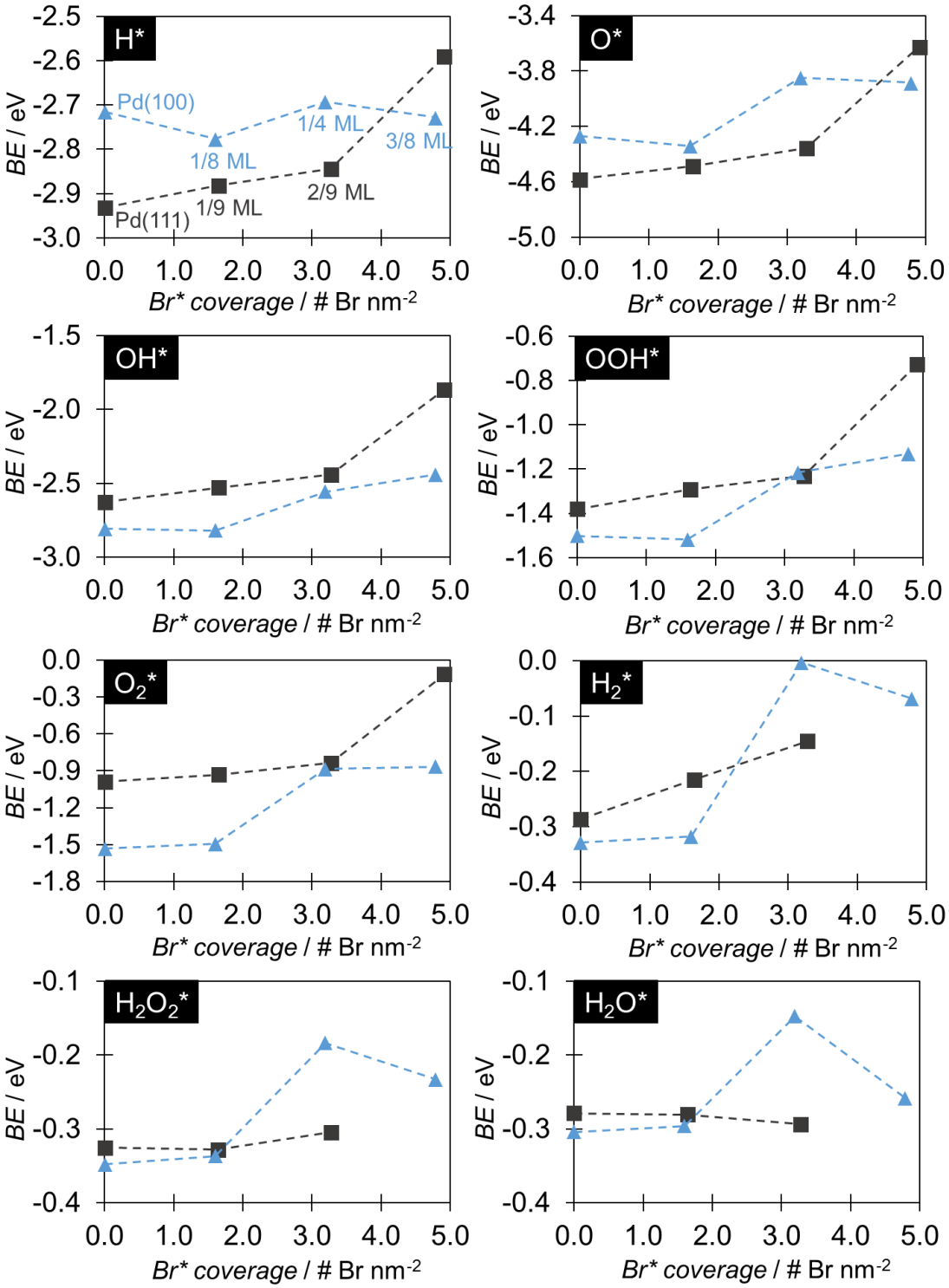

Figure 6.4 Binding energies for each intermediate as a function of Br* coverage on Pd(111) (black squares) and Pd(100) (blue triangles). Dotted lines are to guide the eye. The halogen coverages are normalized to Pd surface area (number of halogen atoms per nm^2), and the corresponding coverages in ML are given in the plot for H*. Data points for H_2*, H_2O_2*, and H_2O* on 1/3 ML Br*-covered Pd(111) are excluded because these species no longer bind exothermically to the Pd surface at that Br* coverage. Binding energy plots for Cl* and I* coverage are similar, and all of the raw BE data are tabulated in Table S6.1.

At the maximum halogen coverages that we studied for adsorption of intermediates on Pd(111) and Pd(100) (1/3 ML and 3/8 ML, respectively), Pd(100) maintains the strongest binding of all intermediates. In particular, O_2* binding remains significantly exothermic by between 0.7 – 0.9 eV on 3/8 ML halogen-covered Pd(100), while at the similar halogen coverage of 1/3 ML on Pd(111) the binding energy of O_2* ranges from exothermic by 0.2 eV on Cl*-covered Pd(111) to unfavorable by 0.11 eV on I*-covered Pd(111) with respect to desorption. This demonstrates that adsorbed halogens should deactivate Pd(111) more rapidly than Pd(100) as a function of their surface coverage, although we must keep in mind that Pd(100) has a stronger affinity for halogens than does Pd(111).

Examination of the pristine halogen adlayer structures (Figure 6.2) can help to rationalize some of the trends in binding energy versus halogen coverage identified in the above discussion. In general, all reaction intermediates tend to maximize their separation from co-adsorbed halogens (neglecting hydrogen-bonding interactions, which are most substantial for H_2O* and H_2O_2* on Cl* adlayers). 1/8 ML of halogen atoms on Pd(100) leaves high-symmetry binding sites (bridge, top, and fourfold hollow) at which the constituent Pd atoms are not coordinated directly to any halogen atoms, and exhibits only long-range interactions with reaction intermediates (primarily through inducing lateral strain in the Pd surface[91]). Accordingly, the binding energies of intermediates do not change significantly from their clean surface values when 1/8 ML of halogens are introduced on Pd(100). 1/4 ML of halogen atoms on Pd(100), wherein all halogens still prefer the fourfold hollow adsorption sites, causes all Pd atoms to be coordinated to one halogen atom (Figure 6.2). This means that in order to co-adsorb a reaction intermediate, the intermediate must either displace a halogen atom from its preferred fourfold hollow site or bind to a site that shares Pd atoms with adsorbed halogens, resulting in large destabilizations in binding strength. A further

increase in halogen coverage to 3/8 ML, although reducing the total number of overall binding sites, does not change the coordination environment of the remaining binding sites, explaining why the incremental change in halogen coverage from 1/4 to 3/8 ML on Pd(100) does not further destabilize reaction intermediates in as a strong manner as does the increase from 1/8 to 1/4 ML halogen coverage.

On Pd(111), high-symmetry binding sites (bridge, top, and fcc) that are not coordinated to any halogen atoms remain at 1/9 and 2/9 ML total halogen surface coverage. These halogen coverages only marginally change the clean-surface binding energies (by < ca. 0.2 eV), which can also be attributed primarily to halogen-induced lateral strain on the Pd lattice (Chapter 5). 1/3 ML halogen coverage represents a critical case in which all surface Pd atoms are coordinated to one halogen atom (because the halogens prefer the threefold fcc binding sites on Pd(111)), and this halogen coverage strongly destabilizes all reaction intermediates. A comparison of the magnitude in BE destabilization between the critical halogen coverages on Pd(111) and Pd(100) (i.e., the coverages at which all Pd atoms coordinate to a halogen atom, which is 1/3 ML for Pd(111) and 1/4 ML for Pd(100)) indicates that the effect of halogen coordination to binding sites is significantly greater on the Pd(111) substrate. The more coordinatively undersaturated Pd(100) metal surface atoms can sustain stronger binding of intermediates when sharing coordination to halogen atoms. We summarize three key factors that determine the strength of interaction between adsorbed halogen atoms and reaction intermediates: (i) the local environment of the intermediate's binding site, specifically its degree of direct coordination to halogen atoms; (ii) the identity of the halogen, with I* generally inducing the largest changes to binding energy and Cl* the smallest; and (iii) the coordinative saturation of surface metal atoms to each other, with a more coordinatively undersaturated surface being less affected by bonds to halogen atoms.

6.3.3 Thermochemistry for H_2O_2 formation and bifurcation points leading to H_2O

The destabilization of reaction intermediates induced by co-adsorbed halogens can affect the thermochemistry of elementary steps. The trends on halogen-covered Pd(100) are reasonably consistent with those on halogen-covered Pd(111): at high coverage of halogens, bond breaking reactions (O-O bond dissociation) generally become more difficult and bond-forming reactions (O-H bond formation) become easier with respect to their thermochemistry on the clean Pd surface. All reaction energies for the elementary steps in Scheme 5.1 are provided in Table S6.2.

The overall energy landscape from reactants to products on halogen-covered Pd deviates significantly from that on clean Pd, becoming less thermochemically driven (shifted to higher energies); populating Pd surfaces with halogens has a similar effect to alloying Pd with metals such as Au that weaken interactions with reaction intermediates.[54, 206] Figure 6.5 displays potential energy surfaces for the direct H_2O_2 formation pathway on clean and halogen-covered Pd(111) and Pd(100). The halogen coverages in this figure [1/3 ML for Pd(111) and 3/8 ML for Pd(100), which are chosen on the basis of representing active site models where all available Pd binding sites are modified by coordination to halogen atoms] are approximately identical in terms of total number of halogen atoms per unit surface area. There is a much larger energetic disparity between halogen-covered Pd(111) and Pd(100) compared with the difference between clean Pd(111) and Pd(100), in part because co-adsorbed halogens more effectively destabilize reaction intermediates on Pd(111).

Not only do co-adsorbed halogens shift the potential energy surfaces for H_2O_2 formation to higher energies, but they also modify the hydrogenation behavior of Pd – and to different degrees depending on the Pd surface structure. We calculate that hydrogenations of O_2* and OOH* by H* (elementary steps 5 and 6 from Scheme 5.1) are endothermic on clean Pd(111) by 0.21 eV

and 0.14 eV, respectively, and on clean Pd(100) by 0.42 eV and 0.02 eV, respectively. However, O_2* hydrogenation becomes exothermic on 1/3 ML Cl*-, Br*-, and I*-covered Pd(111) by over 0.3 eV, while this step remains endothermic on 3/8 ML Br*- and I*-covered Pd(100). OOH* hydrogenation becomes exothermic on all these halogen-covered Pd(111) and Pd(100) surfaces – but to a greater extent on Pd(111). The reaction energies for OOH* hydrogenation to H_2O_2* are -0.29 eV, -0.22 eV, and -0.38 eV on 3/8 ML Cl*-, Br*-, and I*-covered Pd(100), respectively; and -0.51, -0.50, and -0.57 eV on 1/3 ML Cl-, Br-, and I-covered Pd(111), respectively.

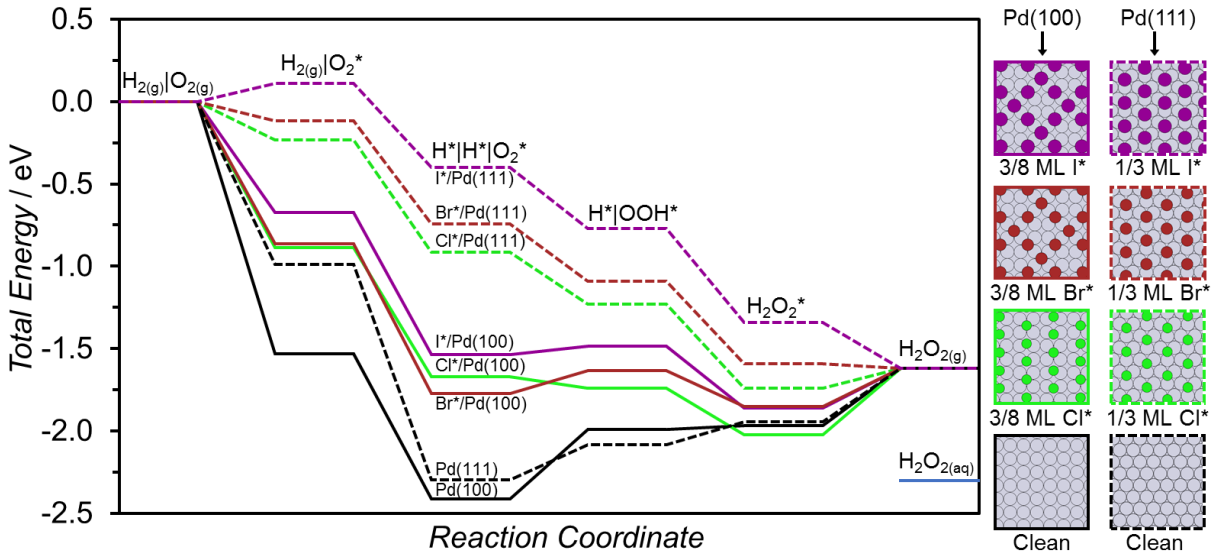

Figure 6.5 Potential energy surface for direct H_2O_2 formation from sequential hydrogenation of O_2 on clean and halogen-covered Pd(111) and Pd(100). Activation energy barriers are not included. The "|" denotes infinite separation of the corresponding intermediates. The energy for aqueous H_2O_2 ($H_2O_{2(aq)}$) with respect to $H_2O_{2(g)}$ is approximated from an experimental Henry's Law correlation[210] and is included to provide the state of product desorption into an aqueous phase. The halogen coverage on Pd(111) is 1/3 ML, and the halogen coverage on Pd(100) is 3/8 ML; the preferred halogen adlayer structures at these coverages (in the absence of other co-adsorbed intermediates) are provided in the graphic to the right of the potential energy surface. Atom colors: I (purple), Br (dark red), Cl (green), and Pd (gray).

Importantly, we next consider the three bifurcation points during the sequential hydrogenation of O_2 to H_2O_2 at which the O-O bond can break and divert flux toward H_2O formation (the undesired product). The large exothermicity of the O-O bond dissociation steps – even on halogen-covered Pd(111) and Pd(100) – suggests that they are essentially irreversible. For

example, O-O bond dissociations in OOH* and H_2O_2* (elementary steps 10 and 11 from Scheme 5.1) are exothermic by over 1.3 eV on 3/8 ML Cl*-, Br*-, and I*-covered Pd(100). We analyze the thermochemical competition between forming hydrogenated dioxygen species [and desorbing the H_2O_2 product] versus forming the O*/OH* dissociation fragments at these three bifurcation points in Figure 6.6, illustrating the effects of halogen coverage, halogen identity, and Pd substrate structure.

The thermochemistry on clean Pd(111) and Pd(100) exhibits a large disparity at each bifurcation point, strongly favoring the O*/OH* dissociation fragments in all cases by over 0.8 eV (and by as much as 2.8 eV) with respect to the hydrogenated dioxygen species. For a given halogen, these differences generally become significantly smaller when the halogen coverage increases; and at a particular halogen coverage, I* almost always minimize the thermochemical differences at the bifurcation points compared to Cl*or Br*. 1/3 ML I*-covered Pd(111) offers the single case in which the hydrogenated dioxygen species at a bifurcation point is thermochemically favored to the O*/OH* dissociation fragments. Comparing the Pd(111) and Pd(100) surfaces, we also observe that when the halogens reach surface coverages wherein their co-adsorption effects become most significant (1/3 ML and 1/4 ML for Pd(111) and Pd(100), respectively), Pd(100) maintains a larger thermochemical driving force to divert selectivity away from sequential hydrogenation of O_2 toward H_2O formation – especially at the second (OOH* hydrogenation to H_2O_2* versus its decomposition to O* and OH*) and third (H_2O_2* desorption versus its decomposition to 2OH*) bifurcation points. The thermochemistry at the third bifurcation point also implies a stronger driving force for H_2O_2 re-adsorption and dissociation to 2OH* on halogen-covered Pd(100) compared with halogen-covered Pd(111).

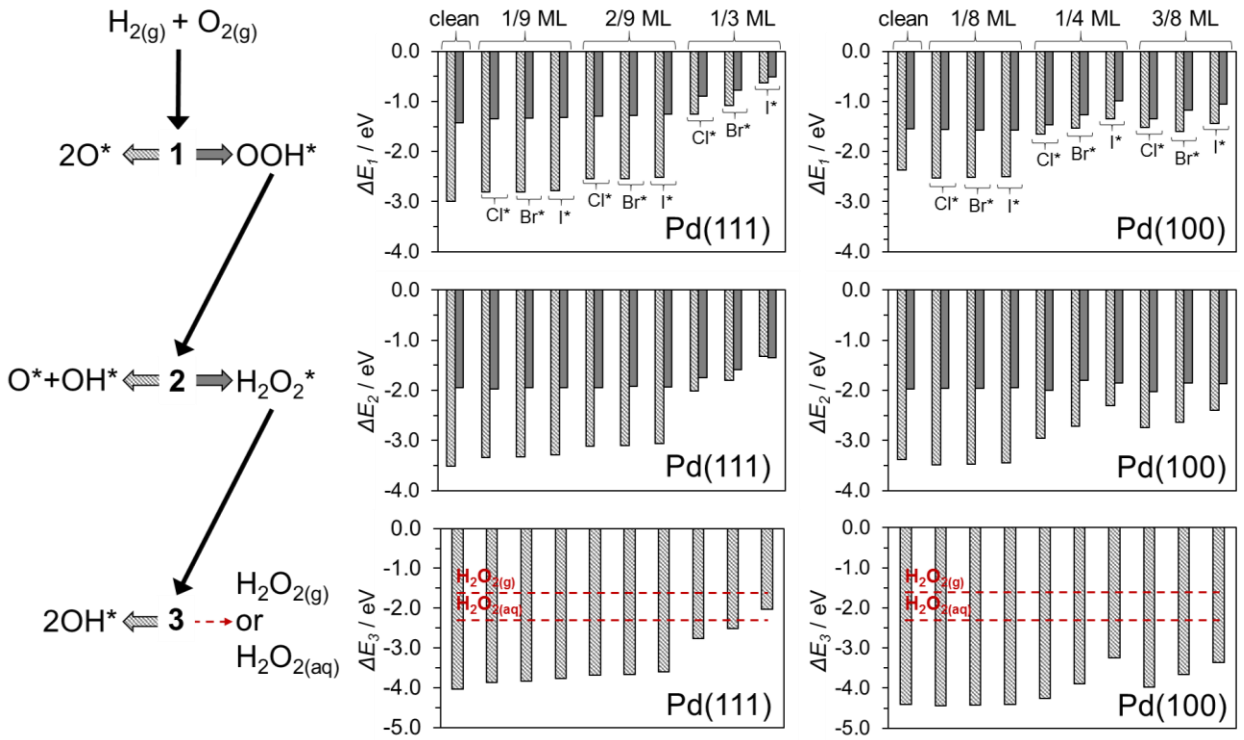

Figure 6.6 Reaction energies (*ΔE*) with respect to the gas-phase H_2 and O_2 reactants at the three bifurcation points, which are defined by O-O bond dissociation events: **(**1**)** 2O* formation from direct O_2 dissociation [$O_{2(g)}$ + 2*→ 2O*] versus OOH* formation from O_2 hydrogenation [$O_{2(g)}$ + ½$H_{2(g)}$ + * → OOH*]; **(**2**)** O* + OH* formation from OOH* dissociation [$O_{2(g)}$ + ½$H_{2(g)}$ + 2* → O* + OH*] versus H_2O_2* formation OOH* hydrogenation [$O_{2(g)}$ + $H_{2(g)}$ + * → H_2O_2*]; and **(**3**)** 2OH* formation from H_2O_2* dissociation [$O_{2(g)}$ + $H_{2(g)}$ + 2* → 2OH*] versus H_2O_2* formation and desorption into the bulk phase [$O_{2(g)}$ + $H_{2(g)}$ + → $H_2O_{2(g)\text{ or }(aq)}$]. For all bar plots: the data are provided as a function of halogen coverage (increasing left to right); within a given coverage, each pair of solid- and hash-filled data bars corresponds to Cl*, Br*, or I* (left to right) as the halogen; the solid-filled data bars correspond to the hydrogenated dioxygen intermediates, and the hash-filled data bars correspond to the O*/OH* fragments resulting from O-O dissociation. The horizontal dotted red lines provide the energies for $H_2O_{2(g)}$ and $H_2O_{2(aq)}$ (the latter represents desorption into an aqeuous phase and is approximated from an experimental Henry's Law correlation[210]).

6.3.4 Kinetic barriers for O-O dissociation at the bifurcation points

Evidently, the kinetics at the bifurcation points must favor the sequential hydrogenation of O_2 [and desorption of H_2O_2*] over O-O bond dissociations in order to achieve high selectivity toward H_2O_2, because the thermochemistry nearly always favors generating the O*/OH* fragments (precursors to H_2O formation) even when halogens are present on the surface. In accordance, one hypothesis from the experimental literature is that modifying Pd catalysts with halogens inhibits O-O bond dissociation kinetics, and this could explain why selectivity toward H_2O_2 is observed to increase when halides are added to the reaction medium.[29, 58, 66, 68, 170] We

calculated kinetic barriers for O-O bond dissociation on clean and halogen-covered Pd(111) (1/3 ML halogen) (Chapter 5) and Pd(100) (3/8 ML halogen) to investigate if this hypothesis is consistent with our halogen-covered Pd surface models, and the results are shown in Figure 6.7.

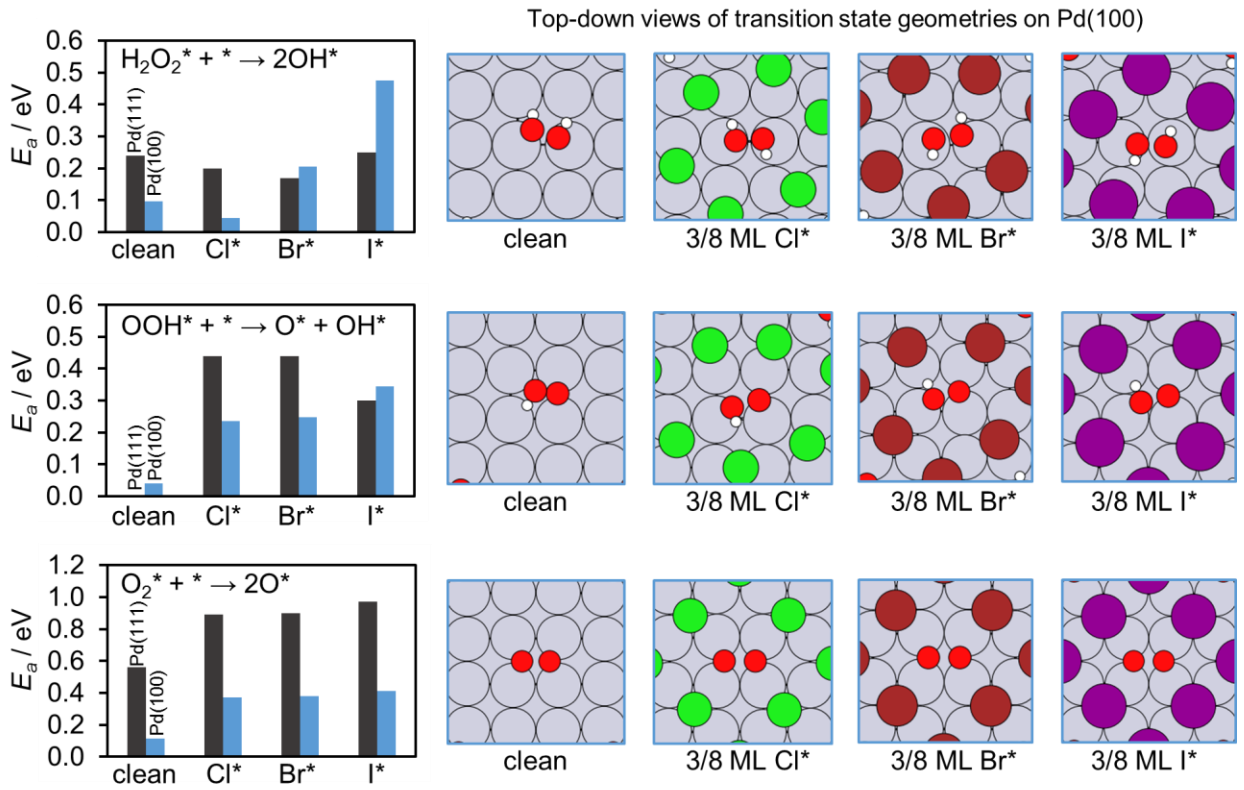

Figure 6.7 (Left) Activation energy barriers for O-O bond dissociation in $H_2O_2^*$, OOH*, and O_2^* on clean Pd(111) and Pd(100) compared to the barriers on 1/3 ML halogen-covered Pd(111) and 3/8 ML halogen-covered Pd(100). Black bars are Pd(111), and blue bars are Pd(100). (Right) Top-down views of the transition states geometries for O-O bond dissociation on clean and 3/8 ML halogen-covered Pd(100). Atom colors: I (purple), Br (dark red), Cl (green), O (light red), H (white), and Pd (gray).

The kinetic barriers for O-O bond dissociation in O_2^*, OOH*, and $H_2O_2^*$ are all less than 0.12 eV on Pd(100). The presence of halogens on Pd(100) increases these kinetic barriers in O_2^* and OOH*, which is the same behavior that we observed in Chapter 5 on Pd(111). (We note that the transition state geometries corresponding to the lowest-energy bond breaking pathways on halogen-covered Pd(100), shown in Figure 6.7, bear a close resemblance to those on the clean surface.)

The O_2* dissociation barrier on clean Pd(100) is significantly smaller than on clean Pd(111) (0.12 eV compared to 0.56 eV). While 1/3 ML of Cl*, Br*, or I* raises this barrier to ca. 0.9 eV on Pd(111), causing O_2* desorption to become kinetically favored to its dissociation, O_2* dissociation on 3/8 ML halogen-covered Pd(100) is easier than on clean Pd(111). Therefore, at the first bifurcation point in the DSHP mechanism, direct O_2* dissociation may become inaccessible on Pd(111) before it does on Pd(100) as halogens populate these surfaces. Blocking the O_2* dissociation channel on Pd(100) may coincide with the halogen coverage wherein Pd(100) is completely deactivated by halogens (1/2 ML, Figure 6.3 and Table 6.1).

We anticipate OOH* to be a very short-lived intermediate on clean Pd surfaces because its dissociation to O* and OH* is nearly spontaneous. The halogens impart some stability to OOH* by raising the kinetic barrier to its dissociation. However, these barriers (which range from 0.24 to 0.44 eV) are still accessible under typical DSHP reaction conditions, and so OOH* dissociation remains an open channel for H_2O formation on 1/3 ML halogen-covered Pd(111) and 3/8 ML halogen-covered Pd(100). Our calculations also show that dissociating OOH* is always kinetically easier than dissociating O_2* on each clean and halogen-covered surface. But, the differences between O-O dissociation barriers in O_2* and OOH* are much larger on Pd(111) than on Pd(100): these differences range from 0.45-0.67 eV (0.07-0.13 eV) on a given clean or halogen-covered Pd(111) surface (Pd(100) surface).

In Chapter 5 we showed that the intrinsic barriers for H_2O_2* dissociation to 2OH* are approximately constant between clean Pd(111) and 1/3 ML halogen-covered Pd(111). On Pd(100), there is a different trend: the O-O bond dissociation barrier increases from 0.04 eV to 0.21 eV to 0.47 eV when changing from Cl* to Br* to I* on 3/8 ML halogen-covered Pd(100). This result can be explained by observing the transition state geometry for H_2O_2* dissociation (Figure 6.7), which

occurs on two top sites across a bridge site. Forming this transition state involves displacing halogen atoms from hollow sites toward bridge sites, and the trend in dissociation barrier closely resembles that of the trend in halogen diffusion barrier (Figure 6.1B). Thus, I* appears to be effective at inhibiting H_2O_2* dissociation on Pd(100) because I* is difficult to displace from hollow sites, restricting formation of the bidentate HO-OH transition state. The transition states for O_2* and OOH* dissociation occur mostly over the unoccupied hollow site on 3/8 ML halogen-covered Pd(100) and do not induce any rearrangement of the I* adlayer (Figure 6.7). H_2O_2* actually becomes the most difficult to dissociate of the dioxygen species on 3/8 ML I*-covered Pd(100), whereas H_2O_2* is the easiest to dissociate on 3/8 ML Cl*- and Br*-covered Pd(100).

3/8 ML of Cl* and Br* appears to be neither sufficient to inhibit H_2O_2* dissociation, nor to prevent H_2O_2 re-adsorption on Pd(100) (Figure 6.7 and Table S6.1). The Cl* and Br* coverages necessary to quench the H_2O_2 decomposition reaction on Pd(100) may then approach the saturation value (1/2 ML) wherein both H_2O_2 *and* O_2 adsorption are blocked. (We note that on Pd(111), 1/3 ML of Br* is sufficient to block H_2O_2 adsorption, but O_2 can still adsorb on this surface – albeit weakly. Interestingly, bromide is often the preferred halide for improving Pd's selectivity toward H_2O_2 in DSHP experiments while maintaining adequate activity.[26])

Our calculations in this section demonstrate that the more coordinatively undersaturated features of Pd generally retain a stronger propensity than Pd(111) to break O-O bonds in the presence of halogens, particularly in O_2*. It may be beneficial to completely poison the more coordinatively undersaturated sites with halogens in order to maximize selectivity toward H_2O_2 in the DSHP.

6.4 Conclusions

In this chapter, we extended our analysis of adsorbed halogens from Chapter 5 to more coordinatively undersaturated features of Pd. We constructed phase diagrams for halogen adsorption on Pd(111), Pd(100), and the Pd(533) step edge as a function of aqueous-phase DSHP reaction conditions – that is, the concentration of dissolved hydrogen halide in the reaction medium and temperature. We predict that the step edge will saturate most rapidly with halogens, followed by Pd(100) and then Pd(111). This may indicate that defect sites on Pd nanoparticles can be selectively poisoned by halogens. Furthermore, we predict that the tendency for the halogens to populate the Pd surfaces increases in the order Cl* < Br* < I*, which is consistent with experiments demonstrating that iodide can completely deactivate Pd catalysts at solution-phase concentrations wherein bromide and chloride maintain a promotional effect.[31, 59, 169]

We then showed that the degree to which adsorbed halogens modify Pd's reactivity depends on three factors:

(i) The *local* environment of the binding site, specifically its degree of coordination to halogen atoms. The reactivity of Pd atoms which are not coordinated to any halogen atoms is only weakly affected by lateral strain induced by halogen atoms at nearest neighbor sites, and so the halogens mainly act as site blockers when they are present at low coverage.

(ii) The identity of the halogen, with I* generally the most effective at decreasing Pd's reactivity toward DSHP intermediates.

(iii) The coordinative saturation of metal surface atoms to each other, with a more coordinatively undersaturated surface, e.g. Pd(100), less affected by bonds to halogen atoms.

An undesirable consequence of (iii) is that the more coordinatively undersaturated Pd facets retain a stronger propensity to break the O-O bond in O_2* and OOH* (both kinetically and thermodynamically), and thus are less likely to be selective toward H_2O_2*. We infer that the optimal solution-phase concentration of halide for the DSHP may exist when the most coordinatively undersaturated Pd sites are completely poisoned, but Pd sites with higher coordination (e.g., on the close-packed facet) are only moderately covered by halides.

Supplementary Figures, Tables, and Methods for Chapter 6

Step 1. For each halogen, on each Pd facet, construct phase diagrams that relate the stability of halogen adlayers to the gas-phase pressure of corresponding hydrogen halide at a specific temperature. The required DFT-calculated data are the binding energies of halogen adlayers on Pd (e.g., Figures 5.2 and 6.2), and the required experimental data are the gas-phase hydrogen halide thermochemical properties. The relevant equations for phase diagram construction were provided in the supplementary section of Chapter 5. A brief summary of this formulation follows:

[We consider an infinite reservoir of gas-phase hydrogen halide with a well-defined ideal gas chemical potential – a function of temperature and pressure. We then calculate the grand potential to determine which halogen adlayer structure minimizes the free energy of system containing the gas-phase hydrogen halide and Pd surface. We assume that: (i) the hydrogen halide adsorbs dissociatively, wherein the binding energy of H* is approximated to be a constant at its clean-surface value, (ii) there is no change in zero-point energy upon adsorption and halogen adatoms have negligible surface entropy, and (iii) there is negligible stabilization of the halogen atoms by a solvent phase. Although some of these assumptions may be severe, we are primarily interested in extracting qualitative trends between the different Pd facets and the different halogens.]

Step 2. On each phase diagram, identify the partial pressures of gas-phase hydrogen halide at which a new halogen adlayer phase becomes the most stable (shown as vertical dotted black lines). Convert these partial pressures to the corresponding aqueous-phase concentrations of hydrogen halide that would be in equilibrium with the reservoir of the gas-phase hydrogen halide (i.e., equivalence of chemical potentials) using experimentally derived equilibrium relations. These equilibrium relations are noted to exhibit Henry's Law behavior (the ratio of hydrogen halide partial pressure to concentration of dissolved hydrogen halide tends to a constant in dilute solutions).

Step 3. Plot the most stable halogen adlayer phases as a function of the aqueous-phase concentrations of hydrogen halide for each facet.

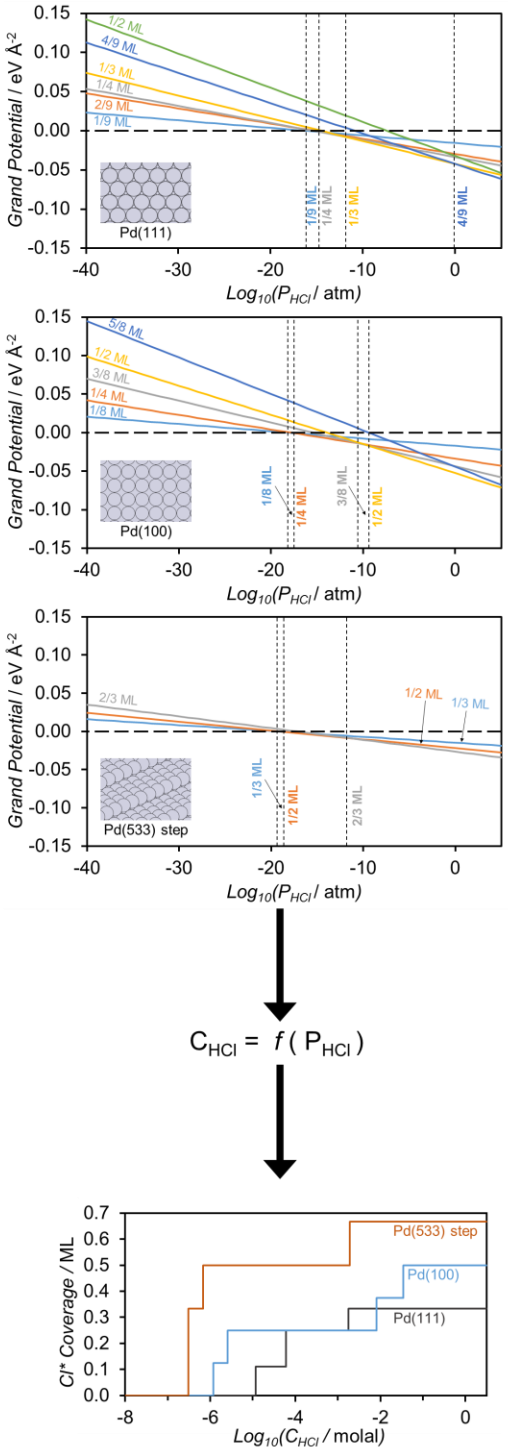

Figure S6.1 Procedure for constructing the phase diagrams in Figure 6.1 for Cl*, Br*, and I* adsorption on Pd(111), Pd(100), and the Pd(533) step edge as a function of aqeuous-phase hydrogen halide concentration. The horizontal dashed black line in each phase diagram from Step 1 represents the clean slab, and the vertical dashed black lines are used to indicate a new stable phase moving left to right on the diagram. All diagrams are constructed at 298 K. Equilibrium relations for Step 2 are taken from reference # [246].

Table S6.1 Binding energies (eV) for reaction intermediates on clean and halogen-covered Pd(100). The reference energy is the gas-phase intermediate infinitely separated from the clean or halogen-covered slab. N/A indicates that adsorption is endothermic.

species	1/8 ML halogen/Pd(100)			1/4 ML halogen/Pd(100)			3/8 ML halogen/Pd(100)			clean Pd(100)
	Cl	Br	I	Cl	Br	I	Cl	Br	I	
O	-4.35	-4.34	-4.33	-3.91	-3.85	-3.76	-3.84	-3.88	-3.80	-4.27
H	-2.78	-2.78	-2.77	-2.70	-2.69	-2.67	-2.67	-2.73	-2.71	-2.72
OH	-2.83	-2.82	-2.81	-2.74	-2.56	-2.23	-2.60	-2.44	-2.29	-2.81
O_2	-1.50	-1.49	-1.47	-1.09	-0.89	-0.64	-0.89	-0.87	-0.67	-1.53
H_2	-0.33	-0.32	-0.31	-0.16	0.00	N/A	-0.15	-0.07	N/A	-0.33
H_2O_2	-0.34	-0.34	-0.33	-0.39	-0.18	-0.24	-0.41	-0.23	-0.24	-0.35
OOH	-1.51	-1.52	-1.52	-1.41	-1.22	-0.94	-1.30	-1.13	-1.00	-1.50
H_2O	-0.34	-0.30	-0.27	-0.34	-0.15	-0.18	-0.45	-0.26	-0.19	-0.30

Table S6.2 Surface reaction energy data (in eV) on clean and halogen-covered Pd(100). Gray rows (steps 5-8) correspond to bond-forming, blue rows (steps 2b, 9-11) correspond to bond-breaking, and green rows (steps 12-17) correspond to bond-transfer, for the reactions as written in the forward direction.

Elementary step	clean Pd(100)	1/8 ML halogen/Pd(100)			1/4 ML halogen/Pd(100)			3/8 ML halogen/Pd(100)		
		Cl	Br	I	Cl	Br	I	Cl	Br	I
5. $H^* + O_2^* \leftrightarrow OOH^* + *$	0.42	0.44	0.43	0.40	0.06	0.04	0.04	-0.07	0.14	0.05
6. $H^* + OOH^* \leftrightarrow H_2O_2^* + *$	0.02	0.10	0.11	0.12	-0.11	-0.12	-0.47	-0.29	-0.22	-0.38
7. $H^* + OH^* \leftrightarrow H_2O^* + *$	-0.24	-0.20	-0.16	-0.15	-0.36	-0.36	-0.74	-0.64	-0.55	-0.65
8. $H^* + O^* \leftrightarrow OH^* + *$	-0.57	-0.45	-0.45	-0.45	-0.87	-0.76	-0.55	-0.84	-0.58	-0.53
2b. $H_2^* + * \leftrightarrow H^* + H^*$	-0.55	-0.68	-0.68	-0.69	-0.69	-0.83	-1.03	-0.64	-0.84	-1.10
9. $O_2^* + * \leftrightarrow O^* + O^*$	-0.84	-1.03	-1.02	-1.03	-0.56	-0.65	-0.71	-0.63	-0.74	-0.76
10. $OOH^* + * \leftrightarrow O^* + OH^*$	-1.84	-1.92	-1.90	-1.88	-1.49	-1.45	-1.31	-1.40	-1.46	-1.35
11. $H_2O_2^* + * \leftrightarrow OH^* + OH^*$	-2.43	-2.47	-2.47	-2.45	-2.25	-2.09	-1.39	-1.95	-1.82	-1.50
12. $H_2O^* + O^* \leftrightarrow OH^* + OH^*$	-0.33	-0.25	-0.29	-0.30	-0.51	-0.40	0.18	-0.19	-0.03	0.12
13. $OOH^* + O^* \leftrightarrow O_2^* + OH^*$	-1.00	-0.89	-0.88	-0.85	-0.93	-0.80	-0.60	-0.77	-0.72	-0.58
14. $H_2O_2^* + O^* \leftrightarrow OOH^* + OH^*$	-0.60	-0.55	-0.57	-0.57	-0.75	-0.64	-0.08	-0.55	-0.36	-0.15
15. $OOH^* + OH^* \leftrightarrow O_2^* + H_2O^*$	-0.66	-0.64	-0.59	-0.55	-0.42	-0.40	-0.78	-0.58	-0.69	-0.70
16. $H_2O_2^* + OH^* \leftrightarrow OOH^* + H_2O^*$	-0.26	-0.30	-0.27	-0.27	-0.25	-0.24	-0.26	-0.36	-0.33	-0.27
17. $OOH^* + OOH^* \leftrightarrow H_2O_2^* + O_2^*$	-0.40	-0.34	-0.31	-0.28	-0.17	-0.16	-0.52	-0.22	-0.36	-0.43

Chapter 7: Direct Synthesis of H_2O_2 over Au-Pd Catalysts Prepared by Electroless Deposition[i]

7.1 Introduction

Our DFT calculations in Chapters 5 and 6 demonstrated that halides, when present at significant concentrations on Pd's surface, can increase O-O bond dissociation barriers in O_2* and OOH*. This is critical to preserving these surface species so that they can be hydrogenated to H_2O_2. However, we also calculated that adsorbed halides do not strongly affect the O-O bond dissociation barrier in H_2O_2 (with the exception of iodide on Pd(100)); we then proposed that the primary function of halides in regards to inhibiting H_2O_2 decomposition is to obstruct H_2O_2 re-adsorption, evidenced by the significant energy required to accommodate H_2O_2 adsorption on the Pd surface when it is sufficiently covered with halides.

[i] A. C. Alba-Rubio, A. Plauck, E. E. Stangland, M. Mavrikakis and J. A. Dumesic, "Direct synthesis of hydrogen peroxide over Au-Pd catalysts prepared by electroless deposition", *Catalysis Letters,* **2015**, *145,* 2057.

Catalyst synthesis and characterization were performed by A. C. Alba-Rubio.

As we discussed in Chapter 1, another experimental strategy to improve the selectivity of Pd toward H_2O_2 is to alloy Pd with Au.[35, 36] Alloy components such as Au may induce ensemble effects and/or modify the electronic state of Pd,[67, 92-95, 173, 261] and similar to the effect of adsorbed halides, Au-Pd alloys can exhibit increased kinetic barriers for O-O bond dissociations in O_2* and OOH* with respect to pure Pd.[54] Hutchings and coworkers have extensively studied Au-Pd catalysts and have demonstrated that the performance of Au-Pd catalysts can be sensitive to the catalyst preparation methodology[24, 35, 173, 262, 263] – including factors such as the choice of support material.[192] The active site(s) for H_2O_2 synthesis, as well as its subsequent decomposition, remain a subject of study on Au-Pd catalysts – especially because commonly employed "bulk" preparation methods such as impregnation often fail to provide precise control over composition and structure in bimetallic systems, thereby complicating studies to link catalytic properties to structural and/or compositional changes in the catalyst.

In this chapter we utilize the technique of electroless deposition (ED) in an effort to deposit controlled amounts of Au onto pre-existing Pd particles supported on silica, but *not* onto the silica support itself. Our goal is to utilize these more well-defined Au-Pd materials to improve our understanding of the types of Au-Pd ensembles that are desirable for selective H_2O_2 synthesis. ED has been described in detail elsewhere,[264-269] and analogous to the approach of Rebelli et al:[267] we prepared Au-Pd/SiO_2 catalysts with different Au coverages; we characterized the nanoparticles using CO chemisorption, scanning transmission electron microscopy and energy dispersive X-ray spectroscopy (STEM-EDS), Fourier transform infrared spectroscopy (FTIR) of adsorbed CO, and inductively coupled plasma- atomic emission spectroscopy (ICP-AES); and we evaluated catalyst performance for the DSHP reaction.

7.2 Experimental Methods

7.2.1 Catalyst synthesis

Two different Pd/SiO_2 monometallic catalysts were prepared as the base catalysts for electroless deposition: one catalyst with nearly monodispersed small particles (~1 nm) and a second material with a wider particle size distribution. The first catalyst was prepared by strong electrostatic adsorption of a palladium precursor ($[Pd(NH_3)_4](NO_3)_2$, Sigma-Aldrich) onto silica (Cab-O-Sil silica EH-5, Cabot Corporation) following the synthesis and post-treatment procedure described elsewhere in detail.[180] The second catalyst was prepared by wet impregnation of palladium acetate ($Pd(C_2H_3O_2)_2$, Sigma-Aldrich) using the same silica support. To promote the formation of larger Pd nanoparticles, this catalyst was reduced in H_2 by heating to 823 K with a 5 K min^{-1} ramp, and then was held at 823 K for 4 h before cooling to room temperature and passivating with 1% O_2 in Ar.

The procedure for ED of Au onto Pd was derived from Rebelli et al[267] using a bath containing $KAu(CN)_2$ as the Au source and hydrazine as reducing agent. The conditions used for the ED baths were a 30:1 molar ratio of N_2H_4 to $Au(CN)_2^-$, and a NaOH solution was added drop-wise to maintain a pH of 9 (above the PZC of the silica support) to avoid Au deposition on the silica. Deposition times were kept constant at 1 h at room temperature under vigorous stirring. The slurry was then filtered and washed repeatedly in deionized water, dried in vacuum at 313 K, and stored in glass vials. Further details of the synthesis protocol can be found in the supplementary section at the end of this chapter.

7.2.2 Catalyst characterization

The percent weight loadings of Au and Pd were determined by inductively coupled plasma-atomic emission spectroscopy (ICP-AES) at Galbraith Laboratories (Knoxville, TN, USA) using a PerkinElmer Optima 5300 V Optical Emission Spectrometer.

Values for the palladium surface site density were determined using CO chemisorption in a Micromeritics ASAP 2020 system. Before CO chemisorption, samples were reduced under H_2 flow at 323 K (heating rate: 2 K min^{-1}), held for 2 h, evacuated for 3 h, and cooled to 308 K. CO was dosed on the catalyst until the equilibrium pressure was 13 mmHg. The CO in the cell was then evacuated at 308 K. CO was again dosed on the catalyst to determine the amount of weakly adsorbed CO. The amount of strongly adsorbed CO was determined by subtracting the two isotherms. A surface stoichiometry of 2:3 CO:Pd was used to calculate the palladium surface site density for all catalysts,[180] assuming that Au does not appreciably adsorb CO under these conditions.

The surface of the bimetallic nanoparticles was examined by Fourier transform infrared spectroscopy (FTIR) of adsorbed CO using a Nicolet 6700 FTIR spectrometer. For each catalyst, a pelletized sample (ca. 15 mg) was loaded in a flow cell and reduced overnight at 473 K in 2 % H_2/He. The cell was then cooled to 298 K, evacuated, and a background spectrum was taken as the reference. 9 Torr of 10 % CO/He was introduced into the cell for 20 minutes at 298 K, and then the cell was evacuated to remove gas-phase and weakly-bound CO before recording a spectrum.

Scanning transmission electron microscopy (STEM) images were recorded in high-angle annular dark field (HAADF) mode using a FEI Titan STEM with C_s probe aberration corrector operated at 200 kV with spatial resolution < 0.1 nm (probe convergence angle of 24.5 mrad, and probe current of ~25 pA). Energy-dispersive X-ray Spectroscopy (EDS) results were obtained

using the same microscope with convergence angle of 24.5 mrad and beam current of ~640 pA, with spatial resolution ~0.5 nm. To prepare samples for STEM, the catalyst samples were first suspended in ethanol, ultra-sonicated for 5 min, and then deposited onto carbon coated Copper TEM grids. STEM samples were plasma cleaned for 15 min immediately before loading into the microscope.

7.2.3 Hydrogen peroxide synthesis and decomposition

Catalyst performance was analyzed using a 50 mL Parr Instrument Company Hastelloy C-276 autoclave. The following procedure was derived from Landon et al.[36] The autoclave was loaded with 5 mg of catalyst (composed of 1 part active catalyst diluted in 10 parts SiO_2 support) and 12 g of a 1:1 molar ratio solution of MeOH:H_2O, purged with 1.5 MPa of CO_2 for five cycles, pressurized with 5 % H_2/CO_2, and cooled to the reaction temperature (278 K) by submersing the autoclave in a cooling bath controlled by a refrigerated bath circulator (ARCTIC A25, Thermo Scientific). Then, the autoclave was pressurized to 3.4 MPa using 25 % O_2/CO_2 (2:1 molar ratio of O_2:H_2 prior to reaction) and stirring was started (1500 rpm). H_2 conversion was determined by gas chromatography (thermal conductivity detector and Restek HayeSep DB 80/100 mesh column, 2 m, 2.0 mm ID). Titration of the final solution (0.05M $Ce(SO_4)_2$ as titrant and ferroin as indicator) gave the quantity of H_2O_2 produced.

The effect of external mass transfer on the reaction rates was assessed by measuring H_2 conversion and H_2O_2 production as a function of the stir rate. Figure S7.1 shows that the H_2 conversion and H_2O_2 produced plateaued at about 1000 rpm, remaining approximately constant over the range 1000-2000 rpm. Moreover, both H_2 conversion and H_2O_2 production were shown to be approximately linear functions of catalyst loading up to ca. 16 mg (Figure S7.2).

The Madon-Boudart test was also utilized to assess the possible importance of internal mass transport limitation.[270] Two Pd/SiO_2 catalysts were prepared by the wet impregnation procedure described above: a 5 wt % Pd/SiO_2 catalyst and a 2.5 wt % Pd/SiO_2 catalyst. The 2.5 wt % Pd/SiO_2 catalyst was reduced at a higher temperature (1073 K) to achieve the same Pd dispersion (ca. 19 % Pd dispersion based on CO chemisorption results) as the 5 wt % Pd/SiO_2 catalyst. The H_2O_2 initial production rates were calculated by fitting a line through a plot of the moles of H_2O_2 produced versus time for conversions lower than 20 % of the limiting reactant (H_2) and normalizing to the total surface Pd sites. The site-normalized initial rate values obtained in this manner were:

(5 wt % Pd/SiO_2, 19.3 % dispersion) = 3.7 ± 0.4 mol H_2O_2 mol surface Pd^{-1} s^{-1}

(2.5 wt % Pd/SiO_2, 18.6 % dispersion) = 4.1 ± 0.6 mol H_2O_2 mol surface Pd^{-1} s^{-1}

Accordingly, we conclude that the rates of production of H_2O_2 reported in this paper are not significantly limited by transport processes.

For decomposition experiments the autoclave was charged with catalyst, purged five times with CO_2 (1.5 MPa), and then filled with 2.9 MPa 5 % H_2/CO_2 or 1.2 MPa 25 % O_2/CO_2 to examine decomposition with or without H_2. Both the autoclave and a 0.1 wt % H_2O_2 feed solution (8.0 g MeOH, 4.0 g H_2O, and 0.04 g of a non-stabilized 30 wt % H_2O_2 solution with < 10 ppb Cl^-, Gigabit, KMG) were cooled to the reaction temperature (278 K). The autoclave was charged with 12 g of the cooled H_2O_2 feed using a high performance liquid chromatography (HPLC) pump (Chrom Tech Series 1), and then stirring (1500 rpm) was started. Conversion of H_2O_2 was again determined by titration of the final solution.

7.3 Results and Discussion

7.3.1 High dispersion (hd) Pd/SiO_2 and Au-Pd/SiO_2 catalysts

The highly dispersed monometallic catalyst prepared by strong electrostatic adsorption had a sharp particle size distribution around 0.77 nm (Figure 7.1a) and is denoted as Pd/SiO_2 (hd) (hd: high dispersion). An ED bath was then prepared, and the amount of monometallic catalyst was adjusted to deposit a half, one, two, and three theoretical monolayers of Au onto the Pd nanoparticles. Following Au deposition, all catalysts showed a reduction in the CO uptake (Table 7.1). The calculated Au coverages based on differences in CO uptake were lower than the expected values based on the amount of Au precursor added to the ED bath, indicating incomplete Au uptake from the bath and/or autocatalytic deposition of Au (Au deposited on Au instead of desired Au on Pd).[267] Table 7.1 also shows that some Pd leached out from the SiO_2 support into the ED solution, based on ICP results.

Table 7.1 Theoretical and actual Au coverages, ICP results, and CO chemisorption results for Pd/SiO_2 and Au-Pd/SiO_2 catalysts.

	Au coverage / ML		wt % metal (ICP)		Pd exposed / μmol g_{cat}^{-1}
	Theoretical	Actual	Au	Pd	
Pd/SiO_2 (hd)	-	-	-	3.5	167
0.16 ML Au-Pd/SiO_2 (hd)	0.5	0.16	1.3	2.9	140
0.40 ML Au-Pd/SiO_2 (hd)	1	0.40	2.6	2.7	101
0.53 ML Au-Pd/SiO_2 (hd)	2	0.53	3.1	2.5	78
Pd/SiO_2 (ld)	-	-	-	5.3	91
0.69 ML Au-Pd/SiO_2 (ld)	1	0.69	1.0	4.7	28
0.74 ML Au-Pd/SiO_2 (ld)	2	0.74	2.3	4.1	24

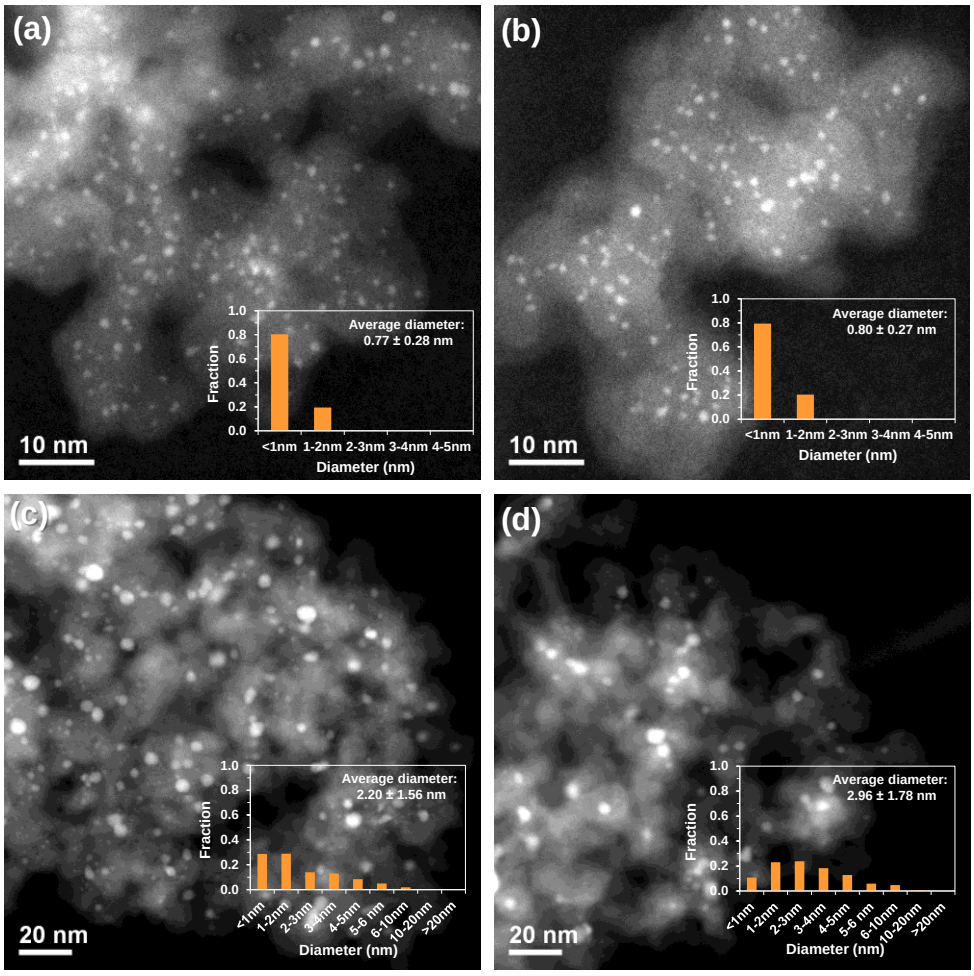

Figure 7.1 STEM images and particle size distribution for: (a) Pd/SiO_2 (hd), (b) 0.53 ML $Au\text{-}Pd/SiO_2$ (hd), (c) Pd/SiO_2 (ld), and (d) 0.74 ML $Au\text{-}Pd/SiO_2$ (ld). ld: low dispersion, hd: high dispersion. 2109, 1164, 1681 and 438 particles were counted for particle size distributions, respectively.

Bimetallic composition was confirmed by EDS analysis of the 0.53 ML $Au\text{-}Pd/SiO_2$ (hd) catalyst. Accurate EDS analysis of particles < 1 nm was not possible due to their small size, but all larger particles analyzed contained both Au and Pd. The particle size distribution remained unchanged after Au deposition (Figure 7.1b).

FTIR spectra of adsorbed CO at 298 K revealed two regions of CO stretching bands on both the Pd/SiO_2 (hd) and 0.53 ML $Au\text{-}Pd/SiO_2$ (hd) catalysts: 2000-2100 cm^{-1} (linearly bonded CO) and 1800-2000 cm^{-1} (nonlinearly (bridge and threefold) bonded CO) (Figure 7.2a, Table S7.1).[267] The absorbance for the linear region is higher than that for the non-linear region for

Pd/SiO_2 (hd), which is consistent with the high Pd dispersion (large number of low coordination sites to accommodate linear CO adsorption). Following Au deposition, the peak intensities decreased (lower CO uptake) and generally shifted to lower frequencies,[267, 271-274] and there was a significantly greater relative loss in linear band intensity – suggesting that Au is preferentially binding to low coordination Pd sites on this highly dispersed Pd catalyst (Table S7.1)[267, 272-274].

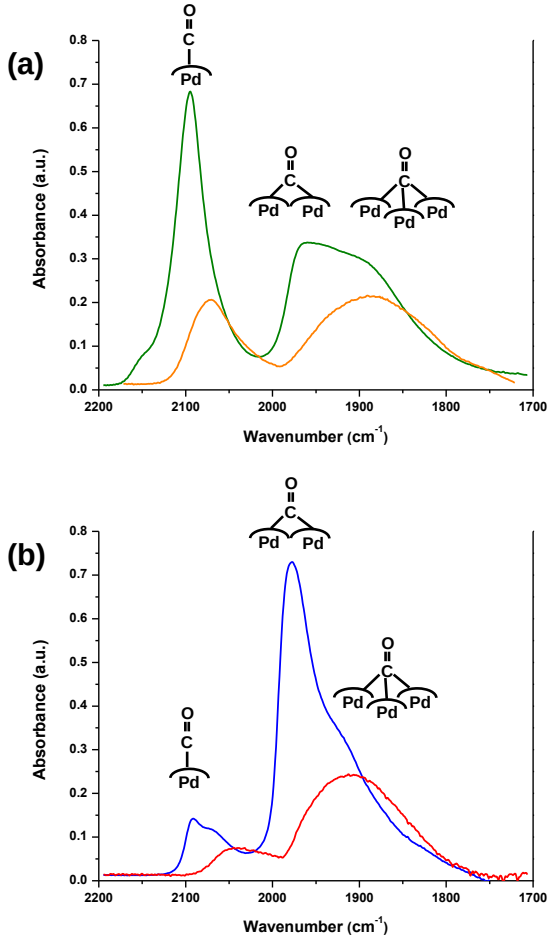

Figure 7.2 Transmission FTIR spectra of CO adsorption on: (a) high dispersion catalysts: monometallic Pd/SiO_2 (hd) (green) and bimetallic 0.53 ML Au-Pd/SiO_2 (hd) (orange); and (b) low dispersion catalysts: monometallic Pd/SiO_2 (ld) (blue) and bimetallic 0.69 ML Au-Pd/SiO_2 (ld) (red).

The performance of the catalysts was evaluated for the direct synthesis of H_2O_2 in a batch reactor, and the results including reaction conditions can be found in Table 7.2 and Figure 7.3. Initial H_2O_2 production rates were estimated from a linear fit to conversion-time data (Figure 7.3)

normalized to the catalyst mass or moles of surface Pd. No significant change in the initial H_2O_2 production rate per gram of catalyst (mol H_2O_2 gcat^{-1} h^{-1}) was observed following addition of Au, and the selectivity remained approximately constant even after ED of up to 0.53 ML Au coverage on the Pd nanoparticles. Further attempts to increase Au coverage on the Pd/SiO_2 (hd) catalyst resulted in significant autocatalytic deposition of Au with minimal decrease in the available Pd sites measured by CO chemisorption. Although Edwards et al[275] were able to achieve 80 % selectivity for H_2O_2 on a Pd/SiO_2 catalyst under similar reaction conditions, we note that (i) those catalysts were calcined in air at 673 K prior to reaction, which has been shown to improve selectivity;[26] (ii) the Pd precursor and SiO_2 support differ from those used in this work; and (iii) the selectivities measured here are consistent with other silica-supported Pd catalysts, although reaction conditions vary.[276, 277] Edwards et al[278] also report productivity for Au-Pd/SiO_2 catalysts prepared by incipient wetness impregnation up to 0.20 mol H_2O_2 g_{cat}^{-1} h^{-1}. Although our measured productivities are higher, we further note that: (i) the productivities from Edwards et al represent an average over the first 30 minutes of reaction, while our reported values are *initial* productivities; (ii) the Pd content in our (hd) catalysts is ca. 50 % higher, and Pd dispersion could also differ; (iii) the different catalyst heat treatment procedures (reduction versus calcination in air) can drastically affect catalyst performance.

Table 7.2 Comparison of selectivity and initial H_2O_2 production rate for the synthesis reaction (hd and ld catalysts). Batch conditions: 5 mg catalyst; 278 K; stir rate 1500 rpm; 2.9 MPa 5 % H_2/CO_2 + 1.2 MPa 25 % O_2/CO_2, 12 g 1:1 molar ratio MeOH:H_2O solution.

	H_2 conversion / %	H_2O_2 selectivity / %	Initial rate per mass / mol H_2O_2 g_{cat}^{-1} h^{-1}	Initial rate per site / mol H_2O_2 mol surface Pd^{-1} s^{-1}
Pd/SiO_2 (hd)	34	30	0.75	1.3
0.53 ML Au-Pd/SiO_2 (hd)	35	28	0.66	2.4
Pd/SiO_2 (ld)	32	26	1.24	3.8
0.69 ML Au-Pd/SiO_2 (ld)	32	26	1.19	11.8

Because of the negligible effect of Au deposition on the selectivity for the Pd/SiO_2 (hd) catalyst, we prepared a second Pd/SiO_2 catalyst with larger particle size. Previous studies suggest that particles with a large density of defect sites readily decompose H_2O_2, in addition to favoring direct H_2O formation through the dissociative chemisorption of O_2.[224, 256, 257]

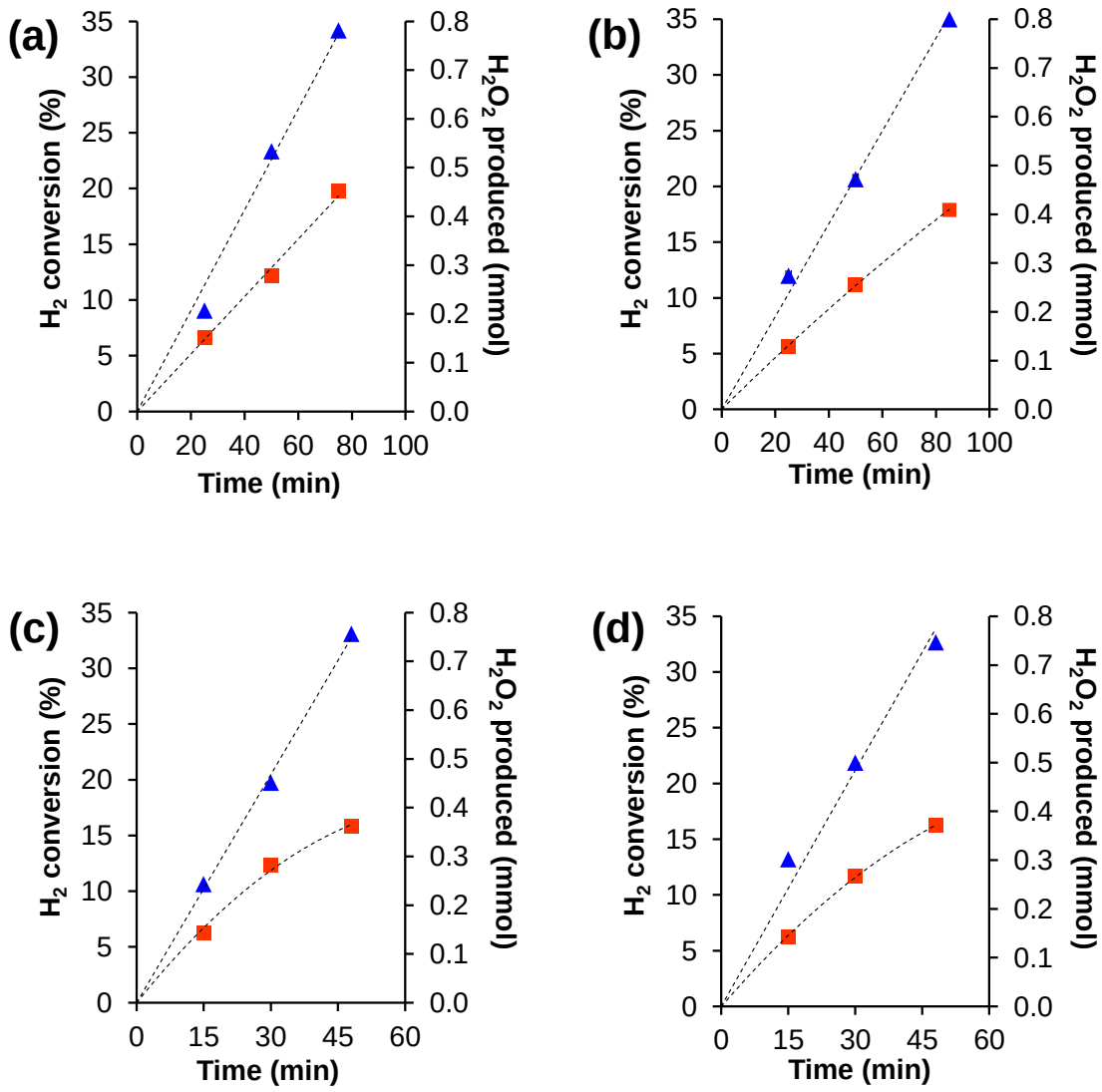

Figure 7.3 (▲) Conversion-time and (■) mmol H_2O_2 produced-time data for (a) Pd/SiO_2 (hd); (b) 0.53 ML Au-Pd/SiO_2 (hd); (c) Pd/SiO_2 (ld); and (d) 0.69 ML Au-Pd/SiO_2 (ld). Dotted lines are to guide the eye. No significant induction period was observed for all catalysts. Initial H_2O_2 production rates are estimated from a linear fit through the first two time points (< 25 % H_2 conversion), forced through the origin. Batch conditions: 5 mg catalyst; 278 K; stir rate 1500 rpm; 2.9 MPa 5 % H_2/CO_2 + 1.2 MPa 25 % O_2/CO_2, 12 g 1:1 molar ratio MeOH:H_2O solution.

7.3.2 Low dispersion (ld) Pd/SiO_2 and Au-Pd/SiO_2 catalysts

The second monometallic catalyst prepared by wet impregnation had a lower Pd dispersion (Figure 7.1c) and is identified as Pd/SiO_2 (ld) (ld: low dispersion).

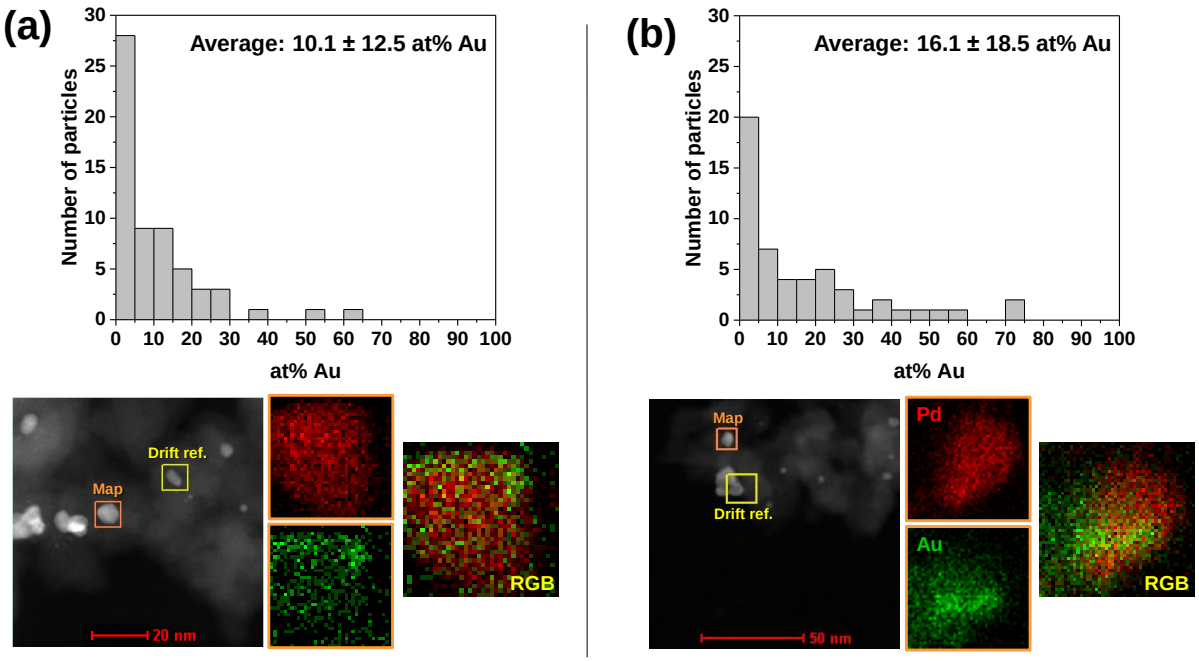

Figure 7.4 Composition distribution obtained by EDS spot-beam analysis, and EDS maps of single particles following electroless deposition of Au: (a) 0.69 ML Au-Pd/SiO_2 (ld), (b) 0.74 ML Au-Pd/SiO_2 (ld).

Noting that low Au coverages did not significantly affect the performance of the Pd/SiO_2 (hd) catalyst, we attempted to deposit close to a full monolayer of Au on the Pd/SiO_2 (ld) catalyst. However, only up to 0.69 ML of Au was deposited by ED on the Pd/SiO_2 (ld) catalyst before autocatalytic Au deposition became dominant (Table 7.1); further deposition of Au resulted in minimal decrease in the CO uptake (see Table 7.1, 0.74 ML Au-Pd/SiO_2 (ld) catalyst). The prevalence of autocatalytic deposition above ca. 0.70 ML of Au is in agreement with the results of Rodriguez et al[269] for a Au-Pd/Carbon catalyst. Both Au and Pd were detected in nearly all particles examined by STEM-EDS for the 0.69 ML Au-Pd/SiO_2 (ld) catalyst. An EDS spot-beam analysis of individual nanoparticles showed a low percentage of Au in these particles, consistent with Au

deposition on the surface of Pd particles (Figure 7.4a). The percentage of Au in the nanoparticles of the 0.74 ML Au-Pd/SiO_2 (ld) catalyst was significantly higher, demonstrating the effect of autocatalytic deposition (Figure 7.4b). In contrast with the highly dispersed catalysts, the low dispersion catalysts exhibited significant changes in the particle size distribution (shifted toward larger particles, Figure 7.1d) indicating particle sintering following Au deposition.

Both the Pd/SiO_2 (ld) and 0.69 ML Au-Pd/SiO_2 (ld) catalysts were characterized by FTIR of adsorbed CO at 298 K (Figure 7.2b, Table S7.1). The monometallic low dispersion catalyst exhibited a higher fraction of bridged CO bonding in comparison with the highly dispersed Pd catalyst; all band intensities decreased upon Au deposition, but the relative intensity ratios of linear and non-linear CO adsorption bands remained roughly constant.

The performance of the low-dispersion catalysts was then evaluated for the direct synthesis of H_2O_2. Interestingly, the Pd/SiO_2 (ld) and the 0.69 ML Au-Pd/SiO_2 (ld) catalysts had nearly identical initial H_2O_2 production rates per gram of catalyst, and both catalysts achieved 26 % selectivity for H_2O_2 at ca. 30 % H_2 conversion (Table 7.2). Assuming that Au remains at the surface in the reaction environment, this result would suggest that the 0.69 ML Au-Pd/SiO_2 (ld) catalyst has a higher H_2O_2 production rate per surface Pd atom. It is also noteworthy that the corresponding H_2O_2 production rates per Pd atom of these catalysts are much higher than those obtained with the more highly dispersed catalysts; similar behavior was observed by Kim et al[256] (i.e. H_2 conversion and H_2O_2 productivity both decreased with decreasing mean Pd particle size), although to a smaller degree.

We also measured the performance of the catalysts for peroxide decomposition reactions using a 0.1 wt % H_2O_2 feed solution, which corresponds to the wt % of H_2O_2 achieved in the synthesis reaction at ca. 30 % H_2 conversion (Table 7.3). Analogous to the findings for the

synthesis reaction, the initial H_2O_2 decomposition rates (estimated from a linear fit to conversion-time data (Figure 7.5) normalized to the catalyst mass or moles of surface Pd) on Pd/SiO_2 (ld) and 0.69 ML $Au\text{-}Pd/SiO_2$ (ld) in the presence of H_2 were similar per gram of catalyst (Table 7.3). Therefore the 0.69 ML $Au\text{-}Pd/SiO_2$ (ld) catalyst was more active per surface Pd atom than its monometallic counterpart. This rate enhancement per exposed Pd atom may result from electronic modification of the Pd atoms by Au, whereby a net electron transfer from Pd to Au has been observed based on X-ray photoelectron spectroscopy (XPS) measurements by Rebelli et al;[267] however any electronic effect appears to increase both the synthesis and hydrogenation rates per exposed Pd atom to the same degree. Due to the low starting concentration of H_2O_2 in comparison with total H_2 charged to the reactor, it was difficult to quantitatively attribute the H_2O_2 decomposition to either the disproportionation or hydrogenation pathways based on H_2 consumption. Separate experiments at higher initial H_2O_2 concentration (2 wt %, Table S7.2) indicated that the major pathway for H_2O_2 loss in the presence of H_2 was likely through hydrogenation to H_2O based on comparing total moles of H_2O_2 decomposed and H_2 consumed. This result is consistent with previous findings for Pd and Au-Pd catalysts in the literature using an acidified methanol-water solvent mixture.[36, 279]

Table 7.3 Comparison of initial rates for the H_2O_2 synthesis and decomposition reactions for (ld) catalysts. Batch conditions: 5 mg catalyst; 278 K; stir rate 1500 rpm; (synthesis) 2.9 MPa 5 % H_2/CO_2 + 1.2 MPa 25 % O_2/CO_2, 12 g 1:1 molar ratio MeOH:H_2O solution; (decomposition, with H_2) 2.9 MPa 5 % H_2/CO_2, 12 g 0.1 wt % H_2O_2 in 1:1 molar ratio MeOH:H_2O solution; (decomposition, without H_2) 1.2 MPa 25 % O_2/CO_2, 12 g 0.1wt % H_2O_2 in 1:1 molar ratio MeOH:H_2O solution.

	Initial rate per mass / mol H_2O_2 g_{cat}^{-1} h^{-1}		Initial rate per site / mol H_2O_2 mol surface Pd^{-1} s^{-1}	
	Pd/SiO_2 (ld)	0.69 ML $Au\text{-}Pd/SiO_2$ (ld)	Pd/SiO_2 (ld)	0.69 ML $Au\text{-}Pd/SiO_2$ (ld)
Synthesis	1.24	1.19	3.8	11.8
Decomposition, without H_2	0.0093	0.0067	0.029	0.067
Decomposition, with H_2	0.20	0.24	0.61	2.35

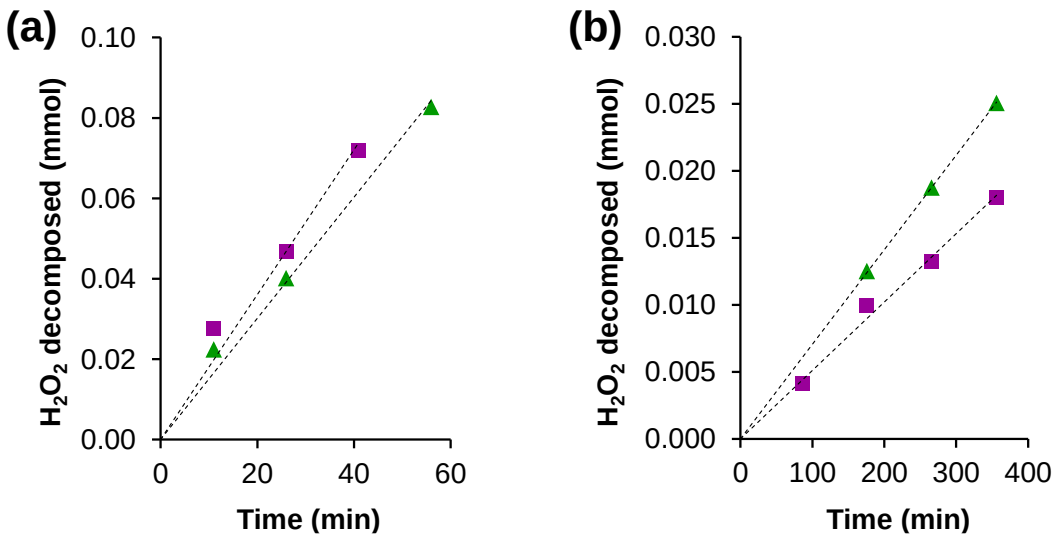

Figure 7.5 mmol H_2O_2 decomposed-time data for (▲) Pd/SiO_2 (ld) and (■) 0.69 ML $Au\text{-}Pd/SiO_2$ (ld) for (a) the decomposition reaction with H_2 present and (b) the decomposition reaction without H_2 present. Note that time zero for these reactions corresponds to 4 minutes after injection of the feed over the dry catalyst, at which time the temperature in the reactor has stabilized (the reported mmol H_2O_2 decomposed is with respect to this time point). Decomposition rates are calculated from the slope of the best fit line through this data, forced through the origin. Batch conditions: 5 mg catalyst; 278 K; stir rate 1500 rpm; 12 g 0.1 wt % H_2O_2 in 1:1 molar ratio MeOH:H_2O solution; 2.9 MPa 5 % H_2/CO_2 (decomposition with H_2); 1.2 MPa 25 % O_2/CO_2 (decomposition without H_2).

Interestingly, the rate of H_2O_2 decomposition for the 0.69 ML $Au\text{-}Pd/SiO_2$ (ld) catalyst was about 30% lower than that of the Pd/SiO_2 (ld) per gram of catalyst in the absence of H_2 (where H_2O_2 can only decompose through disproportionation). However, the calculated rate per surface Pd increased three-fold for the 0.69 ML $Au\text{-}Pd/SiO_2$ catalyst compared with its monometallic counterpart (Table 7.3). Furthermore, the rate of H_2O_2 decomposition in the absence of H_2 was over an order of magnitude slower than when H_2 was present. It is evident from this study and the literature[35] that inhibiting the hydrogenation of H_2O_2 is a key factor for the selective production of high concentrations of H_2O_2.

Our results for the Pd/SiO_2 (ld) and 0.69 ML $Au\text{-}Pd/SiO_2$ (ld) catalysts indicate that deposition of sub-monolayer (< 0.7 ML) amounts of Au onto the surface of pre-existing Pd particles was not sufficient to improve selectivity in the direct synthesis reaction, nor did Au deposition significantly inhibit H_2O_2 decomposition pathways. According to a density functional

theory (DFT) study[54] of Pd ensembles on an Au-Pd surface alloy (a model comparable to the surface of our ED catalyst particles), Pd monomers surrounded by Au atoms are the most desirable active sites for selective H_2O_2 production. Complete coverage of Pd by Au is undesirable from an activity standpoint, as surface Pd sites are necessary to dissociate H_2. The barriers for O-O bond dissociation steps that lead to complete reduction of O_2 to H_2O are calculated to be significantly increased at these Pd monomer sites; however, an ensemble of at least two contiguous Pd atoms is sufficient for facile O-O bond cleavage.[54] The FTIR spectrum of adsorbed CO for the 0.69 ML Au-Pd/SiO_2 (ld) catalyst (Figure 7.2b) indicates that there are still contiguous Pd sites able to adsorb CO at bridged and three-fold sites after Au deposition, and therefore even higher concentrations of Au at the surface may be necessary to promote selective production of H_2O_2 and suppress its decomposition. Qualitatively similar conclusions were reached by Ouyang et al,[280] who prepared a series of Au-Pd catalysts with incremental Au loading by incipient wetness impregnation. However, attempts in this work to deposit more Au on the Pd surface by ED resulted in significant autocatalytic deposition of Au with minimal reduction in the exposed Pd. Furthermore, although Rebelli et al[267] were able to achieve 0.88 ML of Au on Pd by ED, contiguous Pd sites also remained based on their FTIR spectra of adsorbed CO, and the intensity ratios for linear, bridge, and threefold CO adsorption peaks were constant with increasing Au coverage (as with our (ld) catalysts). Consistent with these findings, a plausible growth mechanism for Au on the Pd particles may involve gradual coverage of the Pd surface by islands of Au – rather than Au depositing in a highly dispersed manner – and so completely isolated Pd sites may not be expected until near unity Au coverage.

Even if more effective isolation of the Pd component can be achieved during ED, it is possible that the active surface may restructure under reaction conditions to expose Pd. Reactive

surface intermediates generally included in the elementary mechanism for H_2O_2 synthesis (O, H, OH, and OOH) all bind to Pd much more strongly than to Au,[55, 281, 282] and this stronger binding could provide a driving force to withdraw Pd to the surface[283, 284] – despite the favorable surface segregation energy of Au atoms in a Pd matrix under vacuum conditions.[285, 286] Consequently, large surface Pd ensembles resulting from Pd surface segregation might be expected to exhibit similar catalytic behavior (that is, rapid H_2O_2 decomposition and low selectivity to H_2O_2). A more promising methodology to attain stable, isolated Pd sites in a Au matrix for this reaction may involve the inverse of this synthesis technique – that is, deposition of small amounts of Pd onto pre-formed Au particles. Notably, Zhang et al[287] have demonstrated successful isolation of Pd sites in pre-formed Ag particles through galvanic displacement of Ag by Pd^{2+} salts.

7.4 Conclusions

Electroless deposition is a suitable technique for the preparation of Au-Pd catalysts, as has been demonstrated in the literature.[267-269] However, approaching monolayer coverage of Au on Pd is challenging, because autocatalytic deposition of Au becomes dominant at moderate Au coverages. The resulting Au-Pd catalysts are ineffective for improving selectivity toward H_2O_2 in the direct synthesis reaction, presumably because contiguous Pd ensembles active for O-O bond dissociation remain at the surface. Further studies related with optimization of the ED bath would be necessary to avoid or decrease the effect of the autocatalytic deposition for a more effective Au loading and isolation of Pd sites. Alternate preparation methodologies should also be explored to attain this desirable type of Au-Pd ensemble.[287-289]

Supplementary Figures, Tables, and Methods for Chapter 7

Synthesis of Au-Pd/SiO_2 catalysts by electroless deposition

The Pd site density of the monometallic base catalyst (Pd/SiO_2) was determined by CO chemisorption (using a surface stoichiometry of 2/3 for CO/Pd)[180] to calculate the amount of Au required for certain coverage. For example, the surface site density for the Pd/SiO_2 (ld) catalyst was 91 μmol Pd exposed g^{-1} catalyst by CO chemisorption, which means that 91 μmol Au g^{-1} catalyst should be deposited for a theoretical 1 monolayer (ML) Au coverage. The same bath was used for the preparation of all the bimetallic catalysts, and the amount of added Pd/SiO_2 catalyst was adjusted to obtain the desired coverage. A large bath was prepared by adding 43.5 mg of precursor ($KAu(CN)_2$) and 227 mg of $N_2H_4 \cdot H_2O$ to 240 mL of a NaOH solution with pH 9. That bath was divided into beakers (80 mL in each) and different amounts of Pd/SiO_2 monometallic catalysts were added: 556 mg (for the theoretical 1 ML Au-Pd/SiO_2 catalyst), and 278 mg (for the theoretical 2 ML Au-Pd/SiO_2 catalyst). The third batch (no Pd/SiO_2 added) was used to determine the stability with respect to formation of small Au particles.[267] The UV-Visible adsorption spectrum of the ED bath was measured using a Beckman DU® 520 scanning spectrophotometer. A scan of water at pH 9.0 was used as the reference. The ED bath was stable for at least 3 h at room temperature under stirring (no adsorption bands appeared on the spectrum, not shown), longer than the time used for deposition of Au on Pd/SiO_2.

Characterization of Au-Pd/SiO_2 catalysts by FTIR

Peak assignments for the catalysts analyzed by FTIR can be found in Table S7.1. In the case of Pd/SiO_2 (hd), the linear region was deconvoluted into four bands centered at 2113, 2094, 2065 and 2042 cm^{-1}, and the non-linear region was deconvoluted into four bands centered at 1971, 1952, 1890 and 1816 cm^{-1}. In the case of Pd/SiO_2 (ld), the linear region was deconvoluted into two bands at 2091 and 2066 cm^{-1}, while the non-linear region was deconvoluted into four bands at 1973, 1939, 1891 and 1833 cm^{-1}. Following Au deposition, peak shifts to lower frequencies are generally observed and the peak intensities decrease.[267]

Table S7.1 FTIR peak positions and intensity ratios for Pd/SiO_2 and Au-Pd/SiO_2 catalysts.

	Linear region (L)				**Non-linear region (NL)**				**Linear/non-linear area (L/NL)**
	L1	**L2**	**L3**	**L4**	**NL1**	**NL2**	**NL3**	**NL4**	
Pd/SiO_2 (hd)	2113	2094	2065	2042	1971	1952	1890	1816	0.78
0.53 ML Au-Pd/SiO_2 (hd)			2076	2039		1939	1884	1826	0.46
Pd/SiO_2 (ld)		2091	2066		1973	1939	1891	1833	0.12
0.69 ML Au-Pd/SiO_2 (ld)			2045	2013		1933	1868		0.16

Peak assignments referenced from references # [267, 290]
L1, L2: Pd^0 terraces
L3, L4: low coordination Pd^0
NL1, NL2: bridge sites of low index planes
NL3, NL4: three-fold sites of Pd(111)

Additional reactivity data and evaluation of mass transfer limitations

Table S7.2 Decomposition of H_2O_2 (ld catalysts) using a 2 wt % H_2O_2 feed solution in 1:1 molar ratio MeOH:H_2O solution. H_2 conversion was determined by gas chromatography before/after reaction. Batch conditions: 278 K: 2.9 MPa 5 % H_2/CO_2; stir rate 1500 rpm.

	H_2O_2 conversion / %	H_2O_2 decomposed[a] / %	H_2O_2 decomposed[b] / %
Pd/SiO_2 (ld)	39	83	17
0.69 ML Au-Pd/ SiO_2 (ld)	43	78	22

[a]From hydrogenation, based on H_2 consumed.
[b]From disproportionation, based on difference between H_2O_2 decomposed and H_2 consumed.

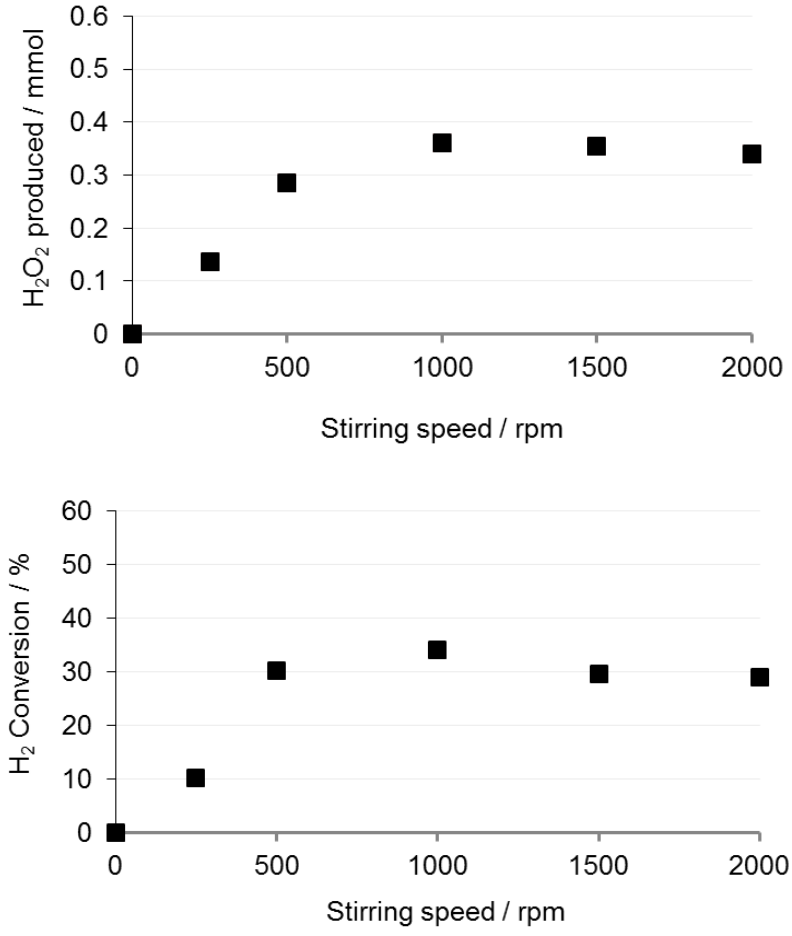

Figure S7.1 Effect of stirring speed on H_2 conversion and H_2O_2 production during H_2O_2 synthesis using 0.69 ML AuPd/SiO_2 catalyst (ld). Batch conditions: 278 K; 2.9 MPa 5 % H_2/CO_2 + 1.2 MPa 25 % O_2/CO_2; 12g of 1:1 molar ratio MeOH:H_2O solution; 12 mg catalyst; 20 minutes reaction time.

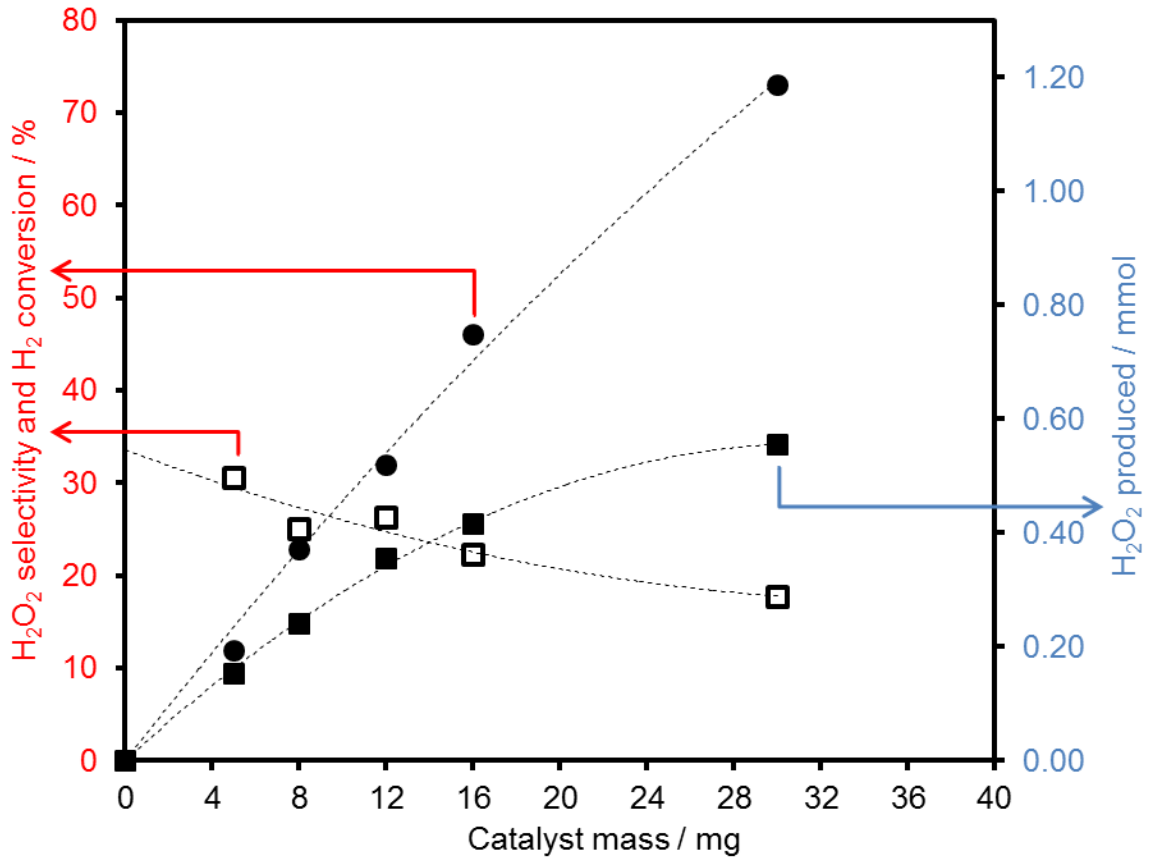

Figure S7.2 (●) H_2 conversion, (□) selectivity to H_2O_2 and (■) mmol of H_2O_2 produced versus mass of 0.69 ML AuPd/SiO_2 catalyst (ld) used in the reaction. Batch conditions: 278 K; 2.9 MPa 5 % H_2/CO_2 + 1.2 MPa 25 % O_2/CO_2; 12 g 1:1 molar ratio MeOH:H_2O solution; stir rate 1500 rpm. Dotted lines are to guide the eye.

Chapter 8: The Effect of Surface, Subsurface, and Bulk Hydrogen on Pd Catalysts

8.1 Introduction

In Chapters 3-6, we considered metallic Pd in our density functional theory models with adsorption restricted to the Pd surface. Our calculations indicated that Pd's reactivity can depend strongly on its surface coverage of reaction intermediates (hydroxyl, Chapter 4) and promoter species (halides, Chapters 5-6). These results underscore the importance of defining physically accurate surface models for DFT calculations that capture the nature of the catalyst surface under reaction conditions.

The DSHP reactants (H_2 and O_2) can also modify the subsurface and bulk regions of Pd nanoparticles. The effects of H or O atoms migrating to the Pd subsurface have not been well-characterized for the DSHP, but subsurface species can play important roles in other transition-metal-catalyzed chemistries such as selective hydrogenation of alkynes,[291, 292] ethylene

epoxidation,[156, 293] and methanol oxidation.[294] Although various DSHP experiments using supported Pd catalysts demonstrate that activity and selectivity strongly depends on the catalyst pretreatment environment (i.e., temperature and presence of H_2, O_2, or an inert gas),[46, 66, 67, 70, 71, 173] there is no consensus regarding which surface/bulk phase(s) of Pd represent its catalytically active state.

In this chapter we utilize DFT calculations to understand the extent to which hydrogen on the surface, in the subsurface, and in the bulk affect the reactivity of Pd in the DSHP. We are particularly interested in the reason why co-fed H_2 is generally observed to enhance the H_2O_2 decomposition activity of Pd catalysts.[31, 36, 51, 59, 169, 170, 295] Hydrogen can readily penetrate into the Pd lattice and form bulk phases at the typical temperatures and H_2 pressures utilized for the DSHP. In fact, Pd is one of the most widely-studied hydrogen storage materials.[296] Bulk Pd forms two phases with hydrogen below the critical temperature of 300 °C: α, a solid solution, and β, the Pd hydride.[297] The former is characterized by a low H:Pd atomic ratio (below ca. 0.1), while the latter is characterized by a higher H:Pd atomic ratio (above ca. 0.5), and there is a phase transition region where both the α- and β-phases coexist. Notably, there is a concomitant expansion of the Pd lattice constant with β-phase formation, which increases with an increasing H:Pd atomic ratio. The lattice constant in the α-phase remains close to that of metallic Pd.[64] These phases, as well as the lattice expansion, have also been characterized for Pd nanoparticles as small as a few nanometers.[298] Furthermore, there is experimental evidence that the presence of an aqueous solvent does not have a significant effect on Pd hydride formation in supported Pd catalysts.[299] Therefore subsurface hydrogen/bulk phase transformation to Pd hydride may be relevant to both gas- and liquid-phase processes for the DSHP or *in situ* H_2O_2 production from H_2 and O_2.

8.2 Computational Methods

All DFT calculations in this chapter were performed using the density functional theory code VASP[137, 226] in the generalized gradient approximation (GGA-PW91).[109] The projector augmented wave (PAW)[227, 228] method was used to describe the electron-ion interactions, and the electron wave functions were expanded using plane waves with an energy cutoff of 400 eV. The convergence criterion for geometric relaxations was 0.02 eV $Å^{-1}$. The Pd(111) substrate was represented by a periodically repeated (2 × 2) unit cell with six atomic layers. This slab was separated in the z-direction from its successive image by a vacuum layer of at least 11 Å. The top three slab layers were allowed to relax, and the bottom three slab layers were fixed at their bulk lattice positions. The calculated lattice constant for pure Pd, 3.96 Å, is in good agreement with the experimentally measured value of 3.89 Å.[141] The first Brillouin zone was sampled with a (6 × 6 × 1) Monkhorst-Pack k-point mesh.[143] Adsorption was modeled by placing adsorbates on one side of the slab, with the electrostatic potential adjusted accordingly.[139, 140] Subsurface hydrogen was modeled by placing hydrogen atoms at the octahedral sites in the Pd(111) slab. All hydrogen atoms in the first three subsurface layers were allowed to relax, while hydrogen atoms in the fourth and fifth subsurface layers were fixed at the lattice positions calculated for the bulk Pd hydride.

Binding energies of intermediates were referenced to the corresponding gas-phase species and either the clean Pd(111) slab:

$$BE = E_{adsorbate+slab} - E_{gas\text{-}phase\ adsorbate} - E_{slab}$$

or the hydrogen-modified Pd(111) slab:

$$BE = E_{adsorbate+hydrogen+slab} - E_{gas\text{-}phase\ adsorbate} - E_{hydrogen+slab}$$

where $E_{adsorbate+slab}$ is the total energy of the clean slab with adsorbate, $E_{gas\text{-}phase\ adsorbate}$ is the total energy of the adsorbate in the gas-phase, E_{slab} is the total energy of the clean slab, $E_{adsorbate+hydrogen+slab}$ is the total energy of the slab with surface/subsurface hydrogen and the adsorbate, and $E_{hydrogen+slab}$ is the total energy of the slab with surface/subsurface hydrogen. Binding energies were verified to be within 0.1 eV (referenced to the BEs calculated using the parameters stated above) upon increasing the k-point set to (8 × 8 × 1), increasing the energy cutoff to 500 eV, or relaxing the fourth metal layer.

The minimum energy paths for elementary steps were calculated using the climbing image nudged elastic band method (CI-NEB[112, 115]) with seven interpolated images. Transition states for non-spontaneous steps were verified by identification of a single imaginary frequency along the reaction coordinate.

8.3 Results and Discussion

Hydrogen on and in the Pd(111) surface can influence adsorption properties and activation energy barriers through introducing lattice strain and modifying Pd's electronic structure.[300] We first discuss the Pd hydride model, and then study the binding strength of atomic oxygen as Pd(111) saturates with hydrogen. We anticipate the trend for atomic oxygen to be representative of the other oxygen-containing intermediates in the DSHP reaction network (OH*, OOH*, O_2*, H_2O_2*), because all these intermediates bind to Pd(111) through the oxygen atom.[253] Then we examine hydrogenation behavior as a function of hydrogen content in Pd(111); we consider both surface hydrogen (H*) and subsurface hydrogen (H^{sub}) as reactants. Finally, we present the energetics for adsorption and dissociation of H_2O_2 on hydrogen-saturated Pd(111).

8.3.1 The Pd hydride model

The Pd lattice retains its fcc structure and expands isotropically when it absorbs hydrogen, with hydrogen atoms occupying the octahedral sites (the crystal structure for a 1:1 bulk atomic ratio of H:Pd is that of NaCl).[64, 301, 302] We calculate the Pd lattice expansion induced by absorbed hydrogen in an analogous manner to the work of Studt et al.[303] We consider five H:Pd atomic ratios (0, 0.25 0.5, 0.75, and 1), and the percent lattice expansion with respect to pure Pd is shown in Figure 8.1 for each composition. These results are in good agreement with the calculations from Studt et al[303] and an empirically derived relationship for the lattice expansion above the Pd hydride critical point from Feenstra, Griessen, and de Groot,[304] which we include in Figure 8.1. (Feenstra, Griessen, and de Groot[304] also show that lower temperature data between 77 K and 298 K agree well with their empirical relation.) Our calculated lattice constant for the 1:1 H:Pd composition (4.15 Å) is 4.8 % larger than that of pure Pd (3.96 Å), and we use this (idealized) stoichiometric model as the limiting case for complete saturation of Pd by hydrogen in the next sections. In real catalytic systems, the stoichiometric hydride may be an unrealistically high hydrogen concentration.[298, 301] However, we are interested primarily in extracting trends in binding energies and activation barriers; and nonetheless it is possible that such dense hydrogen concentrations may exist in local regions of the catalyst.

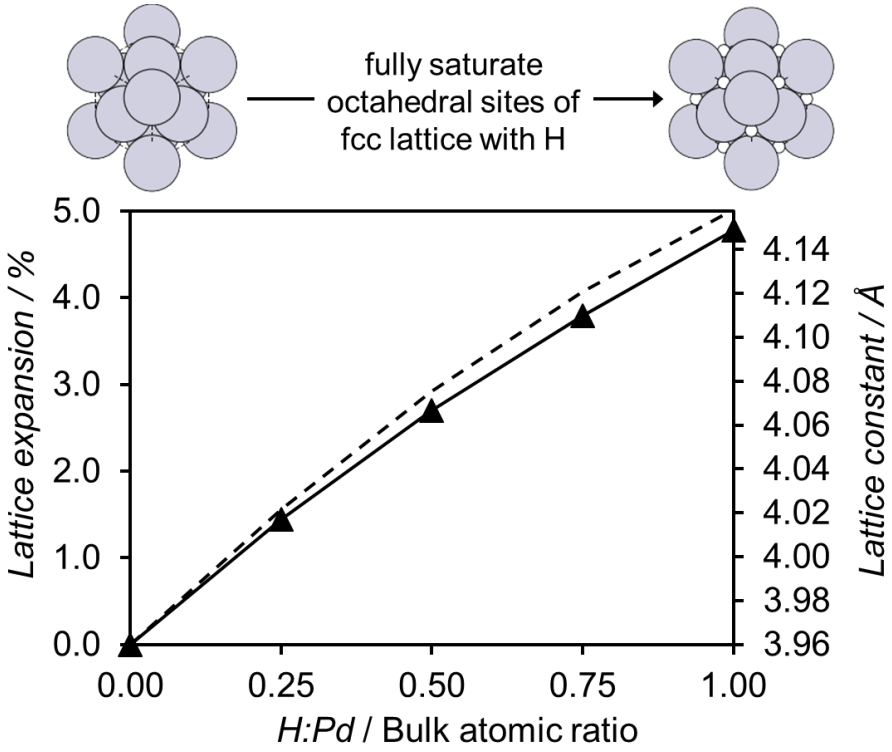

Figure 8.1 DFT-calculated lattice expansion of Pd hydride versus bulk atomic ratio of H:Pd (black triangles). The solid line is to guide the eye. The corresponding lattice constant can be read from the vertical axis on the right. The dashed black line shows the percent lattice expansion calculated from an empirically derived relationship for bulk Pd hydride above the critical point.[304] The image on top of the graph shows the fcc bulk Pd lattice (left) and the fcc bulk Pd lattice with H saturating the octahedral sites, corresponding to a H:Pd atomic ratio of 1:1 (right); the cubic unit cell is marked by dashed black lines. Atom colors: Pd (gray) and H (white).

Our Pd(111) hydride surface model (denoted by PdH(111)) is shown in Figure 8.2. In this model, hydrogen atoms occupy all subsurface octahedral sites and the lattice constant corresponds to that calculated for the 1:1 H:Pd bulk atomic composition. We also populate the surface with a full monolayer (ML) of hydrogen atoms in hcp sites; this configuration is 0.33 eV more stable than having the surface hydrogen atoms in the fcc sites (where they are directly above the hydrogen atoms in the octahedral sites of the first subsurface layer), which agrees qualitatively with previous calculations.[305] We then examined vacancy formation to understand which regions of PdH(111) are likely to be hydrogen-deficient at sub-stoichiometric H:Pd concentrations (Figure 8.2). A single hydrogen vacancy in PdH(111) is most energetically favorable in the first subsurface layer, and a second hydrogen vacancy is also most favorable in this layer. The surface is the least

favorable vacancy position. Thus the first subsurface layer appears most likely to have the lowest population of hydrogen compared to the Pd bulk or surface layer, and there is a thermodynamic driving force for hydrogen from the subsurface layers to repopulate surface hydrogen if it is depleted (e.g., by surface reactions). Teschner et al[306] calculated that diffusion of a hydrogen atom from the fourth subsurface layer to the surface of clean Pd(111) requires overcoming kinetic barriers of only about 0.2 eV, demonstrating that bulk absorbed hydrogen can readily emerge to the surface.

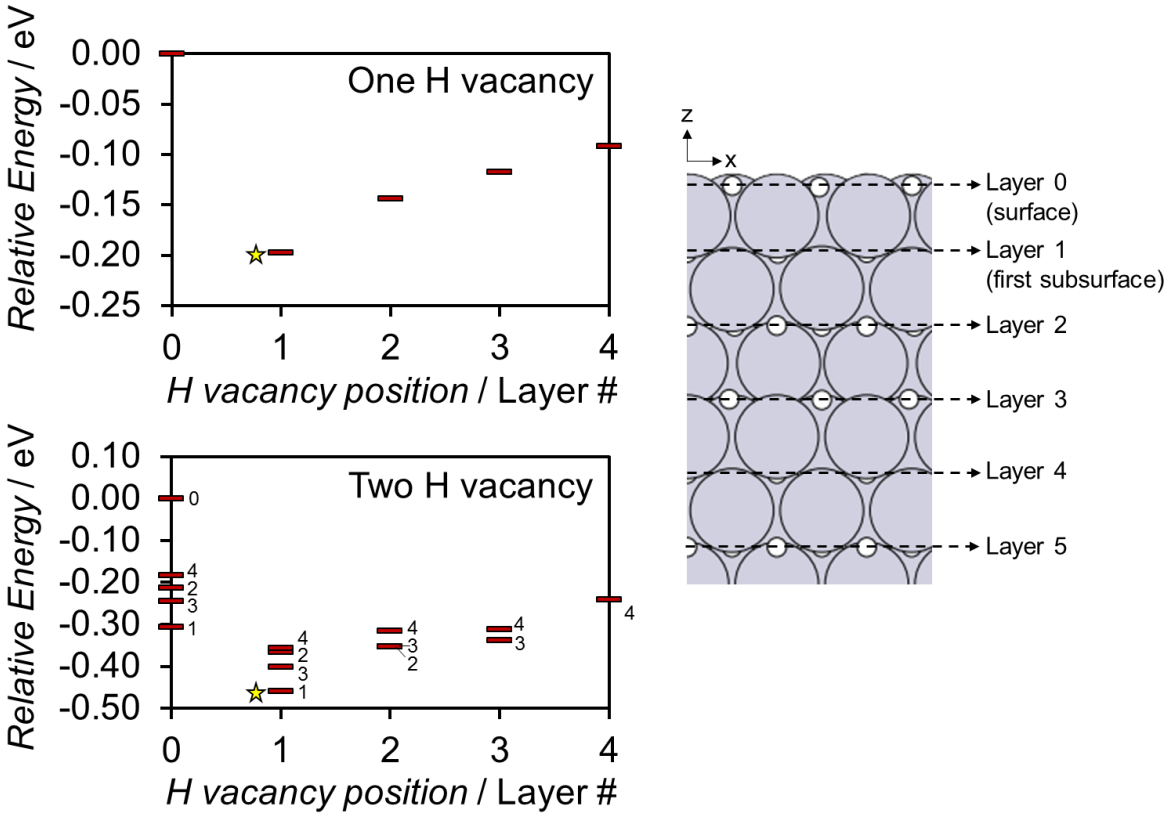

Figure 8.2 Preferred positions for H vacancy formation in the PdH(111) slab. The PdH(111) surface model is saturated with hydrogen on all surface hcp sites and all subsurface octahedral sites, and the Pd lattice constant corresponds to that calculated in Figure 8.1 for a 1:1 H:Pd bulk atomic ratio. The top graph corresponds to a single H vacancy, and the bottom graph corresponds to two H vacancies. In the bottom graph, the numbers next to each red bar represent the layer in which the second H vacancy occurs. The yellow star indicates the most stable vacancy positions for the cases of one and two H vacancies. A side view of the Pd slab is pictured on the right, with the layer numbers corresponding to surface and subsurface hydrogen labeled accordingly. Atom colors: Pd (gray) and H (white).

8.3.2 Oxygen adsorption

Our strategy to probe the extent to which sorbed hydrogen can affect surface chemistry is to first examine the binding strength of atomic oxygen on Pd(111) as a function of increasing hydrogen content. Because the binding energies of the other oxygen-containing species in the DSHP have been shown to scale reasonably well with the binding energy of atomic oxygen,[253, 307] these results may provide a qualitative understanding of how hydrogen coverage affects the overall potential energy surface for the DSHP. We place an oxygen atom at its most stable surface binding sites (the threefold fcc and hcp sites), and then increase the hydrogen content sequentially – first saturating the surface to a full monolayer of adsorbates (including the oxygen atom), then saturating the octahedral sites in the first subsurface layer, and finally saturating the octahedral sites in the remaining subsurface layers and expanding the Pd lattice to form PdH(111). The results are presented in Figure 8.3.

Co-adsorbed surface hydrogen substantially destabilizes atomic oxygen. The decrease in oxygen's binding strength is approximately linear with respect to the H* coverage, and the absolute decrease in binding energy when the surface has a full ML of O* and H* is 0.83 eV with respect to the clean-surface value. These results are the same for O* at the fcc and hcp sites. Adding H^{sub} to the octahedral sites in the first subsurface layer does not cause substantial changes to the binding energy of oxygen at the hcp site (deviations are less than 0.1 eV). However, H^{sub} in the first subsurface layer further destabilizes O* considerably at the fcc site; H^{sub} is directly below the surface-adsorbed O* and H* in this configuration, which causes a greater repulsive interaction than the case of O* at the hcp site.[305] Saturating the remaining octahedral sites and expanding the Pd lattice to form PdH(111) again only weakly affects the binding of oxygen at the hcp site, while

this further destabilizes O* at the fcc site by 0.20 eV with respect to H^{sub} saturating the first subsurface layer.

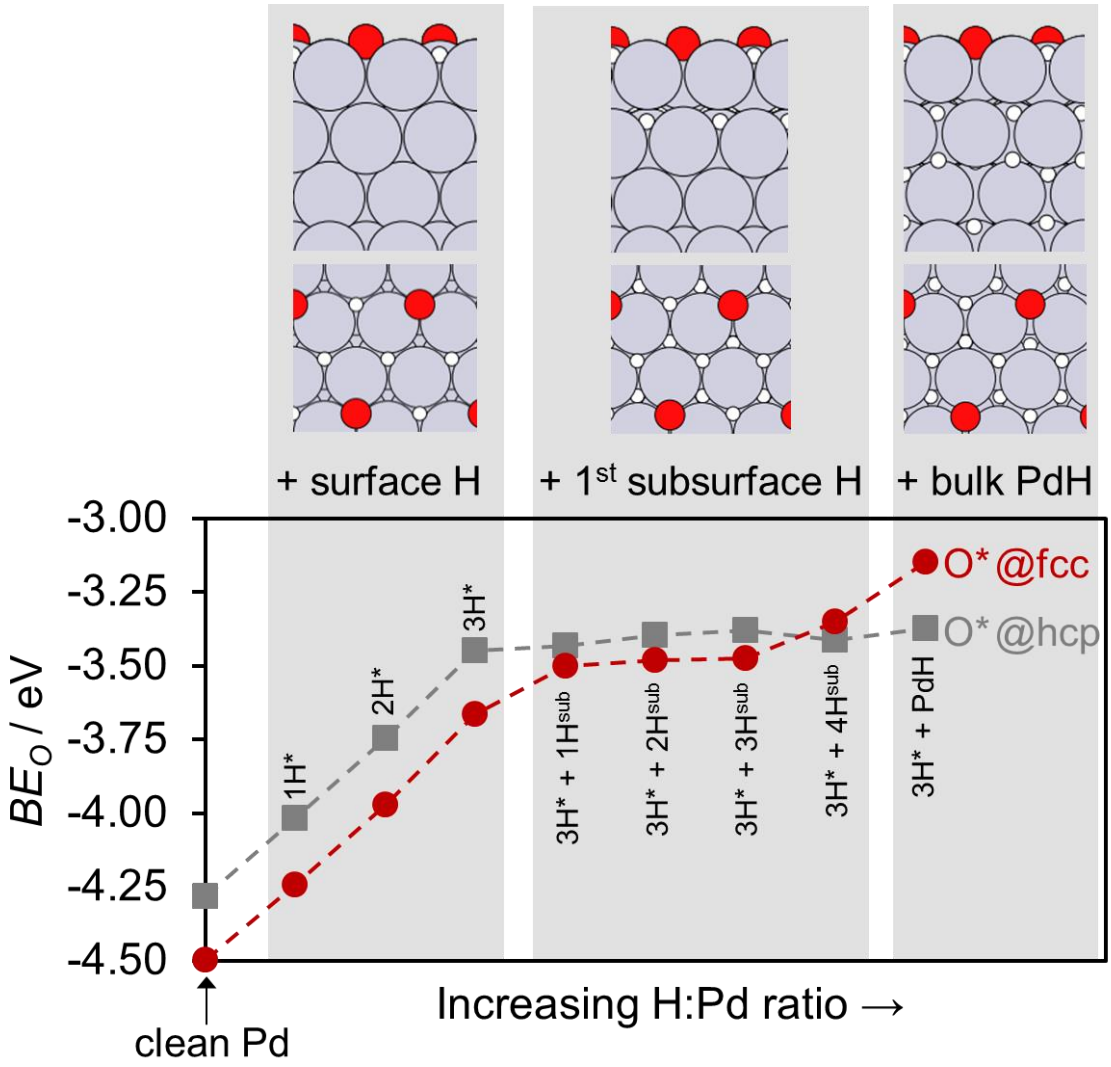

Figure 8.3 Binding energies of atomic oxygen (BE_O) at surface fcc (red circles) and hcp (gray squares) sites as a function of increasing H content on the surface (H*) and in the subsurface (H^{sub}) of Pd(111). Dotted lines are to guide the eye. The PdH(111) surface model is saturated with hydrogen in all subsurface octahedral sites, and the Pd lattice constant corresponds to that calculated in Figure 8.1 for a 1:1 H:Pd bulk atomic ratio. All H atoms on the Pd surface are placed at fcc sites (when O* is in the fcc site) or hcp sites (when O* is in the hcp site). The images on top of the graph depict the side and top-down views of the Pd slab (with O* at the hcp site) corresponding to the highest H content in each shaded gray region. Atom colors: Pd (gray), O (red), and H (white).

Figure 8.3 suggests that increasing the hydrogen content on Pd(111) makes the surface more passive toward adsorption, and a similar effect has also been calculated for the binding of carbon-containing compounds such as ethylene and acetylene to Pd.[303] Our calculations for atomic

oxygen show that the local coverage of *surface* hydrogen has the largest impact on binding energy, but further population of subsurface sites with hydrogen induces only marginal changes – except for the case of surface adsorption sites directly above H-occupied subsurface sites. Furthermore, the decreased interaction strength of oxygen with hydrogen-saturated Pd indicate that, in regions of the catalyst where the local surface concentration of hydrogen is high, activation barriers for elementary steps such as O-O bond dissociation and O-H bond formation may vary significantly from their clean-surface values (see trend in Figure 3.2 and references # [308, 309]).

8.3.3 Oxygen hydrogenation

In Chapter 3 we calculated that direct hydrogenations of oxygen-containing intermediates by H* can require overcoming large activation barriers. The presence of surface and subsurface sorbed hydrogen can potentially modify Pd's hydrogenation ability, and in addition subsurface hydrogen might provide an alternative hydrogen source for these reactions. We take the hydrogenation of atomic oxygen at the hcp site as a case study. Not only is this elementary step pertinent to direct water formation in the DSHP, but it also may play a role in the secondary H_2O_2 decomposition reactions – specifically, the complete hydrogenation of H_2O_2 to water.

The minimum energy pathway for O* hydrogenation at the hcp site is shown in Figure 8.4. H* and O* bind to neighboring hcp sites in the initial state, and OH* binds to a bridge site with its O-H bond tilted away from the surface plane in the final state. The O-H bond length at the transition state is 1.52 Å, and the activation energy barrier is 0.71 eV with respect to the initial state. Interestingly, we find that saturating the remaining surface hcp sites and first subsurface octahedral sites with hydrogen spectators changes the activation barrier for this pathway by less than 0.03 eV – despite a large variation in the reaction energy of 0.41 eV (Figure 8.4). Complete saturation to PdH(111) also has a relatively small effect on the activation barrier. In all cases,

higher hydrogen content in Pd(111) increases the exothermicity of O* hydrogenation. We conclude that the kinetics for O* hydrogenation by H* on Pd(111) can be relatively insensitive to the local hydrogen environment, while the thermochemistry can change significantly; other hydrogenation pathways for O* (and the O_2*, OOH*, and OH* intermediates) should be explored to determine if these results are a general feature for hydrogenations of the oxygen-containing intermediates on hydrogen-modified Pd(111).

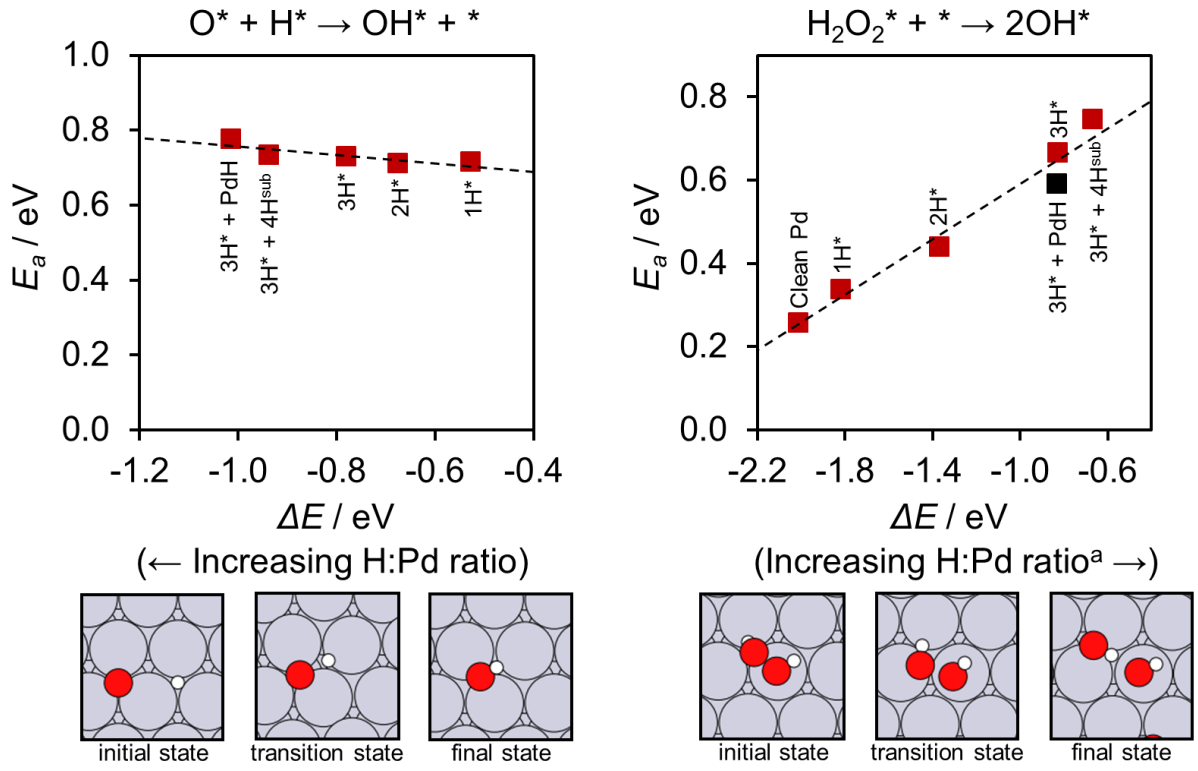

Figure 8.4 Activation energy barriers (E_a) for H_2O_2* decomposition and O* hydrogenation on Pd(111) as a function of the reaction energy (ΔE), at different concentrations of H on the surface (H*) and in the subsurface (H^{sub}). The dotted black line represents the best-fit line through all data points. Energies are with respect to the initial and final states in the NEB pathway. [a]The black point for H_2O_2* decomposition has the highest H:Pd ratio (and corresponds to PdH(111)), but actually has a more exothermic reaction energy and a smaller activation barrier than the cases where only the surface and first subsurface saturate with hydrogen. The images below each graph depict top-down views of the initial, transition, and final states of the NEB pathway under consideration on clean Pd(111) (no spectator hydrogen atoms). The geometries of these states are similar in the presence of the spectator hydrogen atoms. Atom colors: Pd (gray), O (red), and H (white).

We then search for O* hydrogenation pathways involving subsurface hydrogen. For these NEB calculations we use initial states of O* at hcp or fcc sites, and a single hydrogen atom at

octahedral or tetrahedral subsurface sites in the first subsurface layer of Pd(111). We only find a single one-step route for the reaction between H^{sub} and O*; all other routes involve a two-step mechanism whereby H^{sub} first emerges to a surface hcp or fcc site – pushing O* to a neighboring hcp or fcc site if the initial state configuration for H^{sub} is directly beneath O* – and then reacts with O* to form OH*.

The one-step route is shown in Figure 8.5. The initial state contains O* in an fcc site, and H^{sub} in the octahedral site directly beneath O*. H^{sub} moves upward toward O*, and at the transition state the O-H bond length is 1.24 Å. The final state is OH* bound to a bridge site, with the O-H bond pointing away from the surface plane. The activation barrier and reaction energy for this pathway are 1.44 eV and -0.61 eV, respectively. Clearly, the large kinetic barrier for this route make it highly unfavorable compared to the surface reaction between O* and H*. The Pd-Pd bond lengths in the fcc site where O* is adsorbed stretch to 3.00 Å to accommodate the transition state, and at the next-nearest neighbor hcp site the Pd-Pd bond lengths compress to 2.60 Å. (The equilibrium Pd-Pd bond length is 2.80 Å.) This lateral strain might be alleviated by the expansion of the Pd lattice induced by Pd hydride formation (Figure 8.1), and so we also examine this one-step hydrogenation route on our PdH(111) model. Indeed, there is less lateral strain in the top Pd layer of PdH(111) at the transition state; all Pd-Pd bond lengths in the surface layer are stretched or compressed by less than 4.8 % on PdH(111) at the transition state compared to 7.1 % on clean Pd(111) (relative to the respective equilibrium Pd-Pd bond lengths in PdH(111) and Pd(111)). The activation barrier for O* hydrogenation by H^{sub} on PdH(111) is 1.06 eV. This barrier is 0.38 eV lower than the barrier on clean Pd(111), but it is still substantially higher than that of the surface reaction between O* and H*. Similar conclusions were found for methyl radical hydrogenation by subsurface hydrogen on Ni(111): the one-step route, involving subsurface hydrogen reacting

directly with a methyl radical adsorbed above it at a surface threefold site, was calculated to be much less kinetically favorable than the surface reaction between the methyl radical and H*.[310, 311]

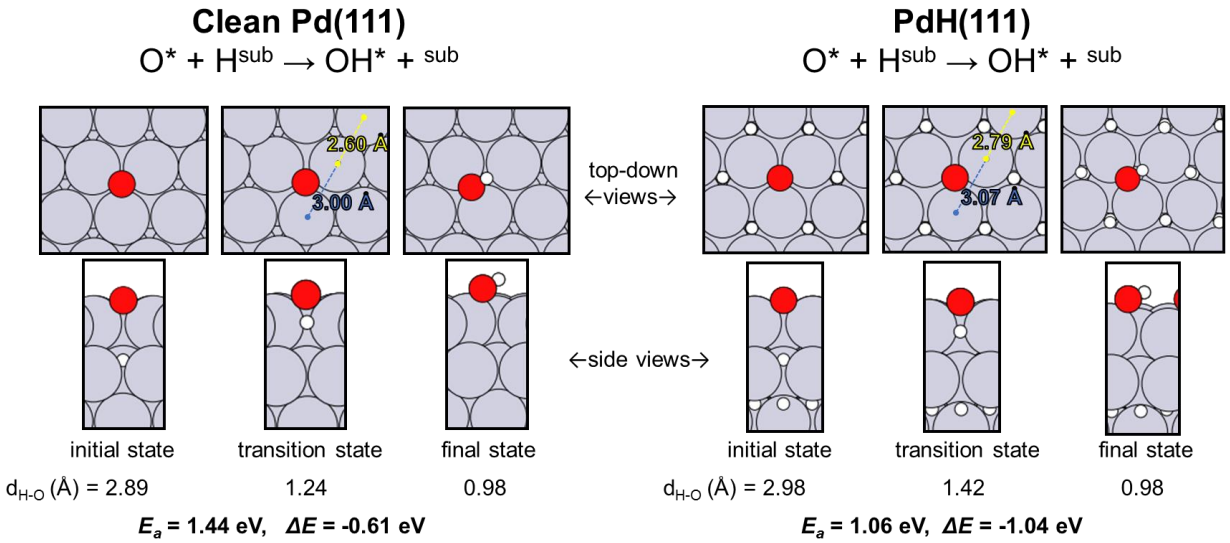

Figure 8.5 Pictorial representation of O* hydrogenation by H^{sub} on (left) clean Pd(111) and (right) PdH(111), including activation barriers (E_a), reaction energies (ΔE), and geometric parameters. The PdH(111) surface model contains H* in all fcc sites. $d_{O\text{-}H}$ corresponds to the distance between O* and the H^{sub} atom involved in the reaction. In the top-down views of the transition state, Pd-Pd bond lengths are provided to demonstrate the lateral strain at the transition state, where yellow represents compressive strain and blue represents expansive strain (equilibrium Pd-Pd bond lengths on clean Pd(111) and PdH(111) are 2.80 Å and 2.93 Å, respectively). Atom colors: Pd (gray), O (red), and H (white).

Although our results suggest that a single-step recombination of subsurface hydrogen with surface intermediates may be kinetically unfavorable on Pd(111) or PdH(111) compared to the direct reaction with surface hydrogen, this route may be more relevant on other surface features of Pd. The direct role of subsurface hydrogen in hydrogenation reactions is an actively investigated subject in both experimental and theoretical literature for transition metal catalysts,[110, 310-316] and one alternative explanation as to how subsurface hydrogen can play a direct role in catalysis invokes a thermodynamic argument: namely, subsurface hydrogen is metastable with respect to surface hydrogen and can produce more active surface hydrogen species upon emerging to the surface – compared to thermally equilibrated surface hydrogen.

8.3.4 H_2O_2 adsorption and dissociation

We end this chapter by investigating the adsorption and dissociation of H_2O_2 in the presence of surface, subsurface, and bulk sorbed hydrogen. This section is motivated by the experimental observation that the presence of H_2 generally increases the total H_2O_2 consumption rate over Pd-based catalysts.[31, 36, 51, 59, 169, 170, 295] The effect can be twofold: first, H_2 can modify the Pd active sites to accelerate H_2O_2 decomposition (Chapter 4), and second, H_2 opens the hydrogenation mechanism wherein H_2 completely reduces H_2O_2 to H_2O. The O* hydrogenation reaction studied in the previous section may play an important role in the hydrogenation mechanism – e.g., sweeping O*, which is a product of O-O bond dissociation, from the Pd surface.

Experimentally decoupling the hydrogenation and decomposition reactions of H_2O_2 on pure Pd catalysts can be difficult due to the fast kinetics and the potential for H_2 to react with the O_2 produced by H_2O_2 decomposition. Choudhary, Samanta, and Jana[59, 295, 317] have demonstrated that unless an aqueous reaction medium is modified with halides, there is a rapid evolution of O_2 during H_2O_2 decomposition in the presence of H_2, followed by a longer period of H_2 consumption; all H_2O_2 was consumed in over an order of magnitude less time than the case for which H_2 was absent – all other reaction conditions being the same.[59] The prolonged period of H_2 consumption is due to its reaction with the O_2 evolved during H_2O_2 decomposition. Their results show that (i) H_2 accelerates H_2O_2 decomposition on pure Pd, and (ii) H_2O_2 is mainly consumed through its decomposition reaction in the absence of catalyst modifiers such as the halides, rather than by a direct hydrogenation reaction between H_2O_2 and H_2. (We note that these experiments were performed at temperatures and H_2 partial pressures wherein Pd can favorably undergo a phase transition to its hydride.[298, 301]) We observed similar phenomena in preliminary H_2O_2

decomposition experiments using our same Pd/SiO_2sp catalyst from Chapter 4 and introducing H_2 into the reactor headspace.

Based on our microkinetic model for H_2O_2 decomposition, the adsorption and O-O bond dissociation energies for H_2O_2 on Pd(111) provide a good approximation to the apparent reaction barrier measured in an aqueous medium (Chapter 4, Figure S4.1). Therefore we examine these steps as a function of hydrogen content in Pd(111) to determine if spectator hydrogens can explain the increased decomposition rate in the presence of H_2. The activation barrier for H_2O_2* dissociation to 2OH* is presented in Figure 8.4. H_2O_2* dissociation is facile on clean Pd(111) with a barrier of 0.26 eV. Increasing the hydrogen content on the surface and in the first subsurface layer of Pd(111) substantially raises the dissociation barrier and lowers the dissociation exothermicity – with the relationship between these two quantities exhibiting a reasonably linear Brønsted-Evans-Polanyi type trend.[251] Moreover, the binding energy for H_2O_2* decreases in magnitude from –0.36 eV on clean Pd(111) to -0.17 eV on Pd(111) with its surface and first subsurface layer covered in hydrogen. The increased activation barrier and decreased adsorption strength of H_2O_2* in the presence of hydrogen spectators is *opposite* the behavior that would be expected for H_2 to accelerate this decomposition reaction (that is, these trends suggest an increased apparent activation barrier for H_2O_2 decomposition as hydrogen saturates Pd(111)).

We then calculated the H_2O_2* dissociation energetics on PdH(111). Although the activation barrier on PdH(111) (0.59 eV) is still much larger than that on clean Pd(111), it is noticeably smaller than that on Pd(111) covered with H* on the surface and H^{sub} in the first subsurface only. This observation prompted us to examine the dissociation step on PdH(111) in more detail, focusing on the effect of strain induced by lattice expansion to the Pd hydride. The effect of strain on the reactivity of metal surfaces is well-known,[92, 318, 319] and DFT calculations

have demonstrated that expansive strain can facilitate bond-breaking reactions such as O_2* dissociation.[320, 321] We consider the hypothetical case wherein H_2 forms a bulk hydride with Pd nanoparticles, expanding its lattice, but there also exist regions of the nanoparticle surface that are hydrogen-deficient. We model this case by removing hydrogen from the surface and subsurface of our PdH(111) slab, but keeping the lattice expanded. The activation energy barrier for H_2O_2* dissociation on this model is reduced to 0.19 eV, and the adsorption energy for H_2O_2* increases to -0.39 eV. Per our results in Chapter 4, this would translate to a one-to-two order of magnitude increase in the first-order rate constant for H_2O_2 decomposition at room temperature compared with the clean Pd(111) surface – assuming the pre-exponential factor does not change (Table 8.1). Thus, only a fractional population of these sites on a Pd hydride nanoparticle (i.e., hydrogen-deficient surface regions) would be necessary to explain the enhanced rate of H_2O_2 decomposition in the presence of H_2.

Table 8.1 Effect of hydride-induced strain on the kinetics for H_2O_2 decomposition at temperatures relevant to a DSHP process. According to our microkinetic model from Chapter 4, the apparent activation barrier for a first-order rate constant for H_2O_2 decomposition on Pd(111) can be well-approximated from the H_2O_2* binding energy (BE_{H2O2}) and dissociation barrier (E_a). This enables us to approximate the ratio of the rates between Pd(111) stretched to the lattice constant of PdH(111) (4.15 Å) and Pd(111) at the bulk lattice constant of pure Pd (3.96 Å) – assuming negligible differences in the pre-exponential factor on these two surfaces.

Temperature (K)	275	300	325
$Rate_{stretched\ Pd(111)} / Rate_{Pd(111)}$	59	43	32

$$Rate_{stretched\ Pd(111)} / Rate_{Pd(111)} \sim \exp(-\Delta\ k_B^{-1}\ T^{-1})$$

$$\text{where } \Delta = (E_{a,\ \text{stretched Pd(111)}} - E_{a,\ \text{Pd(111)}}) + (BE_{\text{H2O2, stretched Pd(111)}} - BE_{\text{H2O2, Pd(111)}})$$

8.4 Conclusions

In this chapter, we studied surface, subsurface, and bulk sorbed hydrogen on Pd(111) using three examples: O* adsorption, O* hydrogenation, and H_2O_2* dissociation. These examples

represent key aspects of the DSHP mechanism (i.e., adsorption of oxygenated intermediates, O-H bond formation, and O-O bond dissociation).

We found that, generally, hydrogen spectators have a passivating influence on Pd(111), with surface-adsorbed hydrogen having the strongest (destabilizing) interaction with oxygen adsorption. We then showed that hydrogenation can be insensitive to the presence of hydrogen spectators: the activation barrier to hydrogenate atomic oxygen varied by less than 0.06 eV between hydrogen-modified and clean Pd(111). In contrast, hydrogen spectators can strongly inhibit O-O bond dissociation: the barrier for H_2O_2 dissociation increased monotonically with increasing hydrogen coverage on the surface and in the first subsurface layer of Pd(111). However, the lattice expansion induced by Pd hydride formation can facilitate H_2O_2 adsorption and reduce its dissociation barrier on Pd sites that are hydrogen-deficient in the local surface and subsurface layers – which we tentatively proposed as an explanation for why the presence of H_2 has been experimentally observed to accelerate H_2O_2 decomposition over Pd catalysts.

Ultimately, our calculations demonstrate that strain and electronic effects induced by spectator hydrogen modify the adsorption properties and kinetic barriers on Pd(111) to varying degrees. Further analyses should be performed to corroborate the effects of spectator hydrogen on a wider range of the O-H bond-forming and O-O bond-dissociation reactions involved in the DSHP – in addition to elucidating possible direct role(s) of subsurface hydrogen species.

Chapter 9: Conclusions and Recommendations for Future Work

9.1 Conclusions

In this thesis, we described the application of density functional theory calculations – as well as kinetics experiments and microkinetic modeling – toward identifying some of the key characteristics of active and selective catalysts for the direct synthesis of hydrogen peroxide (DSHP). Our results highlighted specific mechanistic challenges on Pd catalysts, and provided insight into how these challenges can be mitigated through structural and compositional modifications to Pd.

We used DFT calculations to investigate the reactivity of the (100) facet of the late transition metals (Pd, Pt, Cu, Ag, and Au) toward the direct reaction between H_2 and O_2. We compared our results with previous calculations on the (111) facet of these metals,[55] and determined that O-O bond dissociation is easier and O-H bond formation is more difficult for the dioxygen species on the (100) facet. This suggests that the more coordinatively undersaturated

facets of the transition metals will have a stronger propensity to divert selectivity away from H_2O_2. Furthermore, the kinetic barriers appear to correlate with the binding strength of O on both the (111) and (100) facets, wherein stronger O binding indicates smaller O-O dissociation barriers and larger O-H bond formation barriers; the binding energy of O can potentially be used as a reactivity descriptor (and has been successfully employed as one for the analogous electrochemical oxygen reduction reaction[127]). However, the binding strength of O *does not* capture the H_2 activation ability of the catalyst. We employed a maximum rate analysis and predict that the activity of the noble metals (Cu, Ag, and Au) in the DSHP is limited by the substantial barriers for H_2 dissociation – which is a nearly spontaneous step on Pd and Pt. We therefore proposed that a second reactivity descriptor is necessary for the DSHP: the binding energy of H. Focusing on Pd, our DFT calculations indicate Pd's primary selectivity toward H_2O_2 to be limited by facile O_2 and/or OOH dissociations; the challenge is to modify Pd so as to decrease its affinity for O (more difficult O-O bond dissociation) but maintain its affinity for H (facile H_2 dissociation).

We also developed a self-consistent microkinetic model that describes experimental H_2O_2 decomposition kinetics on a supported Pd catalyst, and determined that the O-O bond-breaking capacity of Pd is the central kinetic parameter governing H_2O_2 decomposition activity. Once the O-O bond breaks, a series of thermodynamically-driven hydrogen-transfer steps closes the catalytic cycle. These latter steps had not been explored on Pd in the computational literature, but we find them essential to explaining Pd's high activity toward H_2O_2 decomposition. Another valuable insight from our microkinetic model is that in addition to the kinetic barrier for O-O bond dissociation, the adsorption energy of H_2O_2 also contributes to the apparent activation barrier. This presents a second approach to inhibiting H_2O_2 decomposition, in addition to modifying Pd's

intrinsic O-O bond dissociation ability: destabilizing the adsorption strength of H_2O_2 relative to the bulk phase.

We then examined how modifications to Pd affect its reactivity, focusing on those that have been widely employed in the experimental literature. We performed DFT calculations on halide-covered Pd(111) and Pd(100) surface models, which revealed multiple causes for the improved performance of Pd catalysts in the presence of halides. These include raising the kinetic barriers for O-O bond dissociation in O_2 and OOH, and blocking H_2O_2 re-adsorption. Our calculations further demonstrated that the beneficial effects of halides are substantially less potent on Pd(100) compared to Pd(111) – but because halides have a stronger affinity for the more coordinatively undersaturated facets, we concluded that halides might also serve to selectively poison these Pd sites.

We additionally characterized a series of Au-Pd catalysts prepared by deposition of Au onto pre-existing Pd nanoparticles. Measurements of H_2O_2 synthesis and decomposition rates on these catalysts clarified a desirable Au-Pd ensemble that should be targeted in future synthesis efforts. Finally, we used DFT calculations to understand how hydrogen surface, subsurface, and bulk spectators on Pd might affect the H_2O_2 decomposition rate. Our calculations suggest that the lattice expansion induced by hydride formation in the bulk of Pd can facilitate the initial adsorption and O-O bond dissociation steps in H_2O_2, but the energetics for these steps are sensitive to the local surface environment of sorbed hydrogen.

9.2 Recommendations for Future Work

There are several potential extensions to the work presented in this thesis, which can be categorized as (i) increasing the complexity of the Pd surface models to better capture the impact

of the reaction environment and (ii) using our theoretical insights to construct a predictive framework for the identification of improved catalysts and conditions.

9.2.1 Increase complexity of Pd surface models

9.2.1.1 Solvent

The DFT calculations in this thesis were gas-phase calculations, but the DSHP is generally performed in a liquid solvent. In addition to modulating the solubility and mass transfer characteristics of the gaseous H_2 and O_2 reactants, the solvent can interact with reaction intermediates, transition states, and promoters such as the halides. For example, many of the reaction intermediates can donate/accept hydrogen bonds. Several experimental studies have demonstrated that the activity and selectivity of Pd-based catalysts in the DSHP can be sensitive to the choice of solvent,[66, 255, 322] but the origin of these apparent solvent effects[323, 324] is not well understood and is often attributed to the solubility differences for the H_2 and O_2 reactants.

The analysis of liquid-solid interfaces by electronic structure calculations such as DFT is significantly more complex than gas-solid interfaces and can be computationally demanding, especially when considering full reaction networks.[325] Continuum solvent models would be the least computationally expensive and could be broadly applied to approximate the energetic effects of different solvents on elementary steps explored in this thesis. However, explicit solvent models may be more valuable to probe localized phenomena such as direct solvent participation in elementary steps.[326] To improve the understanding of solvent effects in the DSHP, we recommend focusing on three specific aspects that build upon our work:

(i) A liquid solvent may facilitate the transfer of hydrogen atoms from the Pd surface to oxygen-containing intermediates. Wilson and Flaherty[58] have also recently proposed a heterolytic pathway

for H_2 dissociation and hydrogenation of O_2 in protic solvents. In this thesis, we calculated gas-phase hydrogenation barriers assuming a direct reaction between surface bound hydrogen atoms and oxygen species (Chapter 3). These barriers may then represent upper-bounds for the hydrogenation kinetics when a liquid solvent is present; DFT calculations can be employed to probe for lower-energy pathways at solid-liquid interfaces – for example, in a manner similar to the work of Desai and Neurock.[327] These results would enable more accurate energetic comparisons of the competing hydrogenation and O-O bond dissociation pathways that govern selectivity toward H_2O_2, and benefit future modeling efforts (particularly, for parameter estimation in microkinetic models).

(ii) A liquid solvent may stabilize H_2O_2 with respect to its decomposition. In Chapter 4, our microkinetic modeling results suggest that the apparent activation barrier for H_2O_2 decomposition contains a positive contribution corresponding to the energy required to remove H_2O_2 from its aqueous solvation shell and bind it to the Pd surface. Solvation models can be used to better approximate this contribution. (We note that our gas-phase DFT calculations give a Pd(111)-H_2O_2 bond energy on the order of hydrogen bonding interactions, and so in protic solvents like water, the degrees of solvent reorganization and retention of the solvent shell upon H_2O_2 adsorption are critical aspects.) These insights can reinforce the conclusions from our microkinetic model and explain how the choice of solvent affects the H_2O_2 decomposition reactions.

(iii) A liquid solvent may affect the adsorption properties of halides and other promoter species. In Chapters 5 and 6, we constructed phase diagrams to approximate the relevant surface coverages of halides on Pd. Our models were based on gas-phase DFT calculations, and it would be valuable to determine their sensitivity to solvation effects at the liquid-solid interface – particularly how strongly the adsorption trends depend on solvent identity, and if such solvent effects exhibit

sensitivity to the Pd substrate structure.[247] (More generally, these findings could be useful in understanding adsorption properties of promoters/impurities in other liquid-phase chemistries that utilize heterogeneous catalysts). The promotional impact of halides has not been well-documented as a function of the solvent in experimental DSHP literature, although different research groups have reported the beneficial effects of halides in a variety of solvents, including water,[59] methanol,[328] methanol-water mixtures,[202] and ethanol.[29]

In addition to improving our understanding of the DSHP mechanism and our computational models, these solvent studies can potentially inform the choice of solvents/co-solvents for the DSHP.

9.2.1.2 Surface, subsurface and bulk modifications to Pd

The active phase of Pd remains an open question in the DSHP literature. As a supplement to our examination of subsurface and bulk hydrogen in Chapter 8, we recommend employing DFT calculations to study effects induced by migration of oxygen from the surface into the Pd lattice,[156, 293] especially due to conflicting literature reports regarding the benefits of oxidative versus reductive pre-treatments on the selectivity and activity of Pd catalysts.[18, 26] Further microkinetic analyses can also be useful in clarifying the active phase of Pd. Analogous to our methodology in Chapter 4, experimentally-consistent microkinetic models for the other DSHP reactions (H_2O_2 and H_2O synthesis, and H_2O_2 hydrogenation) can be developed to determine if the energetic parameters derived from clean, metallic Pd surface models can describe the experimental kinetics – or if surface/subsurface/bulk modifications provide better representations of the active site under reaction conditions. Of course, *in situ* characterization of Pd catalysts (e.g., by spectroscopic measurements of surface intermediates[164] and the oxidation state of Pd[72, 74]) would be valuable to substantiate insights from these models.

9.2.2 Search directions for improved catalysts

Our analysis of the late transition metals in Chapter 3 revealed intrinsic limitations of the monometallic systems toward active and selective H_2O_2 production. For example, our calculations showed that facile O-O bond breaking steps prevent H_2O_2 formation on Pd, Pt, and Cu, and high barriers for H_2 dissociation constrain the activity of Cu, Ag, and Au. These metals require further modification (e.g., alloying) to be suitable for the DSHP – or alternatively, altogether new catalysts can be found. Importantly, two simple thermodynamic descriptors are able to capture trends in the thermodynamic and kinetic mechanistic parameters across the late transition metals: the binding energy of O (BE_O) and the binding energy of H (BE_H).

These descriptors can provide semi-quantitative predictive power through the development of scaling[253] and Brønsted-Evans-Polanyi (BEP)[251, 308, 309, 329-332] relations (see Figure 9.1). Following previous approaches in the literature, scaling and BEP relations enable the determination of the optimal descriptor values that maximize catalytic activity/selectivity (e.g., by constructing volcano plots).[87, 89, 97, 251, 329, 333] The challenge then becomes identifying materials that exhibit these desirable properties (i.e., the optimal BE_O and BE_H). Alloy systems are a natural starting point, and one can systematically identify candidate materials based on knowledge of how physical structure and composition modify electronic structure – e.g. through strain[92, 334] and ligand[93-95] effects.

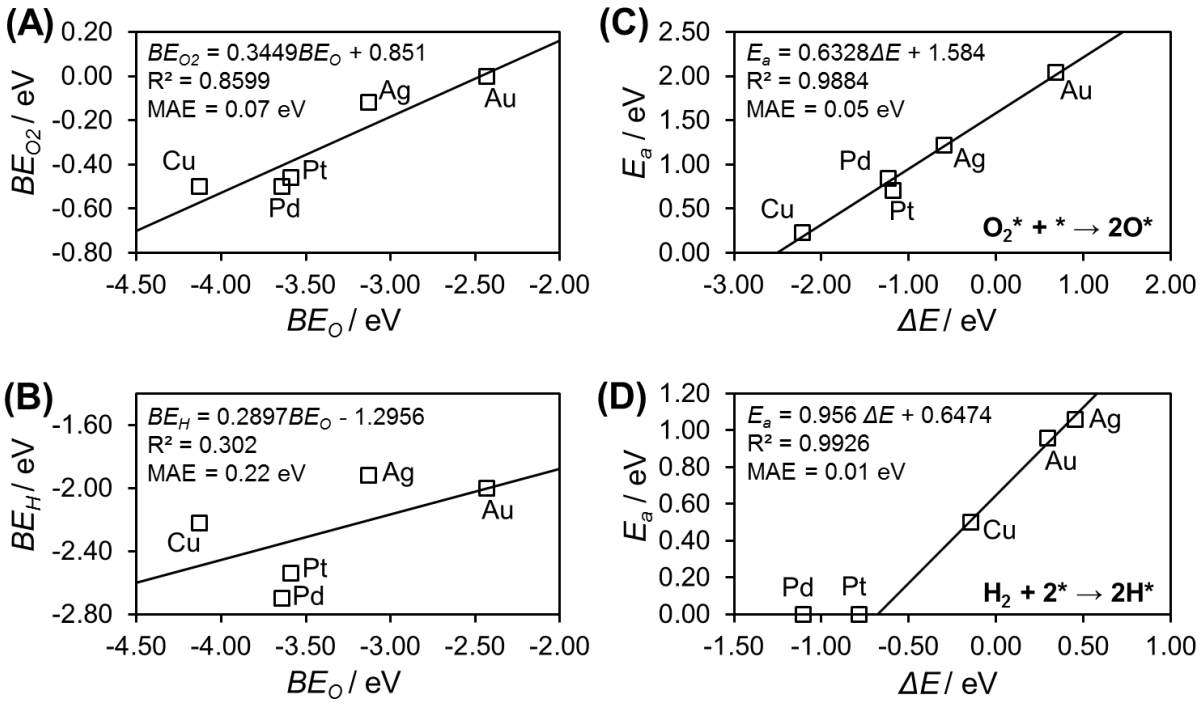

Figure 9.1 (A,B) Select scaling relations and (C,D) BEP relations on the (111) facet of Cu, Pd, Pt, Ag, and Au. Energetic data is from Chapter 3 and reference # [55]. Scaling relations can occur between the binding energies of species that bind through the same atom; in (A) we show there is reasonably linear scaling between the binding energy of O_2 and O – the latter being one of our reactivity descriptors. Similar relations can be derived for the other oxygen-containing intermediates in the DSHP. In (B) we show that the binding energies of O and H do not scale well with each other, which is why these species must be treated as independent reactivity descriptors. BEP relations can exist within similar elementary reaction classes, wherein the activation energies (E_a) exhibit a linear dependence on the respective reaction energies (ΔE). In (C) and (D), we show that O_2 and H_2 dissociation display strong BEP relationships. The H_2 dissociation BEP relation is derived from only the Cu, Au, and Ag data points (i.e., for ΔE more exothermic than -0.68 the E_a will be spontaneous – in agreement with the calculations on Pt and Pd). All figures: MAE is the mean absolute error between the predictions from the scaling or BEP relation and the DFT-calculated values.

We anticipate that this methodology can effectively guide the search for better DSHP catalysts, as has been done for reactions such the closely-related electrochemical oxygen reduction reaction[132, 335, 336] and the hydrogen evolution reaction.[97] Rankin and Greeley[56] have already contributed some work along this thread. Of course, there are opportunities to refine the methodology as more insights are gained into the DSHP. For example, we observed in Chapter 3 that the thermodynamic and kinetic parameters for the DSHP mechanism are sensitive to metal surface structure – which may indicate that the optimal values for the reactivity descriptors also

exhibit structure-dependence.[253] In addition, the reaction network used to describe the DSHP should be revised as new mechanistic information becomes available, such as including elementary steps that had not previously been considered (Chapter 4) and incorporating the possible role(s) of the solvent (Section 9.2.1). There is also the potential to use this methodology to identify catalytic promoters (Chapters 5-6), such as strongly adsorbing co-solvents or additives like the halides,[255] providing another means (supplementary to alloying) to tune surface reactivity; however, the applicability of the scaling- and BEP-based approach to spectator-covered systems, which may be fundamentally different from clean metal surfaces, requires further analysis.

References

1. P. T. Anastas and J. C. Warner, Green Chemistry: Theory and Practice. Oxford University Press, New York, 1998.
2. M. Poliakoff, J. M. Fitzpatrick, T. R. Farren and P. T. Anastas, *Science*, 2002, **297**, 807-810.
3. US Environmental Protection Agency. https://www.epa.gov/greenchemistry (Accessed: September 23, 2016).
4. R. A. Sheldon, *Chemical Communications*, 2008, 3352-3365.
5. R. A. Sheldon, *Chemtech*, 1994, **24**, 38-47.
6. G. Strukul, Catalytic Oxidations with Hydrogen Peroxide as Oxidant, Kluwer Academic Publishers, Boston, 1992.
7. C. W. Jones, Applications of Hydrogen Peroxide and Derivatives, The Royal Society of Chemistry, UK, 1999.
8. P. B. Walsh, *Tappi Journal*, 1991, **74**, 81-83.
9. F. Lopez, M. J. Diaz, M. E. Eugenio, J. Ariza, A. Rodriguez and L. Jimenez, *Bioresource Technology*, 2003, **87**, 255-261.
10. R. Hage and A. Lienke, *Angewandte Chemie-International Edition*, 2006, **45**, 206-222.
11. P. Bautista, A. F. Mohedano, J. A. Casas, J. A. Zazo and J. J. Rodriguez, *Journal of Chemical Technology and Biotechnology*, 2008, **83**, 1323-1338.
12. J. J. Pignatello, E. Oliveros and A. MacKay, *Critical Reviews in Environmental Science and Technology*, 2006, **36**, 1-84.
13. R. Noyori, *Chemical Communications*, 2005, 1807-1811.
14. R. Noyori, M. Aoki and K. Sato, *Chemical Communications*, 2003, 1977-1986.
15. B. Puertolas, A. K. Hill, T. Garcia, B. Solsona and L. Torrente-Murciano, *Catalysis Today*, 2015, **248**, 115-127.

16. Global Industry Analysts, Inc., Hydrogen Peroxide Market Trends. http://www.strategyr.com/MarketResearch/infographTemplate.asp?code=MCP-2080 (Accessed: September 29, 2016).
17. G. Goor, J. Glenneberg and S. Jacobi in Ullmann's Encyclopdedia of Industrial Chemistry, Hydrogen Peroxide, Wiley-VHC Verlag GmbH & Co., 2007.
18. J. M. Campos-Martin, G. Blanco-Brieva and J. L. G. Fierro, *Angewandte Chemie-International Edition*, 2006, **45**, 6962-6984.
19. J. Garcia-Serna, T. Moreno, P. Biasi, M. J. Cocero, J. P. Mikkola and T. O. Salmi, *Green Chemistry*, 2014, **16**, 2320-2343.
20. G. Jenzer, T. Mallat, M. Maciejewski, F. Eigenmann and A. Baiker, *Applied Catalysis A-General*, 2001, **208**, 125-133.
21. M. G. Clerici, G. Bellussi and U. Romano, *Journal of Catalysis*, 1991, **129**, 159-167.
22. H. Henkel and W. Weber, *US1108752*, 1914.
23. Y. H. Yi, L. Wang, G. Li and H. C. Guo, *Catalysis Science & Technology*, 2016, **6**, 1593-1610.
24. J. K. Edwards, S. J. Freakley, A. F. Carley, C. J. Kiely and G. J. Hutchings, *Accounts of Chemical Research*, 2014, **47**, 845-854.
25. J. K. Edwards, S. J. Freakley, R. J. Lewis, J. C. Pritchard and G. J. Hutchings, *Catalysis Today*, 2015, **248**, 3-9.
26. C. Samanta, *Applied Catalysis A-General*, 2008, **350**, 133-149.
27. R. Dittmeyer, J. D. Grunwaldt and A. Pashkova, *Catalysis Today*, 2015, **248**, 149-159.
28. J. K. Edwards and G. J. Hutchings, *Angewandte Chemie-International Edition*, 2008, **47**, 9192-9198.
29. Q. S. Liu and J. H. Lunsford, *Journal of Catalysis*, 2006, **239**, 237-243.
30. T. A. Pospelova, *Russian Journal of Physical Chemistry*, 1961, **35**, 143-147.
31. V. R. Choudhary, C. Samanta and P. Jana, *Applied Catalysis A-General*, 2007, **332**, 70-78.
32. J. K. Edwards, B. E. Solsona, P. Landon, A. F. Carley, A. Herzing, C. J. Kiely and G. J. Hutchings, *Journal of Catalysis*, 2005, **236**, 69-79.
33. J. K. Edwards, B. Solsona, P. Landon, A. F. Carley, A. Herzing, M. Watanabe, C. J. Kiely and G. J. Hutchings, *Journal of Materials Chemistry*, 2005, **15**, 4595-4600.
34. T. Ishihara, Y. Ohura, S. Yoshida, Y. Hata, H. Nishiguchi and Y. Takita, *Applied Catalysis A-General*, 2005, **291**, 215-221.
35. J. K. Edwards, B. Solsona, E. N. N, A. F. Carley, A. A. Herzing, C. J. Kiely and G. J. Hutchings, *Science*, 2009, **323**, 1037-1041.
36. P. Landon, P. J. Collier, A. F. Carley, D. Chadwick, A. J. Papworth, A. Burrows, C. J. Kiely and G. J. Hutchings, *Physical Chemistry Chemical Physics*, 2003, **5**, 1917-1923.
37. J. Xu, L. K. Ouyang, G. J. Da, Q. Q. Song, X. J. Yang and Y. F. Han, *Journal of Catalysis*, 2012, **285**, 74-82.
38. J. K. Edwards, J. Pritchard, L. Lu, M. Piccinini, G. Shaw, A. F. Carley, D. J. Morgan, C. J. Kiely and G. J. Hutchings, *Angewandte Chemie-International Edition*, 2014, **53**, 2381-2384.
39. Q. S. Liu, J. C. Bauer, R. E. Schaak and J. H. Lunsford, *Applied Catalysis A-General*, 2008, **339**, 130-136.
40. G. Bernardotto, F. Menegazzo, F. Pinna, M. Signoretto, G. Cruciani and G. Strukul, *Applied Catalysis A-General*, 2009, **358**, 129-135.

41. N. Gemo, P. Biasi, P. Canu and T. O. Salmi, *Chemical Engineering Journal*, 2012, **207**, 539-551.
42. Y. Voloshin, J. Manganaro and A. Lawal, *Industrial & Engineering Chemistry Research*, 2008, **47**, 8119-8125.
43. Y. Voloshin and A. Lawal, *Applied Catalysis A-General*, 2009, **353**, 9-16.
44. Y. Voloshin, R. Halder and A. Lawal, *Catalysis Today*, 2007, **125**, 40-47.
45. Y. Voloshin and A. Lawal, *Chemical Engineering Science*, 2010, **65**, 1028-1036.
46. S. Melada, R. Rioda, F. Menegazzo, F. Pinna and G. Strukul, *Journal of Catalysis*, 2006, **239**, 422-430.
47. T. Deguchi, H. Yamano and M. Iwamoto, *Catalysis Today*, 2015, **248**, 80-90.
48. T. Deguchi and M. Iwamoto, *Journal of Catalysis*, 2011, **280**, 239-246.
49. T. Moreno, J. Garcia-Serna and M. Jose Cocero, *Journal of Supercritical Fluids*, 2011, **57**, 227-235.
50. I. Huerta, J. Garcia-Serna and M. J. Cocero, *Journal of Supercritical Fluids*, 2013, **74**, 80-88.
51. S. J. Freakley, M. Piccinini, J. K. Edwards, E. N. Ntainjua, J. A. Moulijn and G. J. Hutchings, *ACS Catalysis*, 2013, **3**, 487-501.
52. J. Li, T. Ishihara and K. Yoshizawa, *Journal of Physical Chemistry C*, 2011, **115**, 25359-25367.
53. R. Todorovic and R. J. Meyer, *Catalysis Today*, 2011, **160**, 242-248.
54. H. C. Ham, G. S. Hwang, J. Han, S. W. Nam and T. H. Lim, *Journal of Physical Chemistry C*, 2009, **113**, 12943-12945.
55. D. C. Ford, A. U. Nilekar, Y. Xu and M. Mavrikakis, *Surface Science*, 2010, **604**, 1565-1575.
56. R. B. Rankin and J. Greeley, *ACS Catalysis*, 2012, **2**, 2664-2672.
57. T. Deguchi and M. Iwamoto, *Journal of Physical Chemistry C*, 2013, **117**, 18540-18548.
58. N. M. Wilson and D. W. Flaherty, *Journal of the American Chemical Society*, 2016, **138**, 574-586.
59. V. R. Choudhary and C. Samanta, *Journal of Catalysis*, 2006, **238**, 28-38.
60. S. Chinta and J. H. Lunsford, *Journal of Catalysis*, 2004, **225**, 249-255.
61. D. P. Dissanayake and J. H. Lunsford, *Journal of Catalysis*, 2003, **214**, 113-120.
62. Eds. P. J. Linstrom and W. G. Mallard, NIST Chemistry WebBook, NIST Standard Reference Database Number 69. http://webbook.nist.gov (Accessed: July 20, 2014).
63. M. L. Toebes, J. A. van Dillen and Y. P. de Jong, *Journal of Molecular Catalysis A-Chemical*, 2001, **173**, 75-98.
64. L. L. Jewell and B. H. Davis, *Applied Catalysis A-General*, 2006, **310**, 1-15.
65. E. Lundgren, A. Mikkelsen, J. N. Andersen, G. Kresse, M. Schmid and P. Varga, *Journal of Physics-Condensed Matter*, 2006, **18**, R481-R499.
66. R. Burch and P. R. Ellis, *Applied Catalysis B-Environmental*, 2003, **42**, 203-211.
67. Q. Liu, K. K. Gath, J. C. Bauer, R. E. Schaak and J. H. Lunsford, *Catalysis Letters*, 2009, **132**, 342-348.
68. C. Samanta and V. R. Choudhary, *Applied Catalysis A-General*, 2007, **326**, 28-36.
69. A. G. Gaikwad, S. D. Sansare and V. R. Choudhary, *Journal of Molecular Catalysis A-Chemical*, 2002, **181**, 143-149.
70. V. R. Choudhary, C. Samanta and T. V. Choudhary, *Applied Catalysis A-General*, 2006, **308**, 128-133.

71. L. Ouyang, P. F. Tian, G. J. Da, X. C. Xu, C. Ao, T. Y. Chen, R. Si, J. Xu and Y. F. Han, *Journal of Catalysis*, 2015, **321**, 70-80.
72. P. Centomo, C. Meneghini, S. Sterchele, A. Trapananti, G. Aquilanti and M. Zecca, *Catalysis Today*, 2015, **248**, 138-141.
73. P. Biasi, J. Garcia-Serna, A. Bittante and T. Salmi, *Green Chemistry*, 2013, **15**, 2502-2513.
74. P. Centomo, C. Meneghini, S. Sterchele, A. Trapananti, G. Aquilanti and M. Zecca, *ChemCatChem*, 2015, **7**, 3712-3718.
75. D. S. Sholl and J. A. Steckel, Density Functional Theory: A Practical Introduction, Wiley & Sons, NJ, 2009.
76. M. Ojeda, R. Nabar, A. U. Nilekar, A. Ishikawa, M. Mavrikakis and E. Iglesia, *Journal of Catalysis*, 2010, **272**, 287-297.
77. M. Ojeda, A. W. Li, R. Nabar, A. U. Nilekar, M. Mavrikakis and E. Iglesia, *Journal of Physical Chemistry C*, 2010, **114**, 19761-19770.
78. S. Shetty and R. A. van Santen, *Catalysis Today*, 2011, **171**, 168-173.
79. R. A. van Santen, M. M. Ghouri, S. Shetty and E. M. H. Hensen, *Catalysis Science & Technology*, 2011, **1**, 891-911.
80. L. C. Grabow, A. A. Gokhale, S. T. Evans, J. A. Dumesic and M. Mavrikakis, *Journal of Physical Chemistry C*, 2008, **112**, 4608-4617.
81. A. A. Gokhale, J. A. Dumesic and M. Mavrikakis, *Journal of the American Chemical Society*, 2008, **130**, 1402-1414.
82. A. A. Phatak, W. N. Delgass, F. H. Ribeiro and W. F. Schneider, *Journal of Physical Chemistry C*, 2009, **113**, 7269-7276.
83. L. C. Grabow and M. Mavrikakis, *ACS Catalysis*, 2011, **1**, 365-384.
84. A. Hellman, E. J. Baerends, M. Biczysko, T. Bligaard, C. H. Christensen, D. C. Clary, S. Dahl, R. van Harrevelt, K. Honkala, H. Jonsson, G. J. Kroes, M. Luppi, U. Manthe, J. K. Norskov, R. A. Olsen, J. Rossmeisl, E. Skulason, C. S. Tautermann, A. J. C. Varandas and J. K. Vincent, *Journal of Physical Chemistry B*, 2006, **110**, 17719-17735.
85. A. A. Gokhale, S. Kandoi, J. P. Greeley, M. Mavrikakis and J. A. Dumesic, *Chemical Engineering Science*, 2004, **59**, 4679-4691.
86. J. A. Dumesic, D. F. Rudd, L. M. Aparicio, J. E. Rekoske and A. A. Trevino, The Microkinetics of Heterogeneous Catalysis. American Chemical Society, Washington, DC 1993.
87. J. K. Norskov, T. Bligaard, J. Rossmeisl and C. H. Christensen, *Nature Chemistry*, 2009, **1**, 37-46.
88. M. Neurock, *Journal of Catalysis*, 2003, **216**, 73-88.
89. M. Mavrikakis, *Nature Materials*, 2006, **5**, 847-848.
90. J. Greeley, J. K. Norskov and M. Mavrikakis, *Annual Review of Physical Chemistry*, 2002, **53**, 319-348.
91. B. Hammer and J. K. Norskov, *Advances in Catalysis, Vol 45: Impact of Surface Science on Catalysis*, 2000, **45**, 71-129.
92. M. Mavrikakis, B. Hammer and J. K. Norskov, *Physical Review Letters*, 1998, **81**, 2819-2822.
93. P. Liu and J. K. Norskov, *Physical Chemistry Chemical Physics*, 2001, **3**, 3814-3818.
94. J. R. Kitchin, J. K. Norskov, M. A. Barteau and J. G. Chen, *Physical Review Letters*, 2004, **93**.
95. T. Bligaard and J. K. Norskov, *Electrochimica Acta*, 2007, **52**, 5512-5516.

96. F. Abild-Pedersen, J. Greeley and J. K. Norskov, *Catalysis Letters*, 2005, **105**, 9-13.
97. J. Greeley, T. F. Jaramillo, J. Bonde, I. B. Chorkendorff and J. K. Norskov, *Nature Materials*, 2006, **5**, 909-913.
98. B. Hinnemann, P. G. Moses, J. Bonde, K. P. Jorgensen, J. H. Nielsen, S. Horch, I. Chorkendorff and J. K. Norskov, *Journal of the American Chemical Society*, 2005, **127**, 5308-5309.
99. F. Besenbacher, I. Chorkendorff, B. S. Clausen, B. Hammer, A. M. Molenbroek, J. K. Norskov and I. Stensgaard, *Science*, 1998, **279**, 1913-1915.
100. R. R. Adzic, J. Zhang, K. Sasaki, M. B. Vukmirovic, M. Shao, J. X. Wang, A. U. Nilekar, M. Mavrikakis, J. A. Valerio and F. Uribe, *Topics in Catalysis*, 2007, **46**, 249-262.
101. V. R. Stamenkovic, B. Fowler, B. S. Mun, G. F. Wang, P. N. Ross, C. A. Lucas and N. M. Markovic, *Science*, 2007, **315**, 493-497.
102. J. L. Zhang, M. B. Vukmirovic, Y. Xu, M. Mavrikakis and R. R. Adzic, *Angewandte Chemie-International Edition*, 2005, **44**, 2132-2135.
103. M. C. Payne, M. P. Teter, D. C. Allan, T. A. Arias and J. D. Joannopoulos, *Reviews of Modern Physics*, 1992, **64**, 1045-1097.
104. C. J. Cramer and D. G. Truhlar, *Physical Chemistry Chemical Physics*, 2009, **11**, 10757-10816.
105. W. Koch and M. C. Holthausen, A Chemist's Guide to Density Functional Theory. Wiley-VHC, New York, 2001.
106. P. Hohenberg and W. Kohn, *Physical Review*, 1964, **136**, B864-B871.
107. W. Kohn and L. J. Sham, *Physical Review*, 1965, **140**, A1133-A1138.
108. J. A. White and D. M. Bird, *Physical Review B*, 1994, **50**, 4954-4957.
109. J. P. Perdew, J. A. Chevary, S. H. Vosko, K. A. Jackson, M. R. Pederson, D. J. Singh and C. Fiolhais, *Physical Review B*, 1992, **46**, 6671-6687.
110. J. Greeley and M. Mavrikakis, *Surface Science*, 2003, **540**, 215-229.
111. G. Henkelman and H. Jonsson, *Journal of Chemical Physics*, 1999, **111**, 7010-7022.
112. G. Henkelman and H. Jonsson, *Journal of Chemical Physics*, 2000, **113**, 9978-9985.
113. D. Sheppard, R. Terrell and G. Henkelman, *Journal of Chemical Physics*, 2008, **128**, 134106-1–134106-10.
114. A. Heyden, A. T. Bell and F. J. Keil, *Journal of Chemical Physics*, 2005, **123**, 224101-1 – 224101-14.
115. G. Henkelman, B. P. Uberuaga and H. Jonsson, *Journal of Chemical Physics*, 2000, **113**, 9901-9904.
116. G. Ertl, Mechanisms of Heterogeneous Catalysis in Reactions at Solid Surfaces, John Wiley & Sons, Inc., NJ, 2009.
117. J. L. Gland, G. B. Fisher and E. B. Kollin, *Journal of Catalysis*, 1982, **77**, 263-278.
118. R. Imbihl and G. Ertl, *Chemical Reviews*, 1995, **95**, 697-733.
119. S. Volkening, K. Bedurftig, K. Jacobi, J. Wintterlin and G. Ertl, *Physical Review Letters*, 1999, **83**, 2672-2675.
120. Y. Wang, K. S. Chen, J. Mishler, S. C. Cho and X. C. Adroher, *Applied Energy*, 2011, **88**, 981-1007.
121. M. K. Debe, *Nature*, 2012, **486**, 43-51.
122. R. Meiers and W. F. Holderich, *Catalysis Letters*, 1999, **59**, 161-163.
123. G. Centi, F. Cavani and F. Trifirò, Selective Oxidation by Heterogeneous Catalysis, Springer US, New York, 2001.

124. H. A. Gasteiger, S. S. Kocha, B. Sompalli and F. T. Wagner, *Applied Catalysis B-Environmental*, 2005, **56**, 9-35.
125. F. Menegazzo, M. Manzoli, M. Signoretto, F. Pinna and G. Strukul, *Catalysis Today*, 2015, **248**, 18-27.
126. R. Arrigo, M. E. Schuster, S. Abate, S. Wrabetz, K. Amakawa, D. Teschner, M. Freni, G. Centi, S. Perathoner, M. Haevecker and R. Schloegl, *ChemSusChem*, 2014, **7**, 179-194.
127. J. K. Norskov, J. Rossmeisl, A. Logadottir, L. Lindqvist, J. R. Kitchin, T. Bligaard and H. Jonsson, *Journal of Physical Chemistry B*, 2004, **108**, 17886-17892.
128. V. Viswanathan, H. A. Hansen, J. Rossmeisl and J. K. Norskov, *ACS Catalysis*, 2012, **2**, 1654-1660.
129. M. T. M. Koper, *Journal of Electroanalytical Chemistry*, 2011, **660**, 254-260.
130. X. Wang, S. I. Choi, L. T. Roling, M. Luo, C. Ma, L. Zhang, M. F. Chi, J. Y. Liu, Z. X. Xie, J. A. Herron, M. Mavrikakis and Y. N. Xia, *Nature Communications*, 2015, **6**.
131. S. F. Xie, S. I. Choi, N. Lu, L. T. Roling, J. A. Herron, L. Zhang, J. Park, J. G. Wang, M. J. Kim, Z. X. Xie, M. Mavrikakis and Y. N. Xia, *Nano Letters*, 2014, **14**, 3570-3576.
132. J. Greeley, I. E. L. Stephens, A. S. Bondarenko, T. P. Johansson, H. A. Hansen, T. F. Jaramillo, J. Rossmeisl, I. Chorkendorff and J. K. Norskov, *Nature Chemistry*, 2009, **1**, 552-556.
133. L. C. Grabow, B. Hvolbaek, H. Falsig and J. K. Norskov, *Topics in Catalysis*, 2012, **55**, 336-344.
134. A. Staykov, T. Kamachi, T. Ishihara and K. Yoshizawa, *Journal of Physical Chemistry C*, 2008, **112**, 19501-19505.
135. T. Gomez, E. Florez, J. A. Rodriguez and F. Illas, *Journal of Physical Chemistry C*, 2011, **115**, 11666-11672.
136. B. Hammer, L. B. Hansen and J. K. Norskov, *Physical Review B*, 1999, **59**, 7413-7421.
137. G. Kresse and J. Furthmuller, *Computational Materials Science*, 1996, **6**, 15-50.
138. D. Vanderbilt, *Physical Review B*, 1990, **41**, 7892-7895.
139. L. Bengtsson, *Physical Review B*, 1999, **59**, 12301-12304.
140. J. Neugebauer and M. Scheffler, *Physical Review B*, 1992, **46**, 16067-16080.
141. N. D. Mermin and N. W. Ashcroft, Solid State Physics, Harcourt College Publishers, TX, 1976.
142. D. J. Chadi and M. L. Cohen, *Physical Review B*, 1973, **8**, 5747-5753.
143. H. J. Monkhorst and J. D. Pack, *Physical Review B*, 1976, **13**, 5188-5192.
144. K. Reuter and M. Scheffler, *Physical Review B*, 2002, **65**.
145. C. A. Farberow, J. A. Dumesic and M. Mavrikakis, *ACS Catalysis*, 2014, **4**, 3307-3319.
146. W. Dong, G. Kresse and J. Hafner, *Journal of Molecular Catalysis A-Chemical*, 1997, **119**, 69-76.
147. W. Dong and J. Hafner, *Physical Review B*, 1997, **56**, 15396-15403.
148. A. Gross, *Journal of Chemical Physics*, 2011, **135**, 174707-1 – 174707-12.
149. Z. Y. Duan and G. F. Wang, *Journal of Physical Chemistry C*, 2013, **117**, 6284-6292.
150. C. Sivadinarayana, T. V. Choudhary, L. L. Daemen, J. Eckert and D. W. Goodman, *Journal of the American Chemical Society*, 2004, **126**, 38-39.
151. A. T. Pasteur, S. J. DixonWarren, Q. Ge and D. A. King, *Journal of Chemical Physics*, 1997, **106**, 8896-8904.
152. R. A. Olsen, G. J. Kroes and E. J. Baerends, *Journal of Chemical Physics*, 1999, **111**, 11155-11163.

153. S. Sakong and A. Gross, *Surface Science*, 2003, **525**, 107-118.
154. B. Hammer, M. Scheffler, K. W. Jacobsen and J. K. Norskov, *Physical Review Letters*, 1994, **73**, 1400-1403.
155. A. Eichler, J. Hafner, A. Gross and M. Scheffler, *Physical Review B*, 1999, **59**, 13297-13300.
156. Y. Xu, J. Greeley and M. Mavrikakis, *Journal of the American Chemical Society*, 2005, **127**, 12823-12827.
157. A. Montoya, A. Schlunke and B. S. Haynes, *Journal of Physical Chemistry B*, 2006, **110**, 17145-17154.
158. K. J. Sun, M. Kohyama, S. Tanaka and S. Takeda, *Journal of Physical Chemistry C*, 2014, **118**, 1611-1617.
159. S. Singh, S. Li, R. Carrasquillo-Flores, A. C. Alba-Rubio, J. A. Dumesic and M. Mavrikakis, *AIChE Journal*, 2014, **60**, 1303-1319.
160. A. Plauck, E. E. Stangland, J. A. Dumesic and M. Mavrikakis, *Proceedings of the National Academy of Sciences of the United States of America*, 2016, **113**, E1973-E1982.
161. T. A. Nijhuis, M. Makkee, J. A. Moulijn and B. M. Weckhuysen, *Industrial & Engineering Chemistry Research*, 2006, **45**, 3447-3459.
162. T. A. Nijhuis, T. Visser and B. M. Weckhuysen, *Journal of Physical Chemistry B*, 2005, **109**, 19309-19319.
163. R. B. Getman and W. F. Schneider, *ChemCatChem*, 2010, **2**, 1450-1460.
164. H. S. Casalongue, S. Kaya, V. Viswanathan, D. J. Miller, D. Friebel, H. A. Hansen, J. K. Norskov, A. Nilsson and H. Ogasawara, *Nature Communications*, 2013, **4**.
165. M. Neurock, V. Pallassana and R. A. van Santen, *Journal of the American Chemical Society*, 2000, **122**, 1150-1153.
166. K. Frey, D. J. Schmidt, C. Wolverton and W. F. Schneider, *Catalysis Science & Technology*, 2014, **4**, 4356-4365.
167. R. B. Getman, Y. Xu and W. F. Schneider, *Journal of Physical Chemistry C*, 2008, **112**, 9559-9572.
168. A. D. Smeltz, R. B. Getman, W. F. Schneider and F. H. Ribeiro, *Catalysis Today*, 2008, **136**, 84-92.
169. V. R. Choudhary, C. Samanta and T. V. Choudhary, *Journal of Molecular Catalysis A-Chemical*, 2006, **260**, 115-120.
170. V. R. Choudhary, C. Samanta and P. Jana, *Applied Catalysis A-General*, 2007, **317**, 234-243.
171. S. Abate, M. Freni, R. Arrigo, M. E. Schuster, S. Perathoner and G. Centi, *ChemCatChem*, 2013, **5**, 1899-1905.
172. S. J. Freakley, Q. He, J. H. Harrhy, L. Lu, D. A. Crole, D. J. Morgan, E. N. Ntainjua, J. K. Edwards, A. F. Carley, A. Y. Borisevich, C. J. Kiely and G. J. Hutchings, *Science*, 2016, **351**, 965-968.
173. J. K. Edwards, J. Pritchard, M. Piccinini, G. Shaw, Q. He, A. F. Carley, C. J. Kiely and G. J. Hutchings, *Journal of Catalysis*, 2012, **292**, 227-238.
174. J. R. Monnier, *Applied Catalysis A-General*, 2001, **221**, 73-91.
175. W. Laufer, R. Meiers and W. Holderich, *Journal of Molecular Catalysis A-Chemical*, 1999, **141**, 215-221.
176. C. Popa, T. Zhu, I. Tranca, P. Kaghazchi, T. Jacob and E. J. M. Hensen, *Physical Chemistry Chemical Physics*, 2015, **17**, 2268-2273.

177. B. Lim, M. Jiang, J. Tao, P. H. C. Camargo, Y. Zhu and Y. Xia, *Advanced Functional Materials*, 2009, **19**, 189-200.
178. W. Stober, A. Fink and E. Bohn, *Journal of Colloid and Interface Science*, 1968, **26**, 62-69.
179. A. C. Alba-Rubio, B. J. O'Neill, F. Shi, C. Akatay, C. Canlas, T. Li, R. Winans, J. W. Elam, E. A. Stach, P. M. Voyles and J. A. Dumesic, *ACS Catalysis*, 2014, **4**, 1554-1557.
180. W. Zou and R. D. Gonzalez, *Catalysis Letters*, 1992, **12**, 73-86.
181. B. E. Spiewak, J. Shen and J. A. Dumesic, *Journal of Physical Chemistry*, 1995, **99**, 17640-17644.
182. A. Tessier and W. Forst, *Canadian Journal of Chemistry-Revue Canadienne De Chimie*, 1974, **52**, 794-797.
183. J. Takagi and K. Ishigure, *Nuclear Science and Engineering*, 1985, **89**, 177-186.
184. C. M. Lousada, A. J. Johansson, T. Brinck and M. Jonsson, *Journal of Physical Chemistry C*, 2012, **116**, 9533-9543.
185. A. Hiroki and J. A. LaVerne, *Journal of Physical Chemistry B*, 2005, **109**, 3364-3370.
186. S. S. Lin and M. D. Gurol, *Environmental Science & Technology*, 1998, **32**, 1417-1423.
187. F. Haber and J. Weiss, *The Catalytic Decomposition of Hydrogen Peroxide by Iron Salts*, 1934.
188. W. P. Kwan and B. M. Voelker, *Environmental Science & Technology*, 2002, **36**, 1467-1476.
189. C. M. Lousada, A. J. Johansson, T. Brinck and M. Jonsson, *Physical Chemistry Chemical Physics*, 2013, **15**, 5539-5552.
190. R. Long, K. Mao, X. Ye, W. Yan, Y. Huang, J. Wang, Y. Fu, X. Wang, X. Wu, Y. Xie and Y. Xiong, *Journal of the American Chemical Society*, 2013, **135**, 3200-3207.
191. G. W. Simmons, Y. N. Wang, J. Marcos and K. Klier, *Journal of Physical Chemistry*, 1991, **95**, 4522-4528.
192. N. N. Edwin, J. K. Edwards, A. F. Carley, J. A. Lopez-Sanchez, J. A. Moulijn, A. A. Herzing, C. J. Kiely and G. J. Hutchings, *Green Chemistry*, 2008, **10**, 1162-1169.
193. V. Paunovic, V. V. Ordomsky, V. L. Sushkevich, J. C. Schouten and T. A. Nijhuis, *ChemCatChem*, 2015, **7**, 1161-1176.
194. G. Zheng and E. I. Altman, *Surface Science*, 2000, **462**, 151-168.
195. G. Zheng and E. I. Altman, *Surface Science*, 2002, **504**, 253-270.
196. G. Bianchi, F. Mazza and T. Mussini, *Electrochimica Acta*, 1962, **7**, 457-473.
197. L. C. Grabow, B. Hvolbaek and J. K. Norskov, *Topics in Catalysis*, 2010, **53**, 298-310.
198. C. T. Campbell, *Journal of Catalysis*, 2001, **204**, 520-524.
199. J. A. Dumesic, *Journal of Catalysis*, 1999, **185**, 496-505.
200. R. Atkinson, D. L. Baulch, R. A. Cox, J. N. Crowley, R. F. Hampson, R. G. Hynes, M. E. Jenkin, M. J. Rossi and J. Troe, *Atmospheric Chemistry and Physics*, 2004, **4**, 1461-1738.
201. S. Melada, F. Pinna, G. Strukul, S. Perathoner and G. Centi, *Journal of Catalysis*, 2006, **237**, 213-219.
202. E. Ntainjua N, M. Piccinini, J. C. Pritchard, J. K. Edwards, A. F. Carley, J. A. Moulijn and G. J. Hutchings, *ChemSusChem*, 2009, **2**, 575-580.
203. Q. Liu and J. H. Lunsford, *Applied Catalysis A-General*, 2006, **314**, 94-100.
204. B. Hammer and J. K. Norskov, *Nature*, 1995, **376**, 238-240.
205. H. L. Tierney, A. E. Baber, J. R. Kitchin and E. C. H. Sykes, *Physical Review Letters*, 2009, **103**.

206. J. S. Jirkovsky, I. Panas, E. Ahlberg, M. Halasa, S. Romani and D. J. Schiffrin, *Journal of the American Chemical Society*, 2011, **133**, 19432-19441.
207. A. Verdaguer-Casadevall, D. Deiana, M. Karamad, S. Siahrostami, P. Malacrida, T. W. Hansen, J. Rossmeisl, I. Chorkendorff and I. E. L. Stephens, *Nano Letters*, 2014, **14**, 1603-1608.
208. J. Li, A. Staykov, T. Ishihara and K. Yoshizawa, *Journal of Physical Chemistry C*, 2011, **115**, 7392-7398.
209. R. J. Madon, D. Braden, S. Kandoi, P. Nagel, M. Mavrikakis and J. A. Dumesic, *Journal of Catalysis*, 2011, **281**, 1-11.
210. H. Hwang and P. K. Dasgupta, *Environmental Science & Technology*, 1985, **19**, 255-258.
211. A. Michaelides, *Applied Physics A-Materials Science & Processing*, 2006, **85**, 415-425.
212. Y. Sha, T. H. Yu, Y. Liu, B. V. Merinov and W. A. Goddard, *Journal of Physical Chemistry Letters*, 2010, **1**, 856-861.
213. J. Carrasco, B. Santra, J. Klimes and A. Michaelides, *Physical Review Letters*, 2011, **106**, 4.
214. B. Santra, J. Klimes, A. Tkatchenko, D. Alfe, B. Slater, A. Michaelides, R. Car and M. Scheffler, *Journal of Chemical Physics*, 2013, **139**.
215. C. A. Farberow, A. Godinez-Garcia, G. W. Peng, J. F. Perez-Robles, O. Solorza-Feria and M. Mavrikakis, *ACS Catalysis*, 2013, **3**, 1622-1632.
216. H. C. Ham, J. A. Stephens, G. S. Hwang, J. Han, S. W. Nam and T. H. Lim, *Catalysis Today*, 2011, **165**, 138-144.
217. A. V. Beletskaya, D. A. Pichugina, A. F. Shestakov and N. E. Kuz'menko, *Journal of Physical Chemistry A*, 2013, **117**, 6817-6826.
218. A. M. Joshi, W. N. Delgass and K. T. Thomson, *Journal of Physical Chemistry C*, 2007, **111**, 7384-7395.
219. T. Deguchi, H. Yamano and M. Iwamoto, *Journal of Catalysis*, 2012, **287**, 55-61.
220. J. H. Lunsford, *Journal of Catalysis*, 2003, **216**, 455-460.
221. N. Markovic, H. Gasteiger and P. N. Ross, *Journal of the Electrochemical Society*, 1997, **144**, 1591-1597.
222. Y. F. Han and J. H. Lunsford, *Journal of Catalysis*, 2005, **230**, 313-316.
223. S. Abate, G. Centi, S. Melada, S. Perathoner, F. Pinna and G. Strukul, *Catalysis Today*, 2005, **104**, 323-328.
224. F. Menegazzo, M. Signoretto, G. Frison, F. Pinna, G. Strukul, M. Manzoli and F. Boccuzzi, *Journal of Catalysis*, 2012, **290**, 143-150.
225. P. Centomo, C. Meneghini, S. Sterchele, A. Trapananti, G. Aquilanti and M. Zecca, *ChemCatChem*, 2015, **7**, 3712-3718.
226. G. Kresse and J. Furthmuller, *Physical Review B*, 1996, **54**, 11169-11186.
227. P. E. Blochl, *Physical Review B*, 1994, **50**, 17953-17979.
228. G. Kresse and D. Joubert, *Physical Review B*, 1999, **59**, 1758-1775.
229. A. Migani and F. Illas, *Journal of Physical Chemistry B*, 2006, **110**, 11894-11906.
230. T. Roman, F. Gossenberger, K. Forster-Tonigold and A. Gross, *Physical Chemistry Chemical Physics*, 2014, **16**, 13630-13634.
231. F. Gossenberger, T. Roman and A. Gross, *Surface Science*, 2015, **631**, 17-22.
232. I. A. Pasti and S. V. Mentus, *Electrochimica Acta*, 2010, **55**, 1995-2003.
233. A. Ignaczak and J. Gomes, *Journal of Electroanalytical Chemistry*, 1997, **420**, 71-78.
234. M. T. M. Koper and R. A. van Santen, *Surface Science*, 1999, **422**, 118-131.

235. O. M. Magnussen, *Chemical Reviews*, 2002, **102**, 679-725.
236. D. P. Dissanayake and J. H. Lunsford, *Journal of Catalysis*, 2002, **206**, 173-176.
237. E. Dona, M. Cordin, C. Deisl, E. Bertel, C. Franchini, R. Zucca and J. Redinger, *Journal of the American Chemical Society*, 2009, **131**, 2827-+.
238. W. T. Tysoe and R. M. Lambert, *Surface Science*, 1982, **115**, 37-47.
239. W. T. Tysoe and R. M. Lambert, *Surface Science*, 1988, **199**, 1-12.
240. W. Erley, *Surface Science*, 1980, **94**, 281-292.
241. V. R. Dhanak, A. G. Shard, S. D'Addato and A. Santoni, *Chemical Physics Letters*, 1999, **306**, 341-344.
242. A. Carrasquillo, J. J. Jeng, R. J. Barriga, W. F. Temesghen and M. P. Soriaga, *Inorganica Chimica Acta*, 1997, **255**, 249-254.
243. M. P. Soriaga, J. A. Schimpf, A. Carrasquillo, J. B. Abreu, W. Temesghen, R. J. Barriga, J. J. Jeng, K. Sashikata and K. Itaya, *Surface Science*, 1995, **335**, 273-280.
244. K. Sashikata, Y. Matsui, K. Itaya and M. P. Soriaga, *Journal of Physical Chemistry*, 1996, **100**, 20027-20034.
245. J. A. Schimpf, J. R. McBride and M. P. Soriaga, *Journal of Physical Chemistry*, 1993, **97**, 10518-10520.
246. P. Brimblecombe and S. L. Clegg, *Journal of Atmospheric Chemistry*, 1988, **7**, 1-18.
247. I. T. McCrum, S. A. Akhade and M. J. Janik, *Electrochimica Acta*, 2015, **173**, 302-309.
248. E. P. L. Hunter and S. G. Lias, *Journal of Physical and Chemical Reference Data*, 1998, **27**, 413-656.
249. I. Katsounaros, W. B. Schneider, J. C. Meier, U. Benedikt, P. U. Biedermann, A. Cuesta, A. A. Auer and K. J. J. Mayrhofer, *Physical Chemistry Chemical Physics*, 2013, **15**, 8058-8068.
250. C.-H. Lin, L.-Y. Wei, J.-H. Lee, C.-L. Lien, C.-H. Lu and C.-J. Yuan, *Electrochimica Acta*, 2015, **180**, 64-70.
251. T. Bligaard, J. K. Norskov, S. Dahl, J. Matthiesen, C. H. Christensen and J. Sehested, *Journal of Catalysis*, 2004, **224**, 206-217.
252. H. Thirumalai and J. R. Kitchin, *Surface Science*, 2016, **650**, 196-202.
253. F. Abild-Pedersen, J. Greeley, F. Studt, J. Rossmeisl, T. R. Munter, P. G. Moses, E. Skulason, T. Bligaard and J. K. Norskov, *Physical Review Letters*, 2007, **99**.
254. S. Wang, V. Petzold, V. Tripkovic, J. Kleis, J. G. Howalt, E. Skulason, E. M. Fernandez, B. Hvolbaek, G. Jones, A. Toftelund, H. Falsig, M. Bjorketun, F. Studt, F. Abild-Pedersen, J. Rossmeisl, J. K. Norskov and T. Bligaard, *Physical Chemistry Chemical Physics*, 2011, **13**, 20760-20765.
255. V. Paunovic, V. V. Ordomsky, V. L. Sushkevich, J. C. Schouten and T. A. Nijhuis, *ChemCatChem*, 2015, **7**, 1161-1176.
256. S. Kim, D. W. Lee, K. Y. Lee and E. A. Cho, *Catalysis Letters*, 2014, **144**, 905-911.
257. S. Abate, K. Barbera, G. Centi, G. Giorgianni and S. Perathoner, *Journal of Energy Chemistry*, 2016, **25**, 297-305.
258. A. Carrasquillo Jr., J. Baricuatro, M. Hossain, Y. S. Park, J. J. Jeng and M. P. Soriaga, *ECS Transactions*, 2007, **3**, 169-186.
259. Y. N. Wang, J. A. Marcos, G. W. Simmons and K. Klier, *Journal of Physical Chemistry*, 1990, **94**, 7597-7607.

260. N. Mizuno, G. Centi, S. Perathoner and S. Abate, Direct Synthesis of Hydrogen Peroxide: Recent Advances in Modern Heterogeneous Oxidation Catalysis: Design, Reactions, and Characterization, Wiley-VHC Verlag GmbH & Co., Germany, 2009.
261. L. A. Kibler, A. M. El-Aziz, R. Hoyer and D. M. Kolb, *Angewandte Chemie-International Edition*, 2005, **44**, 2080-2084.
262. M. Sankar, Q. He, M. Morad, J. Pritchard, S. J. Freakley, J. K. Edwards, S. H. Taylor, D. J. Morgan, A. F. Carley, D. W. Knight, C. J. Kiely and G. J. Hutchings, *ACS Nano*, 2012, **6**, 6600-6613.
263. J. C. Pritchard, Q. He, E. N. Ntainjua, M. Piccinini, J. K. Edwards, A. A. Herzing, A. F. Carley, J. A. Moulijn, C. J. Kiely and G. J. Hutchings, *Green Chemistry*, 2010, **12**, 915-921.
264. K. D. Beard, D. Borrelli, A. M. Cramer, D. Blom, J. W. Van Zee and J. R. Monnier, *ACS Nano*, 2009, **3**, 2841-2853.
265. K. D. Beard, J. W. Van Zee and J. R. Monnier, *Applied Catalysis B-Environmental*, 2009, **88**, 185-193.
266. M. Ohashi, K. D. Beard, S. Ma, D. A. Blom, J. St-Pierre, J. W. Van Zee and J. R. Monnier, *Electrochimica Acta*, 2010, **55**, 7376-7384.
267. J. Rebelli, M. Detwiler, S. Ma, C. T. Williams and J. R. Monnier, *Journal of Catalysis*, 2010, **270**, 224-233.
268. J. Rebelli, A. A. Rodriguez, S. Ma, C. T. Williams and J. R. Monnier, *Catalysis Today*, 2011, **160**, 170-178.
269. A. A. Rodriguez, C. T. Williams and J. R. Monnier, *Applied Catalysis A-General*, 2014, **475**, 161-168.
270. R. J. Madon and M. Boudart, *Industrial & Engineering Chemistry Fundamentals*, 1982, **21**, 438-447.
271. B. Pawelec, A. M. Venezia, V. La Parola, E. Cano-Serrano, J. M. Campos-Martin and J. L. G. Fierro, *Applied Surface Science*, 2005, **242**, 380-391.
272. A. M. Venezia, V. La Parola, G. Deganello, B. Pawelec and J. L. G. Fierro, *Journal of Catalysis*, 2003, **215**, 317-325.
273. F. Skoda, M. P. Astier, G. M. Pajonk and M. Primet, *Catalysis Letters*, 1994, **29**, 159-168.
274. E. L. Kugler and M. Boudart, *Journal of Catalysis*, 1979, **59**, 201-210.
275. J. K. Edwards, A. Thomas, A. F. Carley, A. A. Herzing, C. J. Kiely and G. J. Hutchings, *Green Chemistry*, 2008, **10**, 388-394.
276. E. Ghedini, F. Menegazzo, M. Signoretto, M. Manzoli, F. Pinna and G. Strukul, *Journal of Catalysis*, 2010, **273**, 266-273.
277. S. Kim, D.-W. Lee and K.-Y. Lee, *Journal of Molecular Catalysis A-Chemical*, 2014, **391**, 48-54.
278. J. K. Edwards, S. F. Parker, J. Pritchard, M. Piccinini, S. J. Freakley, Q. He, A. F. Carley, C. J. Kiely and G. J. Hutchings, *Catalysis Science & Technology*, 2013, **3**, 812-818.
279. J. Pritchard, L. Kesavan, M. Piccinini, Q. He, R. Tiruvalam, N. Dimitratos, J. A. Lopez-Sanchez, A. F. Carley, J. K. Edwards, C. J. Kiely and G. J. Hutchings, *Langmuir*, 2010, **26**, 16568-16577.
280. L. Ouyang, G. Da, P. Tian, T. Chen, G. Liang, J. Xu and Y. Han, *Journal of Catalysis*, 2014, **311**, 129-136.
281. Y. Santiago-Rodriguez, J. A. Herron, M. C. Curet-Arana and M. Mavrikakis, *Surface Science*, 2014, **627**, 57-69.

282. J. A. Herron, S. Tonelli and M. Mavrikakis, *Surface Science*, 2012, **606**, 1670-1679.
283. J. Greeley and M. Mavrikakis, *Nature Materials*, 2004, **3**, 810-815.
284. J. A. Herron and M. Mavrikakis, *Catalysis Communications*, 2014, **52**, 65-71.
285. A. V. Ruban, H. L. Skriver and J. K. Norskov, *Physical Review B*, 1999, **59**, 15990-16000.
286. A. U. Nilekar, A. V. Ruban and M. Mavrikakis, *Surface Science*, 2009, **603**, 91-96.
287. Y. Y. Zhang, W. J. Diao, J. R. Monnier and C. T. Williams, *Catalysis Science & Technology*, 2015, **5**, 4123-4132.
288. S. H. Hakim, C. Sener, A. C. Alba-Rubio, T. M. Gostanian, B. J. O'Neill, F. H. Ribeiro, J. T. Miller and J. A. Dumesic, *Journal of Catalysis*, 2015, **328**, 75-90.
289. S. Kunz and E. Iglesia, *Journal of Physical Chemistry C*, 2014, **118**, 7468-7479.
290. H. Tiznado, S. Fuentes and F. Zaera, *Langmuir*, 2004, **20**, 10490-10497.
291. M. Armbruster, M. Behrens, F. Cinquini, K. Fottinger, Y. Grin, A. Haghofer, B. Klotzer, A. Knop-Gericke, H. Lorenz, A. Ota, S. Penner, J. Prinz, C. Rameshan, Z. Revay, D. Rosenthal, N. Rupprechter, P. Sautet, R. Schlogl, L. D. Shao, L. Szentmiklosi, D. Teschner, D. Torres, R. Wagner, R. Widmer and G. Wowsnick, *ChemCatChem*, 2012, **4**, 1048-1063.
292. D. Teschner, J. Borsodi, A. Wootsch, Z. Revay, M. Havecker, A. Knop-Gericke, S. D. Jackson and R. Schlogl, *Science*, 2008, **320**, 86-89.
293. J. Greeley and M. Mavrikakis, *Journal of Physical Chemistry C*, 2007, **111**, 7992-7999.
294. G. J. Millar, M. L. Nelson and P. J. R. Uwins, *Journal of Catalysis*, 1997, **169**, 143-156.
295. V. R. Choudhary, C. Samanta and P. Jana, *Industrial & Engineering Chemistry Research*, 2007, **46**, 3237-3242.
296. B. D. Adams and A. C. Chen, *Materials Today*, 2011, **14**, 282-289.
297. R. Lasser and K. H. Klatt, *Physical Review B*, 1983, **28**, 748-758.
298. M. Yamauchi, R. Ikeda, H. Kitagawa and M. Takata, *Journal of Physical Chemistry C*, 2008, **112**, 3294-3299.
299. Z. A. Chase, J. L. Fulton, D. M. Camaioni, D. H. Mei, M. Balasubramanian, V. T. Pham, C. Zhao, R. S. Weber, Y. Wang and J. A. Lercher, *Journal of Physical Chemistry C*, 2013, **117**, 17603-17612.
300. H. A. Aleksandrov, S. M. Kozlov, S. Schauermann, G. N. Vayssilov and K. M. Neyman, *Angewandte Chemie-International Edition*, 2014, **53**, 13371-13375.
301. T. B. Flanagan and W. A. Oates, *Annual Review of Materials Science*, 1991, **21**, 269-304.
302. Y. P. Khodyrev, R. V. Baranova, R. M. Imamov and S. A. Semiletov, *Kristallografiya*, 1978, **23**, 1046-1048.
303. F. Studt, F. Abild-Pedersen, T. Bligaard, R. Z. Sorensen, C. H. Christensen and J. K. Norskov, *Angewandte Chemie-International Edition*, 2008, **47**, 9299-9302.
304. R. Feenstra, R. Griessen and D. G. Degroot, *Journal of Physics F-Metal Physics*, 1986, **16**, 1933-1952.
305. M. Johansson, E. Skulason, G. Nielsen, S. Murphy, R. M. Nielsen and I. Chorkendorff, *Surface Science*, 2010, **604**, 718-729.
306. D. Teschner, J. Borsodi, Z. Kis, L. Szentmiklosi, Z. Revay, A. Knop-Gericke, R. Schlogl, D. Torres and P. Sautet, *Journal of Physical Chemistry C*, 2010, **114**, 2293-2299.
307. J. Greeley, J. Rossmeisl, A. Hellman and J. K. Norskov, *Zeitschrift Fur Physikalische Chemie-International Journal of Research in Physical Chemistry & Chemical Physics*, 2007, **221**, 1209-1220.

308. J. K. Norskov, T. Bligaard, A. Logadottir, S. Bahn, L. B. Hansen, M. Bollinger, H. Bengaard, B. Hammer, Z. Sljivancanin, M. Mavrikakis, Y. Xu, S. Dahl and C. J. H. Jacobsen, *Journal of Catalysis*, 2002, **209**, 275-278.
309. A. Michaelides, Z. P. Liu, C. J. Zhang, A. Alavi, D. A. King and P. Hu, *Journal of the American Chemical Society*, 2003, **125**, 3704-3705.
310. A. Michaelides, P. Hu and A. Alavi, *Journal of Chemical Physics*, 1999, **111**, 1343-1345.
311. V. Ledentu, W. Dong and P. Sautet, *Journal of the American Chemical Society*, 2000, **122**, 1796-1801.
312. G. W. Peng, S. J. Sibener, G. C. Schatz, S. T. Ceyer and M. Mavrikakis, *Journal of Physical Chemistry C*, 2012, **116**, 3001-3006.
313. A. D. Johnson, S. P. Daley, A. L. Utz and S. T. Ceyer, *Science*, 1992, **257**, 223-225.
314. S. P. Daley, A. L. Utz, T. R. Trautman and S. T. Ceyer, *Journal of the American Chemical Society*, 1994, **116**, 6001-6002.
315. J. Greeley, W. R. Krekelberg and M. Mavrikakis, *Angewandte Chemie-International Edition*, 2004, **43**, 4296-4300.
316. B. Bhatia and D. S. Sholl, *Journal of Chemical Physics*, 2005, **122**, 8.
317. C. Samanta and V. R. Choudhary, *Catalysis Communications*, 2007, **8**, 2222-2228.
318. J. A. Rodriguez and D. W. Goodman, *Science*, 1992, **257**, 897-903.
319. J. H. Larsen and I. Chorkendorff, *Surface Science*, 1998, **405**, 62-73.
320. Y. Xu and M. Mavrikakis, *Surface Science*, 2001, **494**, 131-144.
321. Y. Xu and M. Mavrikakis, *Journal of Physical Chemistry B*, 2003, **107**, 9298-9307.
322. M. Piccinini, E. Ntainjua, J. K. Edwards, A. F. Carley, J. A. Moulijn and G. J. Hutchings, *Physical Chemistry Chemical Physics*, 2010, **12**, 2488-2492.
323. U. K. Singh and M. A. Vannice, *Applied Catalysis A-General*, 2001, **213**, 1-24.
324. R. J. Madon and E. Iglesia, *Journal of Molecular Catalysis A-Chemical*, 2000, **163**, 189-204.
325. M. Salciccioli, M. Stamatakis, S. Caratzoulas and D. G. Vlachos, *Chemical Engineering Science*, 2011, **66**, 4319-4355.
326. L. R. Merte, G. W. Peng, R. Bechstein, F. Rieboldt, C. A. Farberow, L. C. Grabow, W. Kudernatsch, S. Wendt, E. Laegsgaard, M. Mavrikakis and F. Besenbacher, *Science*, 2012, **336**, 889-893.
327. S. Desai and M. Neurock, *Electrochimica Acta*, 2003, **48**, 3759-3773.
328. T. Moreno, J. Garcia-Serna and M. Jose Cocero, *Green Chemistry*, 2010, **12**, 282-289.
329. A. Logadottir, T. H. Rod, J. K. Norskov, B. Hammer, S. Dahl and C. J. H. Jacobsen, *Journal of Catalysis*, 2001, **197**, 229-231.
330. M. A. Barteau, *Catalysis Letters*, 1991, **8**, 175-184.
331. V. Pallassana and M. Neurock, *Journal of Catalysis*, 2000, **191**, 301-317.
332. Z. P. Liu and P. Hu, *Journal of Chemical Physics*, 2001, **114**, 8244-8247.
333. P. Ferrin, D. Simonetti, S. Kandoi, E. Kunkes, J. A. Dumesic, J. K. Norskov and M. Mavrikakis, *Journal of the American Chemical Society*, 2009, **131**, 5809-5815.
334. L. Grabow, Y. Xu and M. Mavrikakis, *Physical Chemistry Chemical Physics*, 2006, **8**, 3369-3374.
335. J. A. Herron, J. Jiao, K. Hahn, G. W. Peng, R. R. Adzic and M. Mavrikakis, *Electrocatalysis*, 2012, **3**, 192-202.
336. M. H. Shao, P. Liu, J. L. Zhang and R. Adzic, *Journal of Physical Chemistry B*, 2007, **111**, 6772-6775.